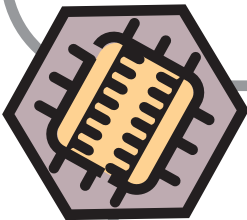
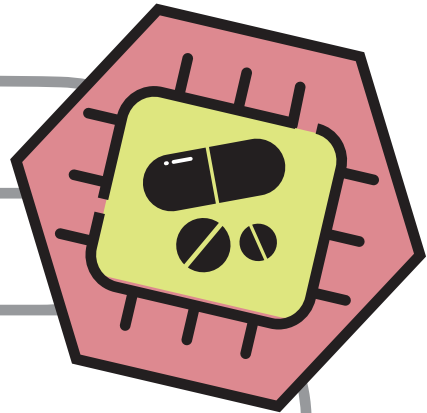


Human gut-on-chip as an intestinal model to predict compound absorption and toxicity



Kornphimol Kulthong

Propositions

1. Gut-on-chip models provide a promising *in vitro* tool to study absorption and toxicity of food-borne chemicals.
(this thesis)
2. The fluid flow applied in gut-on-chip devices influences the experimental outcome.
(this thesis)
3. Diagnostic endpoints detecting signs of a disease without identifying the actual disease involved are useless to define a treatment strategy.
4. Genome wide association studies (GWAS) describing genotype-phenotype connections provide a powerful approach to devise breeding strategies for the development of drought tolerant plants.
5. Comments raised by reviewers during the publication process stimulate formulation of new ideas for future work.
6. Smartphone applications motivate people to physically exercise more in daily life.
7. The most difficult person to deal with during a PhD project is oneself.

Propositions belonging to the thesis, entitled

“Human gut-on-chip as an intestinal model to predict compound absorption and toxicity”

Kornphimol Kulthong

Wageningen, 07 December 2020

***Human gut-on-chip as an intestinal model to
predict compound absorption and toxicity***

Kornphimol Kulthong

Thesis committee**Promotor**

Prof. Dr Ivonne M.C.M. Rietjens
Professor of Toxicology
Wageningen University & Research

Co-promotors

Dr Hans Bouwmeester
Associate Professor of Toxicology
Wageningen University & Research

Dr Meike van der Zande
Scientist
Wageningen Food Safety Research

Other members

Prof. Dr. E.M.J. Sabeth Verpoorte, University of Groningen
Prof. Dr. J.M. Jerry Wells, Wageningen University & Research
Dr. Chuda Chittasupho, Chiang Mai University, Thailand
Dr. Evita van de Steeg, Netherlands Organisation for Applied Scientific Research (TNO),
Zeist

This research was conducted under the auspices of the Graduate School VLAG
(Advanced Studies in Food Technology, Agrobiotechnology, Nutrition and Health
Sciences)

***Human gut-on-chip as an intestinal model to
predict compound absorption and toxicity***

Kornphimol Kulthong

Thesis

submitted in fulfilment of the requirements for the degree of doctor
at Wageningen University

by the authority of the Rector Magnificus

Prof. Dr A.P.J. Mol,

in the presence of the

Thesis Committee appointed by the Academic Board

to be defended in public

on Monday 7th December 2020

at 11.00 hours in the Aula

Human gut-on-chip as an intestinal model to predict compound absorption and toxicity,
210 pages

PhD thesis, Wageningen University, Wageningen, The Netherlands (2020)

With references, with summary in English

ISBN: 978-94-6395-554-6

DOI: <https://doi.org/10.18174/531714>

Table of contents

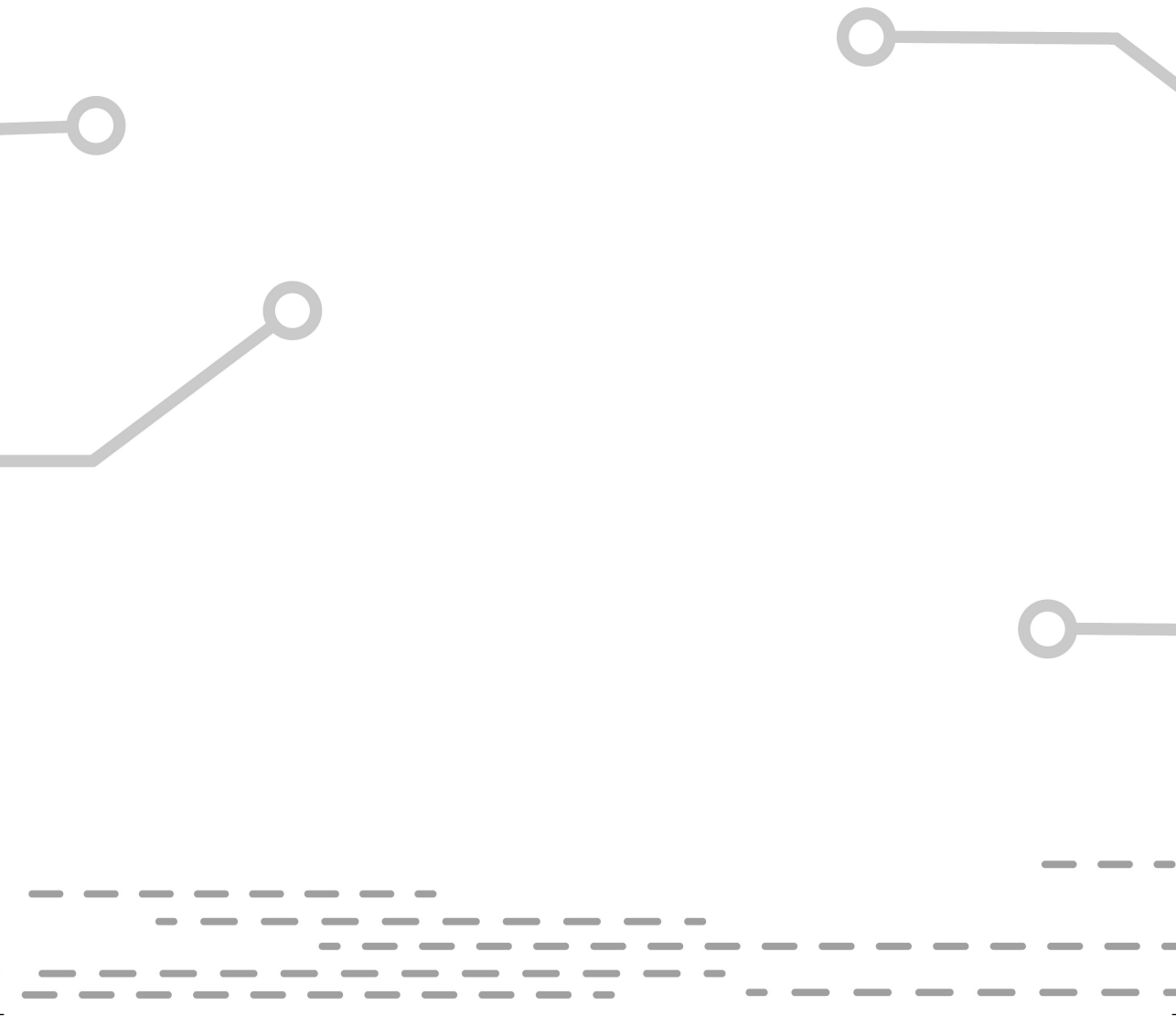
Chapter 1	General introduction	7
Chapter 2	Implementation of a dynamic intestinal gut-on-a-chip barrier model for transport studies of lipophilic dioxin congeners	33
Chapter 3	Microfluidic chip for culturing intestinal epithelial cell layers: Characterization and comparison of drug transport between dynamic and static models	61
Chapter 4	Comparative transcriptomics of epithelial cells grown under static and microfluidic gut-on-chip conditions and benchmarked against human <i>in vivo</i> intestinal cells	85
Chapter 5	Comparative transcriptomes of Caco-2 cells cultured under dynamic and static conditions following exposure to titanium dioxide and zinc oxide nanomaterials	115
Chapter 6	General discussion and future perspectives	181
Chapter 7	Summary	197





CHAPTER 1

General introduction



At present, the golden standard in the field of toxicological risk and safety assessment is still the use of animal models. However, within the field of toxicological research efforts are made to develop and implement *in vitro* models to predict human hazards following exposure to compounds. The potential of *in vitro* models for the intestine for both biokinetic and biodynamic studies is increasingly recognized by regulatory bodies [1-4]. However formal incorporation of these models in regulatory toxicology is still limited [5-7]. Ideally, intestinal *in vitro* models must be easy to implement, relevant, cost effective, accurate, and predictive to the human situation. In this thesis, the development and characterization of an *in vitro* gut-on-chip as a model for the small intestine, in which dynamic condition and cell culture are combined, is presented. Before describing the state-of-the-art of developments in *in vitro* models for the intestine, the anatomy and functions of the intestine will be discussed.

Introduction to the small intestine

The small intestine is a crucial component of the digestive system allowing the digestion of food and absorption of nutrients to supply the body with energy to function properly. The length of the small intestine varies from 10 to 33 feet (3-10 metres, with an average length of approximately 6.5 metres in an adult) [8] and it is divided into three sections (Fig.1). The first section is the duodenum, which is the shortest section, on average measuring from 20 cm to 25 cm in length. It is the most proximal section of small intestine which is connected to the antrum of the stomach, separated by the pylorus. Bile and pancreatic enzymes are secreted in the duodenum via the duodenal papilla. The second section is the jejunum which is roughly 2.5 meters in length. In the jejunum the typical small intestinal macroscopic structure appears consisting of a highly folded mucous membrane containing villi at the top protruding into the lumen, which are much longer than those in the duodenum or ileum. This results in an enlarged surface that facilitates the absorption of the products of digestion. The last section is the ileum, which is approximately 3.5 meters in length and absorbs nutrients that got past the jejunum. The ileum terminates at the ileocecal junction and continues as the large intestine [9, 10].

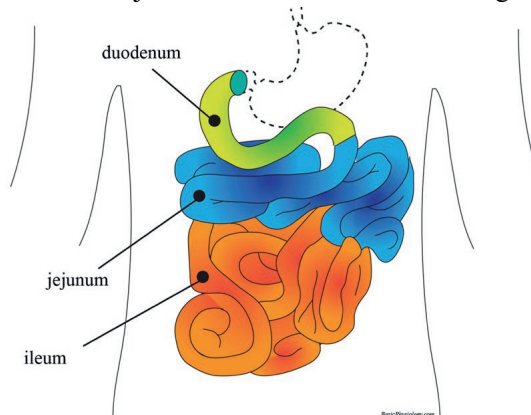


Figure 1. An illustration of the small intestine anatomy (downloaded from BasicPhysiology .com; <http://www.basicphysiology.com/index.html> with permission)

The lumen-facing surface of the small intestine is also called the mucosa. Together with the underlying submucosa, muscularis externa, and the serosa it forms the intestinal tissue (Fig 2). The mucosa itself is composed of three distinct layers, 1) epithelium: a monolayer of different types of cells, each with a specific function, which lines the interior lumen of the gastrointestinal tract, 2) lamina propria: connective tissue supporting the epithelial cells with a dense vascular and lymphatic network, 3) muscularis mucosae: a thin layer of smooth muscle playing an important role in intestinal peristalsis and contraction [10, 11]. In the intestinal epithelium at least eight cell types have been identified. Besides enterocytes, these include cup cells, enteroendocrine cells, goblet cells, M cells, Paneth cells, tuft cells and stem cells, (Table 1), where enterocytes are the major cell type involved in nutrient absorption [12-15]. Enterocytes are polarized columnar cells that contain a brush border at the luminal side consisting of approximately 3000 microvilli per cell that further increases the absorptive surface of the small intestine.

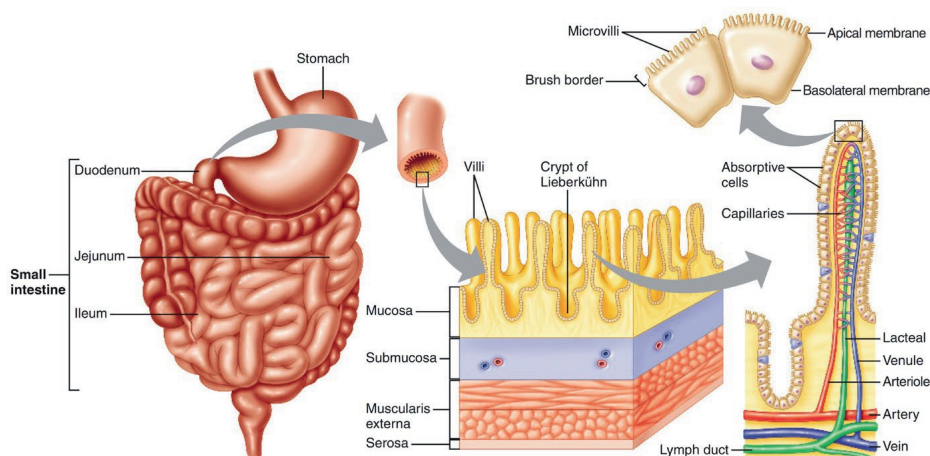


Figure 2. Anatomy of the small intestine. The duodenum, jejunum, and ileum are shown in relation to other GI tract organs; the enlarged views show the structure of villi and microvilli in the duodenum (exported from Principles of human physiology, global edition, page 603, Stanfield, C. L. (2017) with permission from Pearson Education Limited and Copyright) [16].

Table 1. Intestinal epithelial cell types and function

Cell	Structure and Function
Enterocytes	Columnar cells: Most abundant absorptive cells of the small intestine that are located along the crypt-villus axis
Paneth cells	Pyramid-shaped cells: Secretory cells that reside in the crypts and secrete lysozyme and antibiotic proteins
Enteroendocrine cells	Basal-granulated cells: Hormone producing cells (i.e. somatostatin, serotonin, glicentin) that represent up to 1% of all cells in the epithelium and are embedded between enterocytes
Goblet cells	Goblet cells: Mucin-secreting cells that are located between the enterocytes
M cells	Epithelial cells without microvilli: Specialized intestinal epithelial cells that sample antigens and pathogens through endocytosis, these cells are found in the Peyer's patches
Cup cells	Wine glass-shaped cup cells: Still unknown function
Tuft cells	Epithelial cells with unique microfilaments: Chemoreceptor cells that represent approximately 0.5% in the epithelial cell lining
Stem cells	Columnar cells: progenitor cells of epithelial cell lineages that are located in the crypt base

Basic functions of the small intestinal epithelium

The intestinal epithelium is a critical interface between the organism and its environment. The structural properties of the enterocytes provide a physical and immunological barrier that limits access of substances or antigens to the systemic circulation. The barrier regulates the absorptive capacity, the primary function of the small intestine, and local responses of intestinal epithelial cells which both are of most relevance for the work described in this thesis.

Absorption and transport

Epithelial cells form a barrier that offers limited passage of materials in both directions. Cell-cell adhesion is ensured by tight junctions, desmosomes and adherens junctions. Transport across epithelial cells can occur through different pathways, either through the cells (transcellular) or through the cell junctions (paracellular) and with or without the expense of free energy. Which pathway is preferred depends on the size, hydrophobicity and other

chemical characteristics of the molecule to be transported [17-19]. The main routes of transport are:

- Passive transport: This form of transport is non-energy dependent and can be transcellular or paracellular. Chemicals can only be transported along the concentration gradient.
 - Transcellular transport can be simple diffusion, in which chemicals directly pass through the hydrophobic membrane, or facilitated diffusion, in which diffusion is facilitated by transport channels or carriers.
 - Paracellular transport is based on diffusion of small hydrophilic chemicals through the cell junctions.
- Active transport: This form of transcellular transport requires an energy source to drive molecules or ions through the cell membrane.
 - Transporter mediated transport requires a dedicated transporter and is molecule specific.
 - Vesicular transport is based on cellular internalization of compounds by engulfing them with the cell membrane resulting in an intracellular vesicle (i.e. endocytosis, pinocytosis, phagocytosis and receptor-mediated endocytosis).

Innate mucosal immunity

The epithelium in the small intestine allows selective absorption of nutrients while simultaneously protecting against penetration of antigens and pathogens. The defence against pathogens and antigens is a combination of the physical barriers of the epithelium and the immunological function of the barrier [20]. Besides the physical barrier function, imposed by tight junctional complexes allowing only passage of small molecules that are generally not immunogenic, the enterocytes are able to detect pathogens through pathogen recognition receptors (i.e. Toll-like, Nod-like receptors) leading to the activation of three major signalling pathways: the nuclear factor (NF)- κ B, the mitogen-activated protein kinases (MAPKs) and the interferon regulatory factor (IRF) mediated pathways [21, 22]. Activation of these pathways regulates the production of inflammatory and homeostatic cytokines such as TNF, IFN- γ , interleukins, IL-4 and TGF- β , which orchestrate and coordinate trafficking of mucosal inflammatory and immune effector cells and affect barrier permeability [23]. The barrier function of the enterocytes is completed by the glycocalyx which is composed of mucin proteins forming chemical or physical barriers and anti-microbial peptides (AMP), such as β -defensins.

Aim of this thesis

The complex anatomy and physiology of the human small intestine poses a challenge when defining alternative testing strategies to characterise intestinal absorption and toxicity. The present research aimed to characterise the potential of an alternative *in vitro* gut-on-chip

model with a continuous liquid flow to study intestinal absorption and toxicity. This resulted in the following research objectives:

- To optimize and characterize a gut-on-chip model in terms of morphology, selective compound barrier functions, and gene expression profile.
- To determine the potential of the optimized gut-on chip-model as an *in vitro* model for human intestinal permeability and toxicity studies.
- To compare the characteristics and functionality of the developed gut-on chip with those of a static Transwell model and human intestinal tissues.

To achieve these objectives, a glass-based chip was used to culture epithelial cells under the optimized dynamic conditions. Upon morphologic characterization a selected range of model compounds were used for transport studies including 17 dioxin congeners with different physicochemical properties that are well known food contaminants, and selected pharmaceuticals (i.e. antipyrine, ketoprofen, digoxin, amoxicillin) with well-known uptake profiles from traditional static *in vitro* models and from human *in vivo* studies. These studies were followed by a comparative gene expression study of cells cultured in the gut-on-chip and in Transwells and human intestinal tissues. Finally, a comparative gene expression study was performed evaluating the effects on gene expression profiles of a nanomaterial (TiO₂ and ZnO) exposure in the gut-on-chip versus the Transwell model.

Compounds/materials relevant to this thesis

Dioxins

To assesses the barrier properties of the gut-on-chip model, dioxins were selected as an important class of food contaminants, which can enter the human body via the oral exposure route. Dioxins, also called polychlorinated dibenzodioxins, are persistent organic pollutants (POPs) which are a cause of concern for environmental and human health, due to a range of reported adverse effects including reproductive impairment, skin lesions, immune system modulation, hormonal imbalance, and an increase in cancer risk [24, 25]. Because of their lipophilic properties (i.e. log P values ranging from ~ 6 to 8) dioxins accumulate in fatty tissues of animals in the food chain and ingestion is the primary source of dioxin exposure to the human body [26, 27]. About 20 congeners of dioxins may be absorbed through daily meals and 17 of them are present in a reference mixture used for the food monitoring programme of the EU [28]. This mixture is used for the work in this thesis as well. Since the gut epithelium acts as an important barrier to protect the body from exogenous substances present in food, the barrier properties of cells cultured in the gut-on-chip system towards dioxin exposure were evaluated and compared with those of cells cultured in the static condition.

Pharmaceuticals

Some pharmaceuticals (i.e. antipyrine, ketoprofen, digoxin and amoxicillin) were selected as model compounds to determine the barrier function of the gut-on-chip model based on the available information on their *in vitro* permeability and in *in vivo* bioavailability. It was assured that selected compounds fell in high and low permeability compound classes (according to the Biopharmaceuticals Classification System-BCS). These compounds pass the intestinal epithelium employing different absorption mechanisms. Antipyrine, ketoprofen and digoxin are high permeability compounds (Class I and II), whereas amoxicillin is a low permeability compound (Class III) [29, 30]. With regard to the absorption mechanism, antipyrine is absorbed passively and transcellularly [31], while amoxicillin is mainly actively transported via a carrier-mediated system [32]. Ketoprofen is reported to be transported by both active transport and passive transcellular absorption [33, 34] and digoxin is actively transported, as it is a substrate for the efflux pump P-glycoprotein (P-gp). Thus the variety of compounds will show whether or not the gut-on-chip model can be used in studies on absorption and bioavailability of a wide range of substances.

Nanomaterials

Nanomaterials are materials with at least one dimension sized between 1 and 100 nm. They are intensively used in several areas, including food production. Due to their increased use safety concerns for human health have been raised [35, 36]. TiO₂ and ZnO nanomaterials are among the most popular food-related nanomaterials used in the food industry. E171 is a food grade TiO₂ which contains particles in the nano-size range and is authorized to be used in food [37]. ZnO nanomaterials do not have authorization to be used in food, but micro-sized ZnO is considered to be a ‘GRAS’ (generally recognized as safe) substance by the U.S. Food and Drug Administration (FDA) for use in biomedical applications [38]. In addition the two nanomaterials cover extreme physicochemical properties, where TiO₂ remains as a particle in suspension [39, 40], ZnO nanomaterials readily dissolve [41]. Recent studies indicated that E171 regulated genes encoding proteins involved in oxidative stress, inflammation and DNA repair [42, 43] and ZnO nanomaterials regulated genes encoding proteins involved in inflammation and metal responses [44, 45]. The comparative gene expression of these nanomaterials in the gut-on-chip model was investigated to further characterise the potential of the model to provide insight in cellular responses towards these nanoparticles underlying their effects on human health.

Intestinal models to study absorption and local effects

***In vivo/ex vivo/in situ* models**

There is a wide variety of animal models that may be used to assess the bioavailability and (intestinal) toxicity of compounds including mice, rats, dogs and pigs [46-48].

Rodents, like rats and mice, are commonly used *in vivo* animal models, due to their small size and low costs. However, the physiology of the rodent gastrointestinal tract is different from that in humans (e.g. lower intestinal pH and shorter intestinal transit time in

rodents compared to human). This might affect the behaviour and absorption of the compound of interest differently leading to inadequate predictions for humans. For instance, pH sensitive compounds tend to dissolve and be absorbed in the human distal small intestine and colon, where the pH is greater than 7.0, might be insoluble in the rat intestine [49-51]. On the other hand, there is a similarity in gene expression levels of many transporters between human and rats. With the exception for P-gp, multidrug resistance protein 3 (MRP3), glucose transporter 1 and glucose transporter 3, the overall drug transporters share similar expression levels in both human and rat. This allows correlation of intestinal permeability between rats and humans for both carrier-mediated and passive absorption. However, the first-pass metabolism is different between rats and humans, so a rat model may be used to study compound absorption in the small intestine, but it could be poorly predictive for compounds that are sensitive to intestinal metabolism [49, 52]. Besides in compound absorption studies, rodents, especially mice and rats are generally used to investigate intestinal lesions [53], and acute and chronic inflammation, because of similarities to human in gene homology, immune and intestinal function [54].

Dogs are also considered an appropriate animal model to predict the human absorption of compounds. This is attributed to the gross similarity in biochemistry and physiology of their gastrointestinal tract compared to humans. Like rodents, dogs are not a good model for the absorption of pH-sensitive compounds, due to a higher gastric pH in dogs than in humans. Additionally, dogs show more similar metabolic activity (intestine and liver) to humans than rats [55]. Although dogs are reported as the most frequent models used in preclinical studies to determine absorption-related interactions, primarily between food and drugs [49], recent studies indicated the differences in intestinal distribution of transporters (e.g. P-gp, ABCG2) in dogs compared with humans which may contribute to the differences in detected compound bioavailability [56, 57]. The intestinal transit times are also different between dogs and humans which might result in a lower fraction absorbed of some drugs or compounds in dogs compared to in humans [58, 59]. For toxicological studies, dogs are the nonrodent species that is frequently used as intestinal disease model such as for the IBD study because of the similarity to human pathological development [60].

Pigs are another frequently used non-rodent animal model. This is because of their gastrointestinal tract similarities compared to humans in terms of the intestinal length per bodyweight ratio, epithelial cell composition, intestinal absorptive surface area, villus structure, intestine transit time and pH pattern in the intestine. Especially the pH pattern is one distinct advantage of pig models compared to dog models, especially for absorption studies of drugs that are likely to be influenced by the pH [48, 61, 62]. However, the rate of compound absorption in pigs tends to be slower compared to that in humans. Compared to the more common rat and dog models, studies reporting expression levels of intestinal transport/metabolising enzymes in pigs are limited [48]. Pigs are considered the preferred model to study the mechanisms involved in acute and chronic intestinal injury and inflammation because of structural and functional similarities, and comparable microbial

fermentation with human. Nonetheless, the size, slow growth rate and relatively slower reproductive rates of the pig are unfavourable aspects compared to rodent animal model species [54].

Besides the animal models discussed above, where the compound of interest is applied orally and the effects are studied in the intact animal, several alternative approaches have been developed. Examples are the so-called *in situ* approaches, like intestinal single-pass perfusion, intestinal recirculating perfusion and Loc-I-Gut [63], and *ex vivo* approaches, like Ussing chambers and precision-cut intestinal slices [64-66]. In these approaches, experiments are conducted in or on tissues obtained from an organism and maintained under optimal conditions resembling the *in vivo* conditions as much as possible. While the *in situ* and *ex vivo* models might be attractive for specific research questions, these models are technically and instrumentally demanding and still demand the use of animals.

Static *in vitro* models

Even though animal models can resemble the physiology of an entire human organism, the main disadvantages of *in vivo* models are the ethical considerations, high costs and the difficulties in extrapolating results to humans due to differences between species. *In vitro* cell culture models for the intestine have been widely used in bioavailability, metabolic and toxicological studies in both food and pharmaceutical fields of research. In traditional *in vitro* cell culture models, suitable for high-throughput screening, cells are grown as two-dimensional (2D) monolayers on a flat surface, or on permeable membranes (Transwell inserts). The latter design is suitable for permeability studies, where the apical and basolateral compartments represent the intestinal lumen and systemic compartments, respectively. To date, several different intestinal cell types can be cultured separately or in co-cultures aiming to represent the complex functions and morphology of the intestinal epithelium. These cell types range from cell lines to primary cells, while more recently also stem cell-based models are being developed.

Primary human intestinal epithelial cells are obtained from the small intestine or the colon and express all intestinal epithelial cell types. These cells can form a monolayer, as confirmed by TEER measurements, and express intestinal cell-type specific markers. Primary human intestinal epithelial cell models are suitable as cell-based *in vitro* assays to study the intestinal transport of compounds and other endpoints (e.g. immune responses, cytotoxicity) [67-69]. Nonetheless, difficulty to obtain cells, low reproducibility and the short life span of primary tissue cultures are the main drawbacks of the model.

Due to drawbacks of primary cell cultures of small intestinal tissue, cell lines derived from gastrointestinal tumours have been commonly utilized. Cell lines are preferable over complex models if applicable for the research question, because of their easy accessibility, handling and maintenance, which makes them suitable for mechanistic studies or high-throughput screening approaches. A number of different intestinal immortalized cell models exist. Caco-2 cells, a cell line obtained from a human colon adenocarcinoma, are the most

regularly used cells as a model for the intestinal epithelium. They behave similarly to enterocytes after a differentiation period, including absorptive functionality and brush border enzyme expression. Although, there are several apparent differences between the Caco-2 cell model and the *in vivo* tissue, such as higher TEER than those described *in vivo* [70], lack of a mucus layer and lack of other cell types than enterocytes [71], they have been accepted as a standard model for prediction of intestinal drug permeability in humans by pharmaceutical companies and regulatory authorities [72, 73]. The coculture model of Caco-2 and mucus producing HT29-MTX cell lines has been developed to mimic both enterocytes and goblet cells and reported to form a mucus layer as *in vivo* [74, 75]. In addition, more complex models using cell lines have been created by co-culturing with immune cells (Raji, THP-1, RAW264.7 cells) to represent components of the local immune system [76-78].

More recently, adult stem cell and induced pluripotent stem cell (iPSCs) based intestinal models are being explored as an alternative for the use of primary intestinal cells (and cell line models) for intestinal transport and toxicity studies. To date, only a limited number of studies have been performed in which adult stem cells or iPSCs were differentiated into intestinal cells and cultured as a (mono) layer to study drug transports and drug-metabolizing enzymes. In the study of Komada et al., for instance, iPSCs were differentiated to enterocyte-like cells and were able to accurately predict the oral absorption of paracellularly absorbed compounds [79]. Intestinal epithelial cells differentiated from iPSCs also exhibited drug-metabolizing enzymes (i.e. CYP 3A4, CYP2C9, carboxylesterase) more similar to the human small intestinal cells than what was detected in Caco-2 cells [80-82]. The conditions for the long-term culturing of adult intestinal stem cells and their differentiation into enterocytes as a monolayer for compound permeability studies have been also established. It was shown that this cellular model was a superior alternative to the Caco-2 monolayer with respect to expression of a sodium-dependent transporter (SLC28A3) [83]. In addition, an attempt has been made to establish a two-dimensional model for culturing Lgr5+ intestinal stem cells differentiating them into intestinal epithelium cells to enable drug transport studies [84]. However, despite the physiological relevance, the current protocols do not give sufficiently high purity of enterocyte populations which are needed for drug evaluation studies [85]. The costs and time necessary for stem cell differentiation are also major disadvantages of using stem cell models.

Dynamic *in vitro* models

A recent development in the field of *in vitro* models is the introduction of microfluidic technology that is used to develop novel cell culture chips. This novel field is coined as organ-on-chip research. Numerous microfluidic systems or organ-on-chip systems have been published by now. It has been suggested that organ-on-chip platforms will provide important innovations in the field of drug discovery and toxicity testing by enabling high-throughput screening and real-time analysis [86-89]. Uniquely, microfluidic chips accommodate a fluid flow, an important physiological condition *in vivo* that is not present in static culture models,

providing researchers the capability to develop more physiologically relevant models. Improving the physiology and biology of *in vitro* models would ideally lead to models with a higher predictive power than current static *in vitro* models where the behaviour and morphology of the cells is not similar to cells *in vivo*. This could lead to a significant reduction of the use of animal experiments.

Gut-on-chip models

Gut-on-chip devices have been developed in various designs with different dimensions of cell culture chambers including for example circular shapes as seen in conventional culture plates [90, 91], straight channels or tube-like designs [92, 93]. The flow in gut-on-chip devices is generally generated by a pump system; a motor driven (syringe) pump [92], a pressure driven (pneumatic) pump [94] or a peristaltic pump [95]. Another method of generating a flow is by generating a gravity driven flow in alternating directions using a rocker platform [96]. The gut-on-chip (or dynamic intestinal) models described in literature, as well as their applications and the study findings, that are relevant to the work in this thesis are presented in Tables 2 and 3.

At present, most gut-on-chip devices are fabricated using Polydimethylsiloxane (PDMS), which has some advantages and limitations. PDMS is attractive because of its low costs, ease of use, high compliance, microscope compatibility and fast fabrication properties. However, PDMS has a number of important limitations regarding its use in biomedical studies. One of those limitations is adsorption of various molecules (particularly small hydrophobic molecules) by PDMS because of its permeable and hydrophobic properties which could dramatically affect (reduce) free compound concentrations and hence the exposure concentration and subsequent effects [97, 98]. Furthermore, the high permeability of PDMS allows gas exchange, indicating that evaporation can occur during an experiment which could greatly affect the cell microenvironments at micro- and nanolitre fluid volumes [99]. Although techniques have been developed to reduce these issues, like coating of the microchannel surface, they could only partially prevent adsorption which makes PDMS an undesired material for cell biology applications [100, 101]. Given these limitations, alternative materials have been used for organ-on-chip models, such as polylactic acid (PLA) [102], polymethyl methacrylate (PMMA) [103], polycarbonate [104] to avoid non-specific binding. Therefore, in this thesis use was made of a commercially available chip device made from glass consisting of an upper apical (AP) and lower basolateral (BL) chamber separated by a porous membrane on which intestinal epithelial cells can be cultured. The device allows separate flows through the apical and basolateral chamber.

The flow of fluid across the cell surface is directly proportional to the velocity of the surrounding fluid, and causes shear stress on the cells [105]. Variations in the flow rate or pattern (e.g. laminar or turbulent flow) and variations in microfluidic chip geometries result in different shear stress levels on the cells, which is critical in the context of cell culture, as shear forces can alter the cellular behaviour and functions. Literature revealed the potential

of gut-on-chip models to simulate the *in vivo* intestinal physiology and provide improved culturing conditions compared with static models. For example, acceleration of cell differentiation and promotion of microvilli formation and cytochrome P450 expression compared with cells cultured under static conditions have been described, as presented in Table 3. Besides shear stress also peristalsis-like mechanical stress has been incorporated in a gut-on-chip model in order to closely mimic the physiological environment which increased aminopeptidase activity and paracellular permeability of the epithelial cells [92] (Table 3). Gut-on-chip models have the potential to be used to evaluate compound permeability and toxicity. The results described in literature, however, are currently inconclusive. Permeability characteristics varied versus conventional static models. For example, the permeability of compounds has been described to be both lower and higher in comparison with a static model depending on the compound used in studies and the experimental setup (Table 2). For the toxicity study of chemicals, there is no literature revealing a result in comparison between epithelial cells cultured under a dynamic and static model. Another potential advantage of utilizing dynamic gut-on-chip devices is the possibility to combine them with other organ-on-chip platforms, which increases the capability to mimic the *in vivo* situation

Since the field of organ-on-chip technology is still in its infancy with no standard accepted model, the most of the past work on model development has been carried out in academic laboratories generally without good manufacturing practice (GMP) or good laboratory practice (GLP) certifications, which may lead to inconsistencies between different manufacturing batches or biological testing. To bring the most benefit to the development of this technology in terms of biological testing, it is important to focus on the qualification of the devices and the identification of well-defined contexts of use. The typical qualification process applied to organ-on-chip models is to make a comparison between data derived from conventional *in vitro* approaches and human clinical data if available [106], as proposed in this thesis.

Linking *in vitro* models to *in silico* models

Combinations of *in vitro* and *in silico* approaches are increasingly employed in toxicological studies. There are several reasons why the combination of *in vitro* and *in silico* testing methods are heavily studied. First of all, the direct use of *in vitro* toxicity data in risk assessment remains challenging. To extrapolate the *in vitro* obtained concentration-response curves to *in vivo* dose-response curves, physiologically based kinetic (PBK) modelling-based reverse dosimetry is used [107]. In PBK modelling approaches physicochemical data of the compounds and *in vitro* obtained uptake and metabolism data are combined [108-110]. A second reason, and closer to the topic of this thesis, is to include *in silico* modelling into a testing strategy to predict the bioavailability parameters based on physicochemical information of the compounds. Such approaches can provide fast predictions for a large set of compounds. Several theoretical methods for the prediction of bioavailability have been implemented based on molecular structure information of a compound such as in quantitative

structure-activity relationship (QSARs) [111]. These computer programs using QSARs relate various molecular descriptors and physicochemical properties of a compound (e.g., lipophilicity, the logarithmic acid dissociation constant pKa, hydrogen bonds, molecular mass) to crucial pharmaceutical processes [112]. QSAR models evolve in so-called read-across approaches. Then computer-based approaches are used to predict endpoint information for one substance (target substance) by using the available experimental data of (an)other substance. The bioavailability and toxicity of non-tested compounds (or conditions) could be predicted based on information collected from structurally similar compounds that were conducted [113, 114]. Thus depending on the research question several powerful approaches are available to integration of *in vitro* assays with *in silico* models, which are important developments for future studies.

Table 2. Gut-on-chip (dynamic culture) models as intestinal epithelial barriers for biokinetic and local effect studies

Cell model	Fabrication material	Flow rate: Shear stress	Downstream connection	Compared to static model	Findings	Ref.
Caco-2 cells	PDMS	10-100 $\mu\text{L}/\text{min}$: 7.21×10^{-3} dyne/ cm_2	Yes; spectrophotometer	No	- The chip device could be integrated with online detection and used to determine rhodamine 123 permeability. - Cyclophosphamide permeability detected in the chip device was comparable to the static model.	[115]
Caco-2 cells	PDMS and glass	Culture condition; static Transport experiment; 1 $\mu\text{L}/\text{min}$: n/a	No	Yes	- Cyclophosphamide permeability detected in the chip device was comparable to the static model.	[116]
Caco-2 cells	PDMS	Culture condition; static Transport experiment; 20 $\mu\text{L}/\text{h}$: n/a	No	No	- Permeability of antipyrine, propranolol, naproxen, furosemide, verapamil, atenolol, piroxicam, hydrochlorothiazide, cimetidine and carbamazepine was determined in the chip device which was correlated with <i>in vivo</i> human intestine data.	[117]
Caco-2 cells	PDMS and glass	Culture condition; static Compound exposure; 0.4 $\mu\text{L}/\text{min}$: n/a	Yes: liver and breast cancer platforms	No	- The chip device could be used to study cyclophosphamide absorption, metabolism and bioactivity.	[118]
Caco-2 cells	PDMS	0.1 $\mu\text{L}/\text{min}$: n/a	Yes; ESI-Q-TOF MS	No	- The chip device could be integrated with online detection and used to determine curcumin permeability.	[119]
Caco-2 cells	PDMS	Culture condition; static Transport experiment; 200 and 100 $\mu\text{L}/\text{min}$ for AP and BL side: n/a	No	Yes	- Fluorescein permeability obtained from cells exposed to the fluid flow in the chip device was higher than the static model.	[90]
Caco-2 cells	PDMS	0.4 $\mu\text{L}/\text{min}$: 0.02 dyne/ cm_2	No	Yes	- Differentiation, monolayer and microvilli formation of cells was accelerated in the presence of flow. - Permeability of caffeine and atenolol in the chip device was higher than the static model	[120]
Caco-2 cells	PDMS, PMMA, glass and Transwell insert	6.6 and 14.3 $\mu\text{L}/\text{min}$ for AP and BL side: 4×10^{-5} dyne/ cm_2 (AP)	Yes; 3D liver cell platform	No	- The chip device could be used to study pharmacokinetic (PK) profile of acetaminophen.	[121]

Table 2. Gut-on-chip (dynamic culture) models as intestinal epithelial barriers for biokinetic and local effect studies (continued)

Cell model	Fabrication material	Flow rate: Shear stress	Downstream connection	Compared to static model	Findings	Ref.
Caco-2 cells	PDMS and polycarbonate	Culture condition; static Compound exposure; 680 $\mu\text{L}/\text{min}$: n/a	Yes; liver, colon cancer and connective tissue platforms	No	- The four organ-on-chip was established and it enabled to evaluate effects of anticancer drugs (capecitabine, tegafur, and 5-fluorouracil) on cells - Cell differentiation, mucus production, P-gp expression, aminopeptidase level was promoted in the chip device. - Permeability of mannitol and insulin in the chip device was comparable to the static model.	[122]
Caco-2 cells	Thiol-ene-based	3 $\mu\text{L}/\text{min}$: 0.008 dyne/cm ²	No	Yes	- Dose-dependent effects of acetaminophen in culture medium or chyme were observed on cells cultured in the chip device. - The chip device could be used to study effects of acetaminophen metabolites.	[123]
Caco-2 cells and HT29-MTX	PMMA (plexiglass)	3.5 $\mu\text{L}/\text{min}$: n/a	Yes; liver cell platform	No	- The chip device could be used to study first pass metabolism of carboxylated polystyrene nanoparticles - Nanoparticles travelled across gut cell barrier to liver platform have been detected in the chip device.	[124]
Caco-2 cells and HT29-MTX	Silicon	Culture condition; static Transport study; 3.59 $\mu\text{L}/\text{min}$: n/a	Yes; liver cell platform	No	- The chip device could be used to study acetaminophen absorption. - Acetaminophen absorption obtained in the chip device was not significantly affected by a fluid flow.	[125]
Caco-2 cells and HT29-MTX	Transwell insert (with flow-through platform)	Culture condition; static PK study: 0.7 dyne/cm ²	Yes; liver cell platform	NO	- Permeability of verapamil in the dynamic device was comparable to the static model whereas of ergotamine and ergotamine was lower than the static model.	[126]
Caco-2 cells and HT29-MTX	Transwell insert (with flow-through platform)	Culture condition; static Transport experiment; 200 and 100 $\mu\text{L}/\text{min}$ for AP and BL side: n/a	Yes; UPLC-QTOF-MS	Yes		[127]

Table 3. Characterization of gut-on-chip (dynamic culture) models upon exposed to fluid shear stress

Cell model	Fabrication material	Flow rate: Shear stress	Downstream connection	Compared to static model	Findings	Ref.
Caco-2 cells	PDMS	0.5 $\mu\text{L}/\text{min}$: 0.02 dyne/cm ²	No	Yes	- The chip device promoted 3D structure, mucin production and, CYP3A4 expression of cells and regeneration and differentiation of proliferative crypts. - Optimal conditions for mucin production were examined.	[128]
Caco-2 cells	PDMS	0.1-10 $\mu\text{L}/\text{min}$: 0.4-40x10 ⁻⁴ dyne/cm ²	No	Yes	- The chip device promoted cell differentiation, mucin production, microvilli formation, aminopeptidase activity and TEER.	[91]
Caco-2 cells	PDMS	n/a: ~0-0.03 dyne/cm ²	No	Yes	- Application of fluid shear stress significantly altered mucus production, tight junction and microvilli formation, cytoskeleton organization, mitochondrial activity and CYP450 expression of cells.	[129]
Caco-2 cells	PDMS	0.5 $\mu\text{L}/\text{min}$: 0.02 dyne/cm ²	No	No	- A basolateral flow in the chip device was necessary for 3D structure formation of cells.	[130]
Caco-2 cells and LGG bacteria	PDMS	0.5 $\mu\text{L}/\text{min}$: 0.02 dyne/cm ²	No	Yes	- The chip device promoted cell differentiation, monolayer and microvilli formation and TEER. - Combining peristalsis motion with the flow enhanced dextran permeability and aminopeptidase activity. - The chip device could support LGG growth.	[92]

Table 3. Characterization of gut-on-chip (dynamic culture) models upon exposed to fluid shear stress (continued)

Cell model	Fabrication material	Flow rate: Shear stress	Downstream connection	Compared to static model	Findings	Ref.
Caco-2 cells, commensal microbes (8 strains), <i>E. coli</i> and PBMCs	PDMS	0.5 $\mu\text{L}/\text{min}$: 0.02 dyne/cm ₂	No	Yes	- The chip device provided better recapitulation to human tissue in terms of transcriptome profiles and enabled the co-culture cells with bacteria and evaluation of inflammatory responses.	[131]
Caco-2 cells and <i>E. coli</i>	PDMS	0.5-5 $\mu\text{L}/\text{min}$: n/a	No	Yes	- The chip device enabled the co-culture cells with bacteria and evaluation of chloramphenicol effects. - Effects of flow on nutrient supply, cell proliferation and migration, as well as 3D structure formation were observed. - The chip device promoted cell proliferation rates.	[132]
Human primary cells and HIMECs	PDMS	1 $\mu\text{L}/\text{min}$: n/a	No	Yes	- The chip device enabled culture of primary cells. - Co-culture with HIMECs accelerated cell monolayer formation. - The chip device provided better recapitulation to human tissue in terms of gene expression patterns, morphology and multicellular composition.	[133]

Thesis overview

Many gut-on-chip models have been developed and characterized, but almost all chip devices are based on PDMS (as shown in Table 2 and 3), which limits their use for biological studies and large scale manufacturing. Therefore, the objective of this thesis was to optimize and characterize a commercially available glass-based chip which has excellent chemical resistant properties. To this end a novel gut-on-chip model to culture intestinal epithelial cells under fluid flow was optimized, extensively characterized and compared with respect to its functionality for permeability and effect studies to traditionally used static models.

Chapter 1 contains background information about human small intestinal physiology and functionality and about the existing *in vivo* and *vitro* models that are used to mimic the functionality of the human small intestine, with a focus on dynamic culture conditions. In **Chapter 2**, a gut-on-chip model was developed, characterized (e.g. cell barrier integrity and differentiation) and used in a biokinetic study of an important class of environmental contaminants: dioxins (17 congeners). For this, the exposure conditions were optimised for very lipophilic compounds and the results were related to congener specific structural properties using Quantitative Structure-Property Relationship modelling. The development and characterization of the gut-on-chip model was further explored in **Chapter 3** by performing a biokinetic study of drug model compounds (i.e. antipyrine, ketoprofen, digoxin and amoxicillin). The impact of engineering factors on the outcome of experiments was also studied in this chapter. In **Chapter 4 and 5** an increased shear stress on the epithelial cells was applied and the consequences of this shear stress on epithelial cells were characterized. The impact of the fluid flow, and thus the shear stress, on cells was evaluated using transcriptomics analysis and compared with results obtained for cells cultured under static conditions and for *in vivo* duodenum, jejunum, ileum and colon tissues in **Chapter 4**. Effects on gene expression were analysed at both the individual gene level and at the biological pathway level. In **Chapter 5**, the potential nanomaterial toxicity to the small intestine was assessed using the optimized gut-on-chip model and compared to static culture conditions. Gene expression profiles upon E171 (TiO₂) and NM110 (ZnO) exposure of Caco-2 cells were analysed at the single gene and biological pathway level. Lastly, **Chapter 6 and 7** present a general discussion and a summary of the findings obtained throughout this thesis along with the future perspectives.

References

1. EFSA, *Guidance for submission for food additive evaluations* EFSA Journal, 2012. 10(7): p. 2760
2. EMA, *Guideline on the reporting of physiologically based pharmacokinetic (PBPK) modelling and simulation*. 2018: United Kingdom.
3. FDA, *Physiologically Based Pharmacokinetic Analyses -Format and Content Guidance for Industry*. 2018: USA.
4. ECHA, *REACH - Minimisation of Animal Testing*. 2016: United Kingdom.
5. Gellatly, N. and F. Sewell, *Regulatory acceptance of in silico approaches for the safety assessment of cosmetic-related substances*. Computational Toxicology, 2019. 11: p. 82-89.
6. Punt, A., et al., *Expert opinions on the acceptance of alternative methods in food safety evaluations: Formulating recommendations to increase acceptance of non-animal methods for kinetics*. Regulatory Toxicology and Pharmacology, 2018. 92: p. 145-151.
7. Tan, Y.-M., et al., *Challenges Associated With Applying Physiologically Based Pharmacokinetic Modeling for Public Health Decision-Making*. Toxicological sciences : an official journal of the Society of Toxicology, 2018. 162(2): p. 341-348.
8. Gourevitch, D., *The Anatomy and Physiology of the Small Bowel*, in *Upper Gastrointestinal Surgery*. 2005, Springer London: London. p. 39-44.
9. Zheng Fei Ma, Y.Y.L., *Small intestine anatomy and physiology*, in *Clinical and Basic Neurogastroenterology and Motility*, Y.Y.L. Satish S.C. Rao, Uday C. Ghoshal, Editor. 2020, Academic Press. p. 101-111.
10. Volk, N. and B. Lacy, *Anatomy and Physiology of the Small Bowel*. Gastrointest Endosc Clin N Am, 2017. 27(1): p. 1-13.
11. Peled, J.U., A.M. Hanash, and R.R. Jenq, *Role of the intestinal mucosa in acute gastrointestinal GVHD*. Blood, 2016. 128(20): p. 2395-2402.
12. Yamada, T. and D.H. Alpers, *Textbook of gastroenterology*. 2009, Blackwell Pub.: Chichester, West Sussex ;
13. Gerbe, F., C. Legrauerend, and P. Jay, *The intestinal epithelium tuft cells: specification and function*. Cell Mol Life Sci, 2012. 69(17): p. 2907-17.
14. Clevers, H., *The intestinal crypt, a prototype stem cell compartment*. Cell, 2013. 154(2): p. 274-84.
15. Walton, K.D., et al., *Generation of intestinal surface: an absorbing tale*. Development, 2016. 143(13): p. 2261-72.
16. Stanfield, C.L., *Principles of Human Physiology, Global Edition*. Vol. Sixth edition. Global edition. 2017, Boston: Pearson.
17. Metelsky, S.T., *Transport phenomena and membrane digestion in small intestinal mucosa : an electrophysiological approach*. 2011, Pensoft: Sofia, Russia.
18. Byers, J.P. and J.G. Sarver, *Chapter 10 - Pharmacokinetic Modeling*, in *Pharmacology*, M. Hacker, W. Messer, and K. Bachmann, Editors. 2009, Academic Press: San Diego. p. 201-277.
19. Pignatello, R., *1 - Biological membranes and their role in physio-pathological conditions*, in *Drug-Biomembrane Interaction Studies*, R. Pignatello, Editor. 2013, Woodhead Publishing. p. 1-46.
20. Kunisawa, J. and H. Kiyono, *Immune regulation and monitoring at the epithelial surface of the intestine*. Drug Discov Today, 2013. 18(1-2): p. 87-92.
21. Sanz, Y. and G. De Palma, *Gut microbiota and probiotics in modulation of epithelium and gut-associated lymphoid tissue function*. Int Rev Immunol, 2009. 28(6): p. 397-413.
22. Lu, P., C.P. Sodhi, and D.J. Hackam, *Toll-like receptor regulation of intestinal development and inflammation in the pathogenesis of necrotizing enterocolitis*. Pathophysiology, 2014. 21(1): p. 81-93.
23. Castro-Sanchez, P., Martin-Villa, J. M., *Gut immune system and oral tolerance*. Br J Nutr, 2013. 109 Suppl 2: p. S3-11.
24. EFSA. *Dioxin and PCBs*. [<https://www.efsa.europa.eu/en/topics/topic/dioxins-and-pcbs>] 30 January 2018].

25. WHO, *Exposure to Dioxins and Dioxin-like Substances: A Major Public Health Concern*, P.H.a. Environment, Editor. 2010, World Health Organization: Geneva.
26. Milbrath, M.O.G., et al., *Apparent half-lives of dioxins, furans, and polychlorinated biphenyls as a function of age, body fat, smoking status, and breast-feeding*. *Environmental health perspectives*, 2009. 117(3): p. 417-425.
27. Huwe, J.K. and G.L. Larsen, *Polychlorinated dioxins, furans, and biphenyls, and polybrominated diphenyl ethers in a U.S. meat market basket and estimates of dietary intake*. *Environ Sci Technol*, 2005. 39(15): p. 5606-11.
28. EFSA, *Update of the monitoring of levels of dioxins and PCBs in food and feed EFSA EFSA Journal*, 2012. 10(7): p. 2832.
29. Lennernäs, H., *Human in Vivo Regional Intestinal Permeability: Importance for Pharmaceutical Drug Development*. *Molecular Pharmaceutics*, 2014. 11(1): p. 12-23.
30. Wu, C.Y. and L.Z. Benet, *Predicting drug disposition via application of BCS: transport/absorption/elimination interplay and development of a biopharmaceutics drug disposition classification system*. *Pharm Res*, 2005. 22(1): p. 11-23.
31. Zhu, C., et al., *A comparative study of artificial membrane permeability assay for high throughput profiling of drug absorption potential*. *European Journal of Medicinal Chemistry*, 2002. 37(5): p. 399-407.
32. Westphal, J.F., et al., *Nifedipine enhances amoxicillin absorption kinetics and bioavailability in humans*. *J Pharmacol Exp Ther*, 1990. 255(1): p. 312-7.
33. Choi, J.S., M.J. Jin, and H.K. Han, *Role of monocarboxylic acid transporters in the cellular uptake of NSAIDs*. *J Pharm Pharmacol*, 2005. 57(9): p. 1185-9.
34. Li, N., et al., *A fast screening model for drug permeability assessment based on native small intestinal extracellular matrix*. *RSC Advances*, 2018. 8(60): p. 34514-34524.
35. Bahadar, H., et al., *Toxicity of Nanoparticles and an Overview of Current Experimental Models*. *Iran Biomed J*, 2016. 20(1): p. 1-11.
36. Ranjan, S., et al., *Toxicity and regulations of food nanomaterials*. *Environmental Chemistry Letters*, 2019. 17(2): p. 929-944.
37. Rempelberg, C., et al., *Oral intake of added titanium dioxide and its nanofraction from food products, food supplements and toothpaste by the Dutch population*. *Nanotoxicology*, 2016. 10(10): p. 1404-1414.
38. Rasmussen, J.W., et al., *Zinc oxide nanoparticles for selective destruction of tumor cells and potential for drug delivery applications*. *Expert Opin Drug Deliv*, 2010. 7(9): p. 1063-77.
39. Singh, S., et al., *Endocytosis, oxidative stress and IL-8 expression in human lung epithelial cells upon treatment with fine and ultrafine TiO₂: Role of the specific surface area and of surface methylation of the particles*. *Toxicology and Applied Pharmacology*, 2007. 222(2): p. 141-151.
40. Warheit, D.B. and S.C. Brown, *What is the impact of surface modifications and particle size on commercial titanium dioxide particle samples? – A review of in vivo pulmonary and oral toxicity studies – Revised 11-6-2018*. *Toxicology Letters*, 2019. 302: p. 42-59.
41. Mudunkotuwa, I.A., et al., *Dissolution of ZnO nanoparticles at circumneutral pH: a study of size effects in the presence and absence of citric acid*. *Langmuir*, 2012. 28(1): p. 396-403.
42. Dorier, M., et al., *Continuous in vitro exposure of intestinal epithelial cells to E171 food additive causes oxidative stress, inducing oxidation of DNA bases but no endoplasmic reticulum stress*. *Nanotoxicology*, 2017. 11(6): p. 751-761.
43. Proquin, H., et al., *Transcriptome changes in undifferentiated Caco-2 cells exposed to food-grade titanium dioxide (E171): contribution of the nano- and micro- sized particles*. *Sci Rep*, 2019. 9(1): p. 18287.
44. Moos, P.J., et al., *Responses of human cells to ZnO nanoparticles: a gene transcription study*. *Metallomics*, 2011. 3(11): p. 1199-211.
45. Moreno-Olivas, F., E. Tako, and G.J. Mahler, *ZnO nanoparticles affect nutrient transport in an in vitro model of the small intestine*. *Food and Chemical Toxicology*, 2019. 124: p. 112-127.

46. Musther, H., et al., *Animal versus human oral drug bioavailability: do they correlate?* Eur J Pharm Sci, 2014. 57: p. 280-91.
47. Faqi, A.S., *A comprehensive guide to toxicology in preclinical drug development*. 2013, Academic Press: London ;.
48. Henze, L.J., et al., *The pig as a preclinical model for predicting oral bioavailability and in vivo performance of pharmaceutical oral dosage forms: a PEARRL review*. J Pharm Pharmacol, 2019. 71(4): p. 581-602.
49. Tang, C. and T. Prueksritanon, *Use of in vivo animal models to assess pharmacokinetic drug-drug interactions*. Pharm Res, 2010. 27(9): p. 1772-87.
50. McConnell, E.L., A.W. Basit, and S. Murdan, *Measurements of rat and mouse gastrointestinal pH, fluid and lymphoid tissue, and implications for in-vivo experiments*. J Pharm Pharmacol, 2008. 60(1): p. 63-70.
51. Hatton, G.B., et al., *Animal Farm: Considerations in Animal Gastrointestinal Physiology and Relevance to Drug Delivery in Humans*. J Pharm Sci, 2015. 104(9): p. 2747-76.
52. Cao, X., et al., *Why is it challenging to predict intestinal drug absorption and oral bioavailability in human using rat model*. Pharm Res, 2006. 23(8): p. 1675-86.
53. Jacoby, H.I., *Safety Pharmacology and the GI Tract*, in *Toxicology of the Gastrointestinal Tract*, S. Gad, Editor. 2019, CRC Press.
54. Jiminez, J.A., et al., *Animal models to study acute and chronic intestinal inflammation in mammals*. Gut Pathog, 2015. 7: p. 29.
55. Nishimuta, H., et al., *Species differences in hepatic and intestinal metabolic activities for 43 human cytochrome P450 substrates between humans and rats or dogs*. Xenobiotica, 2013. 43(11): p. 948-55.
56. Haller, S., et al., *Expression Profiles of Metabolic Enzymes and Drug Transporters in the Liver and along the Intestine of Beagle Dogs*. Drug Metabolism and Disposition, 2012. 40(8): p. 1603.
57. Martinez, M.N., et al., *Reconciling Human-Canine Differences in Oral Bioavailability: Looking beyond the Biopharmaceutics Classification System*. The AAPS Journal, 2019. 21(5): p. 99.
58. Dressman, J.B., *Comparison of canine and human gastrointestinal physiology*. Pharm Res, 1986. 3(3): p. 123-31.
59. Koziolok, M., et al., *Characterization of the GI transit conditions in Beagle dogs with a telemetric motility capsule*. European Journal of Pharmaceutics and Biopharmaceutics, 2019. 136: p. 221-230.
60. Cerquetella, M., et al., *Inflammatory bowel disease in the dog: differences and similarities with humans*. World journal of gastroenterology, 2010. 16(9): p. 1050-1056.
61. Ziegler, A., L. Gonzalez, and A. Blikslager, *Large Animal Models: The Key to Translational Discovery in Digestive Disease Research*. Cellular and Molecular Gastroenterology and Hepatology, 2016. 2(6): p. 716-724.
62. Patterson, J.K., X.G. Lei, and D.D. Miller, *The pig as an experimental model for elucidating the mechanisms governing dietary influence on mineral absorption*. Exp Biol Med (Maywood), 2008. 233(6): p. 651-64.
63. Dezani, T.M., et al., *Single-Pass Intestinal Perfusion (SPIP) and prediction of fraction absorbed and permeability in humans: A study with antiretroviral drugs*. European Journal of Pharmaceutics and Biopharmaceutics, 2016. 104: p. 131-139.
64. Luo, Z., et al., *Ex vivo and in situ approaches used to study intestinal absorption*. J Pharmacol Toxicol Methods, 2013. 68(2): p. 208-216.
65. Li, M., I.A. de Graaf, and G.M. Groothuis, *Precision-cut intestinal slices: alternative model for drug transport, metabolism, and toxicology research*. Expert Opin Drug Metab Toxicol, 2016. 12(2): p. 175-90.
66. de Graaf, I.A., et al., *Preparation and incubation of precision-cut liver and intestinal slices for application in drug metabolism and toxicity studies*. Nat Protoc, 2010. 5(9): p. 1540-51.

67. Graves, C.L., et al., *A method for high purity intestinal epithelial cell culture from adult human and murine tissues for the investigation of innate immune function*. Journal of Immunological Methods, 2014. 414: p. 20-31.
68. Kauffman, A.L., et al., *Alternative functional in vitro models of human intestinal epithelia*. Front Pharmacol, 2013. 4: p. 79.
69. Eaton, A.D., et al., *Primary human polarized small intestinal epithelial barriers respond differently to a hazardous and an innocuous protein*. Food and Chemical Toxicology, 2017. 106: p. 70-77.
70. Le Ferrec, E., et al., *In vitro models of the intestinal barrier. The report and recommendations of ECVAM Workshop 46. European Centre for the Validation of Alternative methods*. Altern Lab Anim, 2001. 29(6): p. 649-68.
71. Lea, T., *Caco-2 Cell Line*, in *The Impact of Food Bioactives on Health: in vitro and ex vivo models*, K. Verhoeckx, et al., Editors. 2015, Springer International Publishing: Cham. p. 103-111.
72. Hidalgo, I.J., T.J. Raub, and R.T. Borchardt, *Characterization of the human colon carcinoma cell line (Caco-2) as a model system for intestinal epithelial permeability*. Gastroenterology, 1989. 96(3): p. 736-49.
73. Hilgers, A.R., R.A. Conradi, and P.S. Burton, *Caco-2 cell monolayers as a model for drug transport across the intestinal mucosa*. Pharm Res, 1990. 7(9): p. 902-10.
74. Walczak, A.P., et al., *In vitro gastrointestinal digestion increases the translocation of polystyrene nanoparticles in an in vitro intestinal co-culture model*. Nanotoxicology, 2015. 9(7): p. 886-94.
75. Antunes, F., et al., *Establishment of a triple co-culture in vitro cell models to study intestinal absorption of peptide drugs*. European Journal of Pharmaceutics and Biopharmaceutics, 2013. 83(3): p. 427-435.
76. Kämpfer, A.A.M., et al., *Development of an in vitro co-culture model to mimic the human intestine in healthy and diseased state*. Toxicology in Vitro, 2017. 45: p. 31-43.
77. Tanoue, T., et al., *In vitro model to estimate gut inflammation using co-cultured Caco-2 and RAW264.7 cells*. Biochemical and Biophysical Research Communications, 2008. 374(3): p. 565-569.
78. Gullberg, E., et al., *Expression of Specific Markers and Particle Transport in a New Human Intestinal M-Cell Model*. Biochemical and Biophysical Research Communications, 2000. 279(3): p. 808-813.
79. Kodama, N., et al., *Characteristic Analysis of Intestinal Transport in Enterocyte-Like Cells Differentiated from Human Induced Pluripotent Stem Cells*. Drug Metab Dispos, 2016. 44(10): p. 0.
80. Negoro, R., et al., *Modeling of drug-mediated CYP3A4 induction by using human iPS cell-derived enterocyte-like cells*. Biochemical and Biophysical Research Communications, 2016. 472(4): p. 631-636.
81. Kabeya, T., et al., *Cyclic AMP Signaling Promotes the Differentiation of Human Induced Pluripotent Stem Cells into Intestinal Epithelial Cells*. Drug Metab Dispos, 2018. 46(10): p. 1411-1419.
82. Kabeya, T., et al., *Functional analysis of carboxylesterase in human induced pluripotent stem cell-derived enterocytes*. Biochemical and Biophysical Research Communications, 2017. 486(1): p. 143-148.
83. Takenaka, T., et al., *Human Small Intestinal Epithelial Cells Differentiated from Adult Intestinal Stem Cells as a Novel System for Predicting Oral Drug Absorption in Humans*. Drug Metabolism and Disposition, 2014. 42(11): p. 1947.
84. Liu, Y., et al., *Monolayer culture of intestinal epithelium sustains Lgr5+ intestinal stem cells*. Cell Discovery, 2018. 4(1): p. 32.
85. Macedo, M.H., et al., *iPSC-Derived Enterocyte-like Cells for Drug Absorption and Metabolism Studies*. Trends Mol Med, 2018. 24(8): p. 696-708.
86. Sosa-Hernandez, J.E., et al., *Organs-on-a-Chip Module: A Review from the Development and Applications Perspective*. Micromachines (Basel), 2018. 9(10).
87. Probst, C., S. Schneider, and P. Loskill, *High-throughput organ-on-a-chip systems: Current status and remaining challenges*. Current Opinion in Biomedical Engineering, 2018. 6: p. 33-41.
88. Kimura, H., Y. Sakai, and T. Fujii, *Organ/body-on-a-chip based on microfluidic technology for drug discovery*. Drug Metab Pharmacokinet, 2018. 33(1): p. 43-48.
89. Zhang, B., et al., *Advances in organ-on-a-chip engineering*. Nature Reviews Materials, 2018. 3(8): p. 257-278.

90. Giusti, S., et al., *A novel dual-flow bioreactor simulates increased fluorescein permeability in epithelial tissue barriers*. Biotechnol J, 2014. 9(9): p. 1175-84.
91. Chi, M., et al., *A microfluidic cell culture device (muFCCD) to culture epithelial cells with physiological and morphological properties that mimic those of the human intestine*. Biomed Microdevices, 2015. 17(3): p. 9966.
92. Kim, H.J., et al., *Human gut-on-a-chip inhabited by microbial flora that experiences intestinal peristalsis-like motions and flow*. Lab Chip, 2012. 12(12): p. 2165-74.
93. Shah, P., et al., *A microfluidics-based in vitro model of the gastrointestinal human-microbe interface*. Nat Commun, 2016. 7: p. 11535.
94. Jing, B., et al., *Establishment and Application of Peristaltic Human Gut-Vessel Microsystem for Studying Host-Microbial Interaction*. Front Bioeng Biotechnol, 2020. 8: p. 272.
95. Maschmeyer, I., et al., *A four-organ-chip for interconnected long-term co-culture of human intestine, liver, skin and kidney equivalents*. Lab Chip, 2015. 15(12): p. 2688-99.
96. Trietsch, S.J., et al., *Membrane-free culture and real-time barrier integrity assessment of perfused intestinal epithelium tubes*. Nature Communications, 2017. 8(1): p. 262.
97. Berthier, E., E.W. Young, and D. Beebe, *Engineers are from PDMS-land, Biologists are from Polystyrenia*. Lab Chip, 2012. 12(7): p. 1224-37.
98. Chumbimuni-Torres, K.Y., et al., *Adsorption of Proteins to Thin-Films of PDMS and Its Effect on the Adhesion of Human Endothelial Cells*. RSC Adv, 2011. 1(4): p. 706-714.
99. Heo, Y.S., et al., *Characterization and resolution of evaporation-mediated osmolality shifts that constrain microfluidic cell culture in poly(dimethylsiloxane) devices*. Anal Chem, 2007. 79(3): p. 1126-34.
100. van Meer, B.J., et al., *Small molecule absorption by PDMS in the context of drug response bioassays*. Biochemical and Biophysical Research Communications, 2017. 482(2): p. 323-328.
101. Sackmann, E.K., A.L. Fulton, and D.J. Beebe, *The present and future role of microfluidics in biomedical research*. Nature, 2014. 507(7491): p. 181-9.
102. Ongaro, A.E., et al., *Poly(lactic acid) is a Sustainable, Low Absorption, Low Autofluorescence Alternative to Other Plastics for Microfluidic and Organ-on-Chip Applications*. Analytical Chemistry, 2020. 92(9): p. 6693-6701.
103. Nguyen, T., et al., *Robust chemical bonding of PMMA microfluidic devices to porous PETE membranes for reliable cytotoxicity testing of drugs*. Lab on a Chip, 2019. 19(21): p. 3706-3713.
104. Henry, O.Y.F., et al., *Organs-on-chips with integrated electrodes for trans-epithelial electrical resistance (TEER) measurements of human epithelial barrier function*. Lab Chip, 2017. 17(13): p. 2264-2271.
105. Huttmacher, D.W. and H. Singh, *Computational fluid dynamics for improved bioreactor design and 3D culture*. Trends in Biotechnology, 2008. 26(4): p. 166-172.
106. Mastrangeli, M., et al., *Organ-on-chip in development: Towards a roadmap for organs-on-chip*. ALTEX, 2019. 36(4): p. 650-668.
107. Louise, J., K. Beekmann, and I.M. Rietjens, *Use of Physiologically Based Kinetic Modeling-Based Reverse Dosimetry to Predict in Vivo Toxicity from in Vitro Data*. Chem Res Toxicol, 2017. 30(1): p. 114-125.
108. Sjögren, E., H. Thörn, and C. Tannergren, *In Silico Modeling of Gastrointestinal Drug Absorption: Predictive Performance of Three Physiologically Based Absorption Models*. Molecular Pharmaceutics, 2016. 13(6): p. 1763-1778.
109. Matsumura, N., et al., *Prediction Characteristics of Oral Absorption Simulation Software Evaluated Using Structurally Diverse Low-Solubility Drugs*. Journal of Pharmaceutical Sciences, 2020. 109(3): p. 1403-1416.
110. Wang, Q., et al., *Use of Physiologically Based Kinetic Modeling to Predict Rat Gut Microbial Metabolism of the Isoflavone Daidzein to S-Equol and Its Consequences for ERα Activation*. Molecular Nutrition & Food Research, 2020. 64(6): p. 1900912.


111. van de Waterbeemd, H. and E. Gifford, *ADMET in silico modelling: towards prediction paradise?* Nature Reviews Drug Discovery, 2003. 2(3): p. 192-204.
112. Gozalbes, R., et al., *QSAR-based permeability model for drug-like compounds*. Bioorganic & Medicinal Chemistry, 2011. 19(8): p. 2615-2624.
113. van Ravenzwaay, B., et al., *Metabolomics as read-across tool: A case study with phenoxy herbicides*. Regulatory Toxicology and Pharmacology, 2016. 81: p. 288-304.
114. Henderson, R.G., et al., *Oral bioaccessibility testing and read-across hazard assessment of nickel compounds*. Regulatory Toxicology and Pharmacology, 2012. 63(1): p. 20-28.
115. Kimura, H., et al., *An integrated microfluidic system for long-term perfusion culture and on-line monitoring of intestinal tissue models*. Lab Chip, 2008. 8(5): p. 741-6.
116. Imura, Y., et al., *A microfluidic system to evaluate intestinal absorption*. Anal Sci, 2009. 25(12): p. 1403-7.
117. Yeon, J.H. and J.K. Park, *Drug permeability assay using microhole-trapped cells in a microfluidic device*. Anal Chem, 2009. 81(5): p. 1944-51.
118. Imura, Y., K. Sato, and E. Yoshimura, *Micro total bioassay system for ingested substances: assessment of intestinal absorption, hepatic metabolism, and bioactivity*. Anal Chem, 2010. 82(24): p. 9983-8.
119. Gao, D., et al., *Characterization of drug permeability in Caco-2 monolayers by mass spectrometry on a membrane-based microfluidic device*. Lab Chip, 2013. 13(5): p. 978-85.
120. Pocock, K., et al., *Intestine-on-a-Chip Microfluidic Model for Efficient in Vitro Screening of Oral Chemotherapeutic Uptake*. ACS Biomaterials Science & Engineering, 2017. 3(6): p. 951-959.
121. Lee, D.W., et al., *3D gut-liver chip with a PK model for prediction of first-pass metabolism*. Biomed Microdevices, 2017. 19(4): p. 100.
122. Satoh, T., et al., *A multi-throughput multi-organ-on-a-chip system on a plate formatted pneumatic pressure-driven medium circulation platform*. Lab Chip, 2017. 18(1): p. 115-125.
123. Tan, H.Y., et al., *A multi-chamber microfluidic intestinal barrier model using Caco-2 cells for drug transport studies*. PLoS One, 2018. 13(5): p. e0197101.
124. Mahler, G.J., et al., *Characterization of a gastrointestinal tract microscale cell culture analog used to predict drug toxicity*. Biotechnol Bioeng, 2009. 104(1): p. 193-205.
125. Esch, M.B., et al., *Body-on-a-chip simulation with gastrointestinal tract and liver tissues suggests that ingested nanoparticles have the potential to cause liver injury*. Lab Chip, 2014. 14(16): p. 3081-92.
126. Marin, T.M., et al., *Acetaminophen absorption and metabolism in an intestine/liver microphysiological system*. Chem Biol Interact, 2019. 299: p. 59-76.
127. Santbergen, M.J.C., et al., *Dynamic in vitro intestinal barrier model coupled to chip-based liquid chromatography mass spectrometry for oral bioavailability studies*. Anal Bioanal Chem, 2020. 412(5): p. 1111-1122.
128. Kim, H.J. and D.E. Ingber, *Gut-on-a-Chip microenvironment induces human intestinal cells to undergo villus differentiation*. Integr Biol (Camb), 2013. 5(9): p. 1130-40.
129. Delon, L.C., et al., *A systematic investigation of the effect of the fluid shear stress on Caco-2 cells towards the optimization of epithelial organ-on-chip models*. Biomaterials, 2019. 225: p. 119521.
130. Shin, W., et al., *Human Intestinal Morphogenesis Controlled by Transepithelial Morphogen Gradient and Flow-Dependent Physical Cues in a Microengineered Gut-on-a-Chip*. iScience, 2019. 15: p. 391-406.
131. Kim, H.J., et al., *Contributions of microbiome and mechanical deformation to intestinal bacterial overgrowth and inflammation in a human gut-on-a-chip*. Proc Natl Acad Sci U S A, 2016. 113(1): p. E7-15.
132. Gumuscu, B., et al., *Compartmentalized 3D Tissue Culture Arrays under Controlled Microfluidic Delivery*. Sci Rep, 2017. 7(1): p. 3381.
133. Kasendra, M., et al., *Development of a primary human Small Intestine-on-a-Chip using biopsy-derived organoids*. Sci Rep, 2018. 8(1): p. 2871







CHAPTER 2

Implementation of a dynamic intestinal gut-on-a-chip barrier model for transport studies of lipophilic dioxin congeners



Kornphimol Kulthong, Loes Duivenvoorde, Barbara Z. Mizera, Deborah
Rijkers, Guillaume ten Dam, Gerlof Oegema, Tomasz Puzyn, Hans
Bouwmeester, and Meike van der Zande



Based on: RSC Advances (2018), Volume 8, Issue 57, Pages 32440-3245



Abstract

Novel microfluidic technologies allow to manufacture *in vitro* organ-on-a-chip systems that hold great promises to adequately recapitulate the biophysical and functional complexity of organs found *in vivo*. In this study, a gut-on-a-chip model was developed aiming to study the potential cellular association and transport of food contaminants. Intestinal epithelial cells (Caco-2) were cultured on a porous polyester membrane that was tightly clamped between two glass slides to form two separate flow chambers. Glass syringes, polytetrafluoroethylene tubing and glass microfluidic chips were selected to minimize surface adsorption of the studied compounds (*i.e.* highly lipophilic dioxins), during the transport studies. Confocal microscopy studies revealed that, upon culturing under constant flow for 7 days, Caco-2 cells formed complete and polarized monolayers as observed after culturing for 21 days under static conditions in Transwells. We exposed Caco-2 monolayers in the chip and Transwell to a mixture of 17 dioxin congeners (7 polychlorinated dibenzo-p-dioxins and 10 polychlorinated dibenzofurans) for 24 h. Gas chromatography-high resolution mass spectrometry was used to assess the cellular association and transport of individual dioxin congeners across the Caco-2 cell monolayers. After 24 h, the amount of transported dioxin mixture was similar in both the dynamic gut-on-a-chip model and static Transwell model. The transport of individual congeners corresponded with their number of chlorine atoms and substitution patterns as revealed by Quantitative Structure-Property Relationship modelling. These results show that the gut-on-a-chip model can be used, as well as the traditional static Transwell system, to study the cellular association and transport of lipophilic compounds like dioxins.

Introduction

Determination of the oral bioavailability of compounds after ingestion is a crucial element in the toxicological risk assessment of food chemicals and environmental contaminants. Caco-2 cells, a cell line established from human epithelial adenocarcinoma cells, grown in Transwells® have been widely used as a general *in vitro* model for the prediction of *in vivo* intestinal food chemicals and drug absorption and to investigate local effects on the intestinal epithelium [1-3]. However, grown under static conditions, such a model may not fully capture the physical and extracellular complexity found *in vivo*. Two main shortcomings of this model are the relatively long culture period that is needed for these cells to differentiate [4], and the static culturing conditions which fail to mimic the luminal and blood plasma flows as observed *in vivo*.

Recent advances in micro engineering and microfluidics have led to unprecedented organ-on-a-chip models that recapitulate not only *in vivo* fluid flows, but also the structure and function of human tissues [5-9]. For this reason, microfluidic technology has been introduced into the field of drug discovery. This already now has resulted in a variety of models recapitulating specific organ functions, including the small intestine, in so-called gut-on-a-chip models [5, 6, 10, 11]. In a limited number of studies, drug transport has been reported on Caco-2 cell-based microfluidic devices to evaluate the permeability potential of these models [12, 13]. However, for the purpose of gut-on-a-chip model development and optimization, its efficiency for compound permeability should not only be investigated for drugs, but also for chemical substances in general. The gut epithelium acts as the important barrier in defence to protect the body from exogenous substances as present in food. Therefore we assessed the barrier properties of the gut-on-a-chip model for dioxins which are an important class food contaminants. Furthermore, the predictive capacity of a gut-on-a-chip model should be evaluated in terms of the comparison to the Transwell system that has been used in the past decades for this type of studies.

The term dioxins, also called polychlorinated dibenzodioxins, refers to two groups of compounds: polychlorinated dibenzo-p-dioxins (PCDDs) and dibenzofurans (PCDFs) (see Fig. 1). These are a group of chemically-related compounds (i.e. congeners) that are classified as persistent organic pollutants (POPs) and cause concern over environmental and human health impact. Dioxins are highly toxic and longer term exposure can cause reproductive and developmental problems, skin lesions, damage to the immune system, interference with the hormonal balance, and lastly dioxins may also cause cancer [14, 15]. Because of their lipophilic properties, or high logP values (the partition coefficient of a molecule between an aqueous and lipophilic phase, usually octanol and water; Table 1), dioxins accumulate in the food chain, mainly in the fatty tissue of farm animals. Consumption of contaminated food, like contaminated beef and dairy products, is the primary source of dioxin entry into the human body [16-18]. In fact, more than 90% of human dioxin exposure occurs through food ingestion [14, 19]. About 20 congeners of dioxins can be absorbed through daily meals, [20, 21] 17 of these congeners are present in a reference mixture in the legal food monitoring

programmes of the EU [22]. The molecular composition (i.e. degree of chlorination), solubility, and molecular size of each congener influences its absorption rate, toxicity, tissue distribution, and elimination [23].

In this study, we aimed to compare the transport of 17 different dioxin congeners (7 PCDDs and 10 PCDFs) in a dynamic microfluidic Caco-2 model with their transport in a traditional static Transwell Caco-2 model. For this, we developed a dynamic *in vitro* microfluidic gut-on-a-chip model with Caco-2 cells for the purpose of mimicking the *in vivo* conditions. Quantification of the dioxin mixture in the cellular fraction as well as the amount transported across the intestinal monolayers was performed using gas chromatography-high resolution mass spectrometry (GC-HRMS). The GC-HRMS method is considered a highly sensitive method suitable for dioxin measurements at low concentration (0.08-0.30 $\mu\text{g/mL}$) ranges (Table 1) [24]. The resulting cellular association and transport of dioxins were not only compared between the two models, but we also performed Quantitative structure-property relationship modelling to explain different biological behaviour of the dioxin congeners.

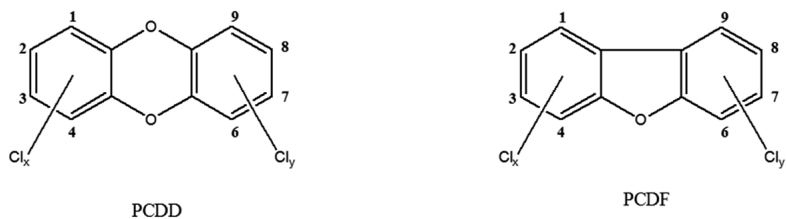


Figure. 1 Structures of investigated compounds

Table 1. The predicted LogP values of dioxin congeners,[25] and limit of quantification (LOQ) by GC-HRMS

Congeners	LogP	LOQ ($\mu\text{g/mL}$)
2,3,7,8-TCDF	6.5	0.086
1,2,3,7,8-PeCDF	6.9	0.201
2,3,4,7,8-PeCDF	6.9	0.185
1,2,3,4,7,8-HxCDF	6.9	0.137
1,2,3,6,7,8-HxCDF	6.9	0.161
2,3,4,6,7,8-HxCDF	7.1	0.186
1,2,3,7,8,9-HxCDF	7.4	0.212
1,2,3,4,6,7,8-HpCDF	7.9	0.165
1,2,3,4,7,8,9-HpCDF	7.5	0.133
OCDF	8.5	0.210
2,3,7,8-TCDD	6.4	0.095
1,2,3,7,8-PeCDD	6.6	0.184
1,2,3,4,7,8-HxCDD	8.4	0.175
1,2,3,6,7,8-HxCDD	7.4	0.185
1,2,3,7,8,9-HxCDD	7.4	0.145
1,2,3,4,6,7,8-HpCDD	7.5	0.147
OCDD	8.1	0.300

Experimental

The gut-on-a-chip device

The microfluidic gut-on-a-chip device consists of three resealable glass slides, with the same width (15 mm) and length (45 mm), upon assembly resulting in two flow chambers separated by a middle layer that contains a cell culture membrane (Fig. 2). In more detail, a polyester (PET) membrane fixed on a glass slide, with a $0.4\ \mu\text{m}$ pore size, $12\ \mu\text{m}$ thickness, 1.6×10^6 pore density and $1\ \text{cm}^2$ surface area, separates the upper apical (AP) and the lower basolateral (BL) chambers (Micronit, Enschede, The Netherlands). Both the upper and lower glass slides were spaced from the middle layer membrane by $0.25\ \text{mm}$ thick silicone bands resulting in a volume of $110\ \text{mm}^3$ and $75\ \text{mm}^3$ for the AP and BL side respectively, which makes the total volume of the device $185\ \text{mm}^3$ (μL). The distance between the middle layer and the top layer was $0.25\ \text{mm}$ and $0.65\ \text{mm}$ for the glass and membrane section, respectively. The distance between the middle layer and bottom layer was $0.25\ \text{mm}$. The chip was mounted with a quick locking mechanism in the chip holder constructed for connecting external tubing to the chip via specific ferrules to ensure tight connections and a leak-free system. Constant flow was carried out using a microsyringe pump (NE-4000, New Era Pump Systems, Inc.) equipped with two glass syringes (5 mL, Luer lock tip, Fortuna[®], Sigma), with each syringe connected to either the AP or the BL compartment of the chip with PTFE (Teflon) tubing ($0.25\ \text{mm}$ inner diameter, $14.5\ \text{cm}$ length). On the outlets of the chip the same tubing was used and connected with glass collecting reservoirs. Before starting experiments, all tubing and chip parts were sterilized by autoclave and 70% ethanol and the tubing was filled with medium in order to eliminate air bubbles in the microfluidic system. The entire system was put in an incubator at $37\ ^\circ\text{C}$ to maintain cell culture conditions. All experiments were performed at a constant flow rate of $25\ \mu\text{L/h}$ resulting in a shear rate in the AP compartment of ~ 0.0001 – $0.0005\ \text{Dyne/cm}^2$ (at the membrane and glass surface, respectively) and in the BL compartment of $\sim 0.0005\ \text{Dyne/cm}^2$.

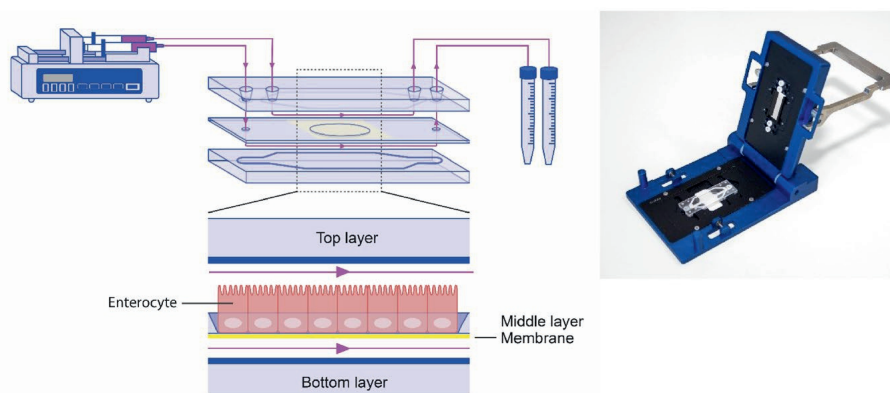


Figure 2. A) Schematic design of the microfluidic system. B) Image of the chip holder used to clamp the chip together and allowing connection of the tubing.

Optimization of the gut-on-a-chip system for dioxin mixture absorption properties

Before starting the transport experiment, the fraction of dioxins absorbed by the different types of tubing and syringes to be used in the microfluidic system was determined. The following conditions were evaluated: glass or polypropylene syringes equipped with Ethylene tetrafluoroethylene (ETFE), stainless steel or Teflon tubing. Different combinations ($n=2$ for each combination) were tested by rinsing with cell culture medium containing 0.2 ng/mL dioxin mixture (in 1% DMSO) at a flow rate of 25 $\mu\text{L/h}$ for 24 h at 37 °C (conditions as used in the final transport experiment). The amount of total dioxins in culture medium before and after flowing through the microfluidic systems was determined by using a most cost effective and sensitive CALUX bioassay that is routinely used in our laboratories, as described previously [26]. Briefly, rat H4IIE hepatoma cells, stably transfected with an AhR-controlled luciferase reporter gene plasmid (pGudLuc1.1), were grown in 48-well microtiter plates. Upon cell confluence, they were exposed in triplicate to standards and the dioxin mixture dissolved in culture medium. After 20–24 h of exposure, the cells were washed, lysed and an aliquot was used to determine the luciferase content using a plate reader (Luminoskan, Labsystems). Dioxin concentrations in the culture medium samples are expressed as total bioanalytical equivalent (BEQ) of 2,3,7,8-Tetrachlorodibenzo-p-dioxin (TCDD), and were estimated from a calibration curve of the reference dioxin mixture samples whose response was fitted with an exponential curve fit. The entire experiment was repeated twice and the average of both experiments is reported.

Culture of human intestine epithelial cells

The Caco-2 cell line (HTB-37), derived from a human colorectal adenocarcinoma, was obtained from The American Type Culture Collection (ATCC, Manassas, VA, USA). They were grown (at passage number 29–45) in Dulbecco's Modified Eagle Medium (Lonza) supplemented with 10% heat-inactivated fetal bovine serum (Gibco, Waltham, MA USA), 1% penicillin-streptomycin (Sigma), 1% non-essential amino acids (Gibco), further referred to as DMEM⁺.

The cells were seeded at density of 40,000 cells per cm^2 in 12-well Transwell polyester inserts (0.4 μm pore size, 1.12 cm^2 surface area, Corning Amsterdam, The Netherlands) cultured in DMEM⁺. During culture period, medium was changed for every other day.

In the microfluidic chip cells were seeded at a density of 75,000 cell per cm^2 , the cells were allowed to attach to the membrane without flow for 72 h and then were perfused with low sodium bicarbonate (10 mM) DMEM⁺ (Sigma) for optimizing pH buffering capacity, through the AP and BL side for 7 days.

Immunohistochemistry

For morphological assessment of the monolayers grown in the microfluidic chips or Transwell cells were seeded ($n=3$) in a separate experiment. After 10 days of culture (i.e. 7

days under flow conditions) the microfluidic chips were opened, and cells were fixed on the membrane. The monolayer of cells was sequentially fixed with 4% formaldehyde at room temperature for 10 min and rinsed with PBS. Cells were then permeabilized with 0.25% Triton X100 in PBS for 10 min, rinsed with PBS and blocked with 1% acetylated bovine serum albumin in PBS for 30 min. Tight junctions were stained with 10 $\mu\text{g/mL}$ of the conjugated antibody ZO-1/TJP1-Alexa Fluor 594 (Invitrogen, Waltham, MA). The nuclei were stained with 5 $\mu\text{g/mL}$ of DAPI (Invitrogen, Waltham, MA) and 4 U/mL of Phalloidin Alexa Fluor 488 (Life technologies) was used to stain actin filaments (i.e. cytoskeleton). The incubation time for all stainings was 10 min. Each membrane was then cut out and placed between two cover slips separated by a spacer (0.12 mm depth x 20 mm diameter). Anti-fading mounting medium was dropped on the membrane. The cells cultured on Transwell membranes for 21 days were stained with the same methods and conditions. The stained monolayers of cells were analysed using a confocal microscope (LSM 510 UVMETA; Carl Zeiss, Germany). Samples were excited with 405, 488 and 543 nm lasers. Multi-tracked images were captured to avoid bleed through. The used pinholes were in the range of 148-152 μm at magnification 40x. The gain and offset for the different channels were kept constant during the entire experiment.

Compounds

The dioxin mixtures were obtained from Cambridge Isotope Laboratories, Inc. (Tewksbury, USA) and contained 10 PCDF congeners: 2,3,7,8-TCDF, 1,2,3,7,8-PeCDF, 2,3,4,7,8-PeCDF, 1,2,3,4,7,8-HxCDF, 1,2,3,6,7,8-HxCDF, 2,3,4,6,7,8-HxCDF, 1,2,3,7,8,9-HxCDF, 1,2,3,4,6,7,8-HpCDF, 1,2,3,4,7,8,9-HpCDF and OCDF, and 7 PCDD congeners: 2,3,7,8-TCDD, 1,2,3,7,8-PeCDD, 1,2,3,4,7,8-HxCDD, 1,2,3,6,7,8-HxCDD, 1,2,3,7,8,9-HxCDD, 1,2,3,4,6,7,8-HpCDD and OCDD.

Cell viability

To exclude cytotoxicity of the dioxin mixture at the concentration used for the transport studies, a WST-1 assay was performed on Caco-2 cells. The WST-1 assay quantifies cellular mitochondrial activity, which directly correlates to cell viability and thus cytotoxicity. For this, cells were seeded in 96-well plates at a density of 50,000 cells per cm^2 and were incubated overnight and were subsequently exposed to the dioxin mixture in DMEM⁺ at various concentration ranging from 0.025 to 2.0 ng/mL , for 24 h. After exposure, the cells were washed with Hank's Balanced Salt Solution (HBSS) and incubated with 10 μL WST-1 reagent (Roche Diagnostics GmbH, Mannheim, Germany) for 3 h. The plate was read at 440 nm and 640 nm using a microplate reader (BioTek, Winooski, VT). The background signal at 640 nm, which is directly correlated with the cell quantity, was subtracted from the reaction signal at 440 nm.

Dioxin mixture transport experiments

In the dynamic gut-on-a-chip model, cells were cultured for 10 days, of which 7 days under continuous flow of 25 $\mu\text{L/h}$. At day 10, DMEM⁺ containing 0.2 ng/mL of each congener of Dioxin (in 1% DMSO) was pumped into the apical channel, and DMEM⁺ without the dioxin mixture was perfused into the basolateral channel. After 24 h, a total of 600 μL of eluent from each compartment was collected for further analysis.

In the Transwell model, cells were cultured for 21 days, and subsequently exposed to 600 μL DMEM⁺ containing 0.2 ng/mL of the dioxin mixture (in 1% DMSO) in the apical compartment. The basolateral compartment was filled with 600 μL DMEM⁺. After 24 h, all DMEM⁺ was collected from both compartments.

In both the chip and Transwell models, cells were collected at the end of the exposure to determine compound accumulation in the cells. For this, cells were trypsinized with 0.025% Trypsin/EDTA, rinsed with HBSS and lysed by three freeze-thaw cycles. To establish a complete mass balance, the fraction of absorbed dioxins on membranes, tubing and culture chambers after exposure was collected by rinsing all compartments with 200 μL hexane. The experiment was performed in triplicate, all collected samples were analysed together using GC-HRMS.

GC-HRMS analysis

Samples were analysed by GC-HRMS using previously described methods [24]. In short, prior to the extraction, the samples were spiked with ¹³C-isotope labelled internal standards (50 pg of each of the 7 PCDDs and of 9 out of 10 PCDFs (except 2,3,4,6,7,8-HxCDF)). Consequently, 1 mL of methanol was added and extracted with once 4 mL hexane and twice with 5 mL hexane. The hexane phases were merged and the samples were purified as described in earlier studies [24]. Using an automated clean-up (PowerPrep system, Fluid Management Systems, Waltham, USA), extracts were purified on an acid silica column, a neutral silica column, a basic alumina column and an activated carbon/Celite column. For the elution of the columns, custom made solvents and mixtures were used, respectively being hexane, hexane/dichloromethane (1:1, v/v), ethyl acetate/toluene (1:1, v/v) and toluene. The volume of the final extract was reduced to 0.5 mL using an automated evaporation system with a fixed endpoint of 0.5 mL. The recovery standards ¹³C-labelled 1,2,3,4-TCDD and 2,3,4,6,7,8-HxCDF, 100 pg, were added for the analysis of PCDD/F, after which the volume of the extracts were again reduced to 0.5 mL. PCDD/F analysis was performed by GC/HRMS using an Agilent (Wilmington, USA) 6890 Series gas chromatograph and an AutoSpec Ultima high resolution mass spectrometer (Waters, Milford, USA) operated at a resolution of 10,000 (10% peak valley). The GC column was a DB5 MS (60 m, 0.25 mm i.d., 0.25 μm ; J&W, Folsom, USA). The mass spectrometer was operated in electron impact ionization mode, using selected-ion monitoring. A large volume injector (LVI) was used to inject 100 μL of the extract containing PCDD/Fs on the GC. The results were corrected for recovery of the ¹³C-labelled internal standards and the performance was checked through an in-house reference sample sunflower oil spiked at approximately 1 pg TEQ g⁻¹ fat PCDD/F, 0.8 pg

TEQ g^{-1} fat dl-PCBs and 15 ng g^{-1} fat non-dioxin like-PCBs. The performance of the methods is regularly checked by participation in PT-tests (EURL dioxins and PCBs twice a year, Folkehelse Institute, once a year), showing good performance.

Quantitative structure-property relationship modelling

Quantitative structure-property relationship (QSPR) modelling is based on the assumption that the structure of compound (i.e. geometry, mass, surface) is responsible for its chemical, physical and biological properties [27]. For the QSPR modelling data were logarithmized to make them more linear and sorted by increasing values. To be able to validate the QSPR models the data were split into two sets: a training set (to calibrate of model equations), and a validation set (used for verifying the predictive ability of the developed models). For this we used the “Z:1” algorithm, which places every Z^{th} compound in the validation set (objects from this set are marked as #2) and all the remaining objects in the training set (those objects are marked as #1). We took $Z=5$ for cellular uptake and association data and $Z=4$ for transport data.

Molecular structures of the PCDD and PCDF congeners were build using the ConGENER software [28]. The molecular geometries energy was optimized in Gaussian package (version 09, Gaussian Inc, Wallingford, Connecticut USA) with the B3LYP/6-311+G* density functional method as described before [29, 30]. After optimization the molecular structures were used to calculate the molecular descriptors, in order to obtain a numerical representation of the compound structure. To this end, we used DRAGON software (version 6.0), [31] which allowed us to obtain a set of 2622 molecular descriptors.

Based on the experimental data and molecular descriptors we calibrated the models equations using a Multiple Linear Regression (MLR) method [32]. In order to select from such a large descriptors set the models that best correlate with the biological endpoint we used genetic algorithm (GA) [33] implemented in the QSARINS software (version 2.2.2) [34]. The genetic algorithm is able to search for the best solutions from a large number of possibilities by a maximizing/minimizing fitness function. The procedure of GA was inspired by evolution mechanism, where the data respond to chromosomes and genes [35]. In our study GA was applied with the following parameters: the population size: 200, the mutation rate: 20%. Due to the small number of compounds in the models training sets we chose 2 descriptors for each model, to avoid their overfitting [36, 37]. The chosen descriptors are presented in the Table 4. We selected four autocorrelation descriptors: ATSC3v and GATS5v for uptake and/or cellular association models, ATS5m and MATS5m for transport models. In general autocorrelation descriptors are based on the autocorrelation function AC_k presented in the Equation 1.

$$A_{ab}^b C_k = \int f(x) \cdot f(x+k) \cdot dx \quad (1)$$

where $f(x)$ is a function of the variable x , k is the lag representing an interval of x and a, b define the total studied interval of the function.[37]

To meet the requirements of QSPR models defined by the Organization for Economic Cooperation and Development, [37] we carried out a two-stage model validation of each model: for the internal validation we chose the leave-one-out method (cross-validation), [38] and for the external validation we used the validation set of data.

After the validation process we examined the applicability domain (AD) of our models. AD is a theoretical space determined by values of molecular descriptors, and so resulting from structural similarity of the compounds, in which the predictions are reliable. For this purpose we calculated leverage values (h) and the standardized residual values. The h values that defines the similarity of i^{th} compound to the training set were calculated according to the Equation 2, where x_i is a vector containing descriptors for i^{th} compound and X is a matrix containing descriptors for every compound from the training set.

$$h_i = x_i^T (X^T X)^{-1} x_i \quad (2)$$

When the h value for a compound is higher than the critical value h^* (calculated based on the Equation 3), then the model predicted the endpoint value for this compound by extrapolation.

$$h^* = 3pn^{-1} \quad (3)$$

where p is the number of variables in model plus one, n is the number of the compounds in the training set [39].

We verified the fitting of the models by determination coefficient (R^2) and root mean square error of calibration (RMSE_C). Their robustness and stability was evaluated by the cross-validation coefficient (Q^2_{CV}) and the root mean square error of cross-validation (RMSE_{CV}). The predicting capabilities of the models were examined by external validation coefficient (Q^2_{EXT}) and root mean square error of prediction (RMSE_{EXT}) [40].

Statistical analysis

SPSS (IBM) was used for all statistical evaluations. The cellular accumulation and transport data was evaluated using an independent paired t-test for the dioxin mixture transport experiment and a one-way ANOVA with Dunnett's post hoc test was used for the cell viability test. A p-value of ≤ 0.05 was considered significant.

Results and discussion

Microfluidic model development for lipophilic compounds

Dioxins are highly lipophilic, and thus tend to adsorb to surfaces of materials used in experiments depending on their chemical composition and their subsequent compound-material interactions [41, 42]. Polydimethylsiloxane (PDMS) is often used to create microfluidic devices because of its low cost, ease of use, high compliance, microscope compatibility and fast fabrication properties [43-45]. However, PDMS has a number of important limitations regarding its use in biological studies [46]. One of those limitations is adsorption of various molecules by PDMS because of its permeable and hydrophobic properties [47]. It has been reported that PDMS based material adsorbed more small-molecules and hydrophobic compounds compared to polystyrene based material, [48, 49]

and glass, [50] and thus dramatically affecting free compound concentrations [49]. Obviously, the degree of adsorption relies on lipophilic properties of compounds [50, 51]. While it has been shown that continuous rinsing with buffer might result in desorption of compounds from PDMS [50], it is clear that PDMS might not be the ideal material for highly lipophilic compounds like dioxins. Therefore, in this study, glass-based chips were used, to reduce the effect of surface adsorption as much as possible. Selection of the optimal type of tubing for the compounds of interest in a microfluidic system is also an essential element of the microfluidic model development, especially since the (relative) surface areas of the capillary tubing is large. Therefore, the concentration of the dioxin mixture in cell culture medium was determined after use in different materials of syringes and tubing (i.e. glass vs. polypropylene syringes and ethylene tetrafluoroethylene (ETFE), stainless steel and Teflon tubing), under the conditions as used in the final experiments. The fraction of dioxin mixture adsorbed onto the material surface after incubation was determined by assessing the amount of dioxins in the cell culture medium expressed in BEQ using the dioxin CALUX bioassay, as a cost effective measurement technique. Highest residual amounts of the dioxin mixture in cell culture media were detected when using glass syringes and Teflon tubes, about 60% higher compared to the set-up with the lowest yield using polypropylene syringes and ETFE tubing (Table 2). Therefore Teflon tubing is used in the final experiments.

Dioxin adsorption to the microfluidic system was also assessed in the exposure/translocation experiment by GC-HRMS. For this, the system was rinsed with hexane after the exposure and the amount of dioxins in this fraction was determined with GC-HRMS and compared to the exposure mixture. On average, hexane rinses of the chip compartments after incubation with the dioxin mixture contained 3% of the total amount of dioxins as present in the exposure mixture in both systems, indicating low adsorption (see Suppl. Table1). This information, together with an average measured mass balance of 93%, (the sum of apical, basolateral and cellular fractions, as discussed in detail later) shows a good recovery in the chip system.

Table 2. Effect of different tubing and syringe material of the microfluidic systems on recovery of the dioxin mixture measured by CALUX (n=2)

Syringes and Tubing	Dioxin concentration (ng BEQ/ml)	Recovery (%)*
Polypropylene + ETFE	0.085±0.005	26±1
Glass + ETFE	0.199±0.006	61±2
Glass + Steel	0.212±0.012	65±4
Glass + Teflon	0.219±0.003	67±1

*The initial concentration of Dioxin in DMEM⁺ is 0.328 ng BEQ/ml.

Morphology of intestinal barriers

Monolayer integrity of Caco-2 cells grown under dynamic flow and static conditions was evaluated using fluorescence confocal microscopy. Representative images are shown in Fig. 3. In the chip the Caco-2 cells were grown using a continuous flow of 25 $\mu\text{L/hr}$ for 7 days. Cells cultured under continuous flow have been described to form intact and polarized monolayers faster compared to Caco-2 cells cultured using traditional static conditions [6]. This is confirmed in the present study by showing complete and polarized monolayers of cells at day 10 (i.e. 7 days of flow) in the chip model. For comparative analysis Caco-2 cells were grown for 21 days under static conditions in Transwells. Cells grown under continuous flow showed a comparable monolayer formation to cells grown without continuous flow, as can be seen from the tight junction immunofluorescence staining (Fig. 3A and B). Cell polarisation was visualized using immunofluorescence staining of actin filaments, nuclei, and tight junctions (Fig. 3C, D, E, F, G and H). Core bundles of actin filaments in the microvilli were seen in cells grown under both conditions. After cell polarisation, the cells grown without continuous flow exhibited densely packed actin filaments on the apical side in the microvilli of the cells, while cells grown under dynamic conditions also exhibited pronounced actin filaments on the basolateral side (Fig. 3E and F). Likely this is caused by the shear stress (0.0001-0.0005 Dyne/cm²), induced by the continuous flow, as shown before for endothelial cells exposed to a shear stress of 15 Dyne/cm² [52], and placenta (i.e. BeWo) cells exposed to shear stresses ranging from 0.001 to 0.12 Dyne/cm² [53]. In addition, we observed that cells grown under continuous flow seem to be larger compared to the cells grown without continuous flow. Likely this can also be explained by the shear stress exposure. Since actin filaments are associated with cell adhesion and mechanics, remodelling of actin filaments might alter cell spread, migration, elongation, or enlargement of the cells [52, 53]. While the thickness of the monolayers of cells grown under both conditions was comparable (10 μm height; Fig. 3G and H), the continuous flow seemed to induce a more pronounced 3D structure, which has more prominently been shown in Caco-2 containing chip models that also employ stretchable membranes (cyclic strain of 0.15 Hz frequency together with a shear stress of 0.02 Dyne/cm²) [6].

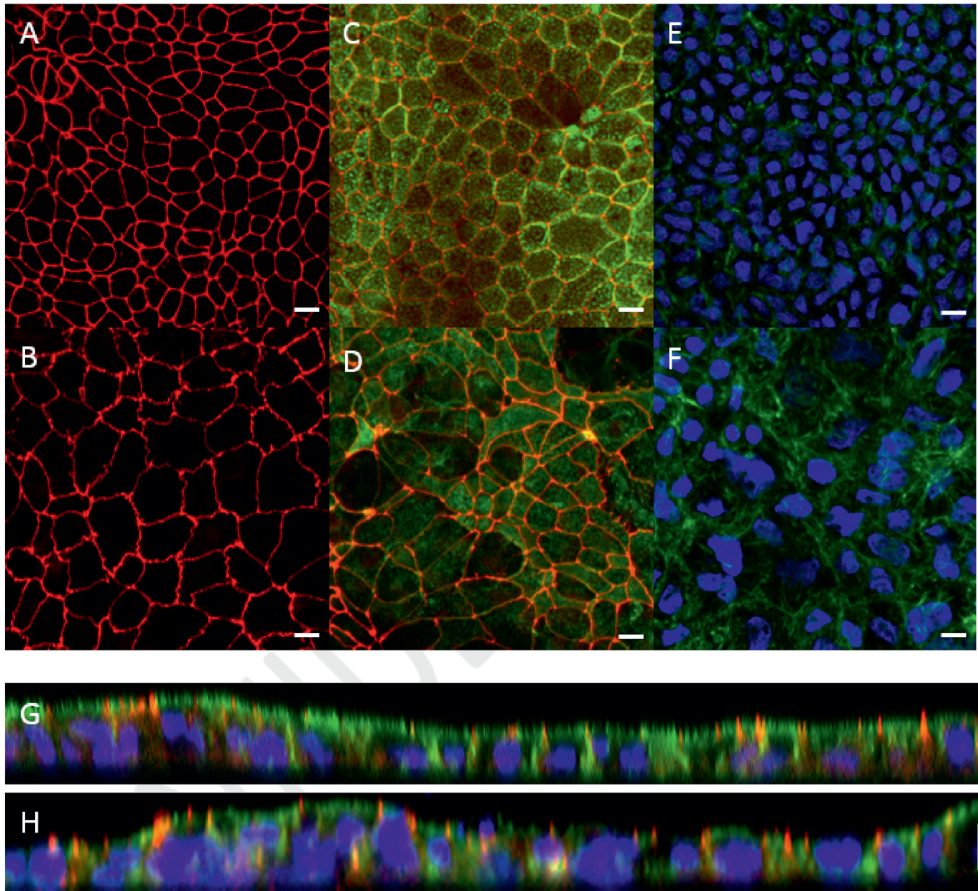


Figure 3. Morphology of Caco-2 cells cultured in a Transwell for 21 days versus in chip for 10 days (of which 7 days under a continuous flow of 25 $\mu\text{l/hr}$) visualized by confocal microscopy. Tight junctions of cells cultured in A) a Transwell and in B) a chip were stained for ZO-1/TJPI (red). Actin filaments on the apical side of the cells, stained by Phalloidin (green), and tight junctions of cells were visualized on merged images in C) a Transwell and D) a chip. Merged images showing nuclei (DAPI; blue) and actin filaments on the basolateral side of cells cultured in E) a Transwell, and F) a chip. Note the more pronounced expression of actin in the chip. Vertical cross-section of the cell monolayer in G) a Transwell and H) a chip. The scale bar represents 10 μm .

Comparative cellular uptake and absorption, and transport of dioxins

The human gut epithelium acts as an important barrier in defence to protect the body from exogenous substances that can be present in our food [54, 55]. To further optimize and implement dynamic gut-on-a-chip models, we determined the transport of 17 individual dioxin congeners across a monolayer of Caco-2 cells under dynamic and static culturing and exposure conditions.

Transport studies can only be reliably performed using dioxin concentrations that do not affect the viability of cells used in the experiment. A WST-1 assay was used to select a non-toxic dioxin mixture concentration. As can be seen in Fig. 4, decreased cell viability

was only observed following an exposure to ≥ 0.6 ng/mL dioxin mixture for 24h ($P < 0.05$, one way ANOVA). For the cellular association and transport studies an exposure concentration of 0.2 ng/mL was used.

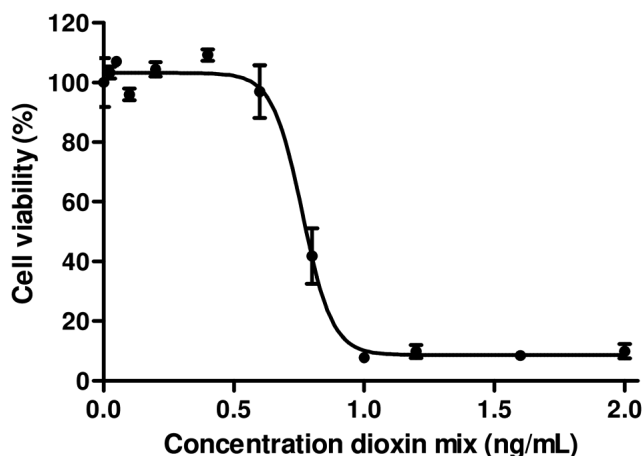


Figure 4. Cytotoxicity of the dioxin mixture in Caco-2 cells after 24 h exposure given as a percentage of viable cells (\pm SEM) of the total number of cells ($n=3$).

After 24 hours of exposure the cells were harvested from the chip and Transwell membranes and the concentration of individual congeners in these fractions, as well as in the medium fractions from the apical and basolateral compartments of both the chip and Transwell, was determined using GC-HRMS. Also, hexane rinses of both the chip and Transwell were evaluated. The so-called mass balance was determined (Table 3), which is the sum of the amount of congeners detected in the AP and BL compartments and the cellular fraction. This indicated mass balances ranging from 75 to 99%, concluding the method and experimental setup suitable for dioxin transport studies.

Table 3. Mass balance from dioxin transport experiments analysed by GC-HRMS ($n=3$)

Components	Mass balance (%)	
	Chip	Transwell
Congener		
2,3,7,8-TCDF	82±5	75±1
1,2,3,7,8-PeCDF	88±5	86±1
2,3,4,7,8-PeCDF	93±7	82±2
1,2,3,4,7,8-HxCDF	97±7	85±2
1,2,3,6,7,8-HxCDF	94±5	93±1
2,3,4,6,7,8-HxCDF	97±7	87±2
1,2,3,7,8,9-HxCDF	91±6	84±2
1,2,3,4,6,7,8-HpCDF	97±5	93±1
1,2,3,4,7,8,9-HpCDF	97±7	83±2
OCDF	96±8	79±2
2,3,7,8-TCDD	85±5	81±2
1,2,3,7,8-PeCDD	92±6	85±2
1,2,3,4,7,8-HxCDD	98±8	84±2
1,2,3,6,7,8-HxCDD	92±5	92±1
1,2,3,7,8,9-HxCDD	93±5	93±1
1,2,3,4,6,7,8-HpCDD	97±7	83±2
OCDD	100±8	82±2

Transport of dioxin congeners across the two barrier models was low and ranged from 0.6% to 3.3% for OCDF and 1,2,3,7,8-PeCDF respectively in the dynamic model, and ranged from 0.2% to 4.4% in the static model for OCDF and 1,2,3,7,8-PeCDF respectively (Fig. 5A). Comparison of the transport and cellular association of the individual congeners between both models showed no significant differences. In addition, a similar trend in congener transport was observed ($R^2=0.96$) between the two models (Fig. 5C). The larger error bars in the chip data compared to the Transwell data could be explained by the more complicated (technical) setup of the chip experiments compared to Transwells. In an earlier study the transport across a monolayer of Caco-2 cells of only 2,3,7,8- TCDD has been studied [56]. The authors quantified the TCDD concentration using a luciferase HepG2 cell assay. They found that 15% of TCDD was transported across the Caco-2 cell monolayer in

24 h [56]. This is higher than the 3% transported 2,3,7,8- TCDD observed by us for both models, which might be explained by differences in exposure concentration. In their study, a 10 fold higher concentration of 2.5 nM of 2,3,7,8-TCDD was used, whereas we used 0.26 nM of 2,3,7,8-TCDD as part of a mixture of dioxins.

Upon 24 h of exposure to the mixture of dioxins the cellular fraction contained relative amount of each congener ranging from 33% for 1,2,3,7,8,9-HxCDD to 61% for OCDD of the total exposure concentration (based on a mass balance calculation) in the dynamic model and relative amount ranging from 22.5% for 1,2,3,7,8,9-HxCDD to 51.8% for OCDD in the static model (Fig. 5B). While the fraction of the dioxin mixture in the cellular fraction seems to be increased in cells cultured under dynamic conditions this was not significantly different. Cellular association and accumulation of dioxins is likely caused by their lipophilicity as reported in the previous studies [57, 58]. Under both culture conditions individual congeners were present in the cellular fraction in a comparable pattern, as a strong correlation between the chip and Transwell cellular amount was observed for the whole series of test compounds ($R^2=0.98$; Fig. 5D).

Dioxins have been investigated extensively *in vitro* with most studies focusing on their potential toxicity and metabolism, focussing specifically on 2,3,7,8 TCDD-aryl hydrocarbon receptor (AhR) interactions. 2,3,7,8 TCDD can induce expression of cytochrome P450 1A1 (CYP1A1), a phase I drug metabolism enzyme, and UDP-glucuronosyltransferase (UGT) isoforms UGT1A6 and UGT1A9, phase II drug metabolism enzymes, in Caco-2 cells [59-62]. On the contrary, intestinal uptake and transport of dioxins has only very limitedly been studied *in vitro* before. We identified only one study that reports cellular association, in this study only a single dioxin congener has been used. For 2,3,7,8 TCDD, a steady-state amount of approximately 13% cellular association has been reported following 90 minutes of exposure to $3.4 \times 10^{-2} \mu\text{Ci/mL}$ U- ^{14}C -TCDD and less than 1.5% of apical concentration was transported to the basal compartment [63]. Our data illustrates an amount of 2,3,7,8-TCDD in the cellular fraction of approximately 39 and 56% in Transwell and chip model, respectively. We observed that the dioxin mixture was more retained in the cellular fraction than passed through the monolayer to the basal side under both experimental conditions. This can be explained by the high lipophilicity of the dioxin congeners and its influence on their partition coefficient, so they are likely to remain in phospholipid bilayers and only slowly diffuse across it [64]. This has been reported also for polychlorinated biphenyls, PCB#52, #118, #153 and #180, which have an extremely high hydrophobicity ($\log P > 5$) [65].

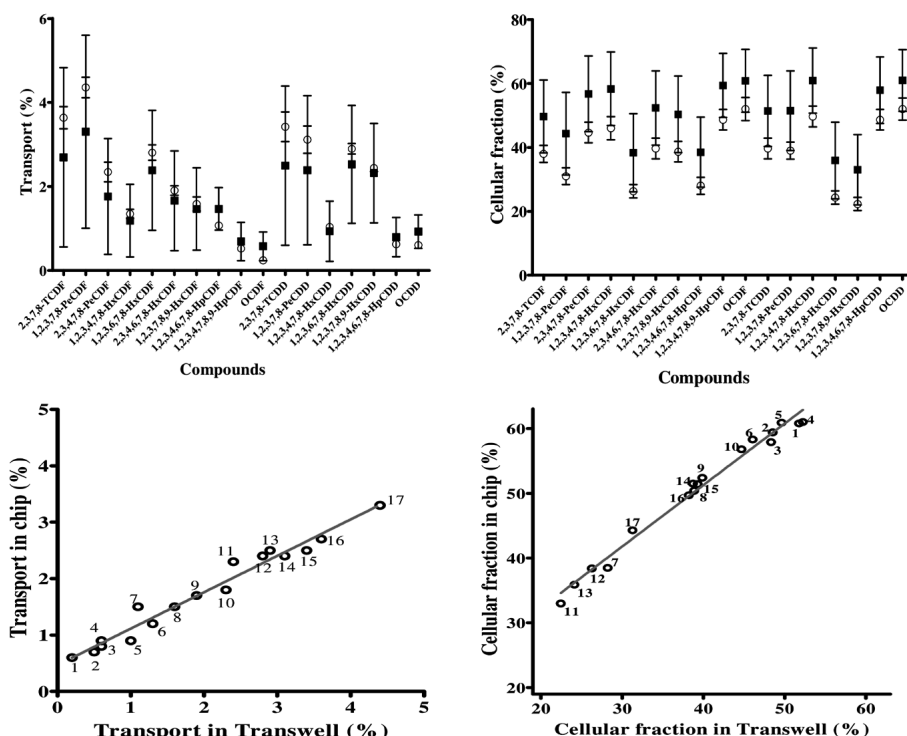


Figure 5. Comparison of dioxin congeners in the cellular fraction and transported over the cell barrier between a dynamic (•) versus a static (o) model. A) Transport of dioxin congeners through the monolayer of cells cultured in chips and Transwells given as a percentage (\pm SEM) of dioxin congeners in the basal side compared to the total exposed amount. B) Fraction of dioxin congeners in the cell fraction given as a percentage (\pm SEM) of dioxin congeners in the cellular fraction compared to the total exposed amount. C) Correlation between transported dioxin congeners in the dynamic versus static model. D) Correlation between dioxin congeners in the cellular fraction in the dynamic versus static model, 1=OCDF; 2=1,2,3,4,7,8,9-HpCDF; 3=1,2,3,4,6,7,8-HpCDD; 4=OCDD; 5=1,2,3,4,7,8-HxCDD; 6=1,2,3,4,7,8-HxCDF; 7=1,2,3,4,6,7,8-HpCDF; 8=1,2,3,7,8,9-HxCDF; 9=2,3,4,6,7,8-HxCDF; 10=2,3,4,7,8-PeCDF; 11=1,2,3,7,8,9-HxCDD; 12=1,2,3,6,7,8-HxCDF; 13=1,2,3,6,7,8-HxCDD; 14=1,2,3,7,8-PeCDD; 15=2,3,7,8-TCDD; 16=2,3,7,8-TCDF; 17=1,2,3,7,8-PeCDF.

QSPR modelling for PCDDs and PCDFs

To further explore the relationship between the physicochemical properties of the used dioxins and their uptake and/or cellular association we used QSPR modelling. QSPR modelling is used to identify correlations between structure and biological effects. In order to build a QSPR model experimental (chip) data is necessary, once a QSPR model is validated it could be used for prioritization of (new) specific compounds for (on-chip) testing based on their molecular structure. Combinations of *in vitro* studies and computational approaches have been identified as a powerful approach to develop alternative testing strategies without the use of animals [66, 67]. For each model equation we chose 2 descriptors, to avoid their overfitting [37]. The chosen descriptors are presented in the Table 4.

Table 4. Molecular descriptor pairs for the developed QSPR models

Pair of models	Descriptors	
Cell QSPR models	ATSC3v	Centred Broto-Moreau autocorrelation of lag 3 weighted by van der Waals volume
	GATS5v	Geary autocorrelation of lag 5 weighted by van der Waals volume
Transport QSPR models	ATS5m	Centred Broto-Moreau autocorrelation of lag 5 weighted by mass
	MATS5m	Moran autocorrelation of lag 5 weighted by mass

We have developed four statistically significant QSPR models describing relationship between the chemical structures of PCDDs and PCDFs and their uptake and/or cellular association and transport across the monolayer of cells. In the process of model calibration we obtained the following equations (4-7):

Model 1 (Uptake-chip): $Y = -9.9324 \text{ ATSC3v} - 52.8616 \text{ GATS5v} + 121.637$ (4)

Model 2 (Uptake-Transwells): $Y = -12.7950 \text{ ATSC3v} - 57.3662 \text{ GATS5v} + 118.7720$ (5)

Model 3 (Transport-chip): $\log Y = -1.0760 \text{ ATS5m} - 0.6038 \text{ MATS5m} + 4.4399$ (6)

Model 4 (Transport-Transwells): $\log Y = -1.7296 \text{ ATS5m} - 0.5969 \text{ MATS5m} + 7.0661$ (7)

The values of determination coefficients (R^2), internal and external validation coefficients (Q^2_{CV} and Q^2_{EXT}) and root mean square errors ($RMSE_C$, $RMSE_{CV}$, $RMSE_{EXT}$) presented in Table 5. indicate good quality, stability and predictive capabilities of the models.

Table 5. Parameters of quality evaluation for developed models

	R^2	$RMSE_C$	Q^2_{CV}	$RMSE_{CV}$	Q^2_{EXT}	$RMSE_{EXT}$
Model 1	0.83	3.83	0.73	4.83	0.87	3.11
Model 2	0.86	3.60	0.80	4.39	0.72	4.31
Model 3	0.91	0.07	0.86	0.08	0.87	0.08
Model 4	0.92	0.01	0.14	0.14	0.96	0.07

This evaluation is additionally confirmed by high correlation between experimental and predicted values of endpoints presented at the Fig. 6.

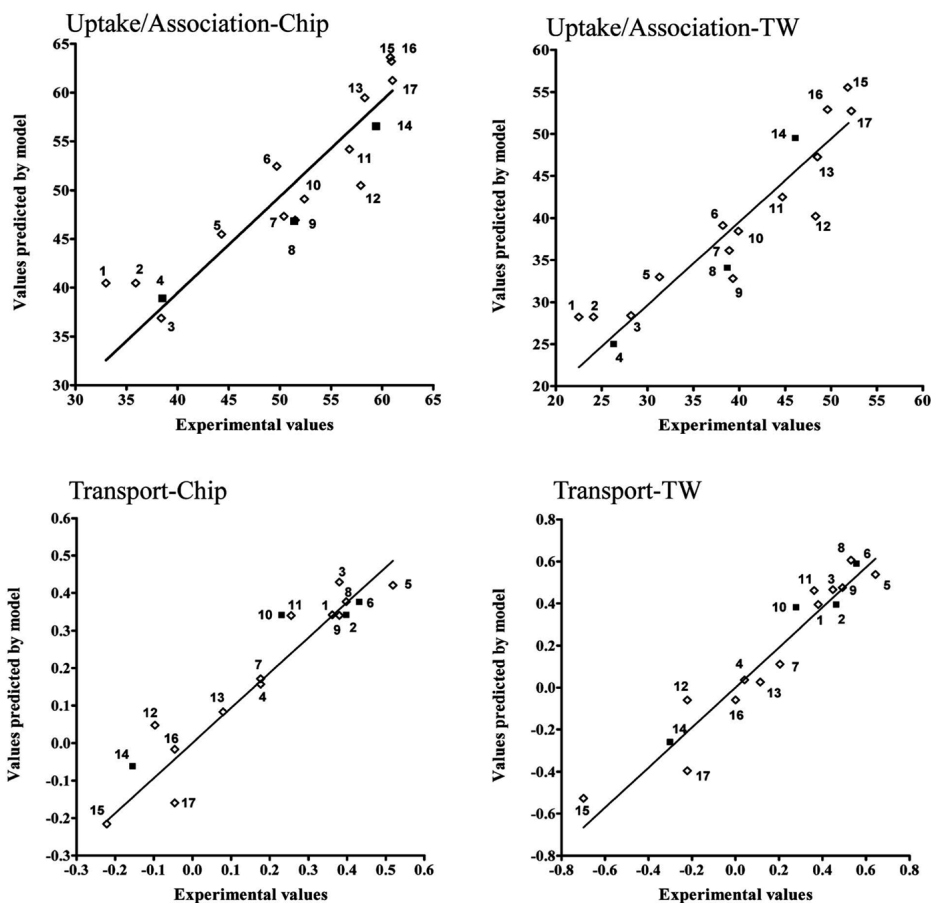


Figure 6. Experimental and predicted values of endpoint for each developed model, the training (◇) and validation set (■). 1=1,2,3,7,8,9-HxCDD; 2=1,2,3,6,7,8-HxCDD; 3=1,2,3,6,7,8-HxCDF; 4=1,2,3,4,6,7,8-HpCDF; 5=1,2,3,7,8-PeCDF; 6=2,3,7,8-TCDF; 7=1,2,3,7,8,9-HxCDF; 8=2,3,7,8-TCDD; 9=1,2,3,7,8-PeCDD; 10=2,3,4,6,7,8-HxCDF; 11=2,3,4,7,8-PeCDF; 12=1,2,3,4,6,7,8-HpCDD; 13=1,2,3,4,7,8-HxCDF; 14=1,2,3,4,7,8,9-HpCDF; 15=OCDF; 16=1,2,3,4,7,8-HxCDD; 17=OCDD

To verify models applicability domains (AD) we applied Williams plots¹¹ (values of standardized residuals versus the leverage values). AD is limited by the critical values of standardized residuals (three standard deviation units- 3σ) and the critical leverage value (h^*). The developed Williams plots are presented in Fig. 7.

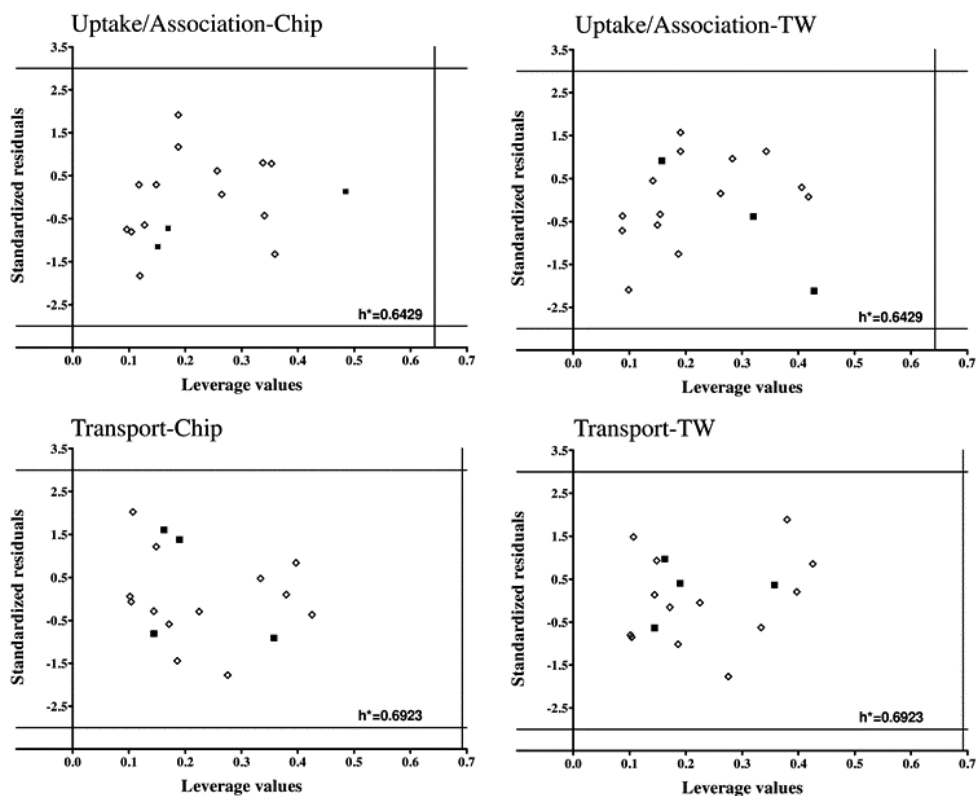


Figure 7. Williams plots for developed models. The lines on the plot ($\pm 3\sigma$ and h^*) define the applicability domain of the model, the training (\diamond) and validation set (\blacksquare).

All the compounds are situated in the range of ± 3 standard deviations from 0 and none of them exceeded the critical leverage value (h^*). It means that all the compounds used to develop the models are structurally similar and the uncertainty of model predictions for them is acceptable. Moreover, it confirms the assumption that PCDDs and PCDFs may belong to the common AD.

Interpretation of QSPR models can be used to hypothesize on mechanism of cellular uptake (and/or association) and subsequent transport of dioxins across the monolayer of cells. Molecular descriptors chosen for the model equation indicate which structural features determine the values of the endpoint. For our models we selected four autocorrelation descriptors: ATSC3v and GATS5v for uptake (and/or association) models, ATS5m and MATS5m for transport models. Autocorrelation descriptors can encode not only the structure of the molecule but also physico-chemical properties attributed to atoms, therefore descriptors of this type are effectively used for modelling compounds' interactions with membranes or their cytotoxicity [68-71]. For the cellular association models we developed (Model 1 and 2) there is a clear relationship between values of the ATSC3v descriptor and the number of chlorine atoms in the compound. These quantities are inversely proportional,

but this descriptor is preceded in model equations by negatives coefficients. Increasing number of chlorine atoms in the molecule is therefore associated with increasing value of PCDDs and PCDFs cellular association. The second descriptor used in uptake models-GATS5v- is connected to the substitution pattern. It takes on higher values when the distribution of chlorine atoms in the molecule is less symmetrical. Thus the GATS5v descriptor describes the distribution of the charge in the compound. This means that the uptake of PCDDs and PCDFs is higher in the case of less symmetrical molecules. This conclusion is also confirmed by the fact that GATS5v descriptor assumes higher values for PCDFs compared to PCDDs.

The results are relatively similar in case of models developed for the transport of PCDDs and PCDFs: first selected descriptor (ATS5m) is also inversely proportional to the number of chlorine atoms in a molecule. It shows, that compounds with higher number of chlorine atoms are more easily transported. The values of the second descriptor, MATS5m, depend on the substitution pattern.

Conclusion

Here we have implemented a dynamic flow gut-on-a-chip model that can be used to study the transport and the cellular accumulation of lipophilic compounds like dioxins. The experimental conditions were optimized to avoid uncontrollable adsorption. By using a very sensitive, dioxin congener specific GC-HRMS detection method, we show that the transport and cellular accumulation profile of dioxins of Caco-2 cells grown under continuous flow and static conditions is comparable. Physicochemical properties, of the dioxin congeners allowed us to predict their transport profiles *in vitro*

Caco-2 cell models have been used to study the absorption and local effects of a variety of compounds, and are recognized as usefully predictive *in vitro* models for the study of passage of substances through the gut wall. However, their conventional culture methods provide some disadvantages, for example, long term cultures time (~3 weeks), not fully mimicking *in vivo* conditions and inability to do on-line measurement. Therefore, a gut-on-a-chip system has been developed and proposed to be used as an *in vitro* alternative model that recapitulates not only *in vivo* fluid flows, but also the structure, transport, of the gut epithelium.

The results illustrate that Caco-2 cells cultured in a dynamic system for 10 days shows similar polarisation and morphological properties as cells cultured for 21 days in a static system. Furthermore, the gut-on-a-chip system also showed transport properties similar to the static system indicating its applicability for transport studies. Thus it now is possible to use an advanced gut-on-a-chip models next to the traditional Transwell model as a screening assay to study effects of compounds on dioxin absorption in order to prevent dioxin ingestion in human. Clearly, there are remaining technical challenges to be addressed in working with organ-on-chips, to allow an easier implementation of these models into routine testing. Precisely controlled injection systems, with flow and pressure control, and easy to use inert chip materials, are the most important technical challenges [72]. This is the first report

comparing the transport of 17 dioxin congener using an *in vitro* system and revealing their structure-transport relationship. Interestingly, using Quantitative Structure-Property Relationship modelling we have been able to reveal the relationship between the degree of chlorination and the chlorination patterning on the cellular association and transport of the individual dioxin congeners across a monolayer of Caco-2 cells.

The implemented gut-on-a-chip system can be used for dioxin transport screening which might be useful for other lipophilic compound study as well. Moreover, the microfluidic organ-on-a-chip model can be coupled to downstream analysis systems, such as mass spectrometry to measure the transported amount of drugs or metabolites in the system in real-time [73-75].

Conflicts of interest

There are no conflicts of interest to declare.

Acknowledgements

This research was financed by the Dutch Ministry of Agriculture, Nature and Food Quality and K. K. is supported by the Royal Thai government Scholarship.

References

1. Pereira, C., et al., 3.3 - *Cell-based in vitro models for intestinal permeability studies*, in *Concepts and Models for Drug Permeability Studies*. 2016, Woodhead Publishing. p. 57-81.
2. van Breemen, R.B. and Y. Li, *Caco-2 cell permeability assays to measure drug absorption*. Expert Opin Drug Metab Toxicol, 2005. 1(2): p. 175-85.
3. Marino, A.M., et al., *Validation of the 96 well Caco-2 cell culture model for high throughput permeability assessment of discovery compounds*. Int J Pharm, 2005. 297(1-2): p. 235-41.
4. Briske-Anderson, M.J., J.W. Finley, and S.M. Newman, *The influence of culture time and passage number on the morphological and physiological development of Caco-2 cells*. Proc Soc Exp Biol Med, 1997. 214(3): p. 248-57.
5. Kim, H.J. and D.E. Ingber, *Gut-on-a-Chip microenvironment induces human intestinal cells to undergo villus differentiation*. Integr Biol (Camb), 2013. 5(9): p. 1130-40.
6. Kim, H.J., et al., *Human gut-on-a-chip inhabited by microbial flora that experiences intestinal peristalsis-like motions and flow*. Lab Chip, 2012. 12(12): p. 2165-74.
7. Gori, M., et al., *Investigating Nonalcoholic Fatty Liver Disease in a Liver-on-a-Chip Microfluidic Device*. PLoS One, 2016. 11(7): p. e0159729.
8. Esch, E.W., A. Bahinski, and D. Huh, *Organs-on-chips at the frontiers of drug discovery*. Nature Reviews Drug Discovery, 2015. 14(4): p. 248-260.
9. Jang, K.J. and K.Y. Suh, *A multi-layer microfluidic device for efficient culture and analysis of renal tubular cells*. Lab on a Chip, 2010. 10(1): p. 36-42.
10. Bhise, N.S., et al., *Organ-on-a-chip platforms for studying drug delivery systems*. Journal of Controlled Release, 2014. 190: p. 82-93.
11. Walton, K.D., et al., *Generation of intestinal surface: an absorbing tale*. Development, 2016. 143(13): p. 2261-72.
12. Yeon, J.H. and J.K. Park, *Drug Permeability Assay Using Microhole-Trapped Cells in a Microfluidic Device*. Analytical Chemistry, 2009. 81(5): p. 1944-1951.
13. Mahler, G.J., et al., *Characterization of a Gastrointestinal Tract Microscale Cell Culture Analog Used to Predict Drug Toxicity*. Biotechnology and Bioengineering, 2009. 104(1): p. 193-205.
14. Organization, W.H., *Preventing disease through healthy environments*, in *Exposure to Dioxins and Dioxin-like Substances: A Major Public Health Concern*. 2010, <http://www.who.int/ipcs/features/dioxins.pdf>.
15. EFSA. *Dioxin and PCBs*. [<https://www.efsa.europa.eu/en/topics/topic/dioxins-and-pcbs>] 30 January 2018.
16. Milbrath, M.O., et al., *Apparent half-lives of dioxins, furans, and polychlorinated biphenyls as a function of age, body fat, smoking status, and breast-feeding*. Environ Health Perspect, 2009. 117(3): p. 417-25.
17. Charnley, G. and J. Doull, *Human exposure to dioxins from food, 1999-2002*. Food Chem Toxicol, 2005. 43(5): p. 671-9.
18. Huwe, J.K. and G.L. Larsen, *Polychlorinated dioxins, furans, and biphenyls, and polybrominated diphenyl ethers in a U.S. meat market basket and estimates of dietary intake*. Environ Sci Technol, 2005. 39(15): p. 5606-11.
19. Liem, A.K., P. Furst, and C. Rappe, *Exposure of populations to dioxins and related compounds*. Food Addit Contam, 2000. 17(4): p. 241-59.
20. Poiger, H. and C. Schlatter, *Pharmacokinetics of 2,3,7,8-Tcdd in Man*. Chemosphere, 1986. 15(9-12): p. 1489-1494.
21. Kitamura, K., et al., *Balance of intake and excretion of 20 congeners of polychlorinated dibenzo-p-dioxin, polychlorinated dibenzofuran and coplanar polychlorinated biphenyl in healthy Japanese men (vol 47, pg 145, 2001)*. Journal of Health Science, 2001. 47(6): p. 591-591.
22. EFSA, *Update of the monitoring of levels of dioxins and PCBs in food and feed EFSA EFSA Journal*, 2012. 10(7): p. 2832.

23. Vandenberg, M., et al., *The Toxicokinetics and Metabolism of Polychlorinated Dibenzo-P-Dioxins (Pcdds) and Dibenzofurans (Pcdfs) and Their Relevance for Toxicity*. Critical Reviews in Toxicology, 1994. 24(1): p. 1-74.
24. Hoogenboom, R., et al., *Polychlorinated dibenzo-p-dioxins and dibenzofurans (PCDD/Fs) and biphenyls (PCBs) in home-produced eggs*. Chemosphere, 2016. 150: p. 311-319.
25. Kim, S., et al., *PubChem Substance and Compound databases*. Nucleic Acids Research, 2016. 44(D1): p. D1202-D1213.
26. Hoogenboom, R., et al., *The use of the DR CALUX (R) bioassay and indicator polychlorinated biphenyls for screening of elevated levels of dioxins and dioxin-like polychlorinated biphenyls in eel*. Molecular Nutrition & Food Research, 2006. 50(10): p. 945-957.
27. Tropsha, A., *Best Practices for QSAR Model Development, Validation, and Exploitation*. Molecular Informatics, 2010. 29(6-7): p. 476-488.
28. Haranczyk, M., T. Puzyn, and P. Sadowski, *ConGENER - A tool for modeling of the congeneric sets of environmental pollutants*. Qsar & Combinatorial Science, 2008. 27(7): p. 826-833.
29. Rybinska, A., et al., *Geometry optimization method versus predictive ability in QSPR modeling for ionic liquids*. Journal of Computer-Aided Molecular Design, 2016. 30(2): p. 165-176.
30. Puzyn, T., et al., *Calculation of quantum-mechanical Descriptors for QSPR at the DFT level: Is it necessary?* Journal of Chemical Information and Modeling, 2008. 48(6): p. 1174-1180.
31. Mauri, A., et al., *Dragon software: An easy approach to molecular descriptor calculations*. Match-Communications in Mathematical and in Computer Chemistry, 2006. 56(2): p. 237-248.
32. Yao, X.J., et al., *Comparative study of QSAR/QSPR correlations using support vector machines, radial basis function neural networks, and multiple linear regression*. Journal of Chemical Information and Computer Sciences, 2004. 44(4): p. 1257-1266.
33. Ghafourian, T. and M.T.D. Cronin, *The impact of variable selection on the modelling of oestrogenicity*. Sar and Qsar in Environmental Research, 2005. 16(1-2): p. 171-190.
34. Gramatica, P., et al., *QSARINS: A new software for the development, analysis, and validation of QSAR MLR models*. Journal of Computational Chemistry, 2013. 34(24): p. 2121-2132.
35. Randy L. Haupt, S.E.H., *Practical Genetic Algorithms*. 2nd ed. 2004, New Jersey: John Wiley & Sons, Inc.
36. Cherkasov, A., et al., *QSAR Modeling: Where Have You Been? Where Are You Going To?* Journal of Medicinal Chemistry, 2014. 57(12): p. 4977-5010.
37. OECD, *Principles for the validation, for regulatory purposes, of (quantitative) structure-activity relationship models*. 2004, OECD: Paris.
38. Wu, J.H., et al., *A Self-Adaptive Genetic Algorithm-Artificial Neural Network Algorithm With Leave-One-Out Cross Validation for Descriptor Selection in QSAR Study*. Journal of Computational Chemistry, 2010. 31(10): p. 1956-1968.
39. Gramatica, P., *Principles of QSAR models validation: internal and external*. Qsar & Combinatorial Science, 2007. 26(5): p. 694-701.
40. Chirico, N. and P. Gramatica, *Real External Predictivity of QSAR Models: How To Evaluate It? Comparison of Different Validation Criteria and Proposal of Using the Concordance Correlation Coefficient*. Journal of Chemical Information and Modeling, 2011. 51(9): p. 2320-2335.
41. Cseh, T., et al., *Adsorption-desorption characteristics of polychlorinated biphenyls on various polymers commonly found in laboratories*. Appl Environ Microbiol, 1989. 55(12): p. 3150-4.
42. Unger, J.K., et al., *Adsorption of xenobiotics to plastic tubing incorporated into dynamic in vitro systems used in pharmacological research - limits and progress*. Biomaterials, 2001. 22(14): p. 2031-2037.
43. McDonald, J.C., et al., *Fabrication of microfluidic systems in poly(dimethylsiloxane)*. Electrophoresis, 2000. 21(1): p. 27-40.
44. Thangawng, A.L., et al., *An ultra-thin PDMS membrane as a bio/micro-nano interface: fabrication and characterization*. Biomedical Microdevices, 2007. 9(4): p. 587-595.

45. Tsao, C.W., *Polymer Microfluidics: Simple, Low-Cost Fabrication Process Bridging Academic Lab Research to Commercialized Production*. Micromachines, 2016. 7(12).
46. Berthier, E., E.W.K. Young, and D. Beebe, *Engineers are from PDMS-land, Biologists are from Polystyrenia*. Lab on a Chip, 2012. 12(7): p. 1224-1237.
47. Chumbimuni-Torres, K.Y., et al., *Adsorption of proteins to thin-films of PDMS and its effect on the adhesion of human endothelial cells*. Rsc Advances, 2011. 1(4): p. 706-714.
48. Toepke, M.W. and D.J. Beebe, *PDMS absorption of small molecules and consequences in microfluidic applications*. Lab on a Chip, 2006. 6(12): p. 1484-1486.
49. van Meer, B.J., et al., *Small molecule absorption by PDMS in the context of drug response bioassays*. Biochem Biophys Res Commun, 2017. 482(2): p. 323-328.
50. Li, N., M. Schwartz, and C. Ionescu-Zanetti, *PDMS compound adsorption in context*. J Biomol Screen, 2009. 14(2): p. 194-202.
51. Wang, J.D., et al., *Quantitative Analysis of Molecular Absorption into PDMS Microfluidic Channels*. Annals of Biomedical Engineering, 2012. 40(9): p. 1862-1873.
52. Noria, S., et al., *Assembly and reorientation of stress fibers drives morphological changes to endothelial cells exposed to shear stress*. American Journal of Pathology, 2004. 164(4): p. 1211-1223.
53. Miura, S., et al., *Fluid shear triggers microvilli formation via mechanosensitive activation of TRPV6*. Nature Communications, 2015. 6.
54. Groschwitz, K.R. and S.P. Hogan, *Intestinal barrier function: molecular regulation and disease pathogenesis*. J Allergy Clin Immunol, 2009. 124(1): p. 3-20; quiz 21-2.
55. Konig, J., et al., *Human Intestinal Barrier Function in Health and Disease*. Clin Transl Gastroenterol, 2016. 7(10): p. e196.
56. Natsume, Y., et al., *Evaluation of intestinal dioxin permeability using human Caco-2 cell monolayers*. Food Science and Technology Research, 2003. 9(4): p. 364-366.
57. Casalegno, M., G. Raos, and G. Sello, *From dioxin to dioxin congeners: understanding the differences in hydrophobic aggregation in water and absorption into lipid membranes by means of atomistic simulations*. Physical Chemistry Chemical Physics, 2016. 18(26): p. 17731-17739.
58. Laznickek, M. and A. Laznickova, *The effect of lipophilicity on the protein binding and blood cell uptake of some acidic drugs*. J Pharm Biomed Anal, 1995. 13(7): p. 823-8.
59. Hamada, M., et al., *TCDD-induced CYP1A1 expression, an index of dioxin toxicity, is suppressed by flavonoids permeating the human intestinal Caco-2 cell monolayers*. Journal of Agricultural and Food Chemistry, 2006. 54(23): p. 8891-8898.
60. Munzel, P.A., et al., *Induction of human UDP glucuronosyltransferases (UGT1A6, UGT1A9, and UGT2B7) by t-butylhydroquinone and 2,3,7,8-tetrachlorodibenzo-p-dioxin in Caco-2 cells*. Drug Metabolism and Disposition, 1999. 27(5): p. 569-573.
61. Daujat, M., et al., *Induction of CYP1A1 gene by benzimidazole derivatives during Caco-2 cell differentiation - Evidence for an aryl-hydrocarbon receptor-mediated mechanism*. European Journal of Biochemistry, 1996. 237(3): p. 642-652.
62. de Waard, W.J., et al., *Gene expression profiling in Caco-2 human colon cells exposed to TCDD, benzo[a]pyrene, and natural Ah receptor agonists from cruciferous vegetables and citrus fruits*. Toxicology in Vitro, 2008. 22(2): p. 396-410.
63. Cavret, S., C. Feidt, and F. Laurent, *Differential transfer of organic micropollutants through intestinal barrier using Caco-2 cell line*. Journal of Agricultural and Food Chemistry, 2005. 53(7): p. 2773-2777.
64. Lodish H, B.A., Zipursky SL, et al, *Diffusion of Small Molecules across Phospholipid Bilayers*, in *Molecular Cell Biology*. 2000, W. H. Freeman: New York.
65. Oomen, A.G., et al., *Availability of polychlorinated biphenyls (PCBs) and lindane for uptake by intestinal Caco-2 cells*. Environmental Health Perspectives, 2001. 109(7): p. 731-737.
66. Hartung, T., *Toxicology for the twenty-first century*. Nature, 2009. 460(7252): p. 208-212.
67. Hartung, T., et al., *Food for Thought ... Integrated Testing Strategies for Safety Assessments*. Altex-Alternatives to Animal Experimentation, 2013. 30(1): p. 3-18.

68. Wagener, M., J. Sadowski, and J. Gasteiger, *Autocorrelation of Molecular-Surface Properties for Modeling Corticosteroid-Binding Globulin and Cytosolic Ah Receptor Activity by Neural Networks*. Journal of the American Chemical Society, 1995. 117(29): p. 7769-7775.
69. Bauknecht, H., et al., *Locating biologically active compounds in medium-sized heterogeneous datasets by topological autocorrelation vectors: Dopamine and benzodiazepine agonists*. Journal of Chemical Information and Computer Sciences, 1996. 36(6): p. 1205-1213.
70. Saiz-Urra, L., M.P. Gonzalez, and M. Teijeira, *2D-autocorrelation descriptors for predicting cytotoxicity of naphthoquinone ester derivatives against oral human epidermoid carcinoma*. Bioorganic & Medicinal Chemistry, 2007. 15(10): p. 3565-3571.
71. Bordas, B., I. Belai, and T. Komives, *Theoretical Molecular Descriptors Relevant to the Uptake of Persistent Organic Pollutants from Soil by Zucchini. A QSAR Study*. Journal of Agricultural and Food Chemistry, 2011. 59(7): p. 2863-2869.
72. Probst, C., S. Schneider, and P. Loskill, *High-throughput organ-on-a-chip systems: Current status and remaining challenges*. Current Opinion in Biomedical Engineering, 2018. 6: p. 33-41.
73. Mao, S.F., et al., *Imitation of drug metabolism in human liver and cytotoxicity assay using a microfluidic device coupled to mass spectrometric detection*. Lab on a Chip, 2012. 12(1): p. 219-226.
74. Gao, D., et al., *Evaluation of the absorption of methotrexate on cells and its cytotoxicity assay by using an integrated microfluidic device coupled to a mass spectrometer*. Anal Chem, 2012. 84(21): p. 9230-7.
75. Gao, D., et al., *Characterization of drug permeability in Caco-2 monolayers by mass spectrometry on a membrane-based microfluidic device*. Lab on a Chip, 2013. 13(5): p. 978-985.

Supp Table 1. Dioxin adsorption during transport experiments. Adsorption was measured by rinsing the systems with hexane and measurement with GC-HRMS.

Congeners	Adsorption in various compartments (%)				Total adsorption (%)	
	Chip		TW		Chip	TW
	AP	BL	AP	BL		
2,3,7,8-TCDF	5.40	0.57	5.08	0.37	5.97	5.45
1,2,3,7,8-PeCDF	3.50	0.44	2.86	0.17	3.94	3.03
2,3,4,7,8-PeCDF	3.88	0.52	3.95	0.11	4.40	4.06
1,2,3,4,7,8-HxCDF	4.03	0.42	3.46	0.05	4.45	3.50
1,2,3,6,7,8-HxCDF	1.87	0.37	1.94	0.05	2.24	1.98
2,3,4,6,7,8-HxCDF	2.20	0.37	2.38	0.05	2.57	2.44
1,2,3,7,8,9-HxCDF	3.43	0.40	3.08	0.06	3.84	3.14
1,2,3,4,6,7,8-HpCDF	1.42	0.36	1.18	0.06	1.78	1.24
1,2,3,4,7,8,9-HpCDF	3.00	0.39	2.60	0.04	3.38	2.64
OCDF	2.57	0.40	1.29	0.11	2.97	1.39
2,3,7,8-TCDD	7.23	0.67	4.91	0.40	7.90	5.31
1,2,3,7,8-PeCDD	4.21	0.52	3.62	0.14	4.74	3.76
1,2,3,4,7,8-HxCDD	4.18	0.43	3.86	0.06	4.61	3.91
1,2,3,6,7,8-HxCDD	1.61	0.34	1.72	0.06	1.95	1.79
1,2,3,7,8,9-HxCDD	1.72	0.31	1.65	0.05	2.03	1.71
1,2,3,4,6,7,8-HpCDD	2.56	0.43	2.12	0.05	3.00	2.18
OCDD	2.78	0.82	1.34	0.18	3.60	1.52

Supp Table 2. The p-value of statistical analysis obtained from an independent samples t-test


Congeners	P-value of Transport analysis	P-value of cellular accumulation analysis
2,3,7,8-TCDF	0.490	0.219
1,2,3,7,8-PeCDF	0.511	0.162
2,3,4,7,8-PeCDF	0.514	0.163
1,2,3,4,7,8-HxCDF	0.762	0.150
1,2,3,6,7,8-HxCDF	0.643	0.167
2,3,4,6,7,8-HxCDF	0.741	0.148
1,2,3,7,8,9-HxCDF	0.849	0.235
1,2,3,4,6,7,8-HpCDF	0.247	0.242
1,2,3,4,7,8,9-HpCDF	0.556	0.147
OCDF	0.161	0.247
2,3,7,8-TCDD	0.453	0.143
1,2,3,7,8-PeCDD	0.524	0.212
1,2,3,4,7,8-HxCDD	0.810	0.188
1,2,3,6,7,8-HxCDD	0.693	0.169
1,2,3,7,8,9-HxCDD	0.873	0.236
1,2,3,4,6,7,8-HpCDD	0.574	0.230
OCDD	0.239	0.254



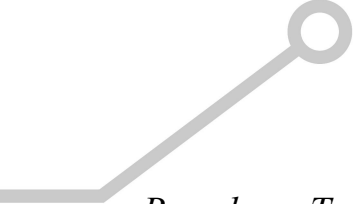


CHAPTER 3

Microfluidic chip for culturing intestinal epithelial cell layers: Characterization and comparison of drug transport between dynamic and static models



Kornphimol Kulthong, Loes Duivenvoorde, Huiyi Sun, Samuel Confederat, Jiaqing Wu, Bert Spenkelink, Laura de Haan, Victor Marin, Meike van der Zande and Hans Bouwmeester



Based on: Toxicology in Vitro (2020), Volume 65, Article 10481



Abstract

Dynamic flow *in vitro* models are currently widely explored for their applicability in drug development research. The application of gut-on-chip models in toxicology is lagging behind. Here we report the application of a gut-on-chip model for biokinetic studies and compare the observed biokinetics of reference compounds with those obtained using a conventional static *in vitro* model. Intestinal epithelial Caco-2 cells were cultured on a porous membrane assembled between two glass flow chambers for the dynamic model, or on a porous membrane in a Transwell model. Confocal microscopy, lucifer yellow translocation, and alkaline phosphatase activity evaluation revealed that cells cultured in the gut-on-chip model formed tight, differentiated, polarized monolayers like in the static cultures. In the dynamic gut-on-chip model the transport of the high permeability compounds antipyrine, ketoprofen and digoxin was lower (i.e. 4.2-, 2.7- and 1.9-fold respectively) compared to the transport in the static Transwell model. The transport of the low permeability compound, amoxicillin, was similar in both the dynamic and static *in vitro* model. The obtained transport values of the compounds are in line with the compound Biopharmaceuticals Classification System. It is concluded that the gut-on-chip provides an adequate model for transport studies of chemicals.

Introduction

Toxicological safety studies of pharmaceuticals and industrial chemicals are an integral part of product development. Traditionally, this implies the use of animals, which not only is time consuming, considered unethical and expensive, but importantly also raises scientific questions related to interspecies differences in biokinetics compared to humans [1, 2]. The combination of these scientific, socioeconomic, and ethical concerns resulted in attempts to refine, reduce, or replace (3Rs) the use of animals for toxicological safety studies [3-6]. Since the launch of the 3Rs principle several *in vitro* models have been proposed as alternative models to reduce animal experiments to study drug permeation across the intestinal epithelium [7-9].

More recently and along these lines, dynamic flow gut-on-chip devices have been proposed as an additional tool to existing static *in vitro* cell culture models. The devices mimic *in vivo* tissue to fluid ratios and fluid flow by using microfluidic technology [10, 11] attempting to better recapitulate the *in vivo* physiological tissue functioning. An additional advantage of gut-on-chip devices for compound transport and effect studies is that they allow for integrated online detection [12, 13] and coupling to other organ-on-chip systems [14, 15]. Gut-on-chip models have been proposed for preclinical [10, 11, 16, 17] and pharmacological applications [18-20]. To emulate human intestinal disease models human stem cell-based intestinal models have been used [21]. However, given the yet unresolved issues on reproducibility and lab variability in stem cell models, cell line based models are preferred for toxicokinetic and toxicodynamic studies [22].

The transport of several compounds has been evaluated using variants of gut-on-chip models, notably: antipyrine, propranolol, naproxen, furosemide, verapamil, atenolol, piroxicam, hydrochlorothiazide, cimetidine, carbamazepine [23], acetaminophen [14, 15, 24], rhodamine 123 [25] and curcumin [12]. Only for a limited number of compounds the transport in a dynamic gut-on-chip model has been compared to that in the conventional Transwell model. These studies have been performed for caffeine, atenolol [26], cyclophosphamide [27], mannitol, insulin [28] acetaminophen [24], verapamil, ergotamin(in)e, food contaminant compounds [29], and the environmental contaminants of the dioxin and PCB group (Kulthong et al., 2018). The observed transport of the compounds in the dynamic gut-on-chip models were consistent with those obtained using a conventional Transwell for most compounds, with the exception of caffeine (higher transport in gut-on chip), atenolol (higher transport) and ergotaminine (lower transport).

Most gut-on-chip devices are manufactured using polydimethylsiloxane (PDMS). This is mainly because PDMS is biologically compatible and allows soft lithography-based production methods, which enable rapid manufacturing of three-dimensional microstructures, [30-32]. In addition PDMS-based devices allow microscopy-based read-outs [33]. However, PDMS has a major disadvantage; it adsorbs a wide range of molecules such as proteins and lipophilic drugs [33-35]. Adsorption can partially be prevented by applying a coating on the PDMS [36], but this might influence the outcome of a biological

study. Therefore, in our studies we used a microfluidic gut-on-chip device that consists of three resealable glass slides that, upon assembly, result in two flow chambers separated by a middle layer that contains a porous cell culture membrane.

In this study, we aimed to evaluate whether our *in vitro* gut-on-chip intestinal barrier model is an adequate model for compound transport studies. To this end we performed a biokinetic study comparing a dynamic gut-on-chip [37] with a conventionally used static Transwell model. We exposed Caco-2 cells, grown in the gut-on-chip or Transwell model to several model compounds for which extensive information on *in vivo* bioavailability and transport mechanisms is available. High and low oral permeability class compounds were selected, known to represent different absorption mechanisms (e.g. passive diffusion and active transport). For these drugs we determined permeability coefficients using both models. In addition, a morphological and functional characterisation of the dynamic gut-on-chip and static Transwell models was performed using confocal microscopy and enzyme activity assays. We report the influence of laminar flow on compound transport, which was evaluated in the gut-on-chip under static and dynamic conditions.

Materials and methods

Chemicals and reagents

Antipyrine, ketoprofen, digoxin, amoxicillin, bovine serum albumin (BSA), Dulbecco's Modified Eagle Medium (DMEM), penicillin-streptomycin, Hank's balanced salt solution (HBSS), trifluoroacetic acid were obtained from Sigma-Aldrich (Zwijndrecht, The Netherlands). Phosphate Buffered Saline (PBS), heat inactivated fetal bovine serum (FBS) and MEM-non-essential amino acids were purchased from Fisher Scientific (Landsmeer, The Netherlands). Amoxicillin-d4 was obtained from CacheSyn (Mississauga, Canada). Acetonitrile was obtained from Biosolve (Valkenswaard, The Netherlands). Formic acid was purchased from VWR international (Darmstadt, Germany).

Design of the gut-on-chip system

The microfluidic gut-on-chip device has been described before [37]. In short, it consists of three 15x45 mm (width x length) re-sealable glass slides that result in two flow chambers (i.e. an upper apical (AP) and lower basolateral (BL) chamber) upon assembly (see Fig. 1 A; Micronit, Enschede, The Netherlands). Both the upper and lower glass slides were spaced from the middle layer membrane by a 0.25 mm thick silicone gasket and the flow chambers were separated by a glass slide containing a porous cell culture membrane that was fixed on the glass slide. The membrane consisted of a polyester (PET) membrane with a 0.4 μm pore size and a 1 cm^2 surface area. The height of the cell culture area was 0.65 mm and the height of the bottom flow channel was 0.25 mm, resulting in a volume of 110 mm^3 and 75 mm^3 for the AP and BL side, respectively, and 185 mm^3 for the total volume of the device (μL). The chip was placed in a chip holder with a quick locking mechanism, constructed for connection

of external capillaries to the chip via specific ferrules to ensure tight connections and a leak-free system.

The flow was induced using a multi-channel air pressure driven pump. Two channels per chip (i.e. one for the AP side and one for the BL side) were connected to the chip inlets using Polyetheretherketone (PEEK) capillary tubing (0.125 mm inner diameter, with a total length of 60 cm). Each flow channel was equipped with a flow sensor to assure precise regulation of the flow, which was located at 40 cm distance from the pump and 20 cm distance from the chip. Fluorinated Ethylene Propylene (FEP) tubing (0.250 mm inner diameter, 40 cm length) was used to connect to the chip outlets to the culture medium reservoirs. Before the start of each experiment, all tubing and chips were sterilized using an autoclave and rinsed with 70% ethanol. Tubing and chips were prefilled with medium to eliminate air bubbles in the system. The entire system was put in an incubator at 37°C to maintain cell culture conditions.

Cell culture

A Caco-2 cell line (HTB-37), derived from a human colorectal adenocarcinoma, was obtained from the American Type Culture Collection (ATCC, Manassas, VA, USA). The cells were grown (at passage number 29-45) in complete culture medium, consisting of DMEM supplemented with 10 % FBS, 1 % penicillin-streptomycin, and 1 % MEM non-essential amino acid, further referred to as DMEM⁺.

The cells were seeded at a density of 75,000 cells per cm² on 12-well Transwell polyester inserts (0.4 µm pore size, 1.12 cm² surface area, Corning Amsterdam, The Netherlands) and cultured in DMEM⁺ for 21 days. The medium was changed every two to three days.

In the microfluidic chip, the cells were seeded at a density of 75,000 cell per cm² and were allowed to attach to the membrane. After 24 h the membrane was inserted in the microfluidic chip. After attachment, the cells were exposed to a continuous flow of 100 µL/h DMEM⁺ for 21 days. By doing so, the shear stress in the AP compartment was ~0.0002 Dyne/cm² at the membrane surface, where the cells are grown. The DMEM⁺ medium contained sodium bicarbonate (10 mM) to optimize the pH buffering capacity.

Caco-2 monolayer integrity

Apical to basal translocation of lucifer yellow was measured in a Caco-2 monolayer under static and dynamic conditions. A lucifer yellow solution of 500 µg/mL in DMEM⁺ was perfused through the apical channel of the chip with a flow rate of 100 µL/h. The basolateral channel was perfused with DMEM⁺ with a flow rate of 100 µL/h. Sample aliquots of 50 µL were collected from the apical and basal outlet every half hour for 3 h. The same concentration of lucifer yellow solution was added apically to the cells in a Transwell (500 µL/insert) and incubated for 1 h before collecting the medium sample from the apical and

basolateral chambers. The fluorescence intensity (485/530 nm) of all collected samples from both systems was measured using a microplate reader (Synergy HT, BioTek, VT).

Fluorescent imaging of *in vitro* epithelial cell morphology

Twenty-one days after seeding, Caco-2 cells, grown in the gut-on-chip or Transwell, were prepared for cell and monolayer morphological assessment. The chips were opened, and cells were fixed with 4% formaldehyde at room temperature for 10 min and rinsed with PBS. Cells were then permeabilized with 0.25% Triton X100 in PBS for 10 min, rinsed with PBS and blocked with 1% acetylated bovine serum albumin in PBS for 30 min. Tight junctions were stained with 10 $\mu\text{g/mL}$ conjugated antibody ZO-1/TJP1-Alexa Fluor 594 (Invitrogen, Waltham, MA). The nuclei were stained with 5 $\mu\text{g/mL}$ DAPI (Invitrogen, Waltham, MA) and 4 U/mL Phalloidin Alexa Fluor 488 (Life technologies, Carlsbad, CA) was used to stain actin filaments (i.e. cytoskeleton). The incubation time for all stainings was 30 min. Each membrane was then cut out and placed between two cover slips separated by a spacer (0.12 mm depth x 20 mm diameter) with a drop of anti-fading mounting medium on the membrane. The cells cultured on Transwell membranes were stained using the same procedure. The stained monolayers of cells were analysed using a confocal microscope (LSM 510 UVMETA; Carl Zeiss, Germany). Samples were excited with 405, 488 and 543 nm lasers. Multi-tracked images were captured to avoid bleed through. The used pinholes were in the range of 148-152 μm at a magnification of 40x. The gain and offset for the different channels were kept constant during the entire experiment.

Caco-2 differentiation

Alkaline phosphatase (ALP) activity was measured in cells cultured for 21 days in both systems using an ALP colorimetric assay kit (ab83369, Abcam, Cambridge, UK) following the protocol of the manufacturer. Briefly, the membranes/inserts were taken from the chip/Transwell chambers. After washing the cells with HBSS at 37 °C, trypsin/EDTA was added to the cells and they were incubated for 5-7 minutes. The cell suspension was collected and centrifuged at 300 g for 5 min at 4 °C. The cell pellet was then resuspended in 200 μL ALP assay buffer and centrifuged at maximum speed, 16,000 RPM for 5 min at 4 °C. The supernatant (sample) was then collected and pipetted into the well of a 96-wells plate before adding the reaction buffer (50 μL /well), containing a p-nitrophenyl Phosphate solution (5 mM). After the plate was incubated in the dark for 60 min at 25 °C, 20 μL stop solution was added to each well of the reaction and shaken gently. Absorbance was read immediately at 405 nm using a microplate reader. A standard curve of p-nitrophenol (pNP) was prepared in a concentration range of 0-20 nmol/well, and converted to concentration after blank subtraction. Enzyme activity was calculated and expressed as nmol of pNP/min and normalised to the total amount of cells in term of protein content, which was measured using a RC-DC assay, a colorimetric protein determination based on the principle of Lowry estimation.

Computational model to calculate shear stress

Computational fluid dynamics was used to calculate the wall shear stress of the cell culture medium in the gut-on-chip using COMSOL Multiphysics® v. 5.3 (www.comsol.com, COMSOLAB, Stockholm, Sweden). The microfluidic device consisted of two rectangular microchambers separated by a glass middle layer containing a PET membrane. The inner dimensions of the rectangular chamber used for simulation consisted of one inlet and one outlet, the maximum inner high was 0.25 mm, the maximum width was 11 mm and length from inlet to outlet was 30 mm, and an oval cavity at the centre with area of 1.0 cm². Considering a steady flowrate of 100 µL/h we obtained laminar flow conditions with a Reynolds number of 0.007. The culture medium was considered as an incompressible and homogeneous, Newtonian fluid with similar conditions to water at 37 °C (density; 997 kg/m³ and viscosity; 6.9x10⁻⁴ Pa s⁻¹). A laminar Flow/Stationary library was used to determine the shear rate. The shear stress was estimated by multiplying the shear rate with the dynamic viscosity of water at 37 °C. An extremely coarse mesh size was used to reduce the computing time. No-slip boundary conditions were applied to the microchannel walls. Since the flow cell is fully made of glass, it was considered rigid with impermeable walls. The shear stress was obtained from the simulation using the height of 0.25 mm (near the inlet) and another position with an additional height of 0.40 mm at the centre of the chamber on the PET membrane. To corroborate this COMSOL calculation we used an adapted Poiseuille equation for rectangular microchannels as a second method [26, 38]. This equation could be applied to our system since the microfluidic chamber width is larger than the height ($h \ll w$). To calculate the shear stress using this method two different heights were taken in consideration: 1) from the top to the glass middle layer (0.25 mm), and 2) from the top to the PET membrane (0.65 mm). Comparison of the COMSOL simulation and the adapted Poiseuille equation showed equal results.

Caco-2 viability

Cytotoxicity was assessed using an MTT assay, a mitochondrial activity-based cell viability assay. Caco-2 cells (50,000 cells/cm²) were seeded in 96-well plates. After 24 h, the medium was discarded and was subsequently replaced with various concentrations of antipyrine (0, 25, 50, 100, 250 or 500 µM), ketoprofen (0, 25, 50, 100, 250 or 300 µM), digoxin (0, 25, 50, 100, 125 or 250 µM), or amoxicillin (0, 25, 50, 100, 250 or 500 µM) in HBSS for 24 h. At the end of the treatment period, cells were washed with 100 µL PBS, and 60 µL of 0.8 mg/mL MTT solution in DMEM⁺ was added to the cells and further incubated for 1.5 h. The medium was then discarded, and the cells were permeabilized resulting in formazan crystals dissolving in 100 µL of DMSO. The absorbance was measured at 570 using a microplate reader and the background absorbance at 650 nm was subtracted. The percentage of cell viability was calculated from the absorbance obtained from the control divided by that of each treatment.

Compound transport studies across a monolayer of intestinal Caco-2 cells

The transport studies were performed following an established protocol for static transport studies using Caco-2 cells [39]. At day 21 post-seeding, a non-toxic concentration of 100 μM antipyrine, 100 μM ketoprofen, 125 μM digoxin, and 250 μM amoxicillin was prepared in a transport medium (HBSS).

In the gut-on-chip studies, each compound solution was perfused through the upper channel with a flow rate of 100 $\mu\text{L/h}$, whereas 4% BSA in HBSS was pumped through the basolateral channel. An aliquot (100 μL) was collected from the apical and basolateral outlet every hour for six hours.

In the Transwell studies, the cells were washed with HBSS for 15-20 min at 37°C (0.5 mL in apical side, and 1.5 mL in basolateral side). Subsequently, HBSS was removed from the basolateral chamber and replaced with 1.2 mL basolateral medium (4% BSA in HBSS). Compound solutions of 0.4 mL in HBSS were then added to the apical side of the inserts. From the basolateral side, aliquots (600 μL) were collected and replaced with the same volume of 4% BSA in HBSS at settled time points (0, 15, 30, 60, 90 and 120 min for antipyrine, ketoprofen and digoxin, and 0, 30, 60, 90, 120, 150 and 180 min for amoxicillin). All the liquid from the apical and basolateral chamber was collected at the last time point in order to calculate a mass balance. All samples were stored in -80 °C before analysis.

The transport was calculated from the experimental data using equation (1) for the Transwell data and (2) for the gut-on-chip data. Equation (2) was derived from equation (1) [23].

$$(1) \quad P_{app} = \left(\frac{dQ}{dt} \right) \left(\frac{1}{AC_0} \right)$$

$$(2) \quad P_{app} = CV \left[\frac{1}{AC_0} \right]$$

Where A is the surface area (cm^2), dQ is the amount of the model compound transported (μmol) over the respective time interval dt (s), C_0 is the initial concentration (μM), C is the concentration in the basolateral compartment (μM), and V is the flow rate (L/s).

Sample quantification (HPLC-UV/LC-MS/MS)

All samples from the transport experiments, except for the amoxicillin samples from experiments with cell monolayer in both models, were analysed using high-performance liquid chromatography (HPLC), as described previously [40], to quantify the amount of compound in the sample. Prior to analysis, one volume of collected sample was mixed with ACN or MeOH for amoxicillin to precipitate the BSA. After centrifugation at 16000 g for 10 minutes, the supernatant was injected in the HPLC column for analysis. Antipyrine and ketoprofen samples (50 μL) were applied to a C18 reverse-phase column (150 mm x 4.6 I.D.

, 5 μm particle size) with a guard column (7.5 mm x 4.6 mm I.D.; Alltech, The Netherlands) and detected by a UV detector (Perkin-Elmer, Waltham, MA) at 260 (antipyrine) and 254 (ketoprofen) nm. Digoxin (100 μL) and amoxicillin (50 μL) samples were injected to the same column and was detected and quantified by UV absorption (Waters, Milford, MA) at 220 and 245 nm, respectively. Trifluoroacetic acid (TFA) 1% in water (solvent A) and ACN (solvent B) were used as the mobile phase for analysis of all test compounds. For analysis of antipyrine, ketoprofen and amoxicillin, elution was applied at a flow rate of 1.0 mL/min, starting at 90% solvent A with a linear decrease to 0% solvent A in 20 minutes. Then, the gradient returned to the initial concentration in 2 minutes, which was maintained for 10 minutes before the next sample was injected. For the analysis of digoxin, the gradient elution started with 78% solvent A at a flow rate of 0.7 mL/min for 2 min, followed by a linear decrease to 0% solvent A in 8 min. Then, the gradient returned to the initial conditions by a linear gradient over 2 min and remained at this condition for 10 min. Calibration curves were made using commercially available reference compounds for each individual set of samples to enable quantification of the obtained results.

In the case of the amoxicillin studies with cells, liquid chromatography–mass spectrometry (LC-MS), was used to detect the amount of amoxicillin in the samples. Briefly, a 250 μL aliquot of the basolateral Transwell samples or 25 μL of gut-on-chip samples and apical Transwell samples was mixed with 10 μL of internal standard working solution (25 $\mu\text{g/L}$ AMOX-d4). Then, 2 mL of ACN was added and the solution was placed in a rotary tumbler for 15 min followed by centrifugation at 3500 g for 10 min. After that, ACN was evaporated with N_2 at 40 °C and the remaining pellet was re-suspended with either 100 μL 25 (v/v)% MeOH for the basolateral Transwell samples or 200 μL for the basolateral gut-on-chip samples. For the apical samples, evaporation was not necessary because of their higher concentrations. For all samples 100 μL was diluted with 900 μL 25% MeOH, and transferred to LC-MS/MS vials. Five μL of the sample was injected into the Acquity liquid chromatographic separation system (Waters, Milford, MA,) through an Acquity UPLC HSS T3 column (2.1 mm x 100 mm I.D., 1.8 μm) (Waters) at 30°C employed under the gradient mixture of 0.001 (v/v)% formic acid in water (A) and 0.001 (v/v)% formic acid in ACN (B) at a flow rate of 0.4 mL/min. The gradient program was as follows: 0-1 min 0% B; 1-2.5 min, from 0 to 25% B; 2.5-5.4 min, from 25 to 70% B; 5.4-5.5 min, from 70 to 100% B; 5.5-8.5 min, 100% B; 8.5-8.6 min, from 100 to 0% B; followed by the re-equilibration at 0% B for 0.9 min before the next injection. The LC eluent was introduced directly into the electrospray ionization source (ESI) of the Q-Trap6500 mass spectrometer (Sciex, Framingham, MA) operating in the negative mode. Nitrogen was used as nebulizing turbo spray gas. The operational parameters of the ESI turbo ion source were as follows: vaporizing temperature 450 °C; curtain gas 35; and ionspray voltage -4000 V. Compound fragmentation was achieved using collision induced dissociation using N_2 as collision gas. The following multiple reaction monitoring (MRM) transitions were used; the precursor ion $[\text{M}+\text{H}]^+$ for amoxicillin was measured at m/z 363.9 and the corresponding product ions were measured

at m/z 222.9 and m/z 206. The declustering potential (DP) was set at -15 V and the collision energy (CE) was -14 V and -24 V, respectively. The precursor ion $[M+H]^+$ for amoxicillin-d4 was measured at m/z 367.9 and the product ion was m/z 227.0. The DP was -45 V, and CE was -14 V. Data processing was carried out using Multiquant software V3.0.2 (Sciex, Framingham, MA). For quantification, the peak areas of the target ions were corrected with those of the internal standard and the concentrations were determined using a matrix matched calibration line.

Statistical analysis

All statistical evaluations were evaluated using an independent paired t-test (SPSS, IBM). A p-value of ≤ 0.05 was considered significant.

Results

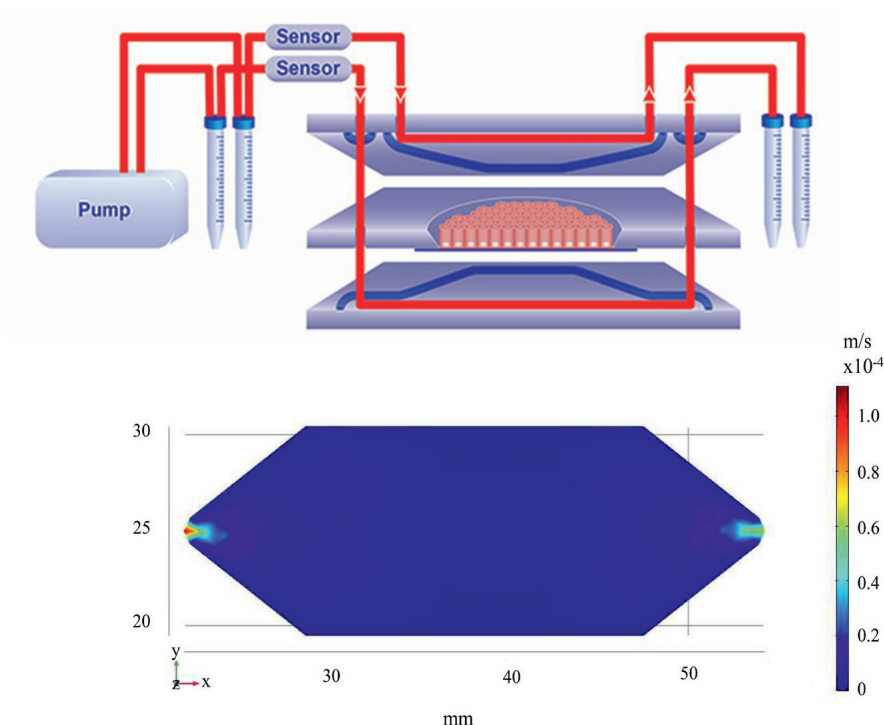
Simulated shear stress in the microfluidic gut-on-chip device

For the gut-on-chip experiments, the chip was placed in a chip holder connected to an eight-channel pump system (for four chips) with a flow sensor for every channel, allowing precise control of the apical (AP) and basolateral (BL) flow (Fig. 1 A). Computational fluid dynamics were used to calculate and visualize the shear stress and flow velocity changes over the geometry of the microfluidic device. As can be seen in Fig. 1 B, the flow velocity is highest near the inlet and decreases as the microchannels broaden until their maximal width (11 mm). In addition, due to an increment in the height of the chamber, the flow velocity was the lowest at the centre of the chamber. The shear stress at the cell culture surface area was calculated at ~ 0.0002 - 0.0017 Dyne/cm².

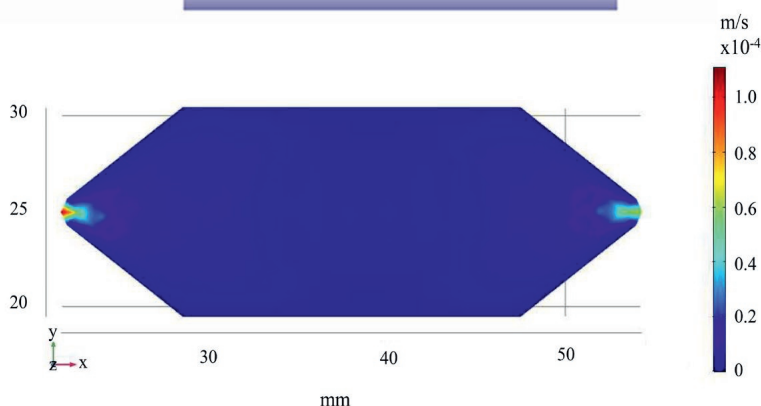
Caco-2 cell monolayer integrity

Caco-2 cells were grown on the membrane in both the gut-on-chip and the Transwell model. Lucifer yellow was used as a fluorescent marker to monitor the integrity of the tight junctions between the Caco-2 cells. As shown in Fig. 2 the paracellular permeability value (P_{app}) of lucifer yellow decreased in time in both tested systems. Both systems demonstrated a tight monolayer after ~ 9 days of culture, but the P_{app} in the gut-on-chip appeared to fluctuate more in the first week of culture. After 9 days of culture, the permeability of lucifer yellow was stable and not significantly different between both systems (1.10×10^{-6} , 0.76×10^{-6} , 0.40×10^{-6} for the Transwell at day 9, 11, 15 and 0.72×10^{-6} , 0.54×10^{-6} , 0.64×10^{-6} cm/s for the gut-on-chip at day 9, 11, 14; $P > 0.05$; Independent t-test).

A)



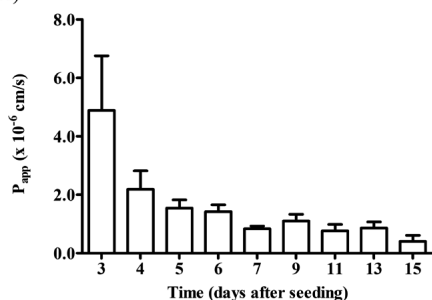
B)



3

Figure 1. Experimental setup of the gut-on-chip A) Schematic design of the microfluidic system. B) Flow velocity simulation of the apical chamber using COMSOL. A horizontal cross-section was taken indicating a steady value of flow velocity inside the flowcell, within the laminar regimen. The picture shows a lower flow speed at the centre of the device.

A)



B)

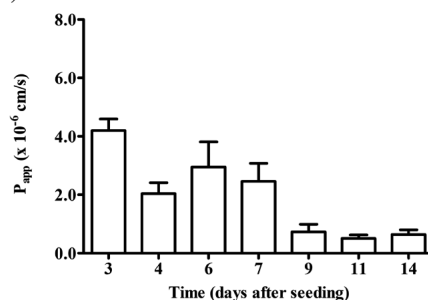


Figure 2. Time dependent P_{app} (apparent permeability constant) reflecting tight junction integrity of a Caco-2 cell monolayer determined by measuring the paracellular translocation of lucifer yellow in a Transwell system A), and a gut-on-chip system B). The values are presented as means \pm SEM; $n=3$ and 7 (Transwell and gut-on-chip).

Assessment of cellular morphology

Caco-2 cells were cultured under continuous flow or static conditions for 21 days, in a gut-on-chip or Transwell, respectively. The cellular morphology was analysed using confocal microscopy, and representative images are shown in Fig. 3. Caco-2 cells grown under both conditions formed a comparable pattern of tight junctions, indicating monolayer formation, at day 5 to day 21 (Fig 3A and B). By creating Z-stacks vertical cross-sections of the monolayers were assessed (Fig. 3C and D). Visual inspection showed an increase in the height of the monolayers in time in both systems, reaching $\sim 10 \mu\text{m}$ at day 21. Marked differences between both culture systems became apparent in the subcellular localization of actin filaments after ~ 11 days of culturing. Monolayers grown under static conditions mainly expressed actin at the apical side, but cells grown under dynamic conditions exhibited more pronounced actin filaments located along the entire height of the cells including the basolateral side of the cells, where the cells were attached to the supporting porous membrane (Fig. 3E and F).

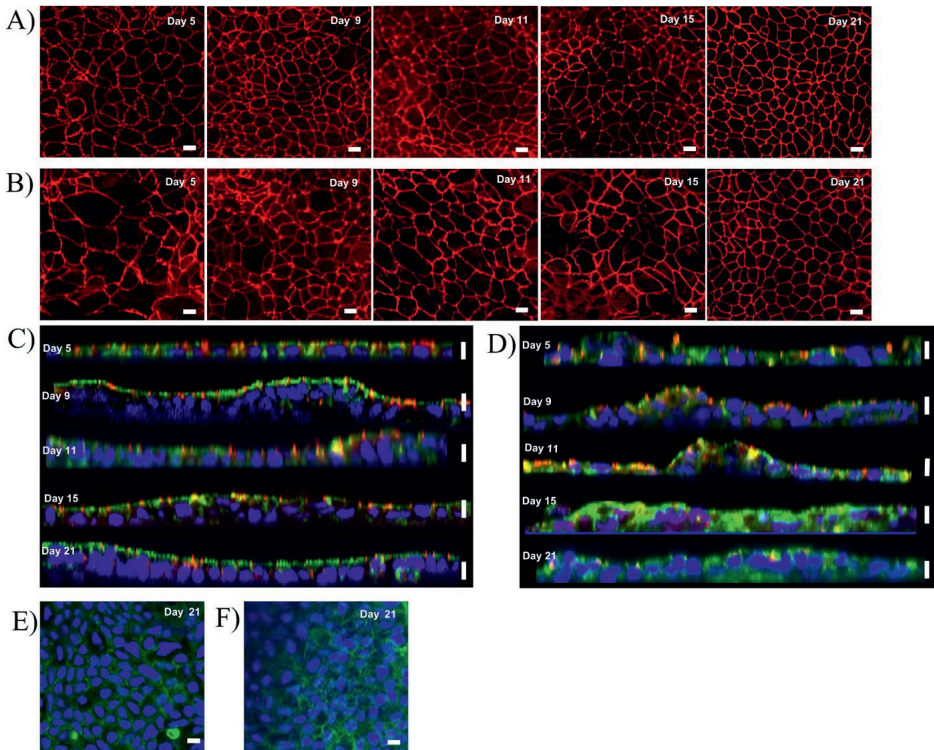


Figure 3. Morphology of Caco-2 cells cultured for 21 days in a static Transwell system or in a gut-on-chip system under a continuous flow of $100 \mu\text{L/h}$, visualized by confocal microscopy. Top views of the cell layer showing comparable tight junction patterns (ZO-1/TJP1) in red over a culture period of 21 days in A) a Transwell and in B)

a gut-on-chip. Vertical cross-sections of the cell monolayer showing actin filaments (Phalloidin) in green, cell nuclei (DAPI) in blue, and tight junctions (ZO-1/TJP1) in red in C) a Transwell and D) a gut-on-chip. Note the increase in actin filaments over the entire cell height in the gut-on-chip versus the Transwell. Horizontal cross-sections at the basolateral side of the cells in E) a Transwell and F) a gut-on-chip further demonstrate the pronounced basolateral presence of actin (Phalloidin; green) in the Transwell versus gut-on-chip. The scale bar represents 10 μm .

Caco-2 cell differentiation

The functional development of the cells in both the gut-on-chip and Transwell model was assessed by determining the ALP activity of the cells. ALP activity is an established marker of epithelial cell differentiation [41-43]. The ALP activity of the cells grown under both conditions are shown in Fig. 4. Cells grown in the gut-on-chip system showed an increase in ALP activity in time, albeit with some fluctuations. At day 21, the ALP activity reached 15.2 ± 5.5 nmol/mg protein/min. Cells grown under static conditions also exhibited an increase in ALP activity in time, reaching 11.4 ± 4.5 nmol/mg protein/min. There were no significant differences in cellular ALP activity between the Caco-2 cells grown in the Transwell and gut-on-chip system at each individual time point ($P > 0.05$; Independent t-test).

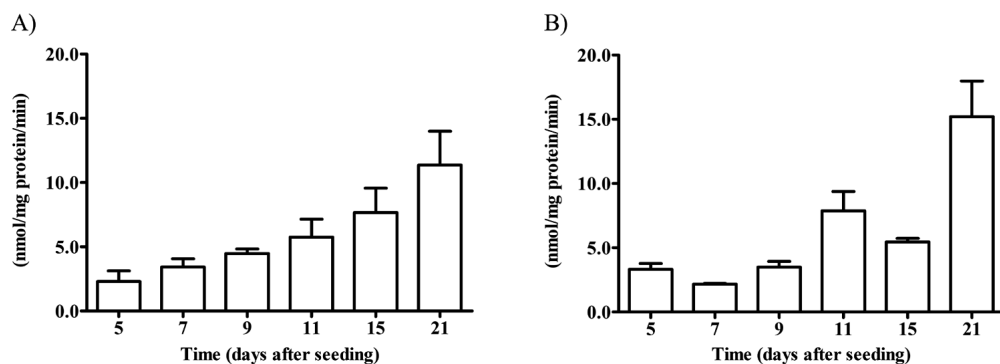


Figure 4. ALP activity in Caco-2 cells grown in Transwell A) or gut-on-chip B). The values are presented as means \pm SEM; $n=3$ and 4 for Transwell and gut-on-chip, respectively.

Selection of non-cytotoxic concentrations of drugs

The MTT assay was used to select non-toxic concentrations of compounds to be applied in the subsequent transport studies. Proliferating (1 day old) cells were exposed to concentrations up to 500 μM , 300 μM , 250 μM and 500 μM of antipyrine, ketoprofen, digoxin, and amoxicillin, respectively, for 24h. As shown in Fig. 5, no cytotoxicity ($>80\%$ viability) was observed for all compounds at the highest tested concentrations.

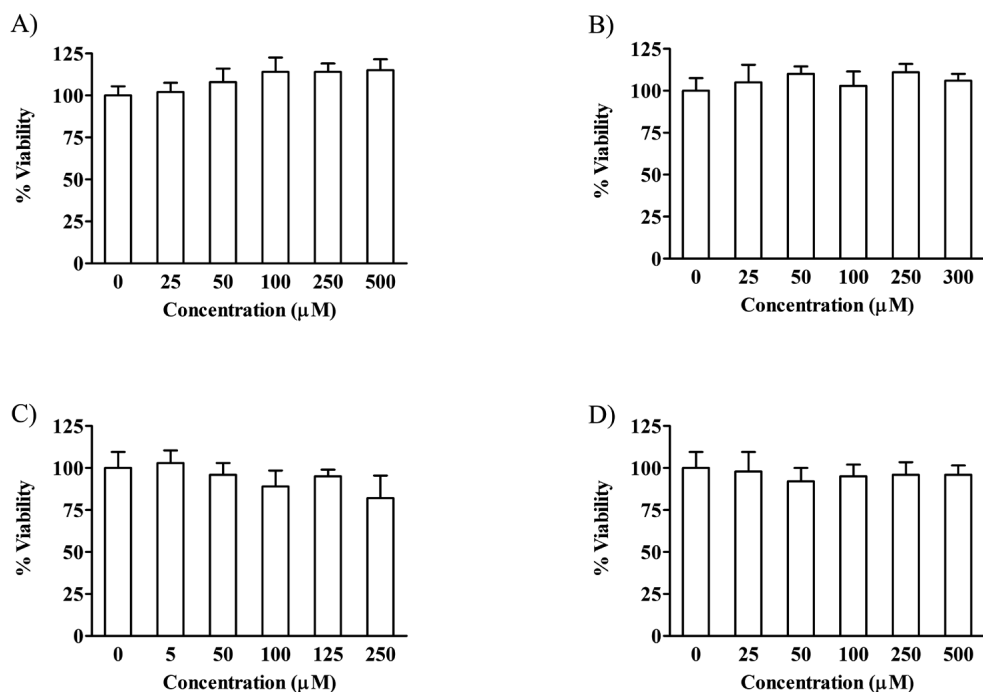


Figure 5. Cell viability of 1-day old Caco-2 cells exposed for 24 h to increasing concentrations of A) antipyrine, B) ketoprofen, C) digoxin, and D) amoxicillin, given as a percentage (\pm SEM) of the negative control ($n=4$)

Comparative drug transport under static and dynamic flow conditions

Compound translocation studies across Caco-2 cell monolayers grown under dynamic (gut-on-chip) and static (Transwell) conditions were performed 21 days after seeding of the cells. The transport of the compounds, antipyrine, ketoprofen, digoxin and amoxicillin, was determined using HPLC or LC-MS. A recovery of 83–118 % for all measurements indicated little loss of compounds due to non-specific binding to the hardware or chemical instability.

The transport of the highly translocated compounds; antipyrine, ketoprofen, and digoxin was significantly lower in the gut-on-chip ($P_{app}=5.4 \times 10^{-6}$, 5.9×10^{-6} and 8.8×10^{-6} cm/s; $p < 0.05$) than in the Transwell ($P_{app}=22.7 \times 10^{-6}$, 16.0×10^{-6} and 16.4×10^{-6} cm/s) (Fig. 6A–C, and Table 1). Whereas the transport of the lowly translocated compound, amoxicillin appeared slightly higher in the gut-on-chip ($P_{app}=5.8 \times 10^{-7}$ cm/s) versus the Transwell ($P_{app}=1.1 \times 10^{-7}$ cm/s), although this difference was not significant ($p > 0.05$) (Fig. 6D and Table 1). To examine the influence of solely the system (i.e. Transwell vs. gut-on-chip) on the transport behaviour of the compounds, both Transwell and gut-on-chip were also exposed to the compounds without cells.

Diffusion (expressed as P_{app}) of all four compounds across the membranes in both the gut-on-chip under dynamic conditions and Transwell (static conditions) without Caco-2 cell monolayers was significantly lower under dynamic flow in the gut-on-chip compared to

the Transwell (i.e. four to seven-fold lower) (Fig. 6). Antipyrine and ketoprofen tested without cells showed translocation values that were comparable to those obtained in the experiments with cells; antipyrine (Transwell; $P_{app}=24.8 \times 10^{-6}$ cm/s, gut-on-chip; $P_{app}=6.0 \times 10^{-6}$) and ketoprofen (Transwell; $P_{app}=18.8 \times 10^{-6}$ cm/s, gut-on-chip; $P_{app}=4.7 \times 10^{-6}$ cm/s). The transport of digoxin through the membrane without cells was also comparable with the transport through the membrane with cells in the Transwell ($P_{app}=19.1 \times 10^{-6}$ cm/s). In the gut-on-chip the transport of digoxin was significantly lower without cells ($P_{app}=2.8 \times 10^{-6}$ cm/s). Amoxicillin showed an increased translocation through the membrane without cells in both the Transwell and gut-on-chip (Transwell; $P_{app}=19.3 \times 10^{-6}$ cm/s, gut-on-chip; $P_{app}=3.7 \times 10^{-6}$ cm/s).

As the diffusion of the four compounds in the gut-on-chip system under dynamic conditions was lower than in the Transwell system as demonstrated by our experiments without the Caco-2 monolayers, the influence of the liquid flow in the gut-on-chip on the transport of antipyrine was examined. For this we examined the transport of antipyrine in gut-on-chip with cells, with or without flow. Without the flow, antipyrine showed a two-fold increased transport ($P_{app}=10.4 \times 10^{-6}$ cm/s) compared to the transport with the flow ($P_{app}=5.4 \times 10^{-6}$ cm/s), but the transport was still two-fold lower than in the Transwell system ($P_{app}=22.7 \times 10^{-6}$ cm/s) (Fig 7). The transport of all four compounds was also tested in the gut-on-chip and Transwell system without cells and without flow, showing approximately 2-fold lower P_{app} values for all compounds in the gut-on-chip system (Suppl. Table 1).

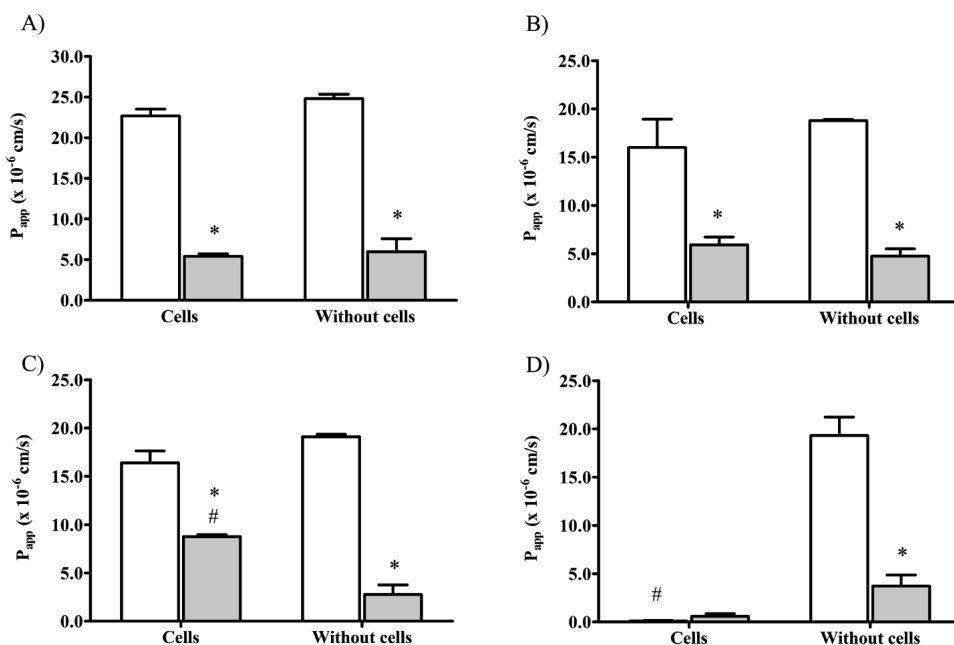


Figure 6. Apparent permeability (P_{app}) values (\pm SEM) of model compounds; A) antipyrine, B) ketoprofen, C) digoxin, and D) amoxicillin under static Transwell (open bare), or dynamic gut-on-chip (gray bar) conditions, with or without 21-day old Caco-2 cells cultured on the porous membrane. * significant difference compared with the static Transwell ($p<0.05$); # significant difference compared with the without cells condition ($p<0.05$); ($n=3$; antipyrine, digoxin, and amoxicillin); ($n=5$; ketoprofen in gut-on-chip system).

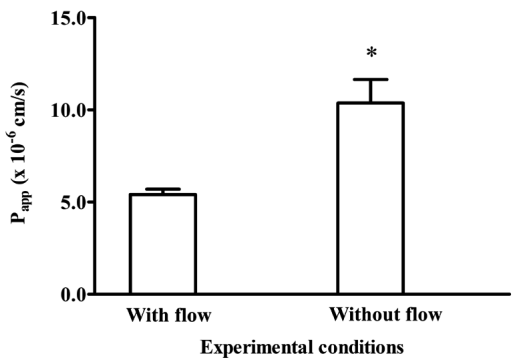


Figure 7. Apparent permeability (P_{app}) values (\pm SEM) of antipyrine in the gut-on-chip system with 21-day old Caco-2 cells, under dynamic (with flow), or under static (without flow) conditions. * significant difference compared with dynamic conditions ($p<0.05$); ($n=3$)

Table 1. Overview of the apparent permeability values (P_{app}) (\pm SEM) of the selected compounds in Caco2-cells cultured under static (Transwell) and dynamic (gut-on-chip) conditions in this study, and *in vitro* and *in vivo* P_{app} values or ranges (obtained from literature).

Compound	P_{app} ($\times 10^{-6}$ cm/s)		Literature <i>in vitro</i> Transwell P_{app} ($\times 10^{-6}$ cm/s)	Human <i>in vivo</i> P_{app} ($\times 10^{-6}$ cm/s)	BCS class	Fa (%)
	Transwell	Gut-on-chip				
Antipyrine	22.7 \pm 0.5	5.4 \pm 0.2	11.3-150.0 ^a	560 ^d	I ^d	100 ^d
Ketoprofen	16.0 \pm 1.6	5.9 \pm 0.4	10.5-93.0 ^a	870 ^d	I ^d	100 ^d
Digoxin	16.4 \pm 0.7	8.8 \pm 0.1	0.59-4.69 ^b	N/A	II ^c	75 ^f
Amoxicillin	0.11 \pm 0.02	0.58 \pm 0.2	0.021-1.8 ^c	30 ^d	III ^d	45-75 ^d

BCS: Biopharmaceutics Classification System. Class I and II: high permeability, class III: low permeability.
Fa: human absorption of compounds, ^a data obtained from [44], ^b data obtained from [45, 46], ^c data obtained from [47-49], ^d data obtained from [50], ^e data obtained from [51] and ^f data obtained from [52]. N/A: not available *in vivo* literature.

Discussion

We aimed to evaluate whether our *in vitro* gut-on-chip intestinal barrier model is an adequate model for compound translocation studies. For this, we performed a biokinetic study comparing our dynamic gut-on-chip [37] with a conventional model using the static Transwell model. In both systems comparable trends in compound specific P_{app} values were

observed. However, we observed marked differences in absolute transport rates in the Transwell versus the gut-on-chip model that most likely were caused by differences in experimental conditions and the design and intrinsic characteristics of the microfluidic chip.

In this study we used glass two-chamber microfluidic chips separated by a PET membrane on which we cultured epithelial cells (Caco-2) under dynamic conditions. Using a largely glass based microfluidic chip avoids the often raised issue of compound binding to PDMS based chips [36]. We successfully observed a high recovery of compounds as we have also shown previously for highly lipophilic compounds [37] indicating that no compounds were lost in the total chip setup, that includes tubing with a relatively large surface area.

To perform biokinetic studies, conventionally Caco-2 cells are used after 21 days of culturing in Transwell systems, when they have developed into a tight monolayer of differentiated cells [53]. We assessed the cell layer integrity in the conventional Transwell model versus the gut-on-chip model by exposing monolayers of cells to a marker for paracellular transport (lucifer yellow). The paracellular translocation dropped quickly for the Caco-2 monolayers in the Transwell model reaching stable low levels in the second week of culturing. A similar trend, albeit more variable, was observed for the Caco-2 monolayers grown under dynamic flow conditions in the chip. Previously, other research groups have characterized Caco-2 cell layer integrity and differentiation in microfluidic chips, but in chips with different designs. Using microfluidic chips with a narrow long channel, full maturation of the cell monolayer and barrier integrity was observed already after 3-5 days of seeding [10, 16], which is faster than observed in our model. Next we evaluated the differentiation of the Caco-2 cells in both the gut-on-chip and Transwell by determining ALP activity, a known marker for intestinal cell differentiation [41-43]. Caco-2 cell differentiation was comparable in both systems, ALP activity increased upon increasing the culture period with a maximum activity reached on day 21. Again, in a chip with a narrow elongated channel, it was observed that brush border aminopeptidase activity already on day 5 reached the same level as following 21 days of culturing in Transwell [10, 16]. Due to the differences in chip design the resulting shear stress experienced by the cells is different in this chip system as compared to ours. In our device, we estimated a shear stress of approximately 0.0002-0.0017 Dyne/cm² which is lower compared to the 0.02 Dyne/cm² reported for the channel chips [10]. Literature data on *in vivo* shear stress in the gut however report highly variable ranges, between ~0.002-12.0 Dyne/cm² [10, 54, 55], depending on the intestinal location and viscosity of digesta. Therefore, to mimic the real shear stress experience by epithelial cells within the intestinal lumen is still challenging *in vitro*. Lastly, we have evaluated the monolayer morphology of Caco-2 cells grown in the gut-on-chip and static Transwell using confocal microscopy. While the cell height was comparable, cells grown under constant flow expressed more actin filaments on the basolateral side compared to cells grown under static conditions, as shown before [37]. Actin filaments are associated with cell adhesion and mechanics, remodelling of actin filaments might alter cell spread, migration, elongation, or enlargement of the cells [56,

57]. The remodelling of the actin filaments did not affect the barrier integrity in the gut-on-chip model.

We exposed differentiated monolayers of Caco-2 cells, grown under dynamic flow conditions in the gut-on-chip and under static conditions in the Transwell system, to four model compounds representing high and low permeability compound classes (Biopharmaceuticals Classification System (BCS)). Monolayers of differentiated Caco-2 cells are regarded representative for the gastrointestinal absorption of compounds *in vivo* with the best correlation for drugs transported by the passive transcellular route [53, 58]. The highly transported compounds antipyrine, ketoprofen and digoxin indeed showed high P_{app} values in both systems. Amoxicillin, a low transported compound, showed low P_{app} values in both systems. The P_{app} values derived from the static experiment were in line with those previously obtained from static *in vitro* Caco-2 experiments for antipyrine, ketoprofen and amoxicillin (see table 1 and references therein). Our digoxin P_{app} value was higher, in both the Transwell and gut-on-chip system than those reported before. This difference likely can be explained by the variable expression of P-glycoprotein 1 by Caco-2 cells, this efflux transporter is responsible for the cellular excretion of digoxin. Variable expression levels can depend on the passage number of the cultured cells [59]. The P_{app} values of the high permeability (class I) compounds antipyrine and ketoprofen were about 4.2 and 2.7 folds lower, respectively, when evaluated using Caco-2 cells under dynamic flow conditions in the gut-on-chip compared to Caco-2 cells under static conditions in Transwell. Given the outcome of our experiments without cells and without flow, we conclude that these differences can be explained by (laminar) flow related effects and by influence of the design of the chip and/or the material of the membrane on diffusion of these compounds. Laminar flow is the fluid flow that occurs in long thin parallel layers with no disruption between them and can be defined by the Reynolds number. The Reynolds number is the ratio of internal force to viscous force. For our gut-on-chip conditions the Reynolds number equals ~ 0.007 . At low Reynolds numbers, viscous forces dominate, which implies a low migration (or diffusion) of dissolved chemicals across layers resulting in less contact of the compounds with the cell surface [60, 61]. In the absence of flow, diffusion is facilitated, this is demonstrated by the ~ 2 times higher P_{app} value of antipyrine in the gut-on-chip with cells without flow versus with flow. Nevertheless, the P_{app} value in the gut-on-chip with cells and without flow was still lower than that in the Transwell. The use of different membranes and the influence of different designs (i.e. apical and basolateral volumes) in the gut-on-chip and Transwell models could have contributed to these observed differences as shown by static experiments using both membranes.

Monolayers of Caco-2 cells, are a standard model used to categorize drugs into the four classes of the Biopharmaceuticals Classification System (BCS) and to predict intestinal absorption of compounds [62, 63]. However, in the literature reported (apparent) permeability values of compounds *in vitro* vary between labs and are lower than those reported for human *in vivo* (Table 1). The latter usually is explained by the higher TEER

values *in vitro* compared to TEER values *in vivo* [44, 53, 64]. Therefore, relative correlation values between *in vitro* and human data have been often used to evaluate the prediction potential of new *in vitro* models and to predict whether absorption of compounds in human will be high or low [48, 52, 65, 66]. The transport data in our study are consistent with the BCS compound classification, showing higher transport of antipyrine, ketoprofen, and digoxin than amoxicillin.

Compound translocation of the four model compounds in the gut-on-chip and Transwell are in line with the compound Biopharmaceuticals Classification System, albeit absolute P_{app} values of class I and II compounds were markedly lower in the gut-on-chip. Clearly the laminar fluid flow in the microfluidic chip affects the transport of compounds, by limiting the diffusions of compounds towards the membrane.. A solution can be to incorporate herringbone-shaped groves to allow mixing as shown by De Haan et al. [67]. Secondly, the shape of the cell compartment affects the shear force and liquid flow patterns. The consequences of these design characteristics, and thus accompanying shear forces, on cell morphology, cell physiology, and cell differentiation and on how this affects compound transport still needs to be assessed. Comparative studies on monolayer morphology related to chip design are emerging [68].

In conclusion, different P_{app} values of the tested compounds were obtained in the gut-on-chip and Transwell models for antipyrine, ketoprofen, and digoxin. The P_{app} value obtained for the low permeability compound amoxicillin was comparable in both models. These results are in line with the compound Biopharmaceuticals Classification System. Thus, both the gut-on-chip and the Transwell model can be used for transport studies of chemicals. The gut-on-chip model allows for integration with on line detection of compounds [29] while the classical static Transwell model is easier to use.

Declaration of Competing Interest

The authors state no conflict of interest.

Acknowledgement

The authors sincerely acknowledge the support and assistance of prof.dr.ir. IMCM (Ivonne) Rietjens. K. K. is supported by a Royal Thai government Scholarship. This work was in part supported by the Dutch Ministry of Agriculture, Nature and Food Quality (project KB-23-002-022).

References

1. Martignoni, M., G.M.M. Groothuis, and R. de Kanter, *Species differences between mouse, rat, dog, monkey and human CYP-mediated drug metabolism, inhibition and induction*. Expert Opinion on Drug Metabolism & Toxicology, 2006. 2(6): p. 875-894.
2. Leppert, E.R., et al., *Thalidomide metabolism and hydrolysis: Mechanisms and implications*. Current Drug Metabolism, 2006. 7(6): p. 677-685.
3. Matthiessen, L., B. Lucaroni, and E. Saez Towards responsible animal research Addressing the ethical dimension of animal experimentation and implementing the ?Three Rs? principle in biomedical research, *EMBO reports Volume 4, Issue 2*. EMBO reports, 2003. 4, 104-107.
4. Russell, W.M.S. and R.L. Burch, *The principles of humane experimental technique*. 1959, London,: Methuen. 238 p.
5. Rollin, B.E., *Toxicology and new social ethics for animals*. Toxicol Pathol, 2003. 31 Suppl: p. 128-31.
6. Eisenbrand, G., et al., *Methods of in vitro toxicology*. Food Chem Toxicol, 2002. 40(2-3): p. 193-236.
7. Kauffman, A.L., et al., *Alternative functional in vitro models of human intestinal epithelia*. Frontiers in Pharmacology, 2013. 4.
8. Guerra, A., N.E. Campillo, and J.A. Paez, *Neural computational prediction of oral drug absorption based on CODES 2D descriptors*. European Journal of Medicinal Chemistry, 2010. 45(3): p. 930-940.
9. Cao, L., et al., *Development of Intestinal Organoids as Tissue Surrogates: Cell Composition and the Epigenetic Control of Differentiation*. Molecular Carcinogenesis, 2015. 54(3): p. 189-202.
10. Kim, H.J., et al., *Human gut-on-a-chip inhabited by microbial flora that experiences intestinal peristalsis-like motions and flow*. Lab on a Chip, 2012. 12(12): p. 2165-2174.
11. Kim, H.J. and D.E. Ingber, *Gut-on-a-Chip microenvironment induces human intestinal cells to undergo villus differentiation*. Integrative Biology, 2013. 5(9): p. 1130-1140.
12. Gao, D., et al., *Characterization of drug permeability in Caco-2 monolayers by mass spectrometry on a membrane-based microfluidic device*. Lab on a Chip, 2013. 13(5): p. 978-985.
13. Santbergen, M.J.C., et al., *Online and in situ analysis of Organs-on-a-chip*. TrAC Trends in Analytical Chemistry, 2019.
14. Mahler, G.J., et al., *Characterization of a Gastrointestinal Tract Microscale Cell Culture Analog Used to Predict Drug Toxicity*. Biotechnology and Bioengineering, 2009. 104(1): p. 193-205.
15. Lee, D.W., et al., *3D gut-liver chip with a PK model for prediction of first-pass metabolism*. Biomedical Microdevices, 2017. 19(4).
16. Chi, M., et al., *A microfluidic cell culture device (muFCCD) to culture epithelial cells with physiological and morphological properties that mimic those of the human intestine*. Biomed Microdevices, 2015. 17(3): p. 9966.
17. Shim, K.Y., et al., *Microfluidic gut-on-a-chip with three-dimensional villi structure*. Biomedical Microdevices, 2017. 19(2).
18. Gupta, N., et al., *Microfluidics-based 3D cell culture models: Utility in novel drug discovery and delivery research*. Bioeng Transl Med, 2016. 1(1): p. 63-81.
19. Barata, D., C. van Blitterswijk, and P. Habibovic, *High-throughput screening approaches and combinatorial development of biomaterials using microfluidics*. Acta Biomaterialia, 2016. 34: p. 1-20.
20. Selimovic, S., et al., *Generating Nonlinear Concentration Gradients in Microfluidic Devices for Cell Studies*. Analytical Chemistry, 2011. 83(6): p. 2020-2028.
21. Workman, M.J., et al., *Enhanced Utilization of Induced Pluripotent Stem Cell-Derived Human Intestinal Organoids Using Microengineered Chips*. Cellular and Molecular Gastroenterology and Hepatology, 2018. 5(4): p. 669-+.
22. Ortmann, D. and L. Vallier, *Variability of human pluripotent stem cell lines*. Curr Opin Genet Dev, 2017. 46: p. 179-185.
23. Yeon, J.H. and J.K. Park, *Drug Permeability Assay Using Microhole-Trapped Cells in a Microfluidic Device*. Analytical Chemistry, 2009. 81(5): p. 1944-1951.

24. Marin, T.M., et al., *Acetaminophen absorption and metabolism in an intestine/liver microphysiological system*. Chem Biol Interact, 2019. 299: p. 59-76.
25. Kimura, H., et al., *An integrated microfluidic system for long-term perfusion culture and on-line monitoring of intestinal tissue models*. Lab Chip, 2008. 8(5): p. 741-6.
26. Pocock, K., et al., *Intestine-on-a-Chip Microfluidic Model for Efficient in Vitro Screening of Oral Chemotherapeutic Uptake*. Acs Biomaterials Science & Engineering, 2017. 3(6): p. 951-959.
27. Imura, Y., et al., *A microfluidic system to evaluate intestinal absorption*. Anal Sci, 2009. 25(12): p. 1403-7.
28. Tan, H.Y., et al., *A multi-chamber microfluidic intestinal barrier model using Caco-2 cells for drug transport studies*. PLoS One, 2018. 13(5): p. e0197101.
29. Santbergen, M.J.C., et al., *Dynamic in vitro intestinal barrier model coupled to chip-based liquid chromatography mass spectrometry for oral bioavailability studies*. Anal Bioanal Chem, 2019.
30. McDonald, J.C., et al., *Fabrication of microfluidic systems in poly(dimethylsiloxane)*. Electrophoresis, 2000. 21(1): p. 27-40.
31. Thangawong, A.L., et al., *An ultra-thin PDMS membrane as a bio/micro-nano interface: fabrication and characterization*. Biomedical Microdevices, 2007. 9(4): p. 587-595.
32. Tsao, C.W., *Polymer Microfluidics: Simple, Low-Cost Fabrication Process Bridging Academic Lab Research to Commercialized Production*. Micromachines, 2016. 7(12).
33. Berthier, E., E.W.K. Young, and D. Beebe, *Engineers are from PDMS-land, Biologists are from Polystyrenia*. Lab on a Chip, 2012. 12(7): p. 1224-1237.
34. Hiram, H., et al., *Glass-based organ-on-a-chip device for restricting small molecular absorption*. J Biosci Bioeng, 2018.
35. Li, N.Z., M. Schwartz, and C. Ionescu-Zanetti, *PDMS Compound Adsorption in Context*. Journal of Biomolecular Screening, 2009. 14(2): p. 194-202.
36. van Meer, B.J., et al., *Small molecule absorption by PDMS in the context of drug response bioassays*. Biochemical and Biophysical Research Communications, 2017. 482(2): p. 323-328.
37. Kulthong, K., et al., *Implementation of a dynamic intestinal gut-on-a-chip barrier model for transport studies of lipophilic dioxin congeners*. Rsc Advances, 2018. 8(57): p. 32440-32453.
38. Zhang, X., et al., *A microfluidic shear device that accommodates parallel high and low stress zones within the same culturing chamber*. Biomicrofluidics, 2014. 8(5): p. 054106.
39. Hubatsch, I., E.G.E. Ragnarsson, and P. Artursson, *Determination of drug permeability and prediction of drug absorption in Caco-2 monolayers*. Nature Protocols, 2007. 2(9): p. 2111-2119.
40. Li, H.Q., et al., *Assessment of an in vitro transport model using BeWo b30 cells to predict placental transfer of compounds*. Archives of Toxicology, 2013. 87(9): p. 1661-1669.
41. Zucco, F., et al., *An inter-laboratory study to evaluate the effects of medium composition on the differentiation and barrier function of Caco-2 cell lines*. Altern Lab Anim, 2005. 33(6): p. 603-18.
42. Jumarie, C. and C. Malo, *Alkaline-Phosphatase and Peptidase Activities in Caco-2 Cells - Differential Response to Triiodothyronine*. In Vitro Cellular & Developmental Biology-Animal, 1994. 30A(11): p. 753-760.
43. Ferruzza, S., et al., *A protocol for differentiation of human intestinal Caco-2 cells in asymmetric serum-containing medium*. Toxicol In Vitro, 2012. 26(8): p. 1252-5.
44. Lee, J.B., et al., *Quantitative analysis of lab-to-lab variability in Caco-2 permeability assays*. European Journal of Pharmaceutics and Biopharmaceutics, 2017. 114: p. 38-42.
45. Djnv, A. and O.G. Nilsen, *Caco-2 Cell Methodology and Inhibition of the P-glycoprotein Transport of Digoxin by Aloe vera Juice*. Phytotherapy Research, 2008. 22(12): p. 1623-1628.
46. Elsby, R., et al., *Validation and application of Caco-2 assays for the in vitro evaluation of development candidate drugs as substrates or inhibitors of P-glycoprotein to support regulatory submissions*. Xenobiotica, 2008. 38(7-8): p. 1140-64.
47. Jung, S.J., et al., *Prediction of the permeability of drugs through study on quantitative structure-permeability relationship*. Journal of Pharmaceutical and Biomedical Analysis, 2006. 41(2): p. 469-475.

48. Irvine, J.D., et al., *MDCK (Madin-Darby canine kidney) cells: A tool for membrane permeability screening*. Journal of Pharmaceutical Sciences, 1999. 88(1): p. 28-33.
49. Gres, M.C., et al., *Correlation between oral drug absorption in humans, and apparent drug permeability in TC-7 cells, a human epithelial intestinal cell line: Comparison with the parental Caco-2 cell line*. Pharmaceutical Research, 1998. 15(5): p. 726-733.
50. Lennernas, H., *Human in Vivo Regional Intestinal Permeability: Importance for Pharmaceutical Drug Development*. Molecular Pharmaceutics, 2014. 11(1): p. 12-23.
51. Wu, C.Y. and L.Z. Benet, *Predicting drug disposition via application of BCS: transport/absorption/elimination interplay and development of a biopharmaceutics drug disposition classification system*. Pharm Res, 2005. 22(1): p. 11-23.
52. Takenaka, T., et al., *Application of a Human Intestinal Epithelial Cell Monolayer to the Prediction of Oral Drug Absorption in Humans as a Superior Alternative to the Caco-2 Cell Monolayer*. Journal of Pharmaceutical Sciences, 2016. 105(2): p. 915-924.
53. Artursson, P., K. Palm, and K. Luthman, *Caco-2 monolayers in experimental and theoretical predictions of drug transport (Reprinted from Advanced Drug Delivery Reviews, vol 22, pg 67-84, 1996)*. Advanced Drug Delivery Reviews, 2001. 46(1-3): p. 27-43.
54. Guo, P., A.M. Weinstein, and S. Weinbaum, *A hydrodynamic mechanosensory hypothesis for brush border microvilli*. Am J Physiol Renal Physiol, 2000. 279(4): p. F698-712.
55. Hardacre, A.K., et al., *Does viscosity or structure govern the rate at which starch granules are digested?* Carbohydrate Polymers, 2016. 136: p. 667-675.
56. Noria, S., et al., *Assembly and reorientation of stress fibers drives morphological changes to endothelial cells exposed to shear stress*. Am J Pathol, 2004. 164(4): p. 1211-23.
57. Miura, S., et al., *Fluid shear triggers microvilli formation via mechanosensitive activation of TRPV6*. Nat Commun, 2015. 6: p. 8871.
58. Cheng, K.C., C. Li, and A.S. Uss, *Prediction of oral drug absorption in humans - from cultured cell lines and experimental animals*. Expert Opinion on Drug Metabolism & Toxicology, 2008. 4(5): p. 581-590.
59. Goto, M., et al., *Decreased expression of P-glycoprotein during differentiation in the human intestinal cell line Caco-2*. Biochem Pharmacol, 2003. 66(1): p. 163-70.
60. Sosa-Hernandez, J.E., et al., *Organs-on-a-Chip Module: A Review from the Development and Applications Perspective*. Micromachines (Basel), 2018. 9(10).
61. Christoffersson, J., *Organs-on-chips for the pharmaceutical development process: design perspectives and implementations in Department of Physics, Chemistry and Biology*. 2018, Linköping University: Linköping, Sweden. p. 79.
62. Smetanova, L., et al., *Caco-2 cells, biopharmaceutics classification system (BCS) and biowaiver*. Acta Medica (Hradec Kralove), 2011. 54(1): p. 3-8.
63. Miret, S., L. Abrahamse, and E.M. de Groene, *Comparison of in vitro models for the prediction of compound absorption across the human intestinal mucosa*. J Biomol Screen, 2004. 9(7): p. 598-606.
64. Lennernas, H., *Human intestinal permeability*. J Pharm Sci, 1998. 87(4): p. 403-10.
65. Li, C., et al., *Development of in vitro pharmacokinetic screens using Caco-2, human hepatocyte, and Caco-2/human hepatocyte hybrid systems for the prediction of oral bioavailability in humans*. J Biomol Screen, 2007. 12(8): p. 1084-91.
66. Marino, A.M., et al., *Validation of the 96 well Caco-2 cell culture model for high throughput permeability assessment of discovery compounds*. International Journal of Pharmaceutics, 2005. 297(1-2): p. 235-241.
67. de Haan, P., et al., *Digestion-on-a-chip: a continuous-flow modular microsystem recreating enzymatic digestion in the gastrointestinal tract*. Lab Chip, 2019. 19(9): p. 1599-1609.
68. Bein, A., et al., *Microfluidic Organ-on-a-Chip Models of Human Intestine*. Cell Mol Gastroenterol Hepatol, 2018. 5(4): p. 659-668.

Supplementary Table 1. The permeability of antipyrine, ketoprofen, digoxin, and amoxicillin in the Transwell and chip system under static conditions without cells (mean±SEM) (n=3 for antipyrine and Digoxin and n=4 for ketoprofen and amoxicillin).

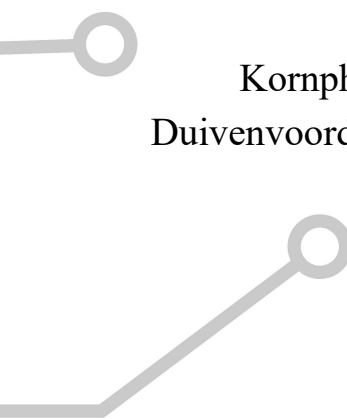
Compound	Permeability (x 10 ⁻⁶ cm/s)	
	TW	Chip
Antipyrine	24.8±0.3	12.7±0.2
Ketoprofen	18.8±0.1	10.7±1.0
Digoxin	19.1±0.1	8.0±0.6
Amoxicillin	18.7±1.2	9.3±0.8





CHAPTER 4

Comparative transcriptomics of epithelial cells grown under static and microfluidic gut-on-chip conditions and benchmarked against human *in vivo* intestinal cells



Kornphimol Kulthong, Guido J.E.J. Hooiveld, Loes Duivenvoorde, Ignacio Miro Estruch, Victor Marin, Meike van der Zande and Hans Bouwmeester

Submitted for publication



Abstract

Gut-on-chip devices enable exposure of cells to a continuous flow of culture medium, inducing shear stresses and could thus better recapitulate the *in vivo* human intestinal environment in an *in vitro* epithelial model compared to static culturing methods. We aimed to study if dynamic culturing conditions affect the gene expression of Caco-2 cells cultured statically or in a gut-on-chip device and how these gene expression patterns compared to that of intestinal segments *in vivo*. For this we applied whole genome transcriptomics analyses. Dynamic culture conditions led to a total of 5927 differentially expressed genes (3280 upregulated and 2647 downregulated genes) compared to static culture conditions. Gene set enrichment analysis revealed upregulated pathways associated with the immune system, signal transduction and cell growth and death, and downregulated pathways associated with drug metabolism, compound digestion and absorption under dynamic culture conditions. Comparison of the *in vitro* gene expression data with transcriptomic profiles of human *in vivo* duodenum, jejunum, ileum and colon tissue samples showed similarities in gene expression profiles with intestinal segments. It is concluded that both the static and the dynamic gut-on-chip model are suitable to study human intestinal epithelial responses as an alternative for animal models.

Introduction

Current toxicological safety studies of chemicals and pharmaceuticals often rely on the use of laboratory animals. The use of animals not only is time consuming, considered unethical and expensive, but importantly also raises scientific questions on the differences in physiology of laboratory animals compared to humans [1-3]. To refine, reduce or ultimately replace the use of animal models (the 3R principle) [4], *in vitro* assays have been intensively studied [5-7]. By using human cells, specific functions of the organ of origin can be emulated *in vitro*. Here, we focused on human intestinal cells that are extensively used to model the human intestinal epithelium.

With the emergence of microfluidic technology several organ-on chip platforms have been launched [8, 9]. More specifically gut-on-chip devices have been introduced that allow to culture epithelial cells under continuous perfusion and physiological shear stress attempting to better recapitulate the functions of the human intestine compared to static culturing methods [10-13]. While stem cell-based intestinal models can be used to study the human intestinal function, the reproducibility and culture efficiency of the models *in vitro* is still challenging [14, 15]. Therefore, human intestinal epithelial cell line-based models, specifically Caco-2 cells, currently remain the most widely used and accepted *in vitro* model for toxicological safety studies [16-18]. Despite the variety in existing gut-on-chip models, there are only a few studies that evaluated the basal gene expression of Caco-2 cells compared to that of human intestinal (*in vivo*) tissues [19]. Kim et al. published such a comparison of a specific subclone of Caco-2 cells, but due to the very limited sample size in this study the results have to be interpreted with caution. We are not aware of other comparative studies. To the best of our knowledge, no other comparative studies addressing this issue in the commonly used wild type Caco-2 cell line have been published so far.

The aim of the current study was to comprehensively investigate the effects of dynamic flow conditions on the gene expression profile and affected biological pathways of Caco-2 cells compared to the gene expression profile of Caco-2 cells cultured under static conditions. Next, the gene expression profiles of Caco-2 cells, cultured under both conditions, were compared with those of healthy human *in vivo* intestinal tissues. For this, we retrieved data from publicly available gene expression databases. Briefly, Caco-2 cells were grown for 21 days in Transwells according to a standard protocol [20], and in our gut-on-chip device [12, 13]. Gene expression data were obtained using a microarray platform and differential expression was determined by a bioinformatics approach. Linear models and an intensity-based moderated t-statistic were used for identification of differentially expressed genes and gene set enrichment analysis (GSEA) for identification of affected biological pathways. The differential expression of intestine-specific genes in Caco-2 cells was compared to those reported for different regions of human intestinal tissues *in vivo* [21].

Materials and Methods

Chemicals and reagents

Bovine serum albumin (BSA), Dulbecco's Modified Eagle Medium (DMEM), penicillin-streptomycin, Hank's balanced salt solution (HBSS), trifluoroacetic acid were obtained from Sigma-Aldrich (Zwijndrecht, The Netherlands). Phosphate Buffered Saline (PBS), heat inactivated fetal bovine serum (FBS) and MEM-non-essential amino acids were purchased from Fisher Scientific (Landsmeer, The Netherlands).

Design of the gut-on-chip system

The microfluidic gut-on-chip device has been developed and described previously [12]. Briefly, the chip consists of three 15x45 mm (width x length) re-sealable glass slides that result in two flow chambers (i.e. an upper apical (AP) and lower basolateral (BL) chamber) upon assembly (see Fig. 1 A; Micronit, Enschede, The Netherlands). Both the upper and lower glass slides were spaced from the middle layer membrane by a 0.25 mm thick silicone gasket. The flow chambers were separated by a glass slide containing a polyester (PET) porous cell culture, membrane with a 0.4 μm pore size and a cell culture area of $\sim 1.6\text{ cm}^2$. The volume of the AP chamber is 75 mm^3 with a chamber height of 0.25 mm (membrane to top layer) and the BL chamber is 110 mm^3 with a chamber height of 0.65 mm (bottom layer to membrane), resulting in a total volume of 185 mm^3 (μL) of the device (Fig. 1A). The chip was placed in a chip holder with a quick locking mechanism, constructed for connection of external capillaries to the chip via specific ferrules to ensure tight connections and a leak-free system.

The constant flow was introduced to the chip using a microsyringe pump (NE-4000, New Era Pump Systems, Inc.) equipped with two polypropylene syringes (30 mL, Luer-locktm, Becton, Dickinson and company), with each syringe connected to either the AP or the BL compartment using Ethylene Propylene (FEP) tubing (0.50 mm inner diameter, with a length of 25 cm and 10 cm for the inlet and outlet, respectively). Before the start of each experiment, all tubing and chips were sterilized using an autoclave and rinsed with 70% ethanol. Tubing and chips were prefilled with medium to eliminate air bubbles in the system. The entire system was put in an incubator at 37°C to maintain cell culture conditions.

Cell culture

A Caco-2 cell line (HTB-37), derived from a human colorectal adenocarcinoma, was obtained from the American Type Culture Collection (ATCC, Manassas, VA, USA). The cells were grown (at passage number 29-45) in DMEM supplemented with 10 % FBS, 1 % penicillin-streptomycin, and 1 % MEM non-essential amino acid, further referred to as DMEM⁺. The cells were seeded at a density of $\sim 75,000$ cells per cm^2 on 12-well Transwell PET inserts (0.4 μm pore size, 1.12 cm^2 surface area, Corning Amsterdam, The Netherlands) and cultured in DMEM⁺ for 21 days. The medium was changed every two to three days.

In the microfluidic device, the cells were seeded at a density of 75,000 cell per cm^2 and were allowed to attach to the membrane for 24 h, without the fluid flow. The membrane

was then inserted in the microfluidic chip and cells were exposed to a continuous flow of 100 $\mu\text{L/h}$ DMEM⁺ until day 21 of culturing (Fig. 1B). By doing so, the shear stress in the AP compartment was ~ 0.002 dyne/cm² at the cell membrane area where the cells were grown. The DMEM⁺ medium contained sodium bicarbonate (10 mM) to optimize the pH buffering capacity.

Fluorescent imaging of epithelial cell morphology

Morphological assessment of the Caco-2 cell monolayers, grown in the gut-on-chip or Transwell for 21 days, was performed as described previously [12]. In short, the chips were opened, and cells were fixed with 4% formaldehyde for 10 min and rinsed with PBS at room temperature. Cells were then permeabilized with 0.25% Triton X100 in PBS for 10 min and blocked with 1% acetylated bovine serum albumin in PBS for 30 min. Conjugated antibody ZO-1/TJP1-Alexa Fluor 594 (Invitrogen, Waltham, MA) at 10 $\mu\text{g/mL}$ was used to stain tight junctions. The nuclei were stained with 5 $\mu\text{g/mL}$ DAPI (Invitrogen, Waltham, MA) and 4 U/mL Phalloidin Alexa Fluor 488 (Life technologies, Carlsbad, CA) was used to stain actin filaments (i.e. cytoskeleton). The incubation time for all stainings was 30 min. The membrane was placed between two cover slips separated by a spacer (0.12 mm depth x 20 mm diameter) with a drop of anti-fading mounting medium. The cells cultured on Transwell membranes were stained using the same procedure. The stained monolayers of cells were analyzed using a confocal microscope (LSM 510 UVMETA; Carl Zeiss, Germany). Samples were excited with 405, 488 and 543 nm lasers. Multi-tracked images were captured to avoid bleed through. The used pinholes were in the range of 148-152 μm at a magnification of 40x. The gain and offset for the different channels were kept constant during the entire experiment.

RNA isolation

Caco-2 cells were grown in the gut-on-chip or Transwell for 21 days. The chips were opened, and cells were washed with PBS. After that, 100 μL of RLT lysis buffer were added to the cell culture membrane and incubated for 1-2 min, then the membrane was rinsed with another 100 μL RLT lysis buffer. Cell lysates were then collected and the total RNA extraction was performed using the Qiagen RNeasy Micro kit according to the manufacturer's instructions. The RNA amount was determined using a Nanodrop (ND-1000 Thermoscientific Wilmington, Delaware, USA).

To the cells cultured on Transwell membranes 350 μL of RLT lysis buffer were added, cell lysates were then collected and analyzed using the same procedure.

Affymetrix microarray processing, and analysis

The isolated RNA (n=4 per group) was subjected to genome-wide expression profiling. In brief, total RNA was labelled using the Whole-Transcript Sense Target Assay (Affymetrix, Santa Clara, CA, USA) and hybridized on Human Gene 2.1 ST arrays (Affymetrix). The quality control and data analysis pipeline has been described in detail previously [22].

Normalized expression estimates of probe sets were computed by the robust multiarray analysis (RMA) algorithm [23, 24] as implemented in the Bioconductor library *affyPLM*. Probe sets were redefined using current genome definitions available from the NCBI database, which resulted in the profiling of 29,635 unique genes (custom CDF version 23) [25]. Differentially expressed probe sets (genes) were identified by using linear models (library *limma*) and an intensity-based moderated t-statistic [26, 27]. Probe sets that satisfied the criterion of a False Discovery Rate (FDR) < 0.01 were considered to be significantly regulated [28]. Microarray data have been submitted to the Gene Expression Omnibus (accession number pending).

Biological interpretation of array data

Changes in gene expression were related to biologically meaningful changes using gene set enrichment analysis (GSEA). It is well accepted that GSEA has multiple advantages over analyses performed on the level of individual genes [29-31]. GSEA evaluates gene expression on the level of gene sets that are based on prior biological knowledge, GSEA is unbiased, because no gene selection step (fold change and/or p-value cutoff) is used; a GSEA score is computed based on all genes in the gene set, which boosts the S/N ratio and allows to detect affected biological processes that are due to only subtle changes in expression of individual genes. Gene sets were retrieved from the expert-curated KEGG database [32], but sets belonging to the categories '6 - Human Disease' and '7 - Drug Development' (BRITE Functional Hierarchy level 1) were excluded. Moreover, only gene sets comprising more than 15 and fewer than 500 genes were taken into account. For each comparison, genes were ranked on their t-value that was calculated by the moderated t-test. Statistical significance of GSEA results was determined using 1000 permutations.

Comparison of Caco-2 and human *in vivo* gastrointestinal tract transcriptome data

To compare the transcriptome profiles of Caco-2 cells grown under dynamic (gut-on-chip) or static conditions (Transwell) with healthy human intestinal tissues, transcriptome data from 5 locations taken along the gastrointestinal tract (duodenum, jejunum, ileum, and colon) in 4 healthy human volunteers was used [21]. Datasets were integrated applying a cumulative proportion transformation using *YuGene* [33], and visualized by principal component analysis (PCA), essentially as described before [34]. In brief, raw data transcriptome (CEL) files from the gastrointestinal were obtained from the Gene Expression Omnibus (GEO) [35] (accession number: GSE10867). Next, each dataset was separately background corrected, log₂-transformed and summarized at the probe set level, which was followed by filtering out all genes that were not shared on the two array platforms. Samples were then combined by rescaling using the cumulative proportion transformation. The combined dataset included the gene expression measurements of 12,746 genes in 22 samples. Before PCA, expression data was centered by dataset. PCA was performed using the library *PCAtools* [36]. A list of 764

intestine-specific genes was obtained from The Human Proteome Atlas [37], and used when indicated.

Results

Cellular morphological assessment

Monolayer integrity of Caco-2 cells grown for 21 days in the gut-on-chip under dynamic flow (Fig. 1A and B) or in the static Transwell was assessed using confocal microscopy imaging. The top views of representative images are shown in Fig. 2A and B. Caco-2 cells grown under continuous flow showed a comparable monolayer formation and cell morphology at day 21 to cells grown under static conditions, as reflected by immunofluorescence staining of nuclei (blue), actin filaments (green) and tight junctions (red). Cells cultured under flow seemed to be slightly larger than those grown under static conditions. Vertical cross-sections of the monolayers, created by Z-stacks (Fig. 2C and D), showed cell polarization with core bundles of actin filaments in the microvilli and tight junctions on the apical side, in cells grown under both conditions. The cell heights were comparable in both systems, reaching $\sim 10\ \mu\text{m}$ at day 21.

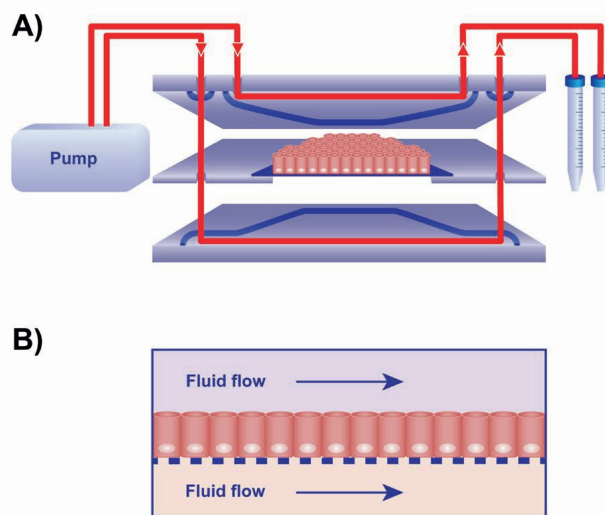


Figure 1. Schematic illustration of the experimental setup of the gut-on-chip A) Schematic design vertical cross-section of the microfluidic system, where the blue lines indicate the boundaries of the compartments, and the red line the flow in and out of both compartments. B) Schematic drawing showing how cells were exposed to fluid flow.

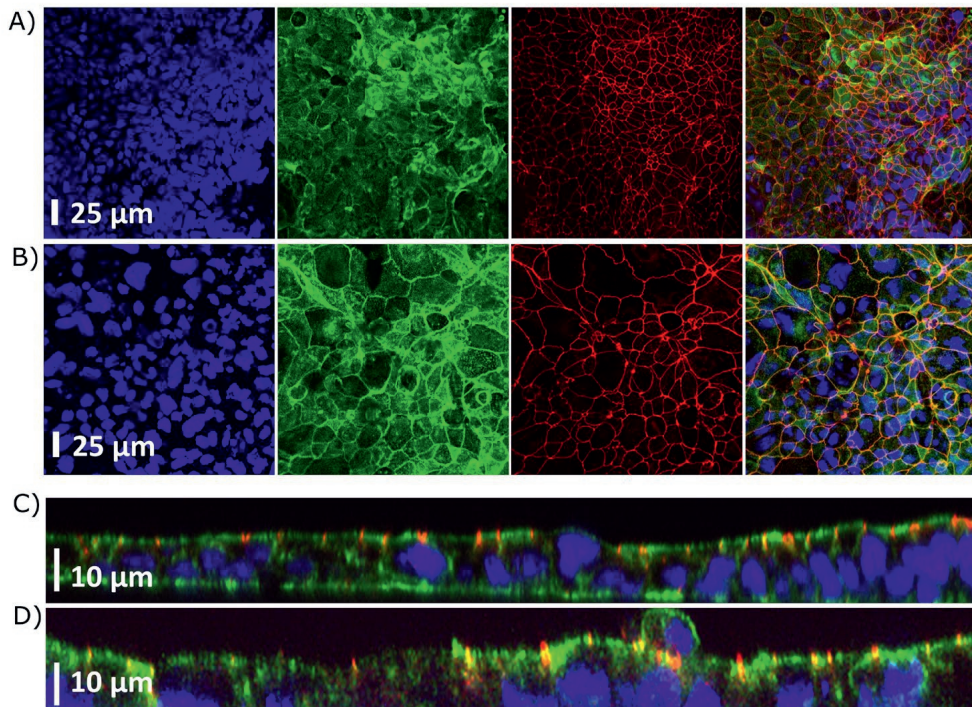


Figure 2. Cell morphology of Caco-2 cells after 21 days of culture under static (Transwell) (A and C) and dynamic (B and D), with a flow of 100 $\mu\text{L/h}$, (gut-on-chip) conditions, visualized by confocal microscopy. Top views of the cell layer in A) the Transwell and in B) the gut-on-chip. Vertical cross-sections of the cell monolayer in C) the Transwell and D) the gut-on-chip. Actin filaments (Phalloidin) in green, cell nuclei (DAPI) in blue, and tight junctions (ZO-1/TJPI) in red. The figures at the right in line A and B present the overlay of the three individually colored pictures.

Gene expression in Caco-2 human epithelial cells under static and dynamic conditions

Genome-wide changes in gene expression in Caco-2 cells grown under dynamic culture conditions in the gut-on-chip were identified by comparison of gene expression of cells grown under static versus dynamic culture conditions. After 21 days of culturing, total RNA was isolated and gene expression was analyzed using Affymetrix GeneChips.

After data processing, differential gene expression was visualized in a volcano plot (Fig. 3A). The expression of 29,635 genes in Caco-2 cells grown in the gut-on-chip device was compared with that in cells grown under static conditions. In total, 5,927 differentially expressed genes were observed in the gut on chip (3,280 upregulated and 2,647 downregulated) with a FDR < 0.01 (Fig. 3B). The top 10 most up- and downregulated genes in cells grown in the gut-on-chip device, compared to cells grown in the Transwell inserts, are listed in Table 1. Compared to the Transwell inserts, the most upregulated gene in cells grown on the gut-on-chip device was metallothionein 1H (*MT1H*; $\log_2\text{FC} = 5.89$) coding for metallothionein 1H protein, whereas the gene glucose-6-phosphatase catalytic subunit

(*G6PC*; $\log_2\text{FC} = -6.79$) coding for glucose-6-phosphatase catalytic subunit protein was most downregulated.

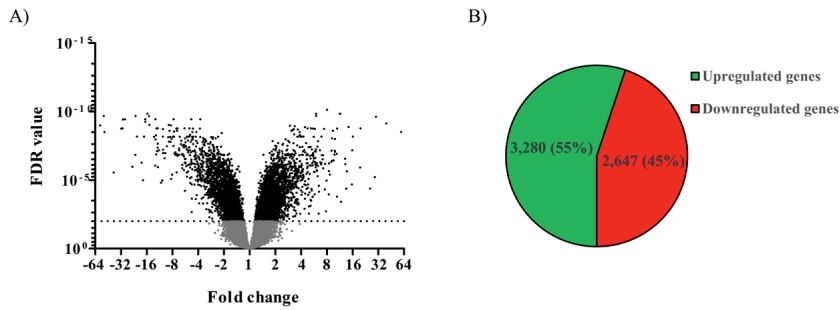


Figure 3. Overview of the differential gene expression in Caco-2 cells grown in a gut-on-chip device versus Transwell inserts after 21 days of culture. A) Volcano plot of all differentially expressed genes where the FDR value of each gene is plotted against the fold change in expression; the dotted line indicates an FDR of 0.01. B) The number and percentages of differentially expressed genes in Caco-2 cells grown in a gut-on-chip device compared to cells grown in Transwell inserts.

Table 1. Top 10 most up- and downregulated genes in Caco-2 cells cultured under dynamic conditions compared to static conditions after 21 days of culture.

EntrezID	Gene Symbol	Gene full name	Core function in cells *	Log2 FC	P-value	FDR
Upregulated genes						
4496	MT1H	Metallothionein 1H	Mineral absorption, Metal binding	5.89	5.6E-12	3.0E-09
4495	MT1G	Metallothionein 1G	Mineral absorption, Metal binding	5.32	5.0E-13	7.4E-10
301	ANXA1	Annexin A1	Anti-inflammation	4.91	8.0E-14	2.4E-10
54658	UGT1A1	UDP glucuronosyltransferase family 1 member A1	Metabolism	4.87	2.1E-07	6.1E-06
10202	DHRS2	Dehydrogenase/reductase 2	Metabolism	4.68	2.3E-06	4.0E-05
4501	MT1X	Metallothionein 1X	Mineral absorption, Metal binding	4.31	1.9E-12	1.7E-09
10410	IFITM3	Interferon induced transmembrane protein 3	Immune system	4.30	2.5E-08	1.2E-06
9120	SLC16A6	Solute carrier family 16 member 6	Membrane transporter	4.02	1.5E-11	6.7E-09
7348	UPLK1B	Uroplakin 1B	Cellular development and growth	3.99	4.3E-10	6.7E-08
3429	IFI27	Interferon alpha inducible protein 27	Immune system	3.98	9.9E-07	2.0E-05
Downregulated genes						
2538	G6PC	Glucose-6-phosphatase catalytic subunit	Metabolism	-6.79	4.7E-13	7.3E-10
229	ALDOB	Aldolase, fructose-bisphosphate B	Metabolism	-5.81	8.3E-13	1.0E-09
284099	C17orf78	Chromosome 17 open reading frame 78	unknown	-5.67	4.3E-14	2.1E-10
56624	ASAH2	N-acylsphingosine amidohydrolase 2	Metabolism, Biosynthesis	-5.64	6.1E-12	3.1E-09
6476	SI	Sucrase-isomaltase	Metabolism, Digestion	-5.28	7.4E-08	2.7E-06
795	S100G	S100 calcium binding protein G	Mineral absorption, Membrane transporter	-4.99	2.2E-12	1.7E-09
1557	CYP2C19	Cytochrome P450 family 2 subfamily C member 19	Metabolism	-4.94	2.0E-12	1.7E-09
4547	MTTP	Microsomal triglyceride transfer protein	Lipid digestion and absorption	-4.92	2.2E-13	3.9E-10
79853	TM4SF20	Transmembrane 4 L six family member 20	Cell growth, proliferation and activities	-4.84	1.7E-13	3.6E-10
51299	NRN1	Interferon alpha inducible protein 27	Neurite outgrowth	-4.55	2.1E-08	1.1E-06

* References on the gene functions are provided in Supplementary Table 3

Overview of gene set enrichment analysis

GSEA was performed to elucidate whether biological processes were potentially affected in cells cultured under dynamic conditions compared to cells cultured under static conditions, based on gene expression data. The studied pathways were derived from the KEGG database. This database is structured into KEGG categories that are subdivided into category subgroups and each category subgroup contains various pathways, each represented by a gene set. As described in the material section we have considered gene sets belonging to 5 categories namely ‘metabolism’, ‘genetic information processing’, ‘environmental information processing’, ‘cellular processes’ and ‘organismal systems’ (BRITE Functional Hierarchy level 1). This resulted in the analysis of 225 gene sets. Of these 225 gene sets, 108 gene sets were differently expressed, of which 52 gene sets were upregulated in Caco-2 cells cultured in the gut-on-chip versus Caco-2 cells cultured in Transwells and 56 gene sets were downregulated in Caco-2 cells grown in the gut-on-chip ($p\text{-value} < 0.05$ and $\text{FDR} < 0.25$). The most prominently upregulated gene set in Caco-2 cells cultured in the gut-on-chip represented the ‘ribosome biogenesis’ pathway (normalized enrichment score, $\text{NES} = 2.52$) under the KEGG category ‘genetic information processing’ and KEGG category subgroup ‘translation’ (suppl. Table 1). The most prominently downregulated pathway in Caco-2 cells cultured under dynamic conditions represented the ‘protein digestion and absorption’ pathway ($\text{NES} = -2.23$) under the KEGG category ‘organismal system’ and KEGG category subgroup ‘digestive system’ (suppl. Table 2). The gene expression analysis was continued by focusing on up- and downregulated gene sets that represent pathways belonging to crucial small intestinal functions, core signaling and cell survival. Twenty-four gene sets, belonging to the KEGG category subgroups: ‘xenobiotics biodegradation and metabolism’, ‘membrane transport’, ‘cellular transport’, ‘immune system’, ‘signal transduction’, ‘cell growth and death’ and ‘digestive system’ (Table 2), were evaluated. Various gene sets in the KEGG category subgroups ‘xenobiotics biodegradation and metabolism’ and ‘digestive system’ were downregulated. Various gene sets in the KEGG category subgroups ‘cellular transport’, ‘immune system’ and ‘cell growth and death’ were upregulated. In the 24 enriched gene sets, there were 575 genes that were contributing most to the enrichment, the so called leading edge genes, which are shown in a heatmap in Fig. 4.

Table 2. Most enriched gene sets representing pathways associated with intestinal cell function, core signaling and cell survival in Caco-2 cells cultured under dynamic conditions compared to static conditions.

KEGG pathway name	KEGG category	KEGG category subgroup	Size	NES	p-value	FDR
<i>Upregulated gene sets</i>						
Endocytosis	Cellular processes	Transport and catabolism	243	1.42	3.4E-03	7.8E-02
NOD-like receptor signaling pathway	Organismal system	Immune system	168	1.93	0.00E+00	5.6E-04
RIG-I-like receptor signaling pathway	Organismal system	Immune system	67	1.60	3.8E-03	2.8E-02
Cytosolic DNA-sensing pathway	Organismal system	Immune system	58	2.01	0.0E+00	1.7E-04
IL-17 signaling pathway	Organismal system	Immune system	93	1.72	3.7E-04	9.5E-03
MAPK signaling pathway	Environmental information processing	Signal transduction	292	1.60	0.0E+00	2.7E-02
TGF-beta signaling pathway	Environmental information processing	Signal transduction	92	1.47	1.3E-02	5.9E-02
Jak-STAT signaling pathway	Environmental information processing	Signal transduction	158	1.41	1.1E-02	8.3E-02
NF-kappa B signaling pathway	Environmental information processing	Signal transduction	97	1.96	0.0E+00	3.5E-04
TNF signaling pathway	Environmental information processing	Signal transduction	110	2.00	0.0E+00	2.2E-04
Cell cycle	Cellular processes	cell growth and death	124	1.92	0.0E+00	6.5E-04
Apoptosis	Cellular processes	cell growth and death	133	1.66	1.8E-04	1.6E-02
Necroptosis	Cellular processes	cell growth and death	128	1.77	0.0E+00	6.2E-03
p53 signaling pathway	Cellular processes	cell growth and death	72	1.70	1.1E-03	1.1E-02
Cellular senescence	Cellular processes	cell growth and death	158	1.39	1.4E-02	9.3E-02

Table 2. Most enriched gene sets representing pathways associated with intestinal cell function, core signaling and cell survival in Caco-2 cells cultured under dynamic conditions compared to static conditions (continued).

KEGG pathway name	KEGG category	KEGG category subgroup	Size	NES	p-value	FDR
<i>Downregulated gene sets</i>						
Drug metabolism-cytochrome P450	Metabolism	Xenobiotics biodegradation and metabolism	62	-2.00	0.0E+00	4.4E-04
Drug metabolism-other enzymes	Metabolism	Xenobiotics biodegradation and metabolism	70	-1.42	2.5E-02	8.5E-02
ABC transporters	Environmental information processing	Membrane transport	45	-1.48	2.9E-02	5.8E-02
Carbohydrate digestion and absorption	Organismal system	Digestive system	39	-2.19	0.0E+00	5.7E-05
Protein digestion and absorption	Organismal system	Digestive system	83	-2.23	0.0E+00	1.1E-04
Fat digestion and absorption	Organismal system	Digestive system	41	-2.17	0.0E+00	3.8E-05
Vitamin digestion and absorption	Organismal system	Digestive system	23	-2.00	0.0E+00	4.8E-04
Phosphatidylinositol signaling pathway	Environmental information processing	Signal transduction	99	-1.60	2.2E-03	2.9E-02
AMPK signaling pathway	Environmental information processing	Signal transduction	119	-1.39	2.1E-02	9.9E-02

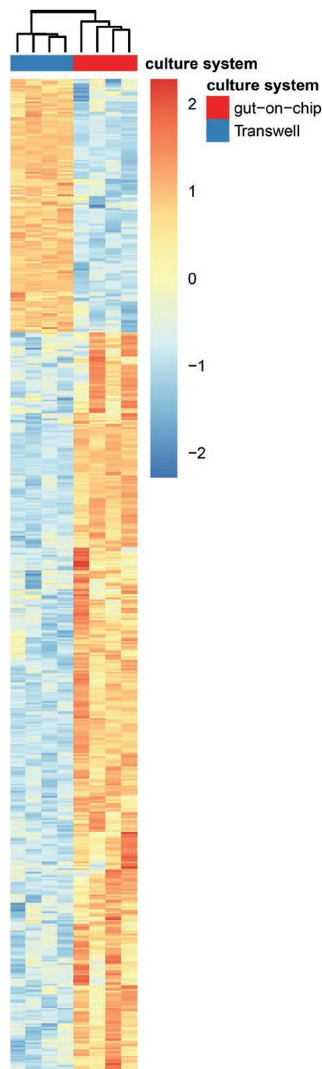


Figure 4. Heatmap showing the leading edge genes (575 genes in total) of 24 enriched gene sets. In the GSEA, gene expression patterns of Caco-2 cells cultured in a gut-on-chip were compared with those of Caco-2 cells cultured in Transwells.

Transcriptomic comparison of Caco-2 cells grown in the gut-on-chips and Transwells, and human *in vivo* data

Next, we compared the gene expression profiles of the Caco-2 cells grown under dynamic and static conditions *in vitro*, with human intestinal *in vivo* gene expression profiles. For this, we selected a publicly available gene expression data set from the human proteome atlas that contained data of human intestinal tissues [37]. The gene expression profiles were evaluated by a principal component analysis (PCA). A PCA scatterplot representing the first two

principal components based on the transcriptome profiles from 14 human *in vivo* samples and 4 samples each of the Transwell and the gut-on-chip cell culturing system is shown in Fig. 5. PC1 and PC2 explain 51.32% and 16.88% of the total variation, respectively. Samples from the cells cultured in the gut-on-chip device and in the Transwells clustered together showing the low variation and high robustness in each *in vitro* data set. This was also observed for the *in vivo* colon samples, while the small intestinal samples (especially the ileum samples) clustered somewhat more scattered. The first component (PC1) indicates that Caco-2 cells cultured in gut-on-chip clusters were more distant from the clusters of jejunum and duodenum samples, and closer to the colon *in vivo* samples than the Caco-2 cells cultured in the Transwell system. The second component (PC2) indicates that the *in vivo* data sets located between the two clusters of the *in vitro* samples (i.e. gut-on-chip and Transwell). In the database of the human proteome atlas, from which we selected the intestinal tissue *in vivo* data sets, 764 genes have been annotated as intestine specific, 483 (63%) of these genes were expressed in our gene expression data from Caco-2 cells cultured under static or dynamic conditions and data from selected tissue samples from human duodenum, jejunum, ileum and colon [21] and were hierarchically clustered (Fig. 6). The clustering pattern of the various *in vitro* and *in vivo* samples as observed by PCA is confirmed by the hierarchical clustering based on the intestine specific 483 genes.

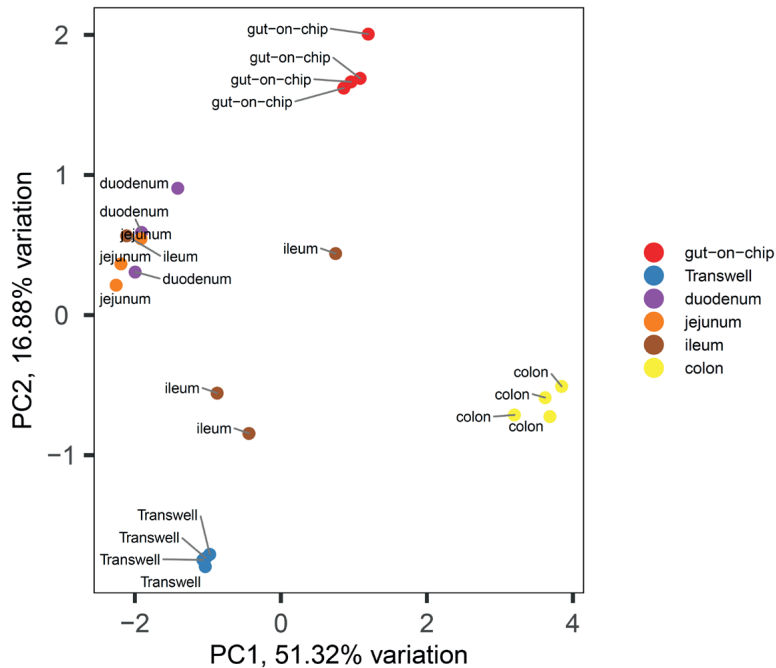


Figure 5. PCA plot of genomic expression data of 483 of human intestine-specific genes [37] from human duodenum, jejunum, ileum and colon tissues, and Caco-2 cells cultured in a gut-on-chip or Transwell system.

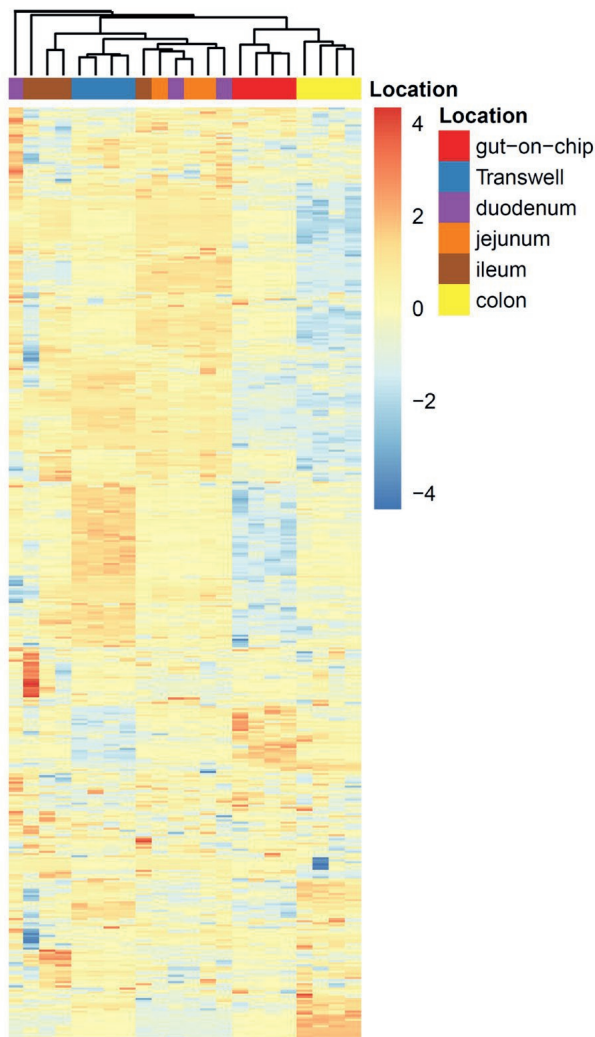


Figure 6. Hierarchical clustering of the expression data of 483 of human intestine-specific genes in Caco-2 cells grown in the gut-on-chip or Transwell and in human intestinal tissue samples.

Discussion

In this study we provide a comprehensive overview on whole genome differential gene expression in Caco-2 cells when cultured under dynamic *in vitro* culturing conditions versus static *in vitro* culturing conditions. In addition, we compared the transcriptome profiles of our *in vitro* experiments with the transcriptome profiles as observed in human (*in vivo*) intestinal segments. Monolayers of Caco-2 cells grown in conventional static systems have been widely used to study effects of exposure to chemicals to predict the *in vivo* human intestinal epithelial responses [38-40]. However, *in vivo* the epithelial cells of the intestinal wall experience physical forces including strain, fluid shear stress, and villous motility. Shear stresses to cells might be important triggers in the development and maturation of epithelial

cells [41]. We here show a differential expression of 5,927 genes in Caco-2 cells induced by dynamic culturing conditions as compared to static culturing conditions. The shear stress of ~ 0.002 dyne/cm² in our model induced comparable changes in gene expression profiles as reported before in a model that exposed Caco-2 cells to an estimated shear stress of ~ 0.02 dyne/cm² [19]. No other studies on the effects of shear forces on Caco-2 cells based on transcriptomics data could be found. Interestingly, for two other types of cells the effects of shear forces have been studied in detail, namely for human vascular endothelial cells (with fluid shear stresses ranging from 1.5 to 15 dyne/cm²; [42, 43]) and on murine proximal tubular epithelial cells (with fluid shear stresses ranging from 0 to 1.9 dyne/cm²; [44]). These studies revealed clear effects of fluid shear stresses on gene expression profiles in the cells, comparison of the findings on affected genes and processes in these studies with our results will be discussed further below.

At the individual gene level, fluid flow applied to Caco-2 cells resulted in the upregulation of several genes related to mineral absorption/metal binding. Highly upregulated genes were the metallothionein genes (i.e. MT1H, MT1G, MT1X) that provide protection against metal toxicity [45] and oxidative stress [46]. Interestingly, the modulation of metallothionein genes has been observed in endothelial cells *in vitro* upon physical stress [43, 47].

The KEGG category ‘xenobiotics biodegradation and metabolism’ was down regulated under dynamic conditions. Various individual genes related to cellular metabolism (i.e. *G6PC*, *ALDOB*, *ASAH2*) were downregulated under dynamic conditions. Exceptions, however, were genes coding for *UGT1A1* and *CYP1A1* that were extremely upregulated in Caco-2 cells cultured under dynamic conditions (top 20 most upregulated genes). The latter genes relate to isoforms of enzymes that are important in drug and xenobiotic metabolism in the small intestine. *UGT1A1* catalyzes glucuronic acid conjugation to a nucleophilic substrate [48, 49] and *CYP1A1* is involved in the modification of aromatic hydrocarbons. Gene expression of *UGT1A1* and *CYP1A1* is regulated by the aryl hydrocarbon receptor (AhR) [50, 51]. The AhR gene and AhR dependent genes (i.e. *CYP1B1*, *TIPARP*, *PTGS2*) were also upregulated under dynamic culturing conditions. The upregulated expression of this functional group of AhR regulated genes has also been observed in human endothelial cells exposed to shear stress [52-54].

We next set off to analyze if the differential gene expression also affected biological pathways using GSEA. The most relevant affected pathways for intestinal functions and core signaling pathways were listed in Table 2. It is of interest that gene sets involved in inflammatory pathways (i.e. IL-17 signaling pathway, cytosolic DNA-sensing pathway) were upregulated in Caco-2 cells that were cultured in the gut-on-chip. This included the upregulation of genes for the NOD-like receptor, RIG-I receptor signaling pathways that are involved in the innate immune responses [55, 56]. This indicates that fluid shear stresses might modulate the defense mechanism of intestinal epithelial cells by stimulating the innate immune response. Miravete et al. observed that human proximal tubular cells (HK-2)

exposed to a shear stress of 0.1 dyne/cm² activated the differentiation of monocytes into macrophages by secretion of TNF-alpha [57], which also are elements of the innate immune system.

Various signaling pathways (e.g. MAPK, TGF-beta, Jak-STAT, NF kappa B, TNF, p53) belonging to the 'signal transduction' and 'cell growth and death' KEGG category subgroups were upregulated in Caco-2 cells grown under dynamic conditions. These pathways have important regulatory roles in a wide variety of cellular processes including cell proliferation, differentiation, apoptosis and stress responses in mammalian cells [58-62]. While the effects of shear stresses on signaling processes in intestinal cells is poorly studied, much more is known from endothelial cells and these findings corroborate the results observed in the present study. In endothelial cells, shear stress-induced IL-8 gene expression (4.2 dyne/cm²) regulated by MAPK signaling [63]. TGF-beta signaling is also described to be induced in endothelial cells by shear stress of 10 dyne/cm² [64]. NF kappa B signaling, stimulating pro-inflammatory cytokine and chemokine release, was activated by a shear stress of 15 dyne/cm² in endothelial cells [65].

Compound metabolism pathways, drug metabolism-cytochrome P450 and other enzymes, belonging to the 'xenobiotics biodegradation and metabolism' KEGG category subgroup were downregulated in Caco-2 cells exposed to shear stress, as was also observed at the individual gene expression level with the exception of *UGT1A1* and *CYP1A1* (*AhR dependent genes*). The study with a different subclone of Caco-2 cells (i.e. Caco-2BBE) cultured under a shear stress of 0.02 dyne/cm² in the study of Kim et al. showed an increase in activity of the drug metabolizing cytochrome CYP3A4 enzyme compared to cells cultured under static condition [11]. In our results, the pathways associated to general cellular metabolism were also downregulated (suppl. table 2). This is in line with a study in renal epithelial cells where a downregulation of gene expression at several levels for cellular homeostasis, including fatty acid, amino acid and cholesterol metabolism, was observed after exposure to a shear stress of 1.9 dyne/cm² [44]. Nutrient digestion and absorption by epithelial cells might also be affected by fluid flow exposure as indicated by the downregulation of gene sets associated with those processes (i.e. gene sets for the protein, carbohydrate and fat digestion and absorption pathways belonging to the 'digestive system' KEGG category subgroup). This has also been observed in endothelial cells, in which shear stresses (20 dyne/cm²) reduced the expression of genes involved in glucose absorption [66].

Lastly, we compared the gene expression patterns of both our *in vitro* models with those of samples taken from different intestinal segments as reported in literature [21]. In a PCA analysis of all data samples from our *in vitro* models cluster together in two separate groups that both are different from the *in vivo* gene expression clusters. The PCA and the unbiased clustering reveal that the gene expression profiles of Caco-2 cells cultured under static conditions more closely recapitulate small intestine gene expression, while those of the Caco-2 cells grown under shear stress cluster together slightly closer to colonic samples (Fig. 5 and 6). Interestingly, the duodenal and jejunum samples clustered together, while the gene

expression of the ileum samples (from the same donors) seem to be much more variable. To the authors knowledge, there is only one other study reporting on the transcriptomes of Caco-2 cells cultured in gut-on-chip and Transwell devices compared with *in vivo* data [19]. However, with the very limited number of samples (n=2) the authors included it is quite challenging to draw the strong conclusion from this study.

In conclusion, our study provides a comprehensive profile of altered gene expression in Caco-2 cells under flow culturing conditions versus culturing under static conditions. The responses were mainly related to cellular homeostasis, immunological responses, cell growth and death, as well as signal transduction. While general cellular metabolism and absorption pathways were repressed, specific genes in xenobiotic biotransformation pathways were induced upon exposure to fluid flow. Interestingly, comparable responses have been noted in endothelial and renal tubular epithelial cells that were also exposed to shear stress. Our unbiased comparison with global gene expression in samples from intestinal segments did not reveal a striking similarity with any of these segments. The results obtained do not apparently favor one of the two *in vitro* models and it can be concluded that both model systems can be equally well used to study human intestinal epithelial responses, while, depending on the endpoint of interest. It should be kept in mind that some specific gene functions are differently modulated in each model. This information may be used to further advance the applicability of flow conditions in *in vitro* cells systems for use as alternatives for animal models.

Acknowledgement

The authors sincerely acknowledge the support and assistance of prof.dr.ir. IMCM (Ivonne) Rietjens. K. K. is supported by a Royal Thai government Scholarship. This work was in part supported by the Dutch Ministry of Agriculture, Nature and Food Quality (project KB-23-002-022)

Author contributions

K.K. performed the experiments and together with M.Z. and H.B. wrote the main manuscript text, L.D. performed the immuno histochemistry, V.M. performed the shear stress simulations, G.H. with the support of K.K. and I.M.E. performed the biostatistical analysis.

Competing interests

The authors declare no competing interests.

References

1. Martignoni, M., G.M.M. Groothuis, and R. de Kanter, *Species differences between mouse, rat, dog, monkey and human CYP-mediated drug metabolism, inhibition and induction*. Expert Opinion on Drug Metabolism & Toxicology, 2006. 2(6): p. 875-894.
2. Komura, H. and M. Iwaki, *In vitro and in vivo small intestinal metabolism of CYP3A and UGT substrates in preclinical animals species and humans: species differences*. Drug Metabolism Reviews, 2011. 43(4): p. 476-498.
3. Punt, A., et al., *Expert opinions on the acceptance of alternative methods in food safety evaluations: Formulating recommendations to increase acceptance of non-animal methods for kinetics*. Regul Toxicol Pharmacol, 2018. 92: p. 145-151.
4. Flecknell, P., *Replacement, reduction and refinement*. ALTEX, 2002. 19(2): p. 73-8.
5. Guerra, A., N.E. Campillo, and J.A. Paez, *Neural computational prediction of oral drug absorption based on CODES 2D descriptors*. Eur J Med Chem, 2010. 45(3): p. 930-40.
6. Kampf, A.A.M., et al., *Development of an in vitro co-culture model to mimic the human intestine in healthy and diseased state*. Toxicol In Vitro, 2017. 45(Pt 1): p. 31-43.
7. Creff, J., et al., *Fabrication of 3D scaffolds reproducing intestinal epithelium topography by high-resolution 3D stereolithography*. Biomaterials, 2019. 221: p. 119404.
8. Bhise, N.S., et al., *Organ-on-a-chip platforms for studying drug delivery systems*. J Control Release, 2014. 190: p. 82-93.
9. Kimura, H., Y. Sakai, and T. Fujii, *Organ/body-on-a-chip based on microfluidic technology for drug discovery*. Drug Metab Pharmacokinet, 2018. 33(1): p. 43-48.
10. Kim, H.J., et al., *Human gut-on-a-chip inhabited by microbial flora that experiences intestinal peristalsis-like motions and flow*. Lab Chip, 2012. 12(12): p. 2165-74.
11. Kim, H.J. and D.E. Ingber, *Gut-on-a-Chip microenvironment induces human intestinal cells to undergo villus differentiation*. Integr Biol (Camb), 2013. 5(9): p. 1130-40.
12. Kulthong, K., et al., *Implementation of a dynamic intestinal gut-on-a-chip barrier model for transport studies of lipophilic dioxin congeners*. Rsc Advances, 2018. 8(57): p. 32440-32453.
13. Kulthong, K., et al., *Microfluidic chip for culturing intestinal epithelial cell layers: Characterization and comparison of drug transport between dynamic and static models*. Toxicol In Vitro, 2020. 65: p. 104815.
14. Ortmann, D. and L. Vallier, *Variability of human pluripotent stem cell lines*. Current Opinion in Genetics & Development, 2017. 46: p. 179-185.
15. Kasendra, M., et al., *Development of a primary human Small Intestine-on-a-Chip using biopsy-derived organoids*. Sci Rep, 2018. 8(1): p. 2871.
16. del Carmen, P.M., G. Jean-Pierre, and L.B. Caroline, *Intestinal in vitro cell culture models and their potential to study the effect of food components on intestinal inflammation (vol 59, pg 1, 2019)*. Critical Reviews in Food Science and Nutrition, 2019. 59(13): p. 2166-2168.
17. Punt, A., et al., *Non-animal approaches for toxicokinetics in risk evaluations of food chemicals*. ALTEX, 2017. 34(4): p. 501-514.
18. Li, C., et al., *Development of in vitro pharmacokinetic screens using Caco-2, human hepatocyte, and Caco-2/human hepatocyte hybrid systems for the prediction of oral bioavailability in humans*. J Biomol Screen, 2007. 12(8): p. 1084-91.
19. Kim, H.J., et al., *Contributions of microbiome and mechanical deformation to intestinal bacterial overgrowth and inflammation in a human gut-on-a-chip*. Proceedings of the National Academy of Sciences of the United States of America, 2016. 113(1): p. E7-E15.
20. Hubatsch, I., E.G. Ragnarsson, and P. Artursson, *Determination of drug permeability and prediction of drug absorption in Caco-2 monolayers*. Nat Protoc, 2007. 2(9): p. 2111-9.
21. Comelli, E.M., et al., *Biomarkers of human gastrointestinal tract regions*. Mamm Genome, 2009. 20(8): p. 516-27.
22. Lin, K., et al., *MADMAX - Management and analysis database for multiple -omics experiments*. J Integr Bioinform, 2011. 8(2): p. 160.

23. Irizarry, R.A., et al., *Exploration, normalization, and summaries of high density oligonucleotide array probe level data*. Biostatistics, 2003. 4(2): p. 249-64.
24. Bolstad, B.M., et al., *A comparison of normalization methods for high density oligonucleotide array data based on variance and bias*. Bioinformatics, 2003. 19(2): p. 185-93.
25. Dai, M.H., et al., *Evolving gene/transcript definitions significantly alter the interpretation of GeneChip data*. Nucleic Acids Research, 2005. 33(20).
26. Ritchie, M.E., et al., *limma powers differential expression analyses for RNA-sequencing and microarray studies*. Nucleic Acids Research, 2015. 43(7).
27. Sartor, M.A., et al., *Intensity-based hierarchical Bayes method improves testing for differentially expressed genes in microarray experiments*. BMC Bioinformatics, 2006. 7.
28. Benjamini, Y. and Y. Hochberg, *Controlling the False Discovery Rate - a Practical and Powerful Approach to Multiple Testing*. Journal of the Royal Statistical Society Series B-Statistical Methodology, 1995. 57(1): p. 289-300.
29. Subramanian, A., et al., *Gene set enrichment analysis: a knowledge-based approach for interpreting genome-wide expression profiles*. Proc Natl Acad Sci U S A, 2005. 102(43): p. 15545-50.
30. Allison, D.B., et al., *Microarray data analysis: from disarray to consolidation and consensus*. Nat Rev Genet, 2006. 7(1): p. 55-65.
31. Abatangelo, L., et al., *Comparative study of gene set enrichment methods*. BMC Bioinformatics, 2009. 10: p. 275.
32. Kanehisa, M., et al., *KEGG: new perspectives on genomes, pathways, diseases and drugs*. Nucleic Acids Res, 2017. 45(D1): p. D353-D361.
33. Le Cao, K.A., et al., *YuGene: a simple approach to scale gene expression data derived from different platforms for integrated analyses*. Genomics, 2014. 103(4): p. 239-51.
34. Rohart, F., et al., *A molecular classification of human mesenchymal stromal cells*. PeerJ, 2016. 4: p. e1845.
35. Clough, E. and T. Barrett, *The Gene Expression Omnibus Database*. Methods Mol Biol, 2016. 1418: p. 93-110.
36. K Blighe, A.L. *PCAtools: everything Principal Components Analysis*. 2018 [cited 2020 13/02/2020]; Available from: <https://github.com/kevinblighe/PCAtools>.
37. Uhlen, M., et al., *Proteomics. Tissue-based map of the human proteome*. Science, 2015. 347(6220): p. 1260419.
38. Meunier, V., et al., *The human intestinal epithelial cell line Caco-2; pharmacological and pharmacokinetic applications*. Cell Biol Toxicol, 1995. 11(3-4): p. 187-94.
39. Sun, H., et al., *The Caco-2 cell monolayer: usefulness and limitations*. Expert Opin Drug Metab Toxicol, 2008. 4(4): p. 395-411.
40. Wang, Z., et al., *(-)-Epicatechin and NADPH oxidase inhibitors prevent bile acid-induced Caco-2 monolayer permeabilization through ERK1/2 modulation*. Redox Biol, 2020. 28: p. 101360.
41. Gayer, C.P. and M.D. Basson, *The effects of mechanical forces on intestinal physiology and pathology*. Cellular Signalling, 2009. 21(8): p. 1237-1244.
42. Chen, B.P., et al., *DNA microh shear stressarray analysis of gene expression in endothelial cells in response to 24-*. Physiol Genomics, 2001. 7(1): p. 55-63.
43. Ohura, N., et al., *Global analysis of shear stress-responsive genes in vascular endothelial cells*. J Atheroscler Thromb, 2003. 10(5): p. 304-13.
44. Kunnen, S.J., et al., *Comprehensive transcriptome analysis of fluid shear stress altered gene expression in renal epithelial cells*. J Cell Physiol, 2018. 233(4): p. 3615-3628.
45. Sigel, A., et al., *Metallothioneins and related chelators*. Metal ions in life sciences,. 2009, Cambridge, UK: RSC Pub. xxix, 514 p.
46. Kumari, M.V., M. Hiramatsu, and M. Ebadi, *Free radical scavenging actions of metallothionein isoforms I and II*. Free Radic Res, 1998. 29(2): p. 93-101.

47. Conway, D.E., et al., *Endothelial metallothionein expression and intracellular free zinc levels are regulated by shear stress*. Am J Physiol Cell Physiol, 2010. 299(6): p. C1461-7.
48. Radominska-Pandya, A., et al., *Structural and functional studies of UDP-glucuronosyltransferases*. Drug Metab Rev, 1999. 31(4): p. 817-99.
49. Miners, J.O. and P.I. Mackenzie, *Drug Glucuronidation in Humans*. Pharmacology & Therapeutics, 1991. 51(3): p. 347-369.
50. Yueh, M.F., J.A. Bonzo, and R.H. Tukey, *The role of ah receptor in induction of human UDP-glucuronosyltransferase 1A1*. Phase Ii Conjugation Enzymes and Transport Systems, 2005. 400: p. 75-+.
51. Brauze, D., et al., *Induction of expression of aryl hydrocarbon receptor-dependent genes in human HepaRG cell line modified by shRNA and treated with beta-naphthoflavone*. Mol Cell Biochem, 2017. 425(1-2): p. 59-75.
52. Han, Z., et al., *Aryl hydrocarbon receptor mediates laminar fluid shear stress-induced CYP1A1 activation and cell cycle arrest in vascular endothelial cells*. Cardiovasc Res, 2008. 77(4): p. 809-18.
53. Lano, G., et al., *Aryl Hydrocarbon Receptor Activation and Tissue Factor Induction by Fluid Shear Stress and Indoxyl Sulfate in Endothelial Cells*. Int J Mol Sci, 2020. 21(7).
54. Conway, D.E., et al., *Expression of CYP1A1 and CYP1B1 in human endothelial cells: regulation by fluid shear stress*. Cardiovasc Res, 2009. 81(4): p. 669-77.
55. Chen, G., et al., *NOD-like receptors: role in innate immunity and inflammatory disease*. Annu Rev Pathol, 2009. 4: p. 365-98.
56. Loo, Y.M. and M. Gale, Jr., *Immune signaling by RIG-I-like receptors*. Immunity, 2011. 34(5): p. 680-92.
57. Miravete, M., et al., *Renal tubular fluid shear stress facilitates monocyte activation toward inflammatory macrophages*. Am J Physiol Renal Physiol, 2012. 302(11): p. F1409-17.
58. Harrison, D.A., *The Jak/STAT pathway*. Cold Spring Harb Perspect Biol, 2012. 4(3).
59. Eric Ho, J.W., *Mitogen-Activated Protein Kinases*, in *Handbook of Cell Signaling* E.A.D. Ralph A. Bradshaw, Editor. 2010, Academic Press. p. 533-538.
60. Veronica Lifshitz, D.F., *TGF- β* , in *Handbook of Biologically Active Peptides*, A.J. Kastin, Editor. 2013, Academic Press. p. 1647-1653.
61. Varfolomeev, E. and D. Vucic, *Intracellular regulation of TNF activity in health and disease*. Cytokine, 2018. 101: p. 26-32.
62. Mitchell, S., J. Vargas, and A. Hoffmann, *Signaling via the NFkappaB system*. Wiley Interdiscip Rev Syst Biol Med, 2016. 8(3): p. 227-41.
63. Cheng, M., et al., *Activation of MAPK participates in low shear stress-induced IL-8 gene expression in endothelial cells*. Clin Biomech (Bristol, Avon), 2008. 23 Suppl 1: p. S96-S103.
64. Walshe, T.E., N.G. dela Paz, and P.A. D'Amore, *The role of shear-induced transforming growth factor-beta signaling in the endothelium*. Arterioscler Thromb Vasc Biol, 2013. 33(11): p. 2608-17.
65. Hay, D.C., et al., *Activation of NF-kappaB nuclear transcription factor by flow in human endothelial cells*. Biochim Biophys Acta, 2003. 1642(1-2): p. 33-44.
66. Doddaballapur, A., et al., *Laminar shear stress inhibits endothelial cell metabolism via KLF2-mediated repression of PFKFB3*. Arterioscler Thromb Vasc Biol, 2015. 35(1): p. 137-45.

Microarray data: <https://www.ncbi.nlm.nih.gov/geo/query/acc.cgi?acc=GSE156269> (password: enujooczduhmkp)

Supplementary Table 1. Upregulated pathways in Caco-2 cells cultured under dynamic culture conditions versus static culture conditions

KEGG pathway name	KEGG Category	KEGG category subgroup	SIZE	ES	NES	NOM p-val	FDR q-val
Ribosome biogenesis in eukaryotes	Genetic information processing	Translation	76	0.77	2.52	0.0E+00	0.0E+00
Proteasome	Genetic information processing	Folding, sorting and degradation	43	0.79	2.37	0.0E+00	0.0E+00
Spliceosome	Genetic information processing	Transcription	128	0.67	2.36	0.0E+00	0.0E+00
RNA transport	Genetic information processing	Translation	146	0.64	2.32	0.0E+00	0.0E+00
Protein processing in endoplasmic reticulum	Genetic information processing	Folding, sorting and degradation	160	0.60	2.18	0.0E+00	0.0E+00
RNA polymerase	Genetic information processing	Transcription	29	0.75	2.05	0.0E+00	8.7E-05
Cytosolic DNA sensing pathway	Organismal systems	Immune system	58	0.64	2.01	0.0E+00	1.7E-04
Antigen processing and presentation	Organismal systems	Immune system	67	0.62	2.01	0.0E+00	1.6E-04
TNF signaling pathway	Environmental information processing	Signal transduction	110	0.58	2.00	0.0E+00	2.2E-04
NF Kappa-B signaling pathway	Environmental information processing	Signal transduction	97	0.58	1.96	0.0E+00	3.5E-04
NOD-like receptor signaling pathway	Organismal systems	Immune system	168	0.53	1.93	0.0E+00	5.6E-04
Cell cycle	Cellular processes	Cell growth and death	124	0.55	1.92	0.0E+00	6.5E-04
mRNA surveillance pathway	Genetic information processing	Translation	87	0.54	1.82	0.0E+00	3.4E-03
Osteoclast differentiation	Organismal systems	Development and regeneration	122	0.51	1.81	0.0E+00	3.6E-03
Necroptosis	Cellular processes	Cell growth and death	128	0.50	1.77	0.0E+00	6.2E-03
Protein export	Genetic information processing	Folding, sorting and degradation	22	0.68	1.76	3.3E-03	6.7E-03
Snare interactions in vesicular transport	Genetic information processing	Folding, sorting and degradation	33	0.62	1.74	3.8E-03	8.1E-03
Mismatch repair	Genetic information processing	Replication and repair	23	0.66	1.74	4.1E-03	8.3E-03
Apoptosis multiple species	Cellular processes	Cell growth and death	31	0.62	1.73	4.7E-03	8.6E-03
IL-17 signaling pathway	Organismal systems	Immune system	93	0.51	1.72	3.7E-04	9.5E-03
p53 signaling pathway	Cellular processes	Cell growth and death	72	0.52	1.70	1.1E-03	1.1E-02
Basal transcription factors	Genetic information processing	Transcription	42	0.57	1.68	4.9E-03	1.3E-02
Cytokine-cytokine receptor interaction	Environmental information processing	Signaling molecules and interaction	284	0.43	1.67	0.0E+00	1.5E-02
Apoptosis	Cellular processes	Cell growth and death	133	0.47	1.66	1.8E-04	1.6E-02
Th17 cell differentiation	Organismal systems	Immune system	105	0.48	1.65	5.6E-04	1.6E-02

DNA replication	Genetic information processing	Replication and repair	36	0.56	1.61	9.8E-03	2.4E-02
Rig-1-like receptor signaling pathway	Organismal systems	Immune system	67	0.50	1.60	3.8E-03	2.8E-02
MAPK signaling pathway	Environmental information processing	Signal transduction	292	0.41	1.60	0.0E+00	2.7E-02
Progesterone mediated oocyte maturation	Organismal systems	Endocrine system	93	0.47	1.59	4.7E-03	2.7E-02
Nucleotide excision repair	Genetic information processing	Replication and repair	43	0.54	1.59	1.1E-02	2.7E-02
C-type lectin receptor signaling pathway	Organismal systems	Immune system	104	0.46	1.58	1.7E-03	2.8E-02
Synaptic vesicle cycle	Organismal systems	Nervous system	78	0.47	1.55	5.8E-03	3.5E-02
Estrogen signaling pathway	Environmental information processing	Signaling molecules and interaction	136	0.43	1.54	1.8E-03	3.8E-02
Hippo signaling pathway multiple species	Environmental information processing	Signal transduction	28	0.57	1.54	2.0E-02	3.7E-02
Autophagy other	Cellular processes	Transport and catabolism	31	0.56	1.54	2.2E-02	3.7E-02
Vasopressin regulated water reabsorption	Organismal systems	Excretory system	44	0.51	1.53	2.2E-02	3.9E-02
Th1 and Th2 cell differentiation	Organismal systems	Immune system	90	0.45	1.51	7.8E-03	4.7E-02
Collecting duct acid secretion	Organismal systems	Excretory system	27	0.56	1.49	3.6E-02	5.1E-02
RNA degradation	Genetic information processing	Folding, sorting and degradation	77	0.46	1.49	1.4E-02	5.2E-02
Oocyte meiosis	Cellular processes	Cell growth and death	119	0.42	1.48	6.3E-03	5.2E-02
Ubiquitin mediated proteolysis	Genetic information processing	Folding, sorting and degradation	136	0.41	1.48	4.6E-03	5.2E-02
TGF-beta signaling pathway	Environmental information processing	Signal transduction	92	0.43	1.47	1.3E-02	5.9E-02
Oxidative phosphorylation	Metabolism	Energy metabolism	115	0.41	1.44	1.3E-02	6.9E-02
Adipocytokine signaling pathway	Organismal systems	Endocrine system	68	0.44	1.43	2.8E-02	7.4E-02
Endocytosis	Cellular processes	Transport and catabolism	242	0.37	1.42	3.4E-03	7.8E-02
Jak- STAT signaling pathway	Environmental information processing	Signal transduction	158	0.39	1.41	1.1E-02	8.3E-02
Cellular senescence	Cellular processes	Cell growth and death	158	0.38	1.39	1.4E-02	9.3E-02
Hippo signaling pathway	Environmental information processing	Signal transduction	150	0.38	1.39	1.3E-02	9.6E-02
Viral protein interaction with cytokine and cytokine receptor	Environmental information processing	Signaling molecules and interaction	96	0.40	1.38	3.0E-02	9.8E-02
Phagosome	Cellular processes	Transport and catabolism	50	0.45	1.37	6.3E-02	1.1E-01
Autophagy animal	Cellular processes	Transport and catabolism	143	0.38	1.36	2.4E-02	1.1E-01
Thermogenesis	Organismal systems	Environmental adaptation	211	0.35	1.33	2.1E-02	1.3E-01

Supplementary Table 2. Downregulated pathways in Caco-2 cells cultured under dynamic culture conditions versus static culture conditions

KEGG pathway name	KEGG Category	KEGG category subgroup	SIZE	ES	NES	NOM p-val	FDR q-val
Protein digestion and absorption	Organismal systems	Digestive system	83	-0.66	-2.23	0.0E+00	1.1E-04
Carbohydrate digestion and absorption	Organismal systems	Digestive system	39	-0.75	-2.19	0.0E+00	5.7E-05
Fat digestion and absorption	Organismal systems	Digestive system	41	-0.73	-2.17	0.0E+00	3.8E-05
Glycolysis gluconeogenesis	Metabolism	Carbohydrate metabolism	68	-0.63	-2.05	0.0E+00	2.7E-04
Vitamin digestion and absorption	Organismal systems	Digestive system	23	-0.76	-2.00	0.0E+00	4.8E-04
Carbon metabolism	Metabolism	Global and overview maps	114	-0.57	-2.00	0.0E+00	4.3E-04
Drug metabolism cytochrome P450	Metabolism	Xenobiotics biodegradation and metabolism	62	-0.62	-2.00	0.0E+00	4.4E-04
Fatty acid degradation	Metabolism	Lipid metabolism	43	-0.65	-1.98	0.0E+00	6.7E-04
Cholesterol metabolism	Organismal systems	Digestive system	49	-0.64	-1.96	0.0E+00	7.9E-04
Steroid biosynthesis	Metabolism	Lipid metabolism	18	-0.79	-1.96	2.1E-04	7.2E-04
Butanoate metabolism	Metabolism	Carbohydrate metabolism	28	-0.71	-1.96	4.2E-04	6.9E-04
Propanoate metabolism	Metabolism	Carbohydrate metabolism	33	-0.69	-1.95	2.1E-04	7.2E-04
Starch and sucrose metabolism	Metabolism	Carbohydrate metabolism	32	-0.67	-1.91	4.2E-04	1.3E-03
Glycine serine and threonine metabolism	Metabolism	Amino acid metabolism	38	-0.65	-1.91	4.3E-04	1.4E-03
Peroxisome	Cellular processes	Transport and catabolism	82	-0.56	-1.90	0.0E+00	1.4E-03
Valine leucine and isoleucine degradation	Metabolism	Amino acid metabolism	47	-0.62	-1.88	4.2E-04	1.9E-03
Pentose phosphate pathway	Metabolism	Carbohydrate metabolism	30	-0.67	-1.87	6.4E-04	2.2E-03
Histidine metabolism	Metabolism	Amino acid metabolism	23	-0.71	-1.87	1.1E-03	2.1E-03
Complement and coagulation cascades	Organismal systems	Immune system	77	-0.56	-1.86	2.1E-04	2.0E-03
Biosynthesis of amino acids	Metabolism	Global and overview maps	71	-0.57	-1.86	0.0E+00	2.2E-03
Glyoxylate and dicarboxylate metabolism	Metabolism	Carbohydrate metabolism	29	-0.67	-1.85	1.5E-03	2.3E-03
Primary bile acid biosynthesis	Metabolism	Lipid metabolism	16	-0.76	-1.83	1.9E-03	3.2E-03
Bile secretion	Organismal systems	Digestive system	71	-0.54	-1.79	6.4E-04	5.2E-03
Tyrosine metabolism	Metabolism	Amino acid metabolism	36	-0.61	-1.77	1.5E-03	6.4E-03
Sphingolipid metabolism	Metabolism	Lipid metabolism	46	-0.58	-1.76	1.7E-03	6.9E-03
Galactose metabolism	Metabolism	Carbohydrate metabolism	31	-0.62	-1.73	4.9E-03	8.8E-03

PPAR signaling pathway	Organismal systems	Endocrine system	73	-0.52	-1.70	6.4E-04	1.2E-02
Fructose and mannose metabolism	Metabolism	Carbohydrate metabolism	32	-0.60	-1.69	4.6E-03	1.3E-02
Proximal tubule bicarbonate reclamation	Organismal systems	Excretory system	22	-0.64	-1.66	8.9E-03	1.7E-02
Nitrogen metabolism	Metabolism	Energy metabolism	16	-0.69	-1.66	1.1E-02	1.8E-02
Inositol phosphate metabolism	Metabolism	Carbohydrate metabolism	74	-0.50	-1.65	1.1E-03	2.0E-02
Tryptophan metabolism	Metabolism	Amino acid metabolism	42	-0.55	-1.64	7.5E-03	2.0E-02
Alanine, aspartate and glutamate metabolism	Metabolism	Amino acid metabolism	34	-0.57	-1.62	1.3E-02	2.4E-02
Fatty acid metabolism	Metabolism	Global and overview maps	55	-0.52	-1.61	5.3E-03	2.5E-02
Phosphatidylinositol signaling system	Environmental information processing	Signal transduction	99	-0.46	-1.60	2.2E-03	2.9E-02
Pancreatic secretion	Organismal systems	Digestive system	93	-0.46	-1.57	3.0E-03	3.7E-02
Citrate cycle (TCA cycle)	Metabolism	Carbohydrate metabolism	29	-0.56	-1.56	2.3E-02	3.8E-02
Glucagon signaling pathway	Organismal systems	Endocrine system	100	-0.45	-1.56	3.9E-03	3.7E-02
Glycerolipid metabolism	Metabolism	Lipid metabolism	61	-0.49	-1.55	8.2E-03	3.8E-02
Glycerophospholipid metabolism	Metabolism	Lipid metabolism	93	-0.45	-1.55	4.0E-03	4.0E-02
Pyruvate metabolism	Metabolism	Carbohydrate metabolism	39	-0.53	-1.54	2.5E-02	3.9E-02
Glycosaminoglycan biosynthesis-heparan sulfate/heparin	Metabolism	Glycan biosynthesis and metabolism	24	-0.58	-1.54	2.7E-02	4.1E-02
Phenylalanine metabolism	Metabolism	Amino acid metabolism	17	-0.62	-1.53	4.0E-02	4.3E-02
Oxocarboxylic acid metabolism	Metabolism	Global and overview maps	16	-0.62	-1.51	4.8E-02	4.8E-02
Linoleic acid metabolism	Metabolism	Lipid metabolism	25	-0.56	-1.50	3.9E-02	5.0E-02
Alpha linolenic acid metabolism	Metabolism	Lipid metabolism	22	-0.57	-1.50	4.4E-02	5.2E-02
ABC transporters	Environmental information processing	Membrane transport	45	-0.49	-1.48	2.9E-02	5.8E-02
Lysosome	Cellular processes	Transport and catabolism	122	-0.41	-1.48	9.3E-03	5.9E-02
Arachidonic acid metabolism	Metabolism	Lipid metabolism	58	-0.47	-1.47	2.3E-02	6.1E-02
Drug metabolism other enzymes	Metabolism	Xenobiotics biodegradation and metabolism	70	-0.43	-1.42	2.5E-02	8.5E-02
Ether lipid metabolism	Metabolism	Lipid metabolism	44	-0.47	-1.42	4.5E-02	8.5E-02
AMPK signaling pathway	Environmental information processing	Signal transduction	119	-0.39	-1.39	2.1E-02	9.9E-02
Serotonergic synapse	Organismal systems	Nervous system	109	-0.39	-1.38	2.8E-02	1.1E-01
Insulin secretion	Organismal systems	Endocrine system	85	-0.40	-1.35	4.6E-02	1.3E-01
cGMP-PKG signaling pathway	Environmental information processing	Signal transduction	164	-0.35	-1.29	3.8E-02	1.7E-01
Neuroactive ligand-receptor interaction	Environmental information processing	Signaling molecules and interaction	330	-0.32	-1.28	1.7E-02	1.8E-01

Supplementary Table 3. References describing the function of genes in the top 10 most significantly up and downregulated genes

Genes	Core function in cells	NCBI Database ¹	KEGG Pathway Database ²	Publications
MTIH	Mineral absorption, Metal binding	X	X	(Dziegiel et al., 2016, Subramanian Vignesh and Deepe, 2017, Cheng et al., 2012)
MTIG	Mineral absorption, Metal binding	X	X	(Dziegiel et al., 2016, Subramanian Vignesh and Deepe, 2017, Cheng et al., 2012)
ANXA1	Anti-inflammation	X	X	(Babbitt et al., 2008, Gavins and Hickey, 2012)
UGT1A1	Metabolism	X	X	(Mackenzie et al., 2010, Vaessen et al., 2017, Paine and Fisher, 2000)
DHRS2	Metabolism	X	X	(Gabrieli and Tofaneli, 2012, Luo et al., 2019)
MTIX	Mineral absorption, Metal binding	X	X	(Dziegiel et al., 2016, Subramanian Vignesh and Deepe, 2017, Cheng et al., 2012)
IFITM3	Immune system	X	X	(Gorman et al., 2016, Feeley et al., 2011)
SLC16A6	Membrane transporter	X	X	(Halestrap and Meredith, 2004, Perez-Escuredo et al., 2016)
UPK1B	Cellular development and growth	X	X	(Carpenter et al., 2016)
IFI27	Immune system	X	NA	(Dooley et al., 2004, Nagasawa et al., 2016, Kraiczky et al., 2019)
G6PC	Metabolism	X	X	(Chou and Mansfield, 2008, Guo et al., 2015)
ALDOB	Metabolism	X	X	(Chang et al., 2008, Chang et al., 2018, Eady et al., 2015)
C17orf78	unknown	NA	NA	-
ASH2	Metabolism, Biosynthesis	X	X	(Kono et al., 2006, Zhu et al., 2010)
SI	Metabolism, Digestion	X	X	(Hoffman and Chang, 1993, Inoue et al., 2011, Gericke et al., 2016)
S100G	Mineral absorption, Membrane transporter	X	X	(Hulst et al., 2017, Choi and Jeung, 2008, Ishiguro et al., 2016)
CYP2C19	Metabolism	X	X	(Galetin and Houston, 2006, Hosohata et al., 2009)
MTTP	Lipid digestion and absorption	X	X	(Xie et al., 2006, Hussain et al., 2011, Liu et al., 2017)
TM4SF20	Cell growth, proliferation and activities	X	NA	(Chen et al., 2014, Denard et al., 2017)
NRN1	Neurite outgrowth	X	NA	(Gao et al., 2014, Feng et al., 2015)

¹<https://www.ncbi.nlm.nih.gov/gene>²<https://www.genome.jp/kegg/genes.html>

- BABBIN, B. A., LAUKOETTER, M. G., NAVA, P., KOCH, S., LEE, W. Y., CAPALDO, C. T., PEATMAN, E., SEVERSON, E. A., FLOWER, R. J., PERRETTI, M., PARKOS, C. A. & NUSRAT, A. 2008. Annexin A1 regulates intestinal mucosal injury, inflammation, and repair. *J Immunol*, 181, 5035-44.
- CARPENTER, A. R., BECKNELL, M. B., CHING, C. B., CUARESMA, E. J., CHEN, X., HAINS, D. S. & MCHUGH, K. M. 2016. Uroplakin 1b is critical in urinary tract development and urothelial differentiation and homeostasis. *Kidney Int*, 89, 612-24.
- CHANG, J., CHANCE, M. R., NICHOLAS, C., AHMED, N., GUILMEAU, S., FLANDEZ, M., WANG, D., BYUN, D. S., NASSER, S., ALBANESE, J. M., CORNER, G. A., HEERDT, B. G., WILSON, A. J., AUGENLICHT, L. H. & MARIADASON, J. M. 2008. Proteomic changes during intestinal cell maturation in vivo. *J Proteomics*, 71, 530-46.
- CHANG, Y. C., YANG, Y. C., TIEN, C. P., YANG, C. J. & HSIAO, M. 2018. Roles of Aldolase Family Genes in Human Cancers and Diseases. *Trends Endocrinol Metab*, 29, 549-559.
- CHEN, Q., LEE, C. E., DENARD, B. & YE, J. 2014. Sustained induction of collagen synthesis by TGF-beta requires regulated intramembrane proteolysis of CREB3L1. *PLoS One*, 9, e108528.
- CHENG, Z. Q., TAKO, E., YEUNG, A., WELCH, R. M. & GLAHN, R. P. 2012. Evaluation of metallothionein formation as a proxy for zinc absorption in an in vitro digestion/Caco-2 cell culture model. *Food & Function*, 3, 732-736.
- CHOI, K. C. & JEUNG, E. B. 2008. Molecular mechanism of regulation of the calcium-binding protein calbindin-D9k, and its physiological role(s) in mammals: a review of current research. *J Cell Mol Med*, 12, 409-20.
- CHOU, J. Y. & MANSFIELD, B. C. 2008. Mutations in the glucose-6-phosphatase-alpha (G6PC) gene that cause type Ia glycogen storage disease. *Human Mutation*, 29, 921-930.
- DENARD, B., CHEN, Q. Y., LEE, C. E., HAN, S., YE, J. & YE, J. 2017. Ceramide Induced Regulated Alternative Translocation of TM4SF20 and Beyond. *Faseb Journal*, 31.
- DOOLEY, T. P., CURTO, E. V., REDDY, S. P., DAVIS, R. L., LAMBERT, G. W., WILBORN, T. W. & ELSON, C. O. 2004. Regulation of gene expression in inflammatory bowel disease and correlation with IBD drugs: screening by DNA microarrays. *Inflamm Bowel Dis*, 10, 1-14.
- DZIEGIEL, P., PULA, B., KOBIERZYCKI, C., STASIOLEK, M. & PODHORSKA-OKOLOW, M. 2016. Metallothioneins in Normal and Cancer Cells. *Adv Anat Embryol Cell Biol*, 218, 1-117.
- EADY, J. J., WORMSTONE, Y. M., HEATON, S. J., HILHORST, B. & ELLIOTT, R. M. 2015. Differential effects of basolateral and apical iron supply on iron transport in Caco-2 cells. *Genes Nutr*, 10, 463.
- FEELEY, E. M., SIMS, J. S., JOHN, S. P., CHIN, C. R., PERTEL, T., CHEN, L. M., GAIHA, G. D., RYAN, B. J., DONIS, R. O., ELLEDGE, S. J. & BRASS, A. L. 2011. IFITM3 inhibits influenza A virus infection by preventing cytosolic entry. *PLoS Pathog*, 7, e1002337.
- FENG, Y. A., LIU, T. E. & WU, Y. 2015. microRNA-182 inhibits the proliferation and migration of glioma cells through the induction of neuritin expression. *Oncol Lett*, 10, 1197-1203.
- GABRIELLI, F. & TOFANELLI, S. 2012. Molecular and functional evolution of human DHRS2 and DHRS4 duplicated genes. *Gene*, 511, 461-9.
- GALETIN, A. & HOUSTON, J. B. 2006. Intestinal and hepatic metabolic activity of five cytochrome P450 enzymes: impact on prediction of first-pass metabolism. *J Pharmacol Exp Ther*, 318, 1220-9.
- GAO, R., WANG, L., SUN, J., NIE, K., JIAN, H., GAO, L., LIAO, X., ZHANG, H., HUANG, J. & GAN, S. 2014. MiR-204 promotes apoptosis in oxidative stress-induced rat Schwann cells by suppressing neuritin expression. *FEBS Lett*, 588, 3225-32.
- GAVINS, F. N. E. & HICKEY, M. J. 2012. Annexin A1 and the regulation of innate and adaptive immunity. *Frontiers in Immunology*, 3.
- GERICKE, B., AMIRI, M. & NAIM, H. Y. 2016. The multiple roles of sucrase-isomaltase in the intestinal physiology. *Mol Cell Pediatr*, 3, 2.
- GORMAN, M. J., PODDAR, S., FARZAN, M. & DIAMOND, M. S. 2016. The Interferon-Stimulated Gene Ifitm3 Restricts West Nile Virus Infection and Pathogenesis. *J Virol*, 90, 8212-25.
- GUO, T., CHEN, T., GU, C., LI, B. & XU, C. J. 2015. Genetic and molecular analyses reveal G6PC as a key element connecting glucose metabolism and cell cycle control in ovarian cancer. *Tumor Biology*, 36, 7649-7658.
- HALESTRAP, A. P. & MEREDITH, D. 2004. The SLC16 gene family-from monocarboxylate transporters (MCTs) to aromatic amino acid transporters and beyond. *Pflugers Arch*, 447, 619-28.
- HOFFMAN, L. R. & CHANG, E. B. 1993. Regional Expression and Regulation of Intestinal Sucrase-Isomaltase. *Journal of Nutritional Biochemistry*, 4, 130-142.
- HOSOHATA, K., MASUDA, S., KATSURA, T., TAKADA, Y., KAIDO, T., OGURA, Y., OIKE, F., EGAWA, H., UEMOTO, S. & INUI, K. 2009. Impact of intestinal CYP2C19 genotypes on the interaction between tacrolimus and omeprazole, but not lansoprazole, in adult living-donor liver transplant patients. *Drug Metab Dispos*, 37, 821-6.


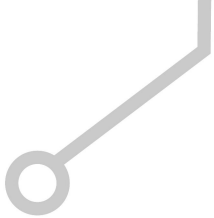
- HULST, M., JANSMAN, A., WIJERS, I., HOEKMAN, A., VASTENHOEW, S., VAN KRIMPEN, M., SMITS, M. & SCHOKKER, D. 2017. Enrichment of in vivo transcription data from dietary intervention studies with in vitro data provides improved insight into gene regulation mechanisms in the intestinal mucosa. *Genes Nutr*, 12, 11.
- HUSSAIN, M. M., NIJSTAD, N. & FRANCESCHINI, L. 2011. Regulation of microsomal triglyceride transfer protein. *Clin Lipidol*, 6, 293-303.
- INOUE, S., MOCHIZUKI, K. & GODA, T. 2011. Jejunal induction of SI and SGLT1 genes in rats by high-starch/low-fat diet is associated with histone acetylation and binding of GCN5 on the genes. *J Nutr Sci Vitaminol (Tokyo)*, 57, 162-9.
- ISHIGURO, K., WATANABE, O., NAKAMURA, M., YAMAMURA, T., ANDO, T., GOTO, H. & HIROOKA, Y. 2016. S100G expression and function in fibroblasts on colitis induction. *Int Immunopharmacol*, 39, 92-96.
- KONO, M., DREIER, J. L., ELLIS, J. M., ALLENDE, M. L., KALKOFEN, D. N., SANDERS, K. M., BIELAWSKI, J., BIELAWSKA, A., HANNUN, Y. A. & PROIA, R. L. 2006. Neutral ceramidase encoded by the Asah2 gene is essential for the intestinal degradation of sphingolipids. *J Biol Chem*, 281, 7324-31.
- KRAICZY, J., ROSS, A. D. B., FORBESTER, J. L., DOUGAN, G., VALLIER, L. & ZILBAUER, M. 2019. Genome-Wide Epigenetic and Transcriptomic Characterization of Human-Induced Pluripotent Stem Cell-Derived Intestinal Epithelial Organoids. *Cell Mol Gastroenterol Hepatol*, 7, 285-288.
- LIU, Y., CONLON, D. M., BI, X., SLOVIK, K. J., SHI, J., EDELSTEIN, H. I., MILLAR, J. S., JAVAHERI, A., CUCHEL, M., PASHOS, E. E., IQBAL, J., HUSSAIN, M. M., HEGELE, R. A., YANG, W., DUNCAN, S. A., RADER, D. J. & MORRISEY, E. E. 2017. Lack of MTP Activity in Pluripotent Stem Cell-Derived Hepatocytes and Cardiomyocytes Abolishes apoB Secretion and Increases Cell Stress. *Cell Rep*, 19, 1456-1466.
- LUO, X., LI, N., ZHAO, X., LIAO, C., YE, R., CHENG, C., XU, Z., QUAN, J., LIU, J. & CAO, Y. 2019. DHRS2 mediates cell growth inhibition induced by Trichothecin in nasopharyngeal carcinoma. *J Exp Clin Cancer Res*, 38, 300.
- MACKENZIE, P. I., HU, D. G. & GARDNER-STEPHEN, D. A. 2010. The regulation of UDP-glucuronosyltransferase genes by tissue-specific and ligand-activated transcription factors. *Drug Metab Rev*, 42, 99-109.
- NAGASAWA, Y., OKUZAKI, D., MUSO, E., YAMAMOTO, R., SHINZAWA, M., IWASAKI, Y., IWATANI, H., NAKANISHI, T., ISAKA, Y. & NOJIMA, H. 2016. IFI27 Is a Useful Genetic Marker for Diagnosis of Immunoglobulin A Nephropathy and Membranous Nephropathy Using Peripheral Blood. *Plos One*, 11.
- PAINE, M. F. & FISHER, M. B. 2000. Immunochemical identification of UGT isoforms in human small bowel and in caco-2 cell monolayers. *Biochem Biophys Res Commun*, 273, 1053-7.
- PEREZ-ESCUREDO, J., VAN HEE, V. F., SBOARINA, M., FALCES, J., PAYEN, V. L., PELLERIN, L. & SONVEAUX, P. 2016. Monocarboxylate transporters in the brain and in cancer. *Biochim Biophys Acta*, 1863, 2481-97.
- SUBRAMANIAN VIGNESH, K. & DEEPE, G. S., JR. 2017. Metallothioneins: Emerging Modulators in Immunity and Infection. *Int J Mol Sci*, 18.
- VAESSEN, S. F., VAN LIPZIG, M. M., PIETERS, R. H., KRUL, C. A., WORTELBOER, H. M. & VAN DE STEEG, E. 2017. Regional Expression Levels of Drug Transporters and Metabolizing Enzymes along the Pig and Human Intestinal Tract and Comparison with Caco-2 Cells. *Drug Metab Dispos*, 45, 353-360.
- XIE, Y., NEWBERRY, E. P., YOUNG, S. G., ROBINE, S., HAMILTON, R. L., WONG, J. S., LUO, J., KENNEDY, S. & DAVIDSON, N. O. 2006. Compensatory increase in hepatic lipogenesis in mice with conditional intestine-specific Mtp deficiency. *J Biol Chem*, 281, 4075-86.
- ZHU, D., SREEKUMAR, P. G., HINTON, D. R. & KANNAN, R. 2010. Expression and regulation of enzymes in the ceramide metabolic pathway in human retinal pigment epithelial cells and their relevance to retinal degeneration. *Vision Res*, 50, 643-51







CHAPTER 5

Comparative transcriptomes of Caco-2 cells cultured under dynamic and static conditions following exposure to titanium dioxide and zinc oxide nanomaterials



Kornphimol Kulthong, Guido J.E.J. Hooiveld, Loes Duivenvoorde, Ignacio Miro Estruch¹, Meike van der Zande and Hans Bouwmeester



In preparation



Abstract

Due to the widespread application of food-relevant inorganic nanomaterials, the gastrointestinal tract is potentially exposed to these materials. Gut-on-chip *in vitro* model systems are proposed for the investigation of compound toxicity as they better recapitulate the *in vivo* human intestinal environment than static models, due to the added shear stresses associated with the flow of medium in line with what cells experience *in vivo*. We aimed to compare the cellular responses of intestinal epithelial Caco-2 cells at the gene expression level upon TiO₂ (E171) and ZnO (NM110) nanomaterial exposure when cultured under dynamic and static conditions. For this, we applied whole genome transcriptome analyses. Differentially expressed genes and related biological processes revealed culture condition specific responses upon exposure to TiO₂ and ZnO nanomaterials. The materials had more effects on cells cultured in the gut-on-chip when compared to the static model, indicating that shear stress might be a major factor in cell susceptibility. This is the first report on application of a gut-on-chip system to evaluate cellular responses upon TiO₂ and ZnO nanomaterials compared to a static system and extends current knowledge on nanomaterial-cell interactions and toxicity assessment. Dynamically cultured cells appear to be more sensitive and the gut-on-chip might thus be an attractive model to be used more extensively in the toxicological hazard characterization.

Introduction

Various metal-oxide nanomaterials (NMs) (e.g. TiO₂, SiO₂, ZnO, MgO) have been used in the food processing industry as food additives, or incorporated in food packaging materials attempting to optimize products and increase their shelf life [1-4]. The rapid increase in production and use of engineered NMs demands a thorough investigation of their potential toxicological effects [5, 6]. As oral exposure to these food-associated NMs can be expected, it is particularly important to study the possibility of harmful effects to occur on the human gastrointestinal tract. Human intestinal epithelial cell line-based models, specifically Caco-2 cells, are frequently used to study the potential effects of NMs on the gastrointestinal epithelium [7-9].

With the emergence of microfluidic technology several organ-on-chip platforms have been launched [10, 11]. More specifically, gut-on-chip devices have been introduced that allow to culture epithelial cells under continuous perfusion resulting in a physiological shear stress [12]. This novel technology is used attempting to better recapitulate the physiological microenvironment and the functionality of the human intestine compared to static culturing methods [12, 13]. Gut-on-chip models have been used to study the cellular response and translocation of drugs and (environmental) chemicals and revealed the potential for these dynamic models as an alternative *in vitro* model to replace animal studies [14-18]. Recent studies along with data from our group indicate differences in gene expression and cellular functions between Caco-2 cells cultured under dynamic and static conditions [19-21] (unpublished Kulthong et al., 2020).

TiO₂ and ZnO NMs are the most produced NMs worldwide [22]. NMs have been extensively used in food products. TiO₂ powders are allowed to be used as food additive (E171) and have shown to contain nano-sized fractions [23]. ZnO micro-sized ZnO is considered a 'GRAS' (generally recognized as safe) substance and allowed to be used in biomedical applications by the FDA [24]. Recent studies on gene expression in epithelial intestinal cells (Caco-2 or Caco-2 co-cultured with HT29 cells) indicated that exposure to TiO₂ NMs (relevant for E171) affected expression of genes involved in oxidative stress, inflammation and DNA repair [25, 26]. Exposure to ZnO NMs affected expression of genes involved in inflammation, and metal responses [27, 28]. Thus, extensive reports are available on effects of TiO₂ and ZnO NMs on gene expression in Caco-2 cells cultured in conventional static models, but no studies so far focused on cellular responses following exposure to these (food-associated) NMs under dynamic culture conditions. For this study, we have selected both TiO₂ and ZnO NMs because of their different material properties. TiO₂ is recognized as a low soluble inorganic material, therefore possible toxicological impacts are likely mainly due to cell-particle contact [29, 30]. ZnO is a more soluble material of which the degree of dissolution depends on particle size, crystal form and the biochemical composition of the solvent the material is dispersed into [31]. Possible biological/toxicological effects are likely (partly) due to zinc ions dissolved from ZnO NMs [32].

The aim of the current comparative study was to investigate the effects of TiO₂ and ZnO NMs exposure of Caco-2 cells on gene expression when cultured under dynamic (gut-on-chip) or static (Transwell) conditions. We used industrial representative NMs. For TiO₂ we used a food grade E171 material, for ZnO we used a representative material from the EU nanomaterials repository (NM110). Briefly, Caco-2 cells were grown for 21 days in Transwells according to a standard protocol [33], and in our gut-on-chip device as previously described [15]. The cells were subsequently treated with non-toxic doses of TiO₂ and ZnO NMs. Gene expression data were obtained using a microarray platform and differential gene expression was determined by a bioinformatics approach. Linear models and intensity-based moderated t-statistics were used for identification of differentially expressed genes and gene set enrichment analysis (GSEA) was applied for identification of affected biological pathways.

Materials and Methods

Chemicals and reagents

Bovine serum albumin (BSA), Dulbecco's Modified Eagle Medium (DMEM), penicillin-streptomycin, Hank's balanced salt solution (HBSS) were obtained from Sigma-Aldrich (Zwijndrecht, The Netherlands). Phosphate Buffered Saline (PBS), heat inactivated fetal bovine serum (FBS) and MEM-non-essential amino acids were purchased from Fisher Scientific (Landsmeer, The Netherlands). TiO₂ NM E171 was provided by the commercial supplier and was characterized and used in earlier studies [34, 35]. NM110 was obtained from the Joined Research Centre (JRC nanomaterials repository, ISPRA, Italy).

Cell culture

A Caco-2 cell line (HTB-37), derived from a human colorectal adenocarcinoma, was obtained from the American Type Culture Collection (ATCC, Manassas, VA, USA). The cells were grown (at passage number 29-45) in complete culture medium, consisting of DMEM supplemented with 10 % FBS, 1 % penicillin-streptomycin, and 1 % MEM non-essential amino acids, further referred to as DMEM⁺. For the Transwell experiments, the cells were seeded at a density of 75,000 cells per cm² on 12-well Transwell polyester inserts (0.4 µm pore size, 1.12 cm² surface area (Corning Amsterdam, The Netherlands) and cultured in DMEM⁺ for 21 days. The medium was changed every two to three days. For the microfluidic chips, the cells were seeded at a density of 75,000 cell per cm² and were allowed for 24h to attach to the membrane on the middle layer of the chip. After attachment the membrane middle layer of the chip was inserted in the microfluidic chip, and the cells were exposed to a continuous flow of 100 µL/h DMEM⁺ until day 21 of culturing. By doing so, the shear stress in the AP compartment was ~0.002 dyne/cm² at the membrane surface, where the cells are grown. The DMEM⁺ medium contained sodium bicarbonate (10 mM) to optimize the pH buffering capacity.

Design of the gut-on-chip system

The microfluidic gut-on-chip device has been developed and described previously [15]. In brief, the chip consists of three 15x45 mm (width x length) re-sealable glass slides that result in two flow chambers (i.e. an upper apical (AP) and lower basolateral (BL) chamber) upon assembly (Micronit, Enschede, The Netherlands). Both the upper and lower glass slides were spaced from the middle layer membrane by a 0.25 mm thick silicone gasket. The flow chambers were separated by a glass slide containing a polyester (PET) porous cell culture membrane with a 0.4 µm pore size and a cell culture area of ~1.6 cm². The volume of the AP chamber is 75 mm³ with a chamber height of 0.25 mm (membrane to top layer) and the BL chamber is 110 mm³ with a chamber height of 0.65 mm (bottom layer to membrane), resulting in a total volume of 185 mm³ (µL) of the device. The chip was placed in a chip holder with a quick locking mechanism, constructed for connection of external capillaries to the chip via specific ferrules to ensure tight connections and a leak-free system.

Constant flow was introduced to the chip using a microsyringe pump (NE-4000, New Era Pump Systems, Inc.) equipped with two polypropylene syringes (30 mL, Luer-locktm, Becton, Dickinson and company), with each syringe connected to either the AP or the BL compartment using Fluorinated Ethylene Propylene (FEP) tubing (0.50 mm inner diameter, with a length of 25 cm and 15 cm for the inlet and outlet, respectively). Before the start of each experiment, all tubing and chips were sterilized using an autoclave and rinsed with 70% ethanol. Tubing and chips were prefilled with medium to eliminate air bubbles in the system. The entire system was put in an incubator at 37°C to maintain cell culture conditions.

Size distribution and sample preparation of NMs

NMs were prepared and dispersed according to the Nanogenotox dispersion protocol [36]. Briefly, an accurately weighed sample of 15.4 mg of finely powdered TiO₂ and ZnO was added to 30 µL of 96% ethanol to pre-wet the NMs followed by addition of 570 µL 0.5 mg/mL BSA solution (final NM concentration 2.6 mg/mL). The mixture was shaken and put on ice. The suspension was then sonicated using a 400W probe sonicator set at 10% amplitude for 16 min (Branson Ultrasonics Sonifier™ S-450). After that, the stock solution was diluted in DMEM⁺ to the concentration used for size measurement (100 and 10 µg/mL for TiO₂ and ZnO, respectively). The hydrodynamic diameter of the NMs was determined using a homebuild dynamic light scattering (DLS) setup with a fixed 90 degrees detection angle. The instrument consists of an ALV/SO SIPD Single Photon Detector with ALV Static and Dynamic Enhancer Fiber optics, an ALV7002-USB correlator and a Cobolt Samba-300 DPSS laser with a wavelength of 532 nm. Samples (n=3) were analyzed with each measurement consisting of 10 technical replicate measurements of 30s each. The results are expressed as the average hydrodynamic diameter (nm) ± standard deviation (SD) that was calculated using AfterALVVR (Dullware, USA).

In vitro sedimentation, diffusion and dosimetry (ISDD) modelling of NMs.

The deposited fraction of the exposure doses of the particles was calculated using the In vitro Sedimentation, Diffusion and Dosimetry (ISDD) model downloaded from Pacific Northwest National Laboratory website [37]. The following parameters were used as input in the ISDD model: the hydrodynamic diameters of the NMs in DMEM⁺ measured by DLS (Table 1), medium column height (44.6 and 0.25 mm, respectively), temperature (310°K), media density 1 g/ml and media viscosity 0.0009 N s/m² [38].

Viability assay

Cytotoxicity of NMs was assessed using a WST-1 assay, a mitochondrial activity-based cell viability assay. Caco-2 cells (50,000 cells/cm²) were seeded in 96-well plates. After 24h, the medium was discarded and was subsequently replaced with various concentrations of TiO₂ (0, 10, 25, 50, 100 or 150 µg/mL) and ZnO (0, 0.4, 2, 10, 50 or 100 µg/mL) NMs dispersed according to the protocol mentioned above and diluted in cell culture medium for 24h. At the end of the treatment period, cells were added with 10 µL WST-1 solution and further incubated for 1 h. The plate was centrifuged at 200g for 10 min, and the 70 µL supernatant were collected. The absorbance of supernatant was measured at 440 and 630 nm using a microplate reader (Synergy HT, BioTek, VT) and the background absorbance of NMs was subtracted. The percentage of cell viability was calculated using the absorbance of the treatment group divided by the absorbance of the negative control (cells without NMs).

NM exposure to Caco-2 cells

At day 21 post-seeding Caco-2 cells in either the gut-on-chip or Transwell were exposed to equal deposited doses based on the ISDD modelling. For the gut-on-chip, NM suspensions of 100 µg/mL TiO₂ (n=4) and 80 µg/mL ZnO (n=4) were prepared in DMEM⁺ (a dispersion solution in DMEM⁺ for each control group (n=4)) and perfused via the upper channel with a flow rate of 100 µL/h. DMEM⁺ without NMs was pumped through the basolateral channel with an equal flow rate. After about 42 min the upper chamber was fully filled with the NM solution and the flow was stopped for 6 h in order to exclude the possible influence of laminar flow in gut-on-chip system resulting in the different exposure doses as reported in our previous study [15]. This will enable the best comparison of the cellular response by cells grown in the two systems.

In the Transwells, the cell culture medium of the AP side was replaced with 500 µL NM suspension of 50 or 10 µg/mL for TiO₂ (n=4) or ZnO (n=4) and the medium of the basolateral side was refreshed with DMEM⁺ without NMs culture medium followed by 6 h incubation.

RNA isolation

Caco-2 cells were treated with NMs in the gut-on-chip or Transwell for 6 h. After the 6 h incubation the apical chamber of the chip was perfused with 100 µL DMEM⁺ to wash the cells. After that, 100 µL RLT lysis buffer was perfused through the chip and incubated for 2

min followed by another 100 µL RLT lysis buffer. The entire RLT solution was collected as cell lysate and total RNA was extracted using the Qiagen RNAeasy Micro kit according to the manufacturer's instructions. The RNA amount was determined using a Nanodrop (ND-1000 ThermoScientific Wilmington, Delaware, USA).

To the cells cultured on Transwell membranes 350 µL of RLT lysis buffer were added after washing the cells with DMEM⁺, cell lysates were then collected and analyzed using the same procedure.

Affymetrix microarray processing, and analysis

The isolated RNA was subjected to genome-wide expression profiling. In brief, total RNA was labelled using the Whole-Transcript Sense Target Assay (Affymetrix, Santa Clara, CA, USA) and hybridized on Human Gene 2.1 ST arrays (Affymetrix). The quality control and data analysis pipeline has been described in detail previously [39]. Normalized expression estimates of probe sets were computed by the robust multiarray analysis (RMA) algorithm [40, 41] as implemented in the Bioconductor library affyPLM. Probe sets were redefined using current genome definitions available from the NCBI database, which resulted in the profiling of 29,597 unique genes (custom CDF version 23) [42]. Differentially expressed probe sets (genes) were identified by using linear models (library limma) and an intensity-based moderated t-statistic [43, 44]. Probe sets that satisfied the criterion of $p < 0.01$ were considered to be significantly regulated. Microarray data have been submitted to the Gene Expression Omnibus (accession number pending). All groups were $n=4$, only one outlier in the TiO₂ NM treatment group in the Transwell was excluded based on multi-dimensional scaling plot resulting in $n=3$ for this group.

Biological interpretation of array data

Changes in gene expression were related to biologically meaningful changes using gene set enrichment analysis (GSEA). It is well accepted that GSEA has multiple advantages over analyses performed on the level of individual genes [45-47]. GSEA evaluates gene expression on the level of gene sets that are based on prior biological knowledge, GSEA is unbiased, because no gene selection step (fold change and/or p-value cutoff) is used; a GSEA score is computed based on all genes in the gene set, which boosts the S/N ratio and allows to detect affected biological processes that are due to only subtle changes in expression of individual genes. Gene sets were retrieved from the expert-curated KEGG database [48] (BRITE Functional Hierarchy level 1). Moreover, only gene sets comprising more than 15 and fewer than 500 genes were taken into account. For each comparison, genes were ranked on their t-value that was calculated by the moderated t-test. Statistical significance of GSEA results was determined using 1000 permutations.

Results

Physicochemical characterization of the NMs

Both TiO₂ and ZnO NMs were obtained in a powdered form, and were dispersed according to the Nanogenotox protocol [36]. The resulting suspension was subjected to DLS analysis to determine the hydrodynamic size of the nanomaterials. The average hydrodynamic sizes of the materials after 1 hour of incubation in DMEM⁺ are given in Table 1. The polydispersity index (PDI), indicating whether the size distribution of the particles in the suspension is homo- or heterogenous, of both suspensions was <0.7 showing a homogenous size distribution [49]. The hydrodynamic sizes of the materials in DMEM⁺ were stable during 24h (data not shown), which is the longest exposure time used in the experiments.

Table 1. Physicochemical characteristics of the selected NMs

Material code	Core material	Product type	Crystal structure	Primary size (nm)	Hydrodynamic diameter (nm) \pm SD of NMs in DMEM ⁺	PDI \pm SD
E171	TiO ₂	Powder	Rutile/anatase	60-300 ^a	262 \pm 21	0.27 \pm 0.11
NM110	ZnO	Powder	Zincite	158 ^b	229 \pm 13	0.17 \pm 0.04

^a[34], ^b[50]

Selection of non-cytotoxic concentrations of NMs

Cytotoxicity experiments, using a WST-1 assay, were performed to select non-toxic concentrations of NMs to be applied in the subsequent gene expression study. Proliferating (1 day old) cells that are generally considered more vulnerable to toxicity or uptake of nanoparticles than differentiated 21 day old Caco-2 cells [51, 52] were exposed to concentrations up to 150 and 100 μ g/mL TiO₂ and ZnO NMs, respectively, for 24h. As shown in Fig. 1, no cytotoxicity (>80% viability) was observed for TiO₂ NMs for any of the tested concentrations, whereas cytotoxic effects of ZnO NMs were observed at concentrations of 50 μ g/mL and higher. As the design of the 96-well plates, the gut-on-chips and Transwells are different, the exposure is also given as the deposited mass of the NMs.

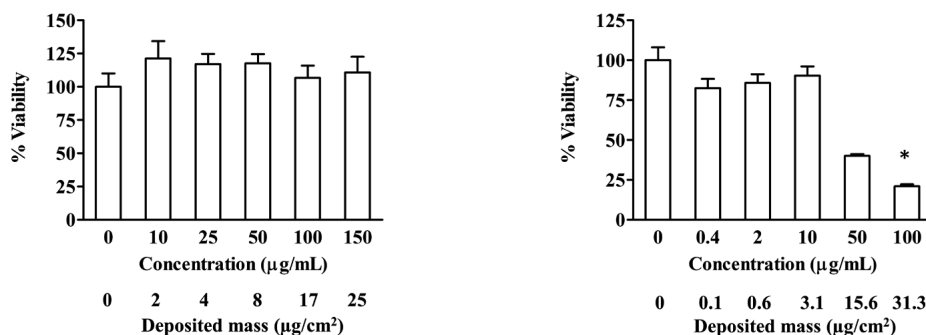


Figure 1. Cell viability of 1-day old Caco-2 cells exposed for 24h to increasing concentrations (also given as deposited mass) of A) TiO₂, or B) ZnO NM, given as a percentage (\pm SEM) of the negative control ($n=3$); * indicates significance difference compared with the negative control group (one-way ANOVA, Dunnett, $p<0.05$)

Prediction of particle sedimentation using the ISDD model

In our experiments we have used three different culturing devices for cell culture (i.e. 96 well plates for the cell viability experiments and Transwells and gut-on-chips for the gene expression experiments). The three different culturing devices have different dimensions (i.e. the height and width of the cell culture compartment). To be able to compare the gene expression profiles, we exposed the cells in the Transwells and gut-on-chips to equal NM deposition mass doses. To achieve this, nominal exposure concentrations were calculated of TiO₂ and ZnO NMs for each culture device using the In vitro Sedimentation, Diffusion and Dosimetry (ISDD) model [37, 46]. To achieve equal deposited NM doses a higher nominal NM concentration was needed for the chip (i.e. 2-fold higher for TiO₂ and 8-fold higher for ZnO NM) compared to the nominal NM concentration in the Transwell. The final selected deposited mass doses of ~ 2.5 and ~ 2.0 $\mu\text{g}/\text{cm}^2$ TiO₂ and ZnO NM, respectively, were lower than the non-toxic doses observed in 96-well plate to accommodate a potential higher sensitivity of cells cultured under shear stress. In addition, for TiO₂, the ~ 2.5 $\mu\text{g}/\text{cm}^2$ TiO₂ NM dose (corresponding to a nominal NM concentration of ~ 10 $\mu\text{g}/\text{mL}$ in the cell viability assay) is a rather low dose when considering the cell viability results, due to the maximum concentration limit to maintain suspension stability. The resulting deposited mass is shown in Table 2.

Table 2. Deposited mass doses and nominal concentrations of NMs in each exposure model

Material	Simulated deposited mass dose ($\mu\text{g}/\text{cm}^2$ *)		
	96 well plate	Transwell	Gut-on-chip
TiO ₂	up to ~25	~2.5	~2.4
ZnO	up to ~3.1	~1.9	~2.1

*Based on ISDD modelling

Gene expression in Caco-2 cells exposed to NMs cultured under dynamic and static conditions

NM induced differentially expressed genes were identified in each cell culture model by comparison of the NM exposure groups (i.e. TiO₂ and ZnO) to their respective control groups. In total, the gene expression of 29,597 genes was evaluated. The total number of differentially expressed genes ($p<0.01$) after NM exposure was higher in the gut-on-chip devices than in the Transwells for both the TiO₂ and ZnO NMs (Fig. 2 and suppl. Table 1 and 2). There were three differentially expressed genes extremely upregulated (>10 -fold) in cells cultured in the gut-on-chip after exposure to ZnO NM.

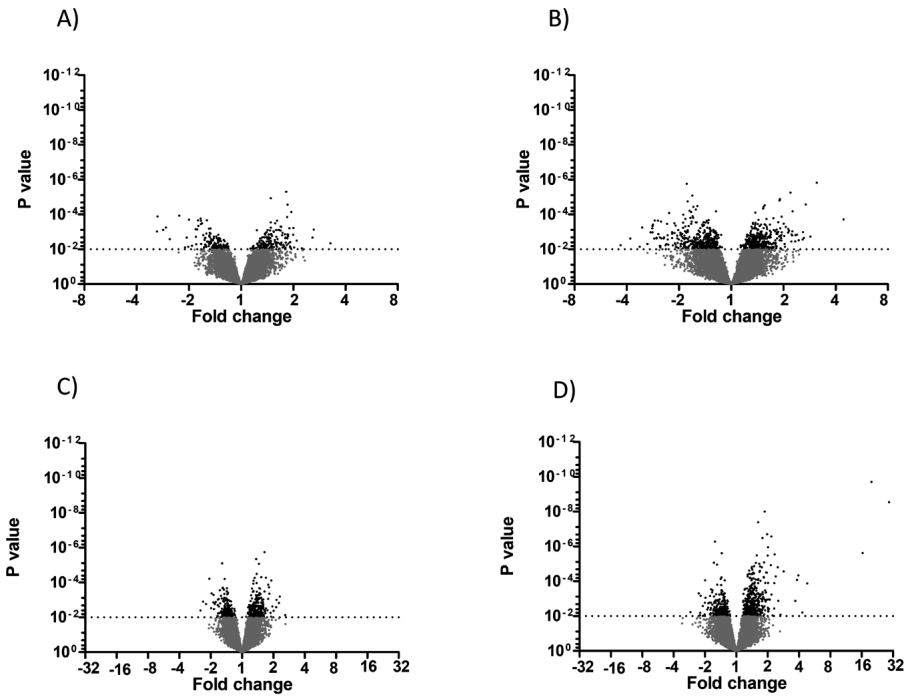


Figure 2. Differential expression of genes in 21-day old Caco-2 cells grown in a gut-on-chip and in a Transwell exposed to NMs for 6 h. A Volcano plot showing the *t*-test statistics (*p* value) plotted against the fold change of genes in response to TiO₂ NM exposure in cells cultured in A) Transwells B) gut-on-chips and ZnO exposure in cells cultured in C) Transwells D) gut-on-chips; the dotted line indicates a *p*-value of 0.01.

Using the FDR, no differentially expressed genes were observed for cells cultured in Transwells exposed to both TiO₂ and ZnO materials, therefore, the criteria for DEG used for further analysis is $p < 0.01$ and $\text{Log}_2 \text{FC} \geq 1.2$ (suppl. Table 3). After TiO₂ NM exposure, a low number of 8 (for cells grown in Transwell) and 41 (for cells grown in the gut-on-chip) differentially expressed genes ($p < 0.01$; $\text{FC} \geq 1.2$) was identified (Fig. 3). There was no overlap of differentially expressed genes between the two models induced by the NM exposure (Fig. 3A; suppl. Table 1). Of the 8 differentially expressed genes in the Transwell after TiO₂ NM exposure, 7 genes had no known biological related function and 1 gene (which was downregulated) was involved in DNA binding processes. Among the 41 differentially expressed genes in the gut-on-chip after exposure to TiO₂ NM, 9 genes had a known biological related function (3 upregulated genes and 6 downregulated genes). The biological functions of the upregulated genes (i.e. *SLC10A5*, *SLC38A4*, *KRT34*) were related to sodium/bile acid transport and cellular structure. While the downregulated genes (i.e. *EBLN2*, *MT1G*, *TAS2R20*, *EID3*) were associated with RNA-binding, metal binding, DNA-repair and taste receptor. The other 32 genes were coding for siRNA, small nucleolus, non-coding RNA or genes without known functions (suppl. Table 4).

Exposure of the Caco-2 cells to ZnO NMs resulted in 5 (in the Transwell) and 21 (in the gut-on-chip) differentially expressed genes ($p < 0.01$; $\text{FC} \geq 1.2$). Like for the TiO₂ NM exposure, there was no overlap in differentially expressed genes between the different culture conditions after ZnO NM exposure (Fig. 3B; suppl. Table 2). All of the differentially expressed genes in the Transwell had an unknown biological related function (e.g. microRNA, uncharacterized genes), whereas in the gut-on-chip 13 (all upregulated) out of 21 differentially expressed genes had a known biological related function. Six upregulated genes (i.e. *MT1B*, *MT1A*, *MT1M*, *MT1E*, *MT1G*, *MT1H*) are coding for metallothionines. The other 7 upregulated genes, namely; *HSPA6*, *SLC30A2*, *OR11H6*, *EGR2*, *GADD45B*, *RGS16* and *USP17L5*, code for genes involved in stress responses, zinc transposers, sensory transduction, transcription regulation, DNA-damage responses, signal transduction and protein metabolism, respectively. The 8 genes that had no biological relevant function were mostly downregulated (suppl. Table 5).

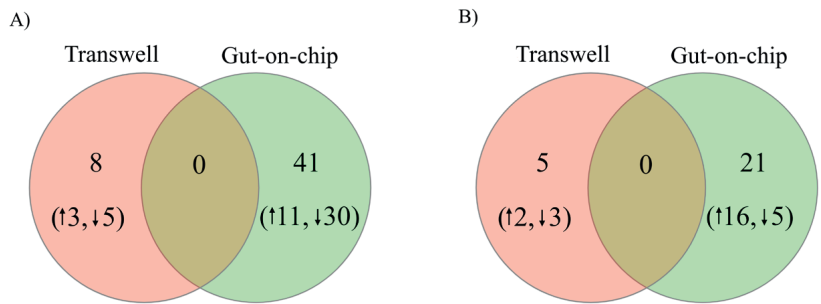


Figure 3. Venn diagrams showing the differentially expressed genes ($p < 0.01$ and $FC > 1.2$) in Caco-2 cells cultured in the gut-on-chip and Transwell after exposure to A) TiO_2 and B) ZnO NMs for 6 h; \uparrow and \downarrow represents up- and downregulation, respectively.

Gene set enrichment analysis on gene expression data in Caco-2 cells exposed to NMs under dynamic and static culture conditions

GSEA was performed to elucidate the response of Caco-2 cells to NM exposure when cultured under dynamic conditions compared to cells cultured under static conditions. The studied pathways were derived from the KEGG database. This database is structured into KEGG categories that are subdivided into category subgroups and each category subgroup contains various pathways, each represented by a gene set. The 7 KEGG categories are: ‘metabolism’, ‘genetic information processing’, ‘environmental information processing’, ‘cellular processes’ and ‘organismal systems’, ‘human disease’ and ‘drug development’ (BRITE Functional Hierarchy level 1).

The overview of enriched pathways in the cells cultured in Transwell and gut-on-chip after exposure to TiO_2 NMs is presented in Fig. 4. The total number of gene sets based on the KEGG database that were analyzed was 312. Of these 312 gene sets 5 and 38 pathways were downregulated in the cells grown in Transwell and gut-on-chip, respectively ($p < 0.05$ and $FDR < 0.25$). There were no significantly upregulated pathways in Caco-2 cells exposed to TiO_2 NM under both culture conditions when compared to their unexposed controls. In addition, none of the affected downregulated pathways overlapped between the two culture models (Fig. 4A).

Following TiO_2 NM exposure of the cells grown in the Transwell, the most prominently downregulated pathway of the 5 pathways represented the ‘allograft rejection’ pathway (normalized enrichment score, $NES = -1.800$) which falls under the KEGG category ‘human disease’ and the KEGG category subgroup ‘immune disease’. In the gut-on-chip 38 pathways were downregulated of which the most prominently downregulated pathway was the ‘homologous recombination’ pathway ($NES = -2.050$), which falls under the KEGG category ‘genetic information processing’ and the KEGG category subgroup ‘replication and repair’ ($p < 0.05$ and $FDR < 0.25$) (suppl. Table 6 and 7). The distribution of the downregulated pathways of each treatment condition over the KEGG categories is presented in Fig. 4B and C. Pathways under the KEGG categories ‘human disease’ and ‘metabolism’ were most

affected in the Transwell and gut-on-chip culturing conditions, respectively. The top 5 most downregulated pathways, selected based on association with epithelial cell functions in both culture models exposed to TiO₂ NM are presented in Table 4.

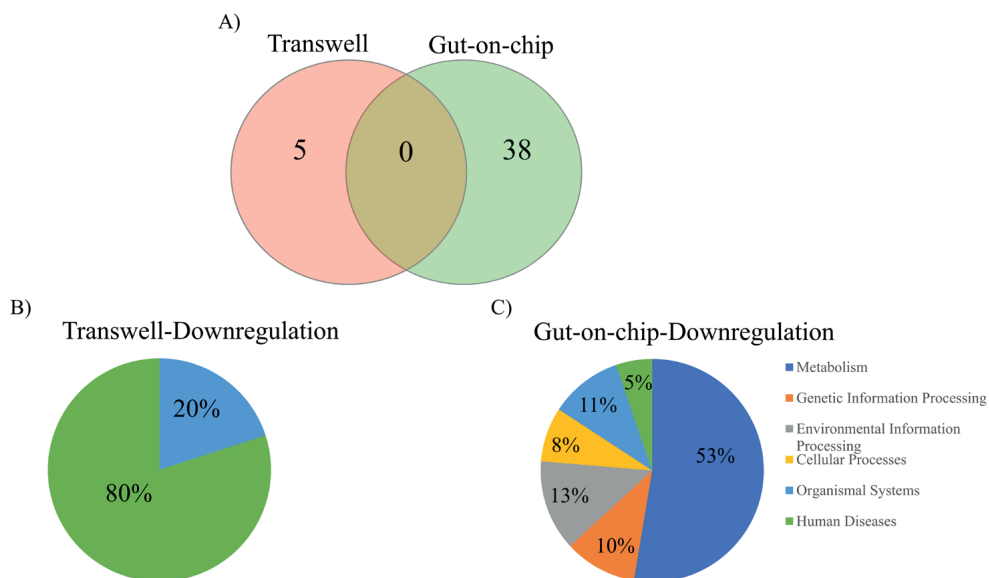


Figure 4. Overview of downregulated pathways in Caco-2 cells cultured in the Transwell and gut-on-chip devices after exposure to TiO₂ NMs. A) Venn diagram showing downregulated pathways under each culture condition. Pie chart showing the distribution (in percentage) of the downregulated pathways over the KEGG categories in B) the Transwell and C) the gut-on-chip.

Upon ZnO NM exposure, 51 pathways were affected in the Transwell (36 up- and 15 downregulated) and 123 pathways were affected in the gut-on-chip (89 up- and 34 downregulated) (suppl. Table 8 – 11) (Fig. 5A and B). The most affected upregulated pathways in the Transwell and gut-on-chip were included in the ‘human diseases’ KEGG category and the most affected downregulated pathways in the ‘metabolism’ KEGG category (Fig. 5C, D, E, and F).

In cells grown in Transwells, the most prominently upregulated pathway represented the ‘mRNA surveillance pathway’ (NES = 2.062) under the KEGG category ‘genetic information processing’ and KEGG category subgroup ‘translation’. The most prominently downregulated gene set was associated with ‘fructose and mannose metabolism’ under the KEGG category ‘metabolism’ and KEGG category subgroup ‘carbohydrate metabolism’ (NES = -1.965). In the cells grown in the gut-on-chip, the most prominently upregulated gene set was associated with ‘mineral absorption’ (NES = 2.439) under the KEGG category ‘digestive system’ and KEGG category subgroup ‘organismal systems’. The most prominently downregulated pathway was the ‘pyruvate metabolism’ under the ‘carbohydrate metabolism’ KEGG category and KEGG category subgroup ‘metabolism’ with a NES of -

2.327. The top 5 of most up- and downregulated gens sets, selected based on association with epithelial cell functions, in both culture models exposed to ZnO NM are presented in Table 5.

The exposure of Caco-2 cells to ZnO NM resulted in 28 enriched pathways that were shared between both culture conditions. Of these pathways 19 were up- and 6 were downregulated, in the same manner ($p<0.05$ and $FDR<0.25$) (Fig. 5A and B; suppl. Table 12). Among the upregulated pathways were pathways associated with epithelial cell function (e.g. ‘autophagy’, ‘colorectal cancer’, ‘TNF signaling pathway’) (Table 6). The downregulated pathways associated with epithelial cell function included ‘propanoate metabolism’, ‘oxidative phosphorylation’, ‘fat digestion and absorption’. Three other pathways were shared between both culture conditions while the responses were the opposite. The enriched pathways ‘cell cycle’, ‘RNA degradation’ and ‘lysine degradation’ were upregulated in Caco-2 cells grown in the Transwell but downregulated in the gut-on-chip (suppl. Table 12).

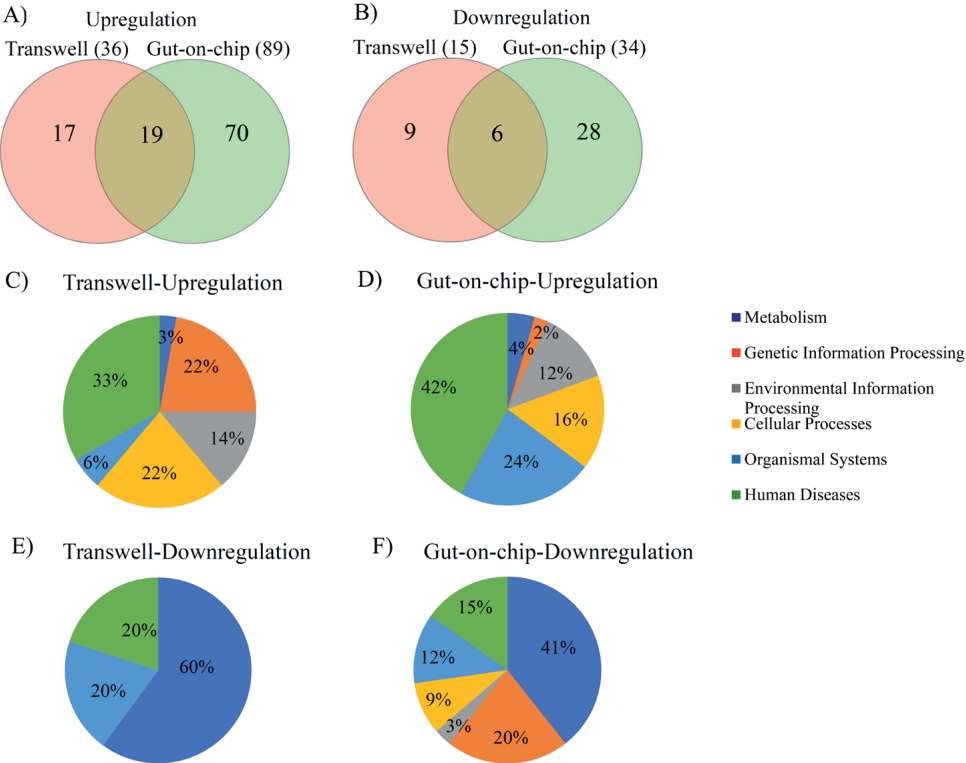


Figure 5. Overview of up- and downregulated pathways in Caco-2 cells cultured in the Transwell and gut-on-chip after exposure to ZnO NMs. A) Venn diagrams showing the A) upregulated and B) downregulated pathways. C-F) Pie charts showing the distribution (in percentage) of the affected pathways over the KEGG categories. Upregulated pathways in C) the Transwell and in D) the gut-on-chip and downregulated pathways in E) the Transwell and in F) the gut-on-chip.

Table 4. Top 5 most enriched gene sets representing pathways associated with epithelial cell function upon TiO₂ NM exposure to Caco-2 cells cultured under dynamic and conditions static conditions

KEGG pathway name	KEGG category	KEGG category subgroup	Size	NES	p-value	FDR
<i><u>Downregulated pathways in Transwell*</u></i>						
Intestinal immune network for IgA production	Organismal systems	Immune system	44	-1.691	0.006	0.112
<i><u>Downregulated pathways in gut-on-chip</u></i>						
Homologous recombination	Genetic information processing	Replication and repair	41	-2.050	0.000	0.008
Carbon metabolism	Metabolism	Global and overview maps	114	-2.040	0.000	0.004
Pyruvate metabolism	Metabolism	Carbohydrate metabolism	39	-1.965	0.000	0.009
Propanoate metabolism	Metabolism	Carbohydrate metabolism	33	-1.894	0.000	0.017
DNA replication	Genetic information processing	Replication and repair	36	-1.880	0.001	0.017

*Only one pathway is applicable in epithelial cells

Table 5. Top 5 most enriched gene sets representing pathways associated with epithelial cell function upon ZnO NM exposure to Caco-2 cells cultured under dynamic and conditions static conditions.

KEGG pathway name	KEGG category	KEGG category subgroup	Size	NES	p-value	FDR
<i><u>Upregulated pathways in Transwell</u></i>						
mRNA surveillance pathway	Genetic information processing	Translation	87	2.062	0.000	0.009
Ribosome biogenesis in eukaryotes	Genetic information processing	Translation	76	2.059	0.000	0.005
RNA transport	Genetic information processing	Translation	146	1.943	0.000	0.013
Mineral absorption	Organismal systems	Digestive system	49	1.862	0.000	0.028
Spliceosome	Genetic information processing	Transcription	128	1.807	0.000	0.040
<i><u>Upregulated pathways in gut-on-chip</u></i>						
Mineral absorption	Organismal systems	Digestive system	49	2.438	0.000	0.000
Protein processing in endoplasmic reticulum	Genetic information processing	Folding, sorting and degradation	160	2.375	0.000	0.000
Apoptosis	Cellular processes	Cell growth and death	133	2.077	0.000	0.001
SNARE interactions in vesicular transport	Genetic information processing	Folding, sorting and degradation	33	2.059	0.000	0.001
Apoptosis-multiple species	Cellular processes	Cell growth and death	31	2.035	0.000	0.001

Table 5. Top 5 most enriched gene sets representing pathways associated with epithelial cell function upon ZnO NM exposure to Caco-2 cells cultured under dynamic and conditions static conditions (continued).

KEGG pathway name	KEGG category	KEGG category subgroup	Size	NES	p-value	FDR
<u>Downregulated pathways- Transwell</u>						
Fructose and mannose metabolism	Metabolism	Carbohydrate metabolism	32	-1.965	0.000	0.021
Folate biosynthesis	Metabolism	Metabolism of cofactors and vitamins	26	-1.700	0.008	0.085
Galactose metabolism	Metabolism	Carbohydrate metabolism	31	-1.628	0.014	0.137
Staphylococcus aureus infection	Human diseases	Infectious disease: bacterial	57	-1.604	0.009	0.127
Citrate cycle (TCA cycle)	Metabolism	Carbohydrate metabolism	29	-1.522	0.032	0.157
<u>Downregulated pathways-in gut-on-chip</u>						
Pyruvate metabolism	Metabolism	Carbohydrate metabolism	39	-2.327	0.000	0.000
DNA replication	Genetic information processing	Replication and repair	36	-2.149	0.000	0.001
Mismatch repair	Genetic information processing	Replication and repair	23	-2.084	0.000	0.001
Ribosome	Genetic information processing	Translation	113	-2.016	0.000	0.002
Homologous recombination	Genetic information processing	Replication and repair	41	-2.001	0.001	0.002

Table 6. Overlapping enriched gene sets representing pathways associated with epithelial cell function upon ZnO NM exposure between to Caco-2 cells cultured under dynamic and conditions static conditi

KEGG pathway name	KEGG category	KEGG category subgroup	Size	NES*	p-value	FDR
<u>Overlapping upregulated pathways</u>						
Mineral absorption	Organismal systems	Digestive system	49	1.862/2.439	0.000/0.000	0.028/0.000
Autophagy-other	Cellular processes	Transport and catabolism	31	1.639/1.532	0.014/0.028	0.117/0.068
Viral carcinogenesis	Human diseases	Cancer: overview	162	1.634/1.592	0.000/0.000	0.146/0.000
Protein processing in endoplasmic reticulum	Genetic information processing	Folding, sorting and degradation	160	1.563/2.375	0.000/0.000	0.146/0.000
Colorectal cancer	Human diseases	Cancer: specific types	86	1.562/1.495	0.006/0.013	0.136/0.078
Hippo signaling pathway-multiple species	Environmental information processing	Signal transduction	28	1.519/1.681	0.035/0.009	0.141/0.031
Ferroptosis	Cellular processes	Cell growth and death	39	1.496/1.663	0.029/0.008	0.148/0.035
Pathogenic Escherichia coli infection	Human diseases	Infectious disease: bacterial	53	1.486/1.405	0.027/0.048	0.154/0.111
Mitophagy-animal	Cellular processes	Transport and catabolism	64	1.462/2.138	0.029/0.000	0.178/0.001
Autophagy-animal	Cellular processes	Transport and catabolism	127	1.457/1.811	0.008/0.000	0.177/0.014
Epithelial cell signaling in helicobacter pylori infection	Human diseases	Infectious disease: bacterial	70	1.456/1.696	0.023/0.002	0.173/0.030
TNF signaling pathway	Environmental information processing	Signal transduction	110	1.405/1.703	0.024/0.001	0.209/0.031
FoxO signaling pathway	Environmental information processing	Signal transduction	129	1.402/1.507	0.018/0.005	0.200/0.072
<u>Overlapping downregulated pathways</u>						
Propanoate metabolism	Metabolism	Carbohydrate metabolism	33	-1.736/-1.952	0.004/0.000	0.152/0.004
Glycolysis/gluconeogenesis	Metabolism	Carbohydrate metabolism	68	-1.708/-1.691	0.002/0.002	0.132/0.027
Valine, leucine and isoleucine degradation	Metabolism	Amino acid metabolism	47	-1.568/-1.915	0.013/0.000	0.155/0.005
Oxidative phosphorylation	Metabolism	Energy metabolism	116	-1.543/-1.684	0.004/0.000	0.172/0.027
Carbon metabolism	Metabolism	Global and overview maps	114	-1.531/-1.570	0.004/0.003	0.173/0.054
Fat digestion and absorption	Organismal systems	Digestive system	41	-1.461/-1.445	0.037/0.040	0.223/0.114

*Transwell/gut-on-chip

Discussion

The aim of this study was to assess the changes in gene expression and associated biological pathways in Caco-2 intestinal epithelial cells cultured dynamically in a gut-on-chip or statically in a Transwell following exposure to TiO₂ (E171) and ZnO (NM110) NMs. *In vivo*

intestinal cells are continuously exposed to shear stress, which has been shown to affect gene expression (unpublished Kulthong 2020) [21], function and morphology [53, 54] of Caco-2 cells *in vitro*. Here we show that, at the level of gene expression, cells cultured in the gut-on-chip respond stronger to exposure to TiO₂ and ZnO NMs compared with cells cultured in a Transwell. These stronger responses were seen both at the individual gene level and in terms of affected pathways. The different responses of cells cultured under dynamic and static condition to compounds or toxicants have been also reported previously in other cell types, endothelial and proximal tubular epithelial cells [55, 56].

We exposed Caco-2 cells to two types of NMs with different physicochemical properties. TiO₂ NMs are generally regarded as stable in suspension and do not dissociate ions in cell culture medium [29, 30]. ZnO NMs are known to dissolve readily under physiological conditions, the dissolution is influenced by the size and surface properties of the NM and by the biochemical conditions of the dispersion solvent [31, 50]. The effects observed following exposure to the ZnO NM (NM110) used in this study can thus likely be attributed to a combination of the ZnO particulate material and Zn ions, whereas the TiO₂ NM (E171) exposure can likely only be attributed to a particulate effect. Therefore, it is not surprising that at the individual gene level, the majority of the exposure induced differentially expressed genes were different upon exposure to TiO₂ or ZnO NMs.

Exposure of Caco-2 cells to TiO₂ NM under both culturing conditions only induced a very limited number of significantly differentially expressed individual genes (all downregulated). Interestingly, significantly downregulated genes were the DNA-binding gene (*ZNF117*) in the cells grown in Transwell and the DNA-repair (*EID3*) gene in the cells grown in gut-on-chip. Both genes are involved in DNA-damage/genotoxicity pathways [57, 58] and have previously been reported to be affected in Caco-2 cells exposed to E171 (TiO₂ NM) [26, 59]. At the pathway level, 5 and 38 gene sets (in the Transwell and gut-on-chip, respectively) were significantly downregulated. The affected pathways were different for the two culturing conditions. For Caco-2 cells grown in Transwells, the pathway associated with the immune response ‘intestinal immune network for IgA production’ was most prominently downregulated. Pathways that were affected in Caco-2 cells grown in the gut-on-chip were associated with DNA damage. The pathway, ‘homologous recombination’ was the most prominently downregulated pathway. These results corroborate previous observations of effects of different types of TiO₂ NMs (including E171) on gene expression in epithelial cells that showed involvement of pathways related to oxidative stress, DNA repair and immune system impairment [25, 26, 59, 60].

Exposure to ZnO NM induced much stronger responses in Caco-2 cells cultured in the gut-on-chip compared to cells grown in the Transwell model at the individual gene expression level. Twenty-one individual genes were differentially regulated in Caco-2 cells grown in the gut-on-chip. Of the 16 upregulated genes, the highest upregulated genes were metallothionein genes (i.e. MT1B, MT1M, MT1H). High upregulation of metallothionein genes is a common response after exposure to metal NMs and especially metallic ions [61, 62], but metallothionein genes have also been shown to be induced by shear stress, as observed in our previous study (unpublished Kulthong et al., 2020). In cells grown in Transwells only 5 genes were differentially expressed, all without a relation to a known biological function. Also, on a pathway level, stronger responses were observed to ZnO NM exposure in cells cultured in the gut-on-chip than in the Transwell. In the cells grown in gut-on-chip a total of 123 pathways was enriched, while in the static system 51 pathways were enriched. 70 pathways were specifically upregulated in cells grown in gut-on-chip which include pathways associated with apoptosis, MAPK-, Jak-STAT-, p53- and NF-Kappa B- and NOD-like receptor signalling. These pathways have important regulatory roles in a wide variety of cellular processes including cell proliferation, differentiation, apoptosis, stress responses and immune responses in mammalian cells [63-66]. Like for the expression of the metallothionein genes, these affected pathways were also shown to be induced at a basal level (without exposure) in Caco-2 cells cultured in the gut-on-chip compared to static culturing, suggesting a partial contribution of shear stress related responses.

Downregulated pathways after ZnO NM exposure related to cellular metabolism (like 'propanoate metabolism' under the 'metabolism' KEGG category) in cells grown under both conditions, while other pathways involved in metabolism were additionally downregulated in cells grown under static (e.g. 'fructose and mannose metabolism') or dynamic (e.g. 'pyruvate and butanoate metabolism') conditions. This might indicate that ZnO NM exposure negatively modulated cellular metabolism, interfering with the cellular energy levels in Caco-2 cells. This corroborates the observed decrease of glucose metabolism in lung epithelial cells exposed to ZnO nanoparticles reported in the study of Lai et al, [67]. The mechanism or degree of modulation of the cellular metabolism, however, also appears to depend on the culture conditions. Downregulation of pathways involved in cellular metabolism was also noticed in our previous study comparing Caco-2 cells cultured under static and dynamic conditions (Kulthong et al 2020). Interestingly, the 25 overlapping gene sets that were modulated in the Caco-2 cells cultured under both culturing conditions included the autophagy pathway. Autophagy has been proposed as a mechanism involved in nanomaterial toxicity [68] and has been identified as a major modulator of ZnO NM induced cellular toxicity [69, 70]. In addition, several other pathways were exclusively downregulated in cells grown under dynamic culturing conditions. Pathways associated with DNA repair and replication (under the 'replication and repair' KEGG category subgroup) were observed as prominently downregulated pathways (i.e. DNA replication, mismatch repair, homologous recombination are in the top 5 of downregulated pathways). This finding is consistent with

the Nanogenotox report where ZnO (NM110) has been considered as potential positive control for genotoxicity (study in Caco-2) [71].

In conclusion, the obtained results showed that there was no overlap in either differential expression of individual genes or of affected pathways in Caco-2 cells cultured under the two different conditions after exposure to TiO₂ NM. However, in both cases genes involved in DNA damage were affected. Following exposure to ZnO NM general stronger effects on the differential gene expression were observed. In spite of the absence of overlap in differentially expressed genes at the individual gene level, some shared pathways were affected between the two different culture conditions. Both materials caused a stronger transcriptional impact at both the individual gene expression and pathway level in cells cultured under dynamic conditions in a gut-on-chip compared to culturing under static conditions in a Transwell. This suggests that shear stress renders the Caco-2 cells more sensitive and might imply the underestimation of cell-nanomaterial interaction of intestinal epithelial cells cultured on a static condition in vitro. Nonetheless, to the authors knowledge, there is no study revealing the gene expression profile of human epithelial cells in vivo upon TiO₂ and ZnO NM exposure, therefore it is quite challenging to clearly indicate which of the two culturing conditions of the Caco-2 cells resembles the human in vivo situation best. This manuscript is a first effort to evaluate the response of (food-associated) NMs in Caco-2 cells cultured under different conditions (i.e. dynamic and static). The data in this study suggest that the dynamically cultured cells are more sensitive, and thus might be an attractive model to be used in the toxicological hazard characterisation more extensively than so far done.

Acknowledgement

The authors sincerely acknowledge the support and critical comments of prof.dr.ir. IMCM (Ivonne) Rietjens. K. K. is supported by a Royal Thai government Scholarship. This work was in part supported by the Dutch Ministry of Agriculture, Nature and Food Quality (project KB-23-002-022)

References

1. Weir, A., et al., *Titanium dioxide nanoparticles in food and personal care products*. Environ Sci Technol, 2012. 46(4): p. 2242-50.
2. Dekkers, S., et al., *Presence and risks of nanosilica in food products*. Nanotoxicology, 2011. 5(3): p. 393-405.
3. P.J.P. Espitia, C.G.O., N.F.F. Soares, *Zinc Oxide Nanoparticles for Food Packaging Applications*, in *Antimicrobial Food Packaging*, J. Barros-Velázquez, Editor. 2016, Academic Press. p. 425-431.
4. He, Y., et al., *Study on the mechanism of antibacterial action of magnesium oxide nanoparticles against foodborne pathogens*. J Nanobiotechnology, 2016. 14(1): p. 54.
5. Ranjan, S., et al., *Toxicity and regulations of food nanomaterials*. Environmental Chemistry Letters, 2019. 17(2): p. 929-944.
6. Bahadar, H., et al., *Toxicity of Nanoparticles and an Overview of Current Experimental Models*. Iran Biomed J, 2016. 20(1): p. 1-11.
7. Bajak, E., et al., *Changes in Caco-2 cells transcriptome profiles upon exposure to gold nanoparticles*. Toxicology Letters, 2015. 233(2): p. 187-199.
8. Mao, X., et al., *Engineered Nanoparticles as Potential Food Contaminants and Their Toxicity to Caco-2 Cells*. J Food Sci, 2016. 81(8): p. T2107-13.
9. Chen, N., et al., *Toxicological Effects of Caco-2 Cells Following Short-Term and Long-Term Exposure to Ag Nanoparticles*. Int J Mol Sci, 2016. 17(6).
10. Bhise, N.S., et al., *Organ-on-a-chip platforms for studying drug delivery systems*. J Control Release, 2014. 190: p. 82-93.
11. Kimura, H., Y. Sakai, and T. Fujii, *Organ/body-on-a-chip based on microfluidic technology for drug discovery*. Drug Metab Pharmacokinet, 2018. 33(1): p. 43-48.
12. Kim, H.J., et al., *Human gut-on-a-chip inhabited by microbial flora that experiences intestinal peristalsis-like motions and flow*. Lab Chip, 2012. 12(12): p. 2165-74.
13. Kim, H.J. and D.E. Ingber, *Gut-on-a-Chip microenvironment induces human intestinal cells to undergo villus differentiation*. Integr Biol (Camb), 2013. 5(9): p. 1130-40.
14. Beaurivage, C., et al., *Development of a Gut-On-A-Chip Model for High Throughput Disease Modeling and Drug Discovery*. Int J Mol Sci, 2019. 20(22).
15. Kulthong, K., et al., *Microfluidic chip for culturing intestinal epithelial cell layers: Characterization and comparison of drug transport between dynamic and static models*. Toxicol In Vitro, 2020. 65: p. 104815.
16. Santbergen, M.J.C., et al., *Dynamic in vitro intestinal barrier model coupled to chip-based liquid chromatography mass spectrometry for oral bioavailability studies*. Anal Bioanal Chem, 2020. 412(5): p. 1111-1122.
17. Shin, W. and H.J. Kim, *Intestinal barrier dysfunction orchestrates the onset of inflammatory host-microbiome cross-talk in a human gut inflammation-on-a-chip*. Proc Natl Acad Sci U S A, 2018. 115(45): p. E10539-E10547.
18. Kulthong, K., et al., *Implementation of a dynamic intestinal gut-on-a-chip barrier model for transport studies of lipophilic dioxin congeners*. Rsc Advances, 2018. 8(57): p. 32440-32453.
19. Chi, M., et al., *A microfluidic cell culture device (muFCCD) to culture epithelial cells with physiological and morphological properties that mimic those of the human intestine*. Biomed Microdevices, 2015. 17(3): p. 9966.
20. Sakharov, D., et al., *Towards embedding Caco-2 model of gut interface in a microfluidic device to enable multi-organ models for systems biology*. BMC Syst Biol, 2019. 13(Suppl 1): p. 19.
21. Kim, H.J., et al., *Contributions of microbiome and mechanical deformation to intestinal bacterial overgrowth and inflammation in a human gut-on-a-chip*. Proc Natl Acad Sci U S A, 2016. 113(1): p. E7-15.
22. Vance, M.E., et al., *Nanotechnology in the real world: Redeveloping the nanomaterial consumer products inventory*. Beilstein J Nanotechnol, 2015. 6: p. 1769-80.

23. Rompelberg, C., et al., *Oral intake of added titanium dioxide and its nanofraction from food products, food supplements and toothpaste by the Dutch population*. *Nanotoxicology*, 2016. 10(10): p. 1404-1414.
24. Rasmussen, J.W., et al., *Zinc oxide nanoparticles for selective destruction of tumor cells and potential for drug delivery applications*. *Expert Opin Drug Deliv*, 2010. 7(9): p. 1063-77.
25. Proquin, H., et al., *Transcriptome changes in undifferentiated Caco-2 cells exposed to food-grade titanium dioxide (E171): contribution of the nano- and micro- sized particles*. *Sci Rep*, 2019. 9(1): p. 18287.
26. Dorier, M., et al., *Continuous in vitro exposure of intestinal epithelial cells to E171 food additive causes oxidative stress, inducing oxidation of DNA bases but no endoplasmic reticulum stress*. *Nanotoxicology*, 2017. 11(6): p. 751-761.
27. Moos, P.J., et al., *Responses of human cells to ZnO nanoparticles: a gene transcription study*. *Metallomics*, 2011. 3(11): p. 1199-211.
28. Moreno-Olivas, F., E. Tako, and G.J. Mahler, *ZnO nanoparticles affect nutrient transport in an in vitro model of the small intestine*. *Food and Chemical Toxicology*, 2019. 124: p. 112-127.
29. Warheit, D.B. and S.C. Brown, *What is the impact of surface modifications and particle size on commercial titanium dioxide particle samples? – A review of in vivo pulmonary and oral toxicity studies – Revised 11-6-2018*. *Toxicology Letters*, 2019. 302: p. 42-59.
30. Singh, S., et al., *Endocytosis, oxidative stress and IL-8 expression in human lung epithelial cells upon treatment with fine and ultrafine TiO₂: Role of the specific surface area and of surface methylation of the particles*. *Toxicology and Applied Pharmacology*, 2007. 222(2): p. 141-151.
31. Mudunkotuwa, I.A., et al., *Dissolution of ZnO nanoparticles at circumneutral pH: a study of size effects in the presence and absence of citric acid*. *Langmuir*, 2012. 28(1): p. 396-403.
32. Cao, Y., et al., *Synergistic effects of zinc oxide nanoparticles and Fatty acids on toxicity to caco-2 cells*. *Int J Toxicol*, 2015. 34(1): p. 67-76.
33. Hubatsch, I., E.G. Ragnarsson, and P. Artursson, *Determination of drug permeability and prediction of drug absorption in Caco-2 monolayers*. *Nat Protoc*, 2007. 2(9): p. 2111-9.
34. Helsper, J.P., et al., *Physicochemical characterization of titanium dioxide pigments using various techniques for size determination and asymmetric flow field flow fractionation hyphenated with inductively coupled plasma mass spectrometry*. *Anal Bioanal Chem*, 2016. 408(24): p. 6679-91.
35. Peters, R.J., et al., *Characterization of titanium dioxide nanoparticles in food products: analytical methods to define nanoparticles*. *J Agric Food Chem*, 2014. 62(27): p. 6285-93.
36. Jensen KA, K.Y., Christiansen E, Jacobsen NR, Wallin H, Guioit C, Spalla O, and Witschger O, *Final protocol for producing suitable manufactured nanomaterial exposure media*, in *Towards a method for detecting the potential genotoxicity of nanomaterials*, K.A.J.a.N. Thieriet, Editor. 2011, The National Research Centre for the Working Environment: Denmark.
37. Hinderliter, P.M., et al., *ISDD: A computational model of particle sedimentation, diffusion and target cell dosimetry for in vitro toxicity studies*. *Particle and Fibre Toxicology*, 2010. 7.
38. Abdelkhalik, A., et al., *Impact of nanoparticle surface functionalization on the protein corona and cellular adhesion, uptake and transport*. *Journal of Nanobiotechnology*, 2018. 16.
39. Lin, K., et al., *MADMAX - Management and analysis database for multiple -omics experiments*. *J Integr Bioinform*, 2011. 8(2): p. 160.
40. Irizarry, R.A., et al., *Exploration, normalization, and summaries of high density oligonucleotide array probe level data*. *Biostatistics*, 2003. 4(2): p. 249-64.
41. Bolstad, B.M., et al., *A comparison of normalization methods for high density oligonucleotide array data based on variance and bias*. *Bioinformatics*, 2003. 19(2): p. 185-93.
42. Dai, M.H., et al., *Evolving gene/transcript definitions significantly alter the interpretation of GeneChip data*. *Nucleic Acids Research*, 2005. 33(20).
43. Ritchie, M.E., et al., *limma powers differential expression analyses for RNA-sequencing and microarray studies*. *Nucleic Acids Research*, 2015. 43(7).

44. Sartor, M.A., et al., *Intensity-based hierarchical Bayes method improves testing for differentially expressed genes in microarray experiments*. BMC Bioinformatics, 2006. 7.
45. Abatangelo, L., et al., *Comparative study of gene set enrichment methods*. BMC Bioinformatics, 2009. 10: p. 275.
46. Allison, D.B., et al., *Microarray data analysis: from disarray to consolidation and consensus*. Nat Rev Genet, 2006. 7(1): p. 55-65.
47. Subramanian, A., et al., *Gene set enrichment analysis: a knowledge-based approach for interpreting genome-wide expression profiles*. Proc Natl Acad Sci U S A, 2005. 102(43): p. 15545-50.
48. Kanehisa, M., et al., *KEGG: new perspectives on genomes, pathways, diseases and drugs*. Nucleic Acids Res, 2017. 45(D1): p. D353-D361.
49. Stetefeld, J., S.A. McKenna, and T.R. Patel, *Dynamic light scattering: a practical guide and applications in biomedical sciences*. Biophys Rev, 2016. 8(4): p. 409-427.
50. Singh, C., Friedrichs, S., Levin, M., Birkedal, R., Jensen, K.J., Pojana, G., Wohlleben, W., Schulte, S., Wiench, K., Turney, T., Koulaeva, O., Marshall, D., Hund-Rinke, K., Kördel, W., Van Doren, E., De Temmerman, P.J., Abi Daoud Francisco, M., Mast, J., N Gibson, N., Koeber, R., Linsinger, T., Klein, C.L., *NM-Series of Representative Manufactured Nanomaterials - Zinc Oxide NM-110, NM-111, NM-112, NM-113: Characterisation and Test Item Preparation*. 2011.
51. Gerloff, K., et al., *Influence of simulated gastrointestinal conditions on particle-induced cytotoxicity and interleukin-8 regulation in differentiated and undifferentiated Caco-2 cells*. Nanotoxicology, 2013. 7(4): p. 353-66.
52. Thompson, C.M., et al., *Assessment of Cr(VI)-induced cytotoxicity and genotoxicity using high content analysis*. PLoS One, 2012. 7(8): p. e42720.
53. Delon, L.C., et al., *A systematic investigation of the effect of the fluid shear stress on Caco-2 cells towards the optimization of epithelial organ-on-chip models*. Biomaterials, 2019. 225: p. 119521.
54. Kim, S.W., et al., *Shear stress induces noncanonical autophagy in intestinal epithelial monolayers*. Mol Biol Cell, 2017. 28(22): p. 3043-3056.
55. Feng, S., et al., *Online Analysis of Drug Toxicity to Cells with Shear Stress on an Integrated Microfluidic Chip*. ACS Sens, 2019. 4(2): p. 521-527.
56. Sakolish, C.M., B. Philip, and G.J. Mahler, *A human proximal tubule-on-a-chip to study renal disease and toxicity*. Biomicrofluidics, 2019. 13(1): p. 014107.
57. Cornu, T.I., et al., *DNA-binding Specificity Is a Major Determinant of the Activity and Toxicity of Zinc-finger Nucleases*. Mol Ther, 2008. 16(2): p. 352-358.
58. Wang, Y., et al., *Upregulation of EID3 sensitizes breast cancer cells to ionizing radiation-induced cellular senescence*. Biomed Pharmacother, 2018. 107: p. 606-614.
59. Proquin, H., et al., *Titanium dioxide food additive (E171) induces ROS formation and genotoxicity: contribution of micro and nano-sized fractions*. Mutagenesis, 2017. 32(1): p. 139-149.
60. Gerloff, K., et al., *Distinctive toxicity of TiO₂ rutile/anatase mixed phase nanoparticles on Caco-2 cells*. Chem Res Toxicol, 2012. 25(3): p. 646-55.
61. van der Zande, M., et al., *Different responses of Caco-2 and MCF-7 cells to silver nanoparticles are based on highly similar mechanisms of action*. Nanotoxicology, 2016. 10(10): p. 1431-1441.
62. Sahu, S.C., *Altered global gene expression profiles in human gastrointestinal epithelial Caco2 cells exposed to nanosilver*. Toxicol Rep, 2016. 3: p. 262-268.
63. Chen, G., et al., *NOD-like receptors: role in innate immunity and inflammatory disease*. Annu Rev Pathol, 2009. 4: p. 365-98.
64. Harrison, D.A., *The Jak/STAT pathway*. Cold Spring Harb Perspect Biol, 2012. 4(3).
65. Eric Ho, J.W., *Mitogen-Activated Protein Kinases*, in *Handbook of Cell Signaling* E.A.D. Ralph A. Bradshaw, Editor. 2010, Academic Press. p. 533-538.
66. Mitchell, S., J. Vargas, and A. Hoffmann, *Signaling via the NFkappaB system*. Wiley Interdiscip Rev Syst Biol Med, 2016. 8(3): p. 227-41.

67. Lai, X., et al., *The effect of Fe₂O₃ and ZnO nanoparticles on cytotoxicity and glucose metabolism in lung epithelial cells*. J Appl Toxicol, 2015. 35(6): p. 651-64.
68. Stern, S.T., P.P. Adiseshaiah, and R.M. Crist, *Autophagy and lysosomal dysfunction as emerging mechanisms of nanomaterial toxicity*. Part Fibre Toxicol, 2012. 9: p. 20.
69. Song, W.J., et al., *Zinc Oxide Nanoparticles Induce Autophagy and Apoptosis via Oxidative Injury and Pro-Inflammatory Cytokines in Primary Astrocyte Cultures*. Nanomaterials (Basel), 2019. 9(7).
70. Roy, R., et al., *Zinc oxide nanoparticles induce apoptosis by enhancement of autophagy via PI3K/Akt/mTOR inhibition*. Toxicol Lett, 2014. 227(1): p. 29-40.
71. Norppa, H., Siivola, K., Fessard, V., Tarantini, A., Apostolova, M., Jacobsen, N.R., Wallin, H., Goetz, M.E., Fieblinger, M., Stepnik, M., Simar, S., Quarre, S., Nessler, F., de Jong, W.H., Marcos, R., Vales, G., Troisfontaines, P., Guichard, Y., Tavares, A., Louro, H., Silva, M.J., *In vitro testing strategy for nanomaterials including database*. 2013, Finnish Institute of Occupational Health Nanosafety Research Center: Helsinki.

Supplementary Table 1. Fold change of differentially expressed genes upon TiO₂ exposure in Caco-2 cells

SYMBOL	TiO ₂ _Ctrl vs transwell_log2FC	TiO ₂ _Ctrl vs transwell_fold change	TiO ₂ _Ctrl vs transwell _p.value	TiO ₂ _Ctrl vs transwell_FDR.BH	GENENAME
LOC105373215	1.72	3.30	0.01	0.97	uncharacterized LOC105373215
LOC105376839	1.51	2.85	0.00	0.63	uncharacterized LOC105376839
SUGTIP3	1.32	2.49	0.00	0.89	SUGT1 pseudogene 3
MIRAS	1.04	2.05	0.00	0.17	muscle RAS oncogene homolog
LOC107984429	1.03	2.04	0.01	0.99	uncharacterized LOC107984429
LOC107986298	1.03	2.04	0.00	0.89	uncharacterized LOC107986298
SRP54-AS1	1.00	2.00	0.00	0.93	SRP54 antisense RNA 1 (head to head)
FKBP1A1	0.97	1.96	0.00	0.80	FKBP prolyl isomerase 1A pseudogene 1
OR13C3	0.97	1.96	0.01	0.97	olfactory receptor family 13 subfamily C member 3
UGT1A4	0.96	1.94	0.01	0.99	UDP glucuronosyltransferase family 1 member A4
RNY3P12	0.94	1.92	0.01	0.96	RNY3 pseudogene 12
LOC105377324	0.93	1.91	0.00	0.15	uncharacterized LOC105377324
LOC105373449	0.91	1.88	0.00	0.88	uncharacterized LOC105373449
OR5T2	0.90	1.87	0.00	0.83	olfactory receptor family 5 subfamily T member 2
OR10Q1	0.90	1.86	0.00	0.07	olfactory receptor family 10 subfamily Q member 1
LOC112268020	0.90	1.86	0.00	0.89	uncharacterized LOC112268020
PLUT	0.89	1.86	0.00	0.84	PDX1 associated lncRNA, upregulator of transcription
FAM157A	0.89	1.85	0.01	0.99	family with sequence similarity 157 member A
LOC107984574	0.88	1.83	0.00	0.80	uncharacterized LOC107984574
LOC102724900	0.87	1.82	0.00	0.49	uncharacterized LOC102724900
LINC02447	0.87	1.82	0.00	0.80	long intergenic non-protein coding RNA 2447
OR4C46	0.86	1.82	0.00	0.89	olfactory receptor family 4 subfamily C member 46
BOK-AS1	0.86	1.81	0.01	0.99	BOK antisense RNA 1
LINC01524	0.85	1.80	0.00	0.93	long intergenic non-protein coding RNA 1524
LOC105379364	0.85	1.80	0.01	0.99	uncharacterized LOC105379364
LOC107986275	0.81	1.75	0.01	0.99	uncharacterized LOC107986275
LINC02595	0.80	1.74	0.00	0.89	long intergenic non-protein coding RNA 2595

LOC105374428	0.79	1.74	0.00	0.84	uncharacterized LOC105374428
SPIN2A	0.78	1.72	0.00	0.89	spindlin family member 2A
PANTR1	0.78	1.72	0.00	0.70	POU3F3 adjacent non-coding transcript 1
CCL27	0.75	1.69	0.01	0.97	C-C motif chemokine ligand 27
TCF7L1-IT1	0.75	1.68	0.00	0.90	TCF7L1 intronic transcript 1
UGT2A1	0.75	1.68	0.01	0.99	UDP glucuronosyltransferase family 2 member A1 complex locus
LOC105369187	0.75	1.68	0.00	0.89	uncharacterized LOC105369187
LOC100506321	0.75	1.68	0.00	0.83	uncharacterized LOC100506321
PABPC3	0.75	1.68	0.00	0.85	poly(A) binding protein cytoplasmic 3
HP	0.74	1.66	0.00	0.80	haptoglobin
MIR548AB	0.73	1.66	0.00	0.80	microRNA 548ab
OR2AG2	0.73	1.66	0.00	0.87	olfactory receptor family 2 subfamily AG member 2
MIR4673	0.72	1.65	0.00	0.80	microRNA 4673
LOC101928323	0.72	1.65	0.00	0.88	uncharacterized LOC101928323
LOC105374748	0.71	1.64	0.00	0.80	uncharacterized LOC105374748
TRIM53AP	0.71	1.63	0.01	0.97	tripartite motif containing 53A, pseudogene
MAGEB4	0.70	1.62	0.00	0.89	MAGE family member B4
PTCSC2	0.69	1.62	0.00	0.56	papillary thyroid carcinoma susceptibility candidate 2
LOC105376941	0.69	1.62	0.00	0.78	uncharacterized LOC105376941
RRAS2	0.69	1.61	0.00	0.96	RAS related 2
LOC441666	0.69	1.61	0.00	0.49	zinc finger protein 91 pseudogene
TREML5P	0.67	1.59	0.01	0.99	triggering receptor expressed on myeloid cells like 5, pseudogene
LOC105379351	0.67	1.59	0.00	0.87	uncharacterized LOC105379351
LOC105373623	0.67	1.59	0.00	0.89	uncharacterized LOC105373623
YY1API	0.65	1.57	0.00	0.93	YY1 associated protein 1
IGKJ3	0.65	1.56	0.01	0.99	immunoglobulin kappa joining 3
LOC105378523	0.63	1.55	0.00	0.80	uncharacterized LOC105378523
LOC102606466	0.63	1.55	0.00	0.92	uncharacterized LOC102606466
RASGRF2-AS1	0.62	1.54	0.00	0.89	RASGRF2 antisense RNA 1
LOC102724945	0.62	1.53	0.01	0.99	uncharacterized LOC102724945
MIR125B1	0.61	1.53	0.00	0.78	microRNA 125b-1
LOC100996637	0.61	1.53	0.00	0.83	P-selectin glycoprotein ligand 1-like
CABP7	0.61	1.52	0.00	0.85	calcium binding protein 7

LINC00996	0.61	1.52	0.00	0.83	long intergenic non-protein coding RNA 996
NGEF	0.60	1.52	0.01	0.99	neuronal guanine nucleotide exchange factor
LINC02471	0.59	1.51	0.00	0.89	long intergenic non-protein coding RNA 2471
LINC02715	0.59	1.51	0.00	0.49	long intergenic non-protein coding RNA 2715
LOC105374951	0.58	1.50	0.00	0.15	uncharacterized LOC105374951
ITIH1	0.58	1.50	0.00	0.83	inter-alpha-trypsin inhibitor heavy chain 1
RGPD3	0.58	1.49	0.00	0.89	RANBP2 like and GRIP domain containing 3
GUSBP2	0.58	1.49	0.01	0.99	GUSB pseudogene 2
MIR1260B	0.57	1.49	0.00	0.92	microRNA 1260b
LOC105378328	0.57	1.49	0.00	0.73	uncharacterized LOC105378328
LINC00571	0.57	1.48	0.01	0.99	long intergenic non-protein coding RNA 571
FGF14-AS1	0.57	1.48	0.01	0.99	FGF14 antisense RNA 1
ZSCAN20	0.56	1.47	0.00	0.82	zinc finger and SCAN domain containing 20
LINC02528	0.56	1.47	0.00	0.80	long intergenic non-protein coding RNA 2528
LOC105371430	0.55	1.46	0.01	0.97	uncharacterized LOC105371430
HOXD8	0.54	1.46	0.01	0.96	homeobox D8
MIR548G	0.54	1.46	0.00	0.80	microRNA 548g
SPATA3	0.54	1.46	0.00	0.83	spermatogenesis associated 3
FMO2	0.54	1.45	0.00	0.88	flavin containing dimethylamine monooxygenase 2
MIR4692	0.54	1.45	0.01	0.96	microRNA 4692
LINC01283	0.53	1.44	0.01	0.99	long intergenic non-protein coding RNA 1283
PLXDC1	0.53	1.44	0.01	0.96	plexin domain containing 1
KRT16P2	0.52	1.44	0.00	0.86	keratin 16 pseudogene 2
IQCF2	0.52	1.43	0.00	0.89	IQ motif containing F2
RNU6-340P	0.51	1.43	0.00	0.88	RNA, U6 small nuclear 340, pseudogene
LOC102723846	0.51	1.43	0.00	0.89	uncharacterized LOC102723846
SMR3A	0.51	1.42	0.00	0.83	submaxillary gland androgen regulated protein 3A
KRTAP10-12	0.50	1.42	0.00	0.89	keratin associated protein 10-12
LINC02501	0.50	1.42	0.00	0.80	long intergenic non-protein coding RNA 2501
ZNF679	0.50	1.41	0.01	0.99	zinc finger protein 679
LINC00901	0.50	1.41	0.01	0.98	long intergenic non-protein coding RNA 901
LOC102724687	0.50	1.41	0.00	0.92	uncharacterized LOC102724687
SMCR5	0.50	1.41	0.01	0.99	Smith-Magenis syndrome chromosome region, candidate 5
RNU4-13P	0.50	1.41	0.01	0.99	RNA, U4 small nuclear 13, pseudogene
PPDC	0.49	1.41	0.00	0.80	phosphopantothenoylcytostine decarboxylase
LINC02740	0.49	1.40	0.01	0.99	long intergenic non-protein coding RNA 2740

	0.49	1.40	0.00	0.80	ankyrin repeat domain 62
ANKRD62					uncharacterized LOC105379168
LOC105379168	0.49	1.40	0.00	0.89	taste 1 receptor member 2
TAS1R2	0.49	1.40	0.00	0.95	uncharacterized LOC107985451
LOC107985451	0.48	1.40	0.01	0.99	uncharacterized LOC105378881
LOC105378881	0.48	1.40	0.00	0.88	microRNA 564
MIR564	0.48	1.40	0.01	0.99	defensin beta 128
DEFB128	0.48	1.39	0.01	0.99	microRNA 183
MIR183	0.48	1.39	0.00	0.93	microRNA 4506
MIR4506	0.47	1.39	0.00	0.82	acyloxyacyl hydrolase (neutrophil)
FAM183BP	0.47	1.38	0.01	0.99	long intergenic non-protein coding RNA 2766
LINC02766	0.46	1.38	0.01	0.97	long intergenic non-protein coding RNA 2533
LINC02533	0.46	1.38	0.01	0.99	ADAM metalloproteinase domain 3A (pseudogene)
ADAM3A	0.46	1.37	0.00	0.87	chromosome 2 open reading frame 16
C2orf16	0.45	1.37	0.01	0.99	uncharacterized LOC101928021
LOC101928021	0.45	1.37	0.01	0.99	mitogen-activated protein kinase kinase kinase 15
MAP3K15	0.45	1.37	0.01	0.99	ATP binding cassette subfamily G member 1
ABCG1	0.45	1.36	0.00	0.89	long intergenic non-protein coding RNA 2463
LINC02463	0.44	1.36	0.00	0.89	olfactory receptor family 52 subfamily E member 6
OR52E6	0.44	1.35	0.01	0.99	uncharacterized LOC112267858
LOC112267858	0.44	1.35	0.00	0.89	uncharacterized LOC107984406
LOC107984406	0.43	1.35	0.01	0.97	deoxythymidylate kinase
DTYMK	0.43	1.35	0.00	0.80	docking protein 1
DOK1	0.42	1.34	0.00	0.89	long intergenic non-protein coding RNA 1075
LINC01075	0.42	1.34	0.00	0.88	T cell receptor alpha variable 16
TRAV16	0.42	1.34	0.01	0.99	RAB39A, member RAS oncogene family
RAB39A	0.42	1.33	0.00	0.88	fatty acid binding protein 9
FABP9	0.41	1.33	0.01	0.99	microRNA 4282
MIR4282	0.39	1.31	0.01	0.99	potassium two pore domain channel subfamily K member 7
KCNK7	0.39	1.31	0.01	0.99	long intergenic non-protein coding RNA 2713
LINC02713	0.38	1.31	0.01	0.99	stimulated by retinoic acid 8
STRA8	0.38	1.30	0.01	0.99	long intergenic non-protein coding RNA 2450
LINC02450	0.37	1.29	0.01	0.98	uncharacterized LOC105374230
LOC105374230	0.36	1.29	0.00	0.89	solute carrier family 66 member 2
SLC66A2	0.36	1.29	0.00	0.89	polypeptide N-acetylgalactosaminyltransferase 4
GALNT4	0.36	1.28	0.01	0.96	testis specific 13
TSGA13	0.36	1.28	0.01	0.96	

LOC105377961	0.35	1.28	0.00	0.92	uncharacterized LOC105377961
TNRC6B	0.35	1.27	0.01	0.99	trinucleotide repeat containing adaptor 6B
STAT5B	0.32	1.24	0.00	0.96	signal transducer and activator of transcription 5B
TAB2-AS1	0.31	1.24	0.01	0.99	TAB2 antisense RNA 1
UTRN	0.30	1.23	0.01	0.99	utrophin
PARG	0.30	1.23	0.00	0.80	poly(ADP-ribose) glycohydrolase
RRAGC	0.29	1.22	0.01	0.99	Ras related GTP binding C
MYCBP2	0.28	1.22	0.01	0.99	MYC binding protein 2
LMTK2	0.24	1.18	0.01	0.99	lemur tyrosine kinase 2
PDLIM5	0.23	1.17	0.01	0.99	PDZ and LIM domain 5
DYNC112	0.23	1.17	0.01	0.99	dyncin cytoplasmic 1 intermediate chain 2
INSR	0.23	1.17	0.01	0.99	insulin receptor
RAB3GAP1	0.18	1.14	0.01	0.99	RAB3 GTPase activating protein catalytic subunit 1
RTRAF	-0.23	-1.17	0.01	0.99	RNA transcription, translation and transport factor
HIGD1A	-0.23	-1.18	0.01	0.99	HIG1 hypoxia inducible domain family member 1A
TALDO1	-0.24	-1.18	0.01	0.99	transaldolase 1
SLC33A1	-0.26	-1.20	0.01	0.99	solute carrier family 33 member 1
HINT3	-0.28	-1.22	0.01	0.99	histidine triad nucleotide binding protein 3
CITED2	-0.29	-1.22	0.01	0.96	Cbp/p300 interacting transactivator with Glu/Asp rich carboxy-terminal domain 2
LOC105373896	-0.30	-1.23	0.01	0.99	uncharacterized LOC105373896
LOC102724379	-0.31	-1.24	0.01	0.99	uncharacterized LOC102724379
PSMG1	-0.33	-1.25	0.00	0.89	proteasome assembly chaperone 1
SNAIL	-0.33	-1.26	0.01	0.99	snail family transcriptional repressor 1
TRAV9-2	-0.33	-1.26	0.01	0.99	T cell receptor alpha variable 9-2
STK31	-0.34	-1.26	0.01	0.99	serine/threonine kinase 31
ZMIZ2	-0.35	-1.27	0.00	0.95	zinc finger MIZ-type containing 2
ATP5F1D	-0.35	-1.27	0.01	0.99	ATP synthase F1 subunit delta
MAP1S	-0.36	-1.28	0.01	0.99	microtubule associated protein 1S
CFAP43	-0.37	-1.29	0.01	0.99	cilia and flagella associated protein 43
PIK3CG	-0.38	-1.30	0.01	0.99	phosphatidylinositol-4,5-bisphosphate 3-kinase catalytic subunit gamma
ILDR2	-0.39	-1.31	0.01	0.99	immunoglobulin like domain containing receptor 2
C4orf46	-0.39	-1.31	0.00	0.93	chromosome 4 open reading frame 46
TRAV7	-0.39	-1.31	0.01	0.99	T cell receptor alpha variable 7

ANP32C	-0.40	-1.32	0.00	0.89	acidic nuclear phosphoprotein 32 family member C
LOC102724950	-0.40	-1.32	0.00	0.89	uncharacterized LOC102724950
TMEM30CP	-0.41	-1.33	0.00	0.89	transmembrane protein 30C, pseudogene
LOC101927811	-0.41	-1.33	0.01	0.99	uncharacterized LOC101927811
LINC01096	-0.41	-1.33	0.00	0.89	long intergenic non-protein coding RNA 1096
MIR217	-0.42	-1.33	0.01	0.99	microRNA 217
RPL36P5	-0.42	-1.33	0.00	0.89	ribosomal protein L36 pseudogene 5
RFX4	-0.42	-1.34	0.01	0.97	regulatory factor X4
PCDH9	-0.42	-1.34	0.00	0.89	protocadherin 9
CCDC198	-0.42	-1.34	0.01	0.99	coiled-coil domain containing 198
LOC105371818	-0.42	-1.34	0.01	0.97	uncharacterized LOC105371818
ZIC4	-0.42	-1.34	0.01	0.96	Zic family member 4
LINC02626	-0.42	-1.34	0.01	0.99	long intergenic non-protein coding RNA 2626
ARC	-0.42	-1.34	0.01	0.99	activity regulated cytoskeleton associated protein
TIGD4	-0.44	-1.36	0.01	0.99	tigger transposable element derived 4
C1QTNF7-AS1	-0.44	-1.36	0.00	0.83	C1QTNF7 antisense RNA 1
LINC01381	-0.44	-1.36	0.01	0.99	long intergenic non-protein coding RNA 1381
KCNH6	-0.44	-1.36	0.01	0.99	potassium voltage-gated channel subfamily H member 6
SSPN	-0.45	-1.37	0.00	0.89	sarcospan
FLRT1	-0.45	-1.37	0.01	0.99	fibronectin leucine rich transmembrane protein 1
CASP14	-0.46	-1.37	0.00	0.92	caspase 14
PRRT1	-0.46	-1.37	0.00	0.89	proline rich transmembrane protein 1
LOC101927999	-0.46	-1.38	0.00	0.94	putative uncharacterized protein FLJ44672
INSM1	-0.46	-1.38	0.00	0.89	INSM transcriptional repressor 1
LOC101929014	-0.47	-1.38	0.01	0.99	uncharacterized LOC101929014
DPYD-AS1	-0.47	-1.38	0.00	0.89	DPYD antisense RNA 1
UGT2B25P	-0.47	-1.38	0.01	0.99	UDP glucuronosyltransferase family 2 member B25, pseudogene
SLC22A8	-0.48	-1.39	0.01	0.99	solute carrier family 22 member 8
GOLGA8K	-0.48	-1.40	0.01	0.99	golgin A8 family member K
ZNF692	-0.49	-1.40	0.00	0.83	zinc finger protein 692
SYNE4	-0.49	-1.41	0.01	0.99	spectrin repeat containing nuclear envelope family member 4
LINC00630	-0.49	-1.41	0.00	0.94	long intergenic non-protein coding RNA 630
PRMT8	-0.50	-1.41	0.01	0.99	protein arginine methyltransferase 8

MAGEA8	-0.50	-1.41	0.01	0.99	MAGE family member A8
LOC105369728	-0.50	-1.42	0.01	0.98	uncharacterized LOC105369728
LOC100506688	-0.51	-1.43	0.01	0.97	uncharacterized LOC100506688
LOC101928841	-0.52	-1.43	0.01	0.99	collagen alpha-1(I) chain-like
LOC101927045	-0.52	-1.43	0.01	0.99	uncharacterized LOC101927045
PDE2A	-0.52	-1.43	0.00	0.94	phosphodiesterase 2A
H2AZ1-DT	-0.52	-1.44	0.01	0.99	H2AZ1 divergent transcript
RAB41	-0.53	-1.44	0.01	0.99	RAB41, member RAS oncogene family
HBD	-0.54	-1.45	0.00	0.84	hemoglobin subunit delta
CCDC175	-0.54	-1.45	0.01	0.99	coiled-coil domain containing 175
CACTIN-AS1	-0.54	-1.46	0.01	0.99	CACTIN antisense RNA 1
LOC105378844	-0.55	-1.46	0.00	0.89	uncharacterized LOC105378844
LOC105371836	-0.55	-1.46	0.00	0.89	uncharacterized LOC105371836
NR2E3	-0.55	-1.46	0.00	0.80	nuclear receptor subfamily 2 group E member 3
DNASE2	-0.55	-1.47	0.00	0.93	deoxyribonuclease 2, lysosomal
MIR196B	-0.56	-1.47	0.01	0.99	microRNA 196b
LOC105372330	-0.56	-1.47	0.01	0.99	uncharacterized LOC105372330
OR1K1	-0.56	-1.47	0.01	0.99	olfactory receptor family 1 subfamily K member 1
TEX52	-0.56	-1.47	0.00	0.89	testis expressed 52
LOC101927919	-0.56	-1.47	0.00	0.88	uncharacterized LOC101927919
OR5AR1	-0.56	-1.47	0.01	0.99	olfactory receptor family 5 subfamily AR member 1 (gene/pseudogene)
TMC1	-0.56	-1.48	0.00	0.89	transmembrane channel like 1
LOC101929188	-0.56	-1.48	0.01	0.99	uncharacterized LOC101929188
LOC101929415	-0.56	-1.48	0.00	0.88	uncharacterized LOC101929415
LOC105372676	-0.56	-1.48	0.01	0.99	uncharacterized LOC105372676
SEBOX	-0.57	-1.48	0.01	0.99	SEBOX homeobox
OR5B17	-0.57	-1.48	0.01	0.97	olfactory receptor family 5 subfamily B member 17
LOC105372331	-0.58	-1.49	0.01	0.99	uncharacterized LOC105372331
GABRG2	-0.59	-1.51	0.01	0.99	gamma-aminobutyric acid type A receptor gamma2 subunit
HOTAIR	-0.59	-1.51	0.01	0.97	HOX transcript antisense RNA
DAB1-AS1	-0.61	-1.52	0.00	0.87	DAB1 antisense RNA 1
LINC02218	-0.61	-1.52	0.00	0.73	long intergenic non-protein coding RNA 2218
TP1IP3	-0.62	-1.53	0.01	0.99	triosephosphate isomerase 1 pseudogene 3
RNU6-145P	-0.62	-1.53	0.00	0.80	RNA, U6 small nuclear 145, pseudogene
LOC105372937	-0.62	-1.54	0.00	0.80	uncharacterized LOC105372937

LOC101928118	-0.63	-1.55	0.00	0.80	uncharacterized LOC101928118
MAPRE3-AS1	-0.63	-1.55	0.00	0.80	MAPRE3 antisense RNA 1
C1orf68	-0.64	-1.56	0.00	0.80	chromosome 1 open reading frame 68
LOC107985535	-0.65	-1.57	0.00	0.85	uncharacterized LOC107985535
LINC01556	-0.65	-1.57	0.00	0.89	long intergenic non-protein coding RNA 1556
ZNF613	-0.66	-1.58	0.00	0.89	zinc finger protein 613
LINC02306	-0.67	-1.59	0.00	0.83	long intergenic non-protein coding RNA 2306
SH3D21	-0.67	-1.59	0.00	0.49	SH3 domain containing 21
OR10P1	-0.68	-1.60	0.01	0.99	olfactory receptor family 10 subfamily P member 1
EMB	-0.68	-1.61	0.01	0.99	embigin
LOC112268257	-0.70	-1.63	0.00	0.84	uncharacterized LOC112268257
DDX11L2	-0.72	-1.65	0.00	0.89	DEAD/H-box helicase 11 like 2
FAM47C	-0.73	-1.66	0.00	0.83	family with sequence similarity 47 member C
SLC9A7P1	-0.73	-1.66	0.00	0.84	solute carrier family 9 member 7 pseudogene 1
LOC107984461	-0.74	-1.67	0.00	0.73	uncharacterized LOC107984461
LINC02783	-0.75	-1.69	0.01	0.99	long intergenic non-protein coding RNA 2783
LOC102723430	-0.76	-1.69	0.01	0.99	uncharacterized LOC102723430
SNORD13E	-0.76	-1.70	0.00	0.80	small nucleolar RNA, C/D box 13E
SNORD114-4	-0.77	-1.70	0.00	0.63	small nucleolar RNA, C/D box 114-4
FOLR3	-0.77	-1.70	0.00	0.73	folate receptor gamma
LOC105372157	-0.77	-1.71	0.00	0.49	uncharacterized LOC105372157
IGHV2-26	-0.78	-1.72	0.00	0.49	immunoglobulin heavy variable 2-26
LOC102724100	-0.80	-1.74	0.00	0.89	uncharacterized LOC102724100
LOC105377500	-0.81	-1.76	0.01	0.99	uncharacterized LOC105377500
ADGRFP1	-0.82	-1.76	0.00	0.73	adhesion G protein-coupled receptor F5 pseudogene 1
MIR4653	-0.83	-1.78	0.00	0.80	microRNA 4653
NDUFA4	-0.85	-1.80	0.01	0.99	NDUFA4 mitochondrial complex associated
LINC01032	-0.87	-1.83	0.00	0.89	long intergenic non-protein coding RNA 1032
ZNF528	-0.88	-1.84	0.00	0.48	zinc finger protein 528
NPBWR1	-0.89	-1.85	0.00	0.70	neuropeptides B and W receptor 1
OR2A2	-0.90	-1.86	0.00	0.83	olfactory receptor family 2 subfamily A member 2
ZNF382	-0.96	-1.95	0.01	0.99	zinc finger protein 382
LOC101927391	-0.99	-1.99	0.00	0.89	uncharacterized LOC101927391
PLG	-1.06	-2.08	0.00	0.48	plasminogen
LOC101928051	-1.11	-2.15	0.00	0.89	uncharacterized LOC101928051
LOC112268248	-1.19	-2.28	0.00	0.94	uncharacterized LOC112268248

LOC107986884	-1.19	-2.29	0.00	0.49	uncharacterized LOC107986884
LOC102724919	-1.41	-2.65	0.00	0.84	uncharacterized LOC102724919
LOC101928608	-1.48	-2.79	0.00	0.70	uncharacterized LOC101928608
H19	-1.52	-2.86	0.00	0.80	H19 imprinted maternally expressed transcript
ZNF117	-1.64	-3.13	0.00	0.49	zinc finger protein 117
LOC642 361	-1.68	-3.20	0.00	0.80	uncharacterized LOC642361

Supplementary Table 2. Fold change of differentially expressed genes upon ZnO exposure in Caco-2 cells

SYMBOL	ZnO_Ctrl vs gut-on-chip_log2FC	ZnO_Ctrl vs chip_fold change	ZnO_Ctrl vs chip_p-value	ZnO_Ctrl vs chip_FDR_BH	GENENAME
EGR1	0.72	1.65	0.00	0.05	early growth response 1
GPRC5A	0.45	1.37	0.00	0.06	G protein-coupled receptor class C group 5 member A
ERC2-IT1	-0.63	-1.55	0.00	0.06	ERC2 intronic transcript 1
MIR614	0.54	1.46	0.00	0.06	microRNA 614
ERRF1	0.47	1.38	0.00	0.18	ERBB receptor feedback inhibitor 1
SLC30A1	0.62	1.53	0.00	0.18	solute carrier family 30 member 1
LOC107987223	0.76	1.70	0.00	0.18	uncharacterized LOC107987223
KLF6	0.40	1.32	0.00	0.18	Kruppel like factor 6
MTRNR2L8	-1.04	-2.06	0.00	0.18	MT-RNR2 like 8
SLC39A10	-0.55	-1.47	0.00	0.18	solute carrier family 39 member 10
CARD8-AS1	0.94	1.91	0.00	0.19	CARD8 antisense RNA 1
TNFRSF12A	0.37	1.29	0.00	0.19	TNF receptor superfamily member 12A
TRIB1	0.47	1.38	0.00	0.24	tribbles pseudokinase 1
CNOT2	0.36	1.29	0.00	0.25	CCR4-NOT transcription complex subunit 2
MIR378H	0.83	1.78	0.00	0.26	microRNA 378h
MIR1226	0.86	1.82	0.00	0.31	microRNA 1226
MIR4328	-0.61	-1.53	0.00	0.31	microRNA 4328
EPX	-0.61	-1.53	0.00	0.31	eosinophil peroxidase
MT2A	0.55	1.47	0.00	0.31	metallothionein 2A
LINC01689	-0.48	-1.40	0.00	0.31	long intergenic non-protein coding RNA 1689
MCL1	0.32	1.25	0.00	0.31	MCL1 apoptosis regulator, BCL2 family member
GPR22	0.58	1.49	0.00	0.31	G protein-coupled receptor 22
CARNS1	-0.57	-1.49	0.00	0.32	carnosine synthase 1
DEFB131A	-0.71	-1.63	0.00	0.35	defensin beta 131A
GCLC	0.37	1.29	0.00	0.35	glutamate-cysteine ligase catalytic subunit
MRPS2	-0.49	-1.40	0.00	0.35	mitochondrial ribosomal protein S2
LOC105375299	0.72	1.65	0.00	0.35	uncharacterized LOC105375299

OSGIN1	0.47	1.39	0.00	0.35	oxidative stress induced growth inhibitor 1
YWHAH	0.35	1.27	0.00	0.35	tyrosine 3-monooxygenase/tryptophan 5-monooxygenase activation protein eta
EEF1A1P17	-0.45	-1.36	0.00	0.37	eukaryotic translation elongation factor 1 alpha 1 pseudogene 17
ENPP2	0.56	1.47	0.00	0.37	ectonucleotide pyrophosphatase/phosphodiesterase 2
LOC105372656	-0.97	-1.96	0.00	0.37	uncharacterized LOC105372656
LINC00886	0.88	1.84	0.00	0.37	long intergenic non-protein coding RNA 886
LOC105378180	-0.56	-1.48	0.00	0.37	uncharacterized LOC105378180
LINC02053	-0.46	-1.38	0.00	0.37	long intergenic non-protein coding RNA 2053
MAL2-AS1	0.59	1.51	0.00	0.37	MAL2 antisense RNA 1
ZNF766	-0.47	-1.39	0.00	0.37	zinc finger protein 766
VXN	-0.91	-1.88	0.00	0.37	vexin
CNTN4-AS2	0.52	1.43	0.00	0.37	CNTN4 antisense RNA 2
NFYC	0.45	1.36	0.00	0.37	nuclear transcription factor Y subunit gamma
LOC105373637	0.54	1.46	0.00	0.37	uncharacterized LOC105373637
TPST1	0.45	1.37	0.00	0.37	tyrosylprotein sulfotransferase 1
AKAP1	0.29	1.22	0.00	0.37	A-kinase anchoring protein 1
DMWD	0.49	1.41	0.00	0.37	DM1 locus, WD repeat containing
LINC01913	-0.67	-1.59	0.00	0.38	long intergenic non-protein coding RNA 1913
RNU6-1316P	1.21	2.31	0.00	0.41	RNA, U6 small nuclear 1316, pseudogene
NMNAT3	0.46	1.37	0.00	0.44	nicotinamide nucleotide adenyllyltransferase 3
RPS6KA2	0.61	1.53	0.00	0.44	ribosomal protein S6 kinase A2
CCDC160	-0.56	-1.48	0.00	0.44	coiled-coil domain containing 160
MTIX	0.54	1.45	0.00	0.44	metallothionein IX
MIR4733	-0.51	-1.42	0.00	0.44	microRNA 4733
LOC107986223	0.56	1.48	0.00	0.44	uncharacterized LOC107986223
ZNF71	-0.65	-1.57	0.00	0.44	zinc finger protein 71
LATS2	0.32	1.25	0.00	0.44	large tumor suppressor kinase 2
LINC01889	0.49	1.40	0.00	0.44	long intergenic non-protein coding RNA 1889
MIR4755	0.84	1.79	0.00	0.44	microRNA 4755
SNORA63C	-0.59	-1.50	0.00	0.44	small nucleolar RNA, H/ACA box 63C
IL1B	-0.74	-1.67	0.00	0.44	interleukin 1 beta
RMDN2	0.53	1.44	0.00	0.44	regulator of microtubule dynamics 2
NOSTRIN	0.43	1.35	0.00	0.44	nitric oxide synthase trafficking

151

		0.42	1.34	0.00	0.48	docking protein 1
DOK1						
LOC105369673		-0.88	-1.84	0.00	0.48	uncharacterized LOC105369673
OR8S1		-0.70	-1.62	0.00	0.49	olfactory receptor family 8 subfamily S member 1
CYP11A1		-0.45	-1.37	0.00	0.49	cytochrome P450 family 1 subfamily A member 1
RASGRP2		-0.53	-1.44	0.00	0.51	RAS guanyl releasing protein 2
RNU1-42P		-0.86	-1.82	0.00	0.51	RNA, U1 small nuclear 42, pseudogene
ID1		0.66	1.58	0.00	0.51	inhibitor of DNA binding 1, HLH protein
LINC02188		-1.15	-2.22	0.00	0.51	long intergenic non-protein coding RNA 2188
RPLP0		-0.54	-1.45	0.00	0.51	ribosomal protein lateral stalk subunit P0
CBX4		0.35	1.27	0.00	0.52	chromobox 4
LOC107984257		0.68	1.60	0.00	0.52	uncharacterized LOC107984257
ALDOA		-0.42	-1.34	0.00	0.54	aldolase, fructose-bisphosphate A
IER3		0.36	1.28	0.00	0.54	immediate early response 3
LOC107984118		-0.78	-1.71	0.00	0.54	uncharacterized LOC107984118
QPCTL		-0.34	-1.27	0.00	0.54	glutaminyl-peptide cyclotransferase like
PPP3R1		0.22	1.17	0.00	0.54	protein phosphatase 3 regulatory subunit B, alpha
LINC01455		0.41	1.33	0.00	0.54	long intergenic non-protein coding RNA 1455
MOB3C		0.40	1.32	0.00	0.54	MOB kinase activator 3C
EWSR1		0.28	1.21	0.00	0.54	EWS RNA binding protein 1
PCDHGA6		0.46	1.37	0.00	0.54	protocadherin gamma subfamily A, 6
RNF148		0.50	1.41	0.00	0.54	ring finger protein 148
MAP3K10		-0.47	-1.39	0.00	0.54	mitogen-activated protein kinase kinase kinase 10
LOC105374317		0.67	1.59	0.00	0.54	uncharacterized LOC105374317
ZNF350		0.59	1.51	0.00	0.54	zinc finger protein 350
SKIL		0.39	1.31	0.00	0.54	SKI like proto-oncogene
LOC642648		-0.56	-1.47	0.00	0.54	uncharacterized LOC642648
HSPD1		0.31	1.24	0.00	0.54	heat shock protein family D (Hsp60) member 1
TMEM141		-0.39	-1.31	0.00	0.54	transmembrane protein 141
FHL3		0.38	1.31	0.00	0.54	four and a half LIM domains 3
HAP1		0.47	1.39	0.00	0.54	huntingtin associated protein 1
ZFAT-AS1		0.54	1.45	0.00	0.54	ZFAT antisense RNA 1
C4orf50		-0.40	-1.32	0.00	0.54	chromosome 4 open reading frame 50
PSMC6		0.32	1.25	0.00	0.55	proteasome 26S subunit, ATPase 6
HSFX4		0.97	1.96	0.00	0.55	heat shock transcription factor family, X-linked member 4
LOC107986979		-0.74	-1.67	0.00	0.55	uncharacterized LOC107986979

SYS1	0.35	1.27	0.00	0.55	SYS1 golgi trafficking protein
LOC101928762	0.64	1.56	0.00	0.55	uncharacterized LOC101928762
POU2F2	0.54	1.45	0.00	0.55	POU class 2 homeobox 2
HPN-AS1	-0.45	-1.36	0.00	0.55	HPN antisense RNA 1
EDN1	0.44	1.36	0.00	0.55	endothelin 1
LOC105378678	-0.54	-1.45	0.00	0.55	uncharacterized LOC105378678
LOC641367	0.61	1.53	0.00	0.55	cyclin Y like 1 pseudogene
MIR3163	0.68	1.60	0.00	0.55	microRNA 3163
ATP2B1	0.23	1.18	0.00	0.55	ATPase plasma membrane Ca2+ transporting 1
SAPCD2	0.38	1.30	0.00	0.55	suppressor APC domain containing 2
SHB	0.30	1.23	0.00	0.55	SH2 domain containing adaptor protein B
MT1G	1.09	2.13	0.00	0.55	metallothionein 1G
GJE1	0.43	1.35	0.00	0.55	gap junction protein epsilon 1
LOC105377324	0.56	1.47	0.00	0.55	uncharacterized LOC105377324
MIR516B2	0.68	1.60	0.00	0.55	microRNA 516b-2
PTBP1	0.19	1.14	0.00	0.55	polypyrimidine tract binding protein 1
IL18	0.41	1.33	0.00	0.55	interleukin 18
JAG1	0.26	1.20	0.00	0.55	jagged canonical Notch ligand 1
C2orf83	-0.45	-1.37	0.00	0.55	chromosome 2 open reading frame 83
MYC	0.38	1.30	0.00	0.55	MYC proto-oncogene, bHLH transcription factor
PHC2	0.52	1.44	0.00	0.55	polyhomeotic homolog 2
MIR4420	-0.55	-1.47	0.00	0.55	microRNA 4420
DDX5	0.24	1.18	0.00	0.55	DEAD-box helicase 5
HAUS7	-0.41	-1.33	0.00	0.55	HAUS augmin like complex subunit 7
USP38	0.31	1.24	0.00	0.55	ubiquitin specific peptidase 38
TSPAN4	-0.45	-1.36	0.00	0.56	tetraspanin 4
OR1E1	0.56	1.47	0.00	0.56	olfactory receptor family 1 subfamily E member 1
SF1	0.28	1.21	0.00	0.56	splicing factor 1
LOC105375660	0.58	1.50	0.00	0.56	uncharacterized LOC105375660
LOC105369750	0.64	1.56	0.00	0.56	uncharacterized LOC105369750
DUSP6	0.33	1.26	0.00	0.56	dual specificity phosphatase 6
TRAJ52	-0.55	-1.46	0.00	0.56	T cell receptor alpha joining 52
LOC401471	-0.98	-1.98	0.00	0.56	uncharacterized LOC401471
SUCLG2	-0.31	-1.24	0.00	0.56	succinate-CoA ligase GDP-forming beta subunit
MIR1224	0.76	1.70	0.00	0.56	microRNA 1224
ZNF471	-0.52	-1.43	0.00	0.56	zinc finger protein 471
ANXA1	0.58	1.49	0.00	0.56	annexin A1

AGBL5-AS1	0.63	1.54	0.00	0.56	AGBL5 antisense RNA 1
PPCDC	-0.40	-1.32	0.00	0.56	phosphopantothenoylcysteine decarboxylase
LOC105375191	0.68	1.60	0.00	0.56	uncharacterized LOC105375191
GOLGA8R	-0.64	-1.56	0.00	0.56	golgin A8 family member R
CLPSL2	-0.49	-1.40	0.00	0.56	colipase like 2
PER2	0.41	1.33	0.00	0.57	period circadian regulator 2
RNF141	-0.24	-1.18	0.00	0.57	ring finger protein 141
LOC102723409	0.54	1.45	0.00	0.57	uncharacterized LOC102723409
GPR158-AS1	-0.46	-1.38	0.00	0.57	GPR158 antisense RNA 1
MIR596	-0.89	-1.85	0.00	0.58	microRNA 596
C1orf174	0.35	1.27	0.00	0.59	chromosome 1 open reading frame 174
ZXDC	0.33	1.25	0.00	0.59	ZXD family zinc finger C
MID1IP1	-0.36	-1.28	0.00	0.59	MID1 interacting protein 1
SQSTM1	0.24	1.18	0.00	0.59	sequestosome 1
KDM4D	-0.49	-1.41	0.00	0.59	lysine demethylase 4D
LOC105370461	-0.58	-1.50	0.00	0.59	uncharacterized LOC105370461
GSX2	-0.54	-1.45	0.00	0.59	GS homeobox 2
SLC7A6	0.28	1.22	0.00	0.59	solute carrier family 7 member 6
LOC105375392	-0.46	-1.37	0.00	0.59	uncharacterized LOC105375392
OTOPI1	-0.48	-1.39	0.00	0.59	otopetrin 1
PACRG-AS1	-0.43	-1.35	0.00	0.59	PACRG antisense RNA 1
ADA	-0.40	-1.32	0.00	0.59	adenosine deaminase
GRM8-AS1	0.49	1.41	0.00	0.59	GRM8 antisense RNA 1
LOC107984851	-0.49	-1.41	0.00	0.59	uncharacterized LOC107984851
LINC02659	0.43	1.35	0.00	0.59	long intergenic non-protein coding RNA 2659
CHIT1	0.71	1.64	0.00	0.59	chitinase 1
HTN3	0.61	1.52	0.00	0.59	histatin 3
IFRD1	0.32	1.25	0.00	0.59	interferon related developmental regulator 1
LINC01708	-0.44	-1.35	0.00	0.59	long intergenic non-protein coding RNA 1708
APIAR	0.30	1.23	0.00	0.59	adaptor related protein complex 1 associated regulatory protein
FLJ22447	-0.45	-1.37	0.00	0.59	uncharacterized LOC400221
SNORA9B	0.73	1.66	0.00	0.59	small nuclear RNA, H/ACA box 9B
RNU6-797P	0.82	1.76	0.00	0.59	RNA, U6 small nuclear 797, pseudogene
ZBTB20-AS4	-0.38	-1.31	0.00	0.59	ZBTB20 antisense RNA 4
LOC105369864	-1.33	-2.51	0.00	0.59	uncharacterized LOC105369864
ADAMTS3	-0.47	-1.38	0.00	0.59	ADAM metalloproteinase with thrombospondin type 1 motif 3
TIAM2	0.33	1.25	0.00	0.59	TIAM Rac1 associated GEF 2

155

	0.38	1.30	0.00	0.60	ATP binding cassette subfamily C member 5
ABCC5					
NOP16	0.52	1.44	0.00	0.60	NOP16 nucleolar protein
COX7A2	-0.41	-1.33	0.00	0.60	cytochrome c oxidase subunit 7A2
SNORD88C	-0.52	-1.44	0.00	0.60	small nucleolar RNA, C/D box 88C
PLK2	0.61	1.53	0.00	0.60	polo like kinase 2
FAM107B	0.52	1.44	0.01	0.60	family with sequence similarity 107 member B
TRBV25-1	-0.49	-1.41	0.01	0.60	T cell receptor beta variable 25-1
IFNL3	-0.64	-1.56	0.01	0.60	interferon lambda 3
ZNF524	-0.47	-1.39	0.01	0.60	zinc finger protein 524
TRAPPC10	0.20	1.15	0.01	0.60	trafficking protein particle complex 10
PDCD2	0.41	1.33	0.01	0.60	programmed cell death 2
PYHIN1	-0.38	-1.30	0.01	0.60	pyrin and HIN domain family member 1
LINC01333	-0.43	-1.35	0.01	0.60	long intergenic non-protein coding RNA 1333
MBL1P	-0.59	-1.50	0.01	0.60	mammos binding lectin 1, pseudogene
FAM225A	-0.56	-1.48	0.01	0.60	family with sequence similarity 225 member A
GHRH	0.51	1.42	0.01	0.60	growth hormone releasing hormone
PAQR9	-0.69	-1.62	0.01	0.60	progesterin and adipoQ receptor family member 9
FIBCD1	-0.41	-1.33	0.01	0.60	fibrinogen C domain containing 1
LOC112267911	0.66	1.58	0.01	0.60	putative uncharacterized protein FLJ44672
ARHGAP39	0.51	1.42	0.01	0.60	Rho GTPase activating protein 39
ARIH2OS	-0.44	-1.36	0.01	0.60	ariadne RBR E3 ubiquitin protein ligase 2 opposite strand
LOC107986649	-0.70	-1.62	0.01	0.60	uncharacterized LOC107986649
LOC284600	-0.39	-1.31	0.01	0.60	uncharacterized LOC284600
LOC105370515	0.61	1.53	0.01	0.60	uncharacterized LOC105370515
LINC01934	-0.63	-1.55	0.01	0.60	long intergenic non-protein coding RNA 1934
LOC105373496	-0.41	-1.32	0.01	0.60	uncharacterized LOC105373496
DUSP18	0.29	1.23	0.01	0.60	dual specificity phosphatase 18
RANBP1	0.39	1.31	0.01	0.60	RAN binding protein 1
SUPT5H	0.23	1.17	0.01	0.60	SPT5 homolog, DSIF elongation factor subunit
GPR31	0.92	1.89	0.01	0.60	G protein-coupled receptor 31
NLGN4X	-0.56	-1.48	0.01	0.60	neuroligin 4 X-linked
NR2F2-AS1	-0.57	-1.48	0.01	0.60	NR2F2 antisense RNA 1
CYTIP	0.44	1.35	0.01	0.60	cytohesin 1 interacting protein
LINC02443	-0.53	-1.44	0.01	0.60	long intergenic non-protein coding RNA 2443
MIR4759	0.48	1.39	0.01	0.60	microRNA 4759
SMIM23	-0.36	-1.29	0.01	0.60	small integral membrane protein 23
SNORD46	-0.40	-1.32	0.01	0.60	small nucleolar RNA, C/D box 46

KRT14	-0.73	-1.66	0.01	0.60	keratin 14
HTR4	-0.37	-1.29	0.01	0.60	5-hydroxytryptamine receptor 4
MIR4294	0.57	1.49	0.01	0.60	microRNA 4294
LOC105370022	0.62	1.54	0.01	0.60	uncharacterized LOC105370022
MIR544A	-0.57	-1.48	0.01	0.60	microRNA 544a
PDXDC2P-NPIB14P	0.75	1.68	0.01	0.60	nuclear pore complex-interacting protein
BTN3A1	-0.46	-1.37	0.01	0.60	butyrophilin subfamily 3 member A1
PRICKLE1	0.48	1.39	0.01	0.60	prickle planar cell polarity protein 1
ZNF383	0.57	1.49	0.01	0.60	zinc finger protein 383
IFT122	-0.30	-1.23	0.01	0.60	intraflagellar transport 122
SRSF3	0.19	1.14	0.01	0.60	serine and arginine rich splicing factor 3
SPAG11B	-0.76	-1.69	0.01	0.60	sperm associated antigen 11B
VAT1	-0.25	-1.19	0.01	0.60	vesicle amine transport 1
LOC400553	-0.63	-1.55	0.01	0.60	uncharacterized LOC400553
BHLHE23	-0.49	-1.41	0.01	0.60	basic helix-loop-helix family member c23
MIR3119-2	0.37	1.29	0.01	0.60	microRNA 3119-2
MIR1263	-0.43	-1.34	0.01	0.60	microRNA 1263
ZNF385D	-0.37	-1.29	0.01	0.60	zinc finger protein 385D
GPR18	0.38	1.30	0.01	0.60	G protein-coupled receptor 18
RNF31	0.33	1.26	0.01	0.60	ring finger protein 31
BNC2-AS1	-0.43	-1.35	0.01	0.60	BNC2 antisense RNA 1
RNU1-148P	-0.57	-1.48	0.01	0.60	RNA, U1 small nuclear 148, pseudogene
SLC25A32	0.30	1.23	0.01	0.60	solute carrier family 25 member 32
LOC105377127	-0.37	-1.29	0.01	0.60	uncharacterized LOC105377127
KRTAP3-3	0.44	1.36	0.01	0.60	keratin associated protein 3-3
MIG7	-0.44	-1.36	0.01	0.60	mig-7
FLT4	-0.42	-1.33	0.01	0.60	fms related tyrosine kinase 4
ZNF227	0.29	1.22	0.01	0.60	zinc finger protein 227
CCAR1	0.21	1.16	0.01	0.60	cell division cycle and apoptosis regulator 1
AKTIP	0.28	1.22	0.01	0.60	AKT interacting protein
GKAP1	0.45	1.37	0.01	0.60	G kinase anchoring protein 1
TGIF1	0.30	1.23	0.01	0.60	TGFB induced factor homeobox 1
LONRF3	0.49	1.41	0.01	0.60	LON peptidase N-terminal domain and ring finger 3
LOC105370168	-0.47	-1.38	0.01	0.60	uncharacterized LOC105370168
SLC6A18	-0.43	-1.35	0.01	0.60	solute carrier family 6 member 18
MSH2-OT1	-0.62	-1.53	0.01	0.60	MSH2 overlapping transcript 1

LOC107985939	0.59	1.50	0.01	0.60	uncharacterized LOC107985939
LOC105369579	0.49	1.41	0.01	0.60	uncharacterized LOC105369579
LIRC26	-0.48	-1.40	0.01	0.60	leucine rich repeat containing 26
C22orf24	0.55	1.46	0.01	0.60	chromosome 22 open reading frame 24
LOC728660	0.61	1.53	0.01	0.60	uncharacterized LOC728660
DEFB124	-0.52	-1.44	0.01	0.60	defensin beta 124
REG3G	-0.60	-1.51	0.01	0.60	regenerating family member 3 gamma
NDRG1	-0.30	-1.23	0.01	0.60	N-myc downstream regulated 1
MIR181C	-0.51	-1.43	0.01	0.60	microRNA 181c
LOC105372971	-0.40	-1.32	0.01	0.60	uncharacterized LOC105372971
ABCB11	0.40	1.32	0.01	0.60	ATP binding cassette subfamily B member 11
SLC26A8	0.42	1.33	0.01	0.60	solute carrier family 26 member 8
SNORA68	-0.33	-1.26	0.01	0.60	small nucleolar RNA, H/ACA box 68
MCM8-AS1	0.52	1.43	0.01	0.60	MCM8 antisense RNA 1
ENKUR	-0.52	-1.43	0.01	0.60	enkurin, TRPC channel interacting protein
TLE7	-0.45	-1.37	0.01	0.60	TLE family member 7
LGALS1-DT	-0.61	-1.53	0.01	0.60	LGALS1 divergent transcript
RPS28	0.59	1.51	0.01	0.60	ribosomal protein S28
F2RL3	-0.46	-1.38	0.01	0.60	F2R like thrombin or trypsin receptor 3
SPRY4	0.39	1.31	0.01	0.60	sprouty RTK signaling antagonist 4
LLCFC1	-0.57	-1.48	0.01	0.60	LLLL and CFNLAS motif containing 1
LILRB4	-0.56	-1.47	0.01	0.60	leukocyte immunoglobulin like receptor B4
RTP2	-0.42	-1.34	0.01	0.60	receptor transporter protein 2
AVEN	0.40	1.32	0.01	0.60	apoptosis and caspase activation inhibitor
BRPF1	0.35	1.28	0.01	0.60	bromodomain and PHD finger containing 1
ITLN2	-0.51	-1.42	0.01	0.60	intelectin 2
TSNAXIP1	0.40	1.32	0.01	0.60	translin associated factor X interacting protein 1
LINC01291	-0.54	-1.45	0.01	0.60	long intergenic non-protein coding RNA 1291
ATP5MG	0.37	1.29	0.01	0.60	ATP synthase membrane subunit g
KRTAP5-3	-0.61	-1.53	0.01	0.60	keratin associated protein 5-3
SNORA70E	0.64	1.56	0.01	0.60	small nucleolar RNA, H/ACA box 70E
THBS1	0.48	1.40	0.01	0.60	thrombospondin 1
ENC1	0.33	1.26	0.01	0.60	ectodermal-neural cortex 1
LOC105370497	0.36	1.28	0.01	0.60	uncharacterized LOC105370497
MIR181B2	0.52	1.44	0.01	0.60	microRNA 181b-2
SOX18	-0.44	-1.36	0.01	0.60	SRY-box transcription factor 18
RERG	-0.49	-1.40	0.01	0.60	RAS like estrogen regulated growth inhibitor

OMD	-0.34	-1.27	0.01	0.60	osteomodulin
FSD1L	0.42	1.34	0.01	0.60	fibronectin type III and SPRY domain containing 1 like
PCDHGB3	-0.47	-1.39	0.01	0.60	protocadherin gamma subfamily B, 3
SLC30A2	0.69	1.61	0.01	0.60	solute carrier family 30 member 2
LINC00641	0.62	1.54	0.01	0.60	long intergenic non-protein coding RNA 641
ANGPTL6	-0.40	-1.32	0.01	0.61	angiopoietin like 6
ELMO3	-0.34	-1.27	0.01	0.61	engulfment and cell motility 3
LOC105373109	-0.32	-1.25	0.01	0.61	uncharacterized LOC105373109
EPHA2	0.40	1.32	0.01	0.61	EPH receptor A2
LOC112268441	-0.38	-1.30	0.01	0.61	uncharacterized LOC112268441
ADH1	0.29	1.23	0.01	0.61	alcohol dehydrogenase 1
TIMM23	0.25	1.19	0.01	0.61	translocase of inner mitochondrial membrane 23
LOC105374836	1.38	2.60	0.01	0.61	uncharacterized LOC105374836
LOC105376236	0.52	1.44	0.01	0.61	uncharacterized LOC105376236
LOC105373588	0.47	1.39	0.01	0.61	uncharacterized LOC105373588
MPZL2	-0.22	-1.17	0.01	0.61	myelin protein zero like 2
USP43	0.38	1.30	0.01	0.61	ubiquitin specific peptidase 43
ITGB8	0.48	1.40	0.01	0.61	integrin subunit beta 8
TRIM48	0.50	1.41	0.01	0.61	tripartite motif containing 48
SOBP	-0.36	-1.28	0.01	0.61	sine oculis binding protein homolog
SLC12A4	0.26	1.19	0.01	0.61	solute carrier family 12 member 4
EGFLAM-AS4	-0.38	-1.30	0.01	0.61	EGFLAM antisense RNA 4
PCYOX1L	-0.34	-1.27	0.01	0.61	prenylcysteine oxidase 1 like
LOC101929420	-0.44	-1.36	0.01	0.61	uncharacterized LOC101929420
SAMD5	0.46	1.37	0.01	0.61	sterile alpha motif domain containing 5
FGF6	-0.40	-1.32	0.01	0.61	fibroblast growth factor 6
MIR196B	-0.51	-1.43	0.01	0.61	microRNA 196b
KLF17	-0.38	-1.30	0.01	0.61	Kruppel like factor 17
LOC105369649	-0.52	-1.43	0.01	0.61	uncharacterized LOC105369649
TRAV26-1	-0.43	-1.35	0.01	0.61	T cell receptor alpha variable 26-1
FAM92A1P2	-0.50	-1.42	0.01	0.61	family with sequence similarity 92, member A3
CFAP61	-0.39	-1.31	0.01	0.61	cilia and flagella associated protein 61
ECI2	-0.29	-1.22	0.01	0.61	enoyl-CoA delta isomerase 2
CNPY4	0.43	1.35	0.01	0.61	canopy FGF signaling regulator 4
ETS2	0.28	1.21	0.01	0.61	ETS proto-oncogene 2, transcription factor
EIF5A2	0.37	1.29	0.01	0.61	eukaryotic translation initiation factor 5A2
LOC107985819	-0.61	-1.52	0.01	0.61	uncharacterized LOC107985819

LY6G6F- LY6G6D	0.64	1.56	0.01	0.61	LY6G6F-LY6G6D readthrough
TTC6	0.36	1.28	0.01	0.61	tetratricopeptide repeat domain 6
PRH2	-0.53	-1.45	0.01	0.61	proline rich protein HaeIII subfamily 2
LINC01093	-0.54	-1.46	0.01	0.61	long intergenic non-protein coding RNA 1093
LOC102724301	0.48	1.40	0.01	0.61	uncharacterized LOC102724301
LOC100128164	-0.45	-1.37	0.01	0.61	four and a half LIM domains 1 pseudogene
TGFB2-AS1	0.46	1.38	0.01	0.61	TGFB2 antisense RNA 1 (head to head)
MS4A1	-0.48	-1.40	0.01	0.61	membrane spanning 4-domains A1
CLEC5A	-0.31	-1.24	0.01	0.61	C-type lectin domain containing 5A
TTY10	0.43	1.35	0.01	0.61	testis-specific transcript, Y-linked 10
SEC22A	-0.33	-1.25	0.01	0.61	SEC22 homolog A, vesicle trafficking protein
INAFM1	0.57	1.49	0.01	0.61	InaF motif containing 1
KRTAP20-1	-0.78	-1.72	0.01	0.61	keratin associated protein 20-1
PPP2CA	0.29	1.22	0.01	0.61	protein phosphatase 2 catalytic subunit alpha
CHRNA10	0.39	1.31	0.01	0.61	cholinergic receptor nicotinic alpha 10 subunit
KRTAP3-1	0.70	1.62	0.01	0.61	keratin associated protein 3-1
C8orf33	0.31	1.24	0.01	0.61	chromosome 8 open reading frame 33
LOC105370053	-0.38	-1.30	0.01	0.61	uncharacterized LOC105370053
LOC100129203	0.59	1.51	0.01	0.61	uncharacterized LOC100129203
RP2	0.24	1.18	0.01	0.61	RP2 activator of ARL3 GTPase
CPA1	0.35	1.28	0.01	0.61	carboxypeptidase A1
ANAPC11	-0.31	-1.24	0.01	0.61	anaphase promoting complex subunit 11
LOC105373805	-0.42	-1.34	0.01	0.61	uncharacterized LOC105373805
FAM186B	0.39	1.31	0.01	0.61	family with sequence similarity 186 member B
LOC100507548	-0.64	-1.55	0.01	0.61	uncharacterized LOC100507548
RBPJL	-0.41	-1.33	0.01	0.61	recombination signal binding protein for immunoglobulin kappa J region like
SOWAHC	0.35	1.28	0.01	0.61	sosondowah ankyrin repeat domain family member C
NUDT16P1	-0.39	-1.31	0.01	0.61	nudix hydrolase 16 pseudogene 1
SLC22A24	0.41	1.33	0.01	0.61	solute carrier family 22 member 24
ZNRF3-AS1	0.39	1.31	0.01	0.61	ZNRF3 antisense RNA 1
TRAV4	0.61	1.53	0.01	0.61	T cell receptor alpha variable 4
ZNF396	0.44	1.36	0.01	0.61	zinc finger protein 396
NAPA-AS1	-0.36	-1.28	0.01	0.61	NAPA antisense RNA 1
NKD2	-0.43	-1.35	0.01	0.61	NKD inhibitor of WNT signaling pathway 2
MBD1	0.31	1.24	0.01	0.61	methyl-CpG binding domain protein 1

TMEM186	0.35	1.27	0.01	0.61	transmembrane protein 186
LOC100507516	-0.51	-1.43	0.01	0.61	uncharacterized LOC100507516
ZNF30	0.35	1.27	0.01	0.61	zinc finger protein 30
AKR1B1P6	-0.45	-1.37	0.01	0.61	aldo-keto reductase family 1 member B1 pseudogene 6
LOC105370361	-0.37	-1.29	0.01	0.61	uncharacterized LOC105370361
LOC105369435	0.37	1.30	0.01	0.61	uncharacterized LOC105369435
HSPB3	-0.43	-1.35	0.01	0.61	heat shock protein family B (small) member 3
SCAND2P	0.59	1.51	0.01	0.61	SCAN domain containing 2 pseudogene
TEX29	0.52	1.44	0.01	0.61	testis expressed 29
PPM1M	0.35	1.27	0.01	0.62	protein phosphatase, Mg ²⁺ /Mn ²⁺ dependent 1M
LINC02531	-0.41	-1.33	0.01	0.62	long intergenic non-protein coding RNA 2531
CACNG1	-0.47	-1.38	0.01	0.62	calcium voltage-gated channel auxiliary subunit gamma 1
COPRS	0.28	1.21	0.01	0.62	coordinator of PRMT5 and differentiation stimulator
CTC-338M12.4	0.47	1.39	0.01	0.62	uncharacterized LOC101928649
LOC645188	-0.45	-1.37	0.01	0.62	uncharacterized LOC645188
AMELX	0.43	1.35	0.01	0.62	amelogenin X-linked
DKK1	0.50	1.41	0.01	0.62	Dickkopf WNT signaling pathway inhibitor 1
RAP1GDS1	0.31	1.24	0.01	0.62	Rap1 GTPase-GDP dissociation stimulator 1
LINC02365	0.66	1.58	0.01	0.62	long intergenic non-protein coding RNA 2365
SOWAHD	-0.53	-1.44	0.01	0.62	sosondawah ankyrin repeat domain family member D
LOC100289333	0.93	1.91	0.01	0.62	uncharacterized LOC100289333
SPINK14	-0.32	-1.25	0.01	0.62	serine peptidase inhibitor, Kazal type 14 (putative)
SPTBN1	0.13	1.10	0.01	0.62	spectrin beta, non-erythrocytic 1
LRRC75B	-0.35	-1.28	0.01	0.62	leucine rich repeat containing 75B
PCDHB9	0.56	1.48	0.01	0.62	protocadherin beta 9
ANP32D	-0.44	-1.36	0.01	0.62	acidic nuclear phosphoprotein 32 family member D
RNF151	0.35	1.27	0.01	0.62	ring finger protein 151
LOC105370739	-0.64	-1.55	0.01	0.62	uncharacterized LOC105370739
KIRREL3-AS3	0.32	1.25	0.01	0.62	KIRREL3 antisense RNA 3
MIR3688-1	0.34	1.26	0.01	0.62	microRNA 3688-1
SNORD115-48	0.35	1.27	0.01	0.62	small nucleolar RNA, C/D box 115-48
DNAJB13	-0.46	-1.38	0.01	0.62	DnaJ heat shock protein family (Hsp40) member B13
LOC102724800	-0.52	-1.43	0.01	0.62	uncharacterized LOC102724800

PHKA2	0.22	1.17	0.01	0.62	phosphorylase kinase regulatory subunit alpha 2
DAND5	-0.48	-1.39	0.01	0.62	DAN domain BMP antagonist family member 5
SNORA36C	0.48	1.39	0.01	0.62	small nucleolar RNA, H/ACA box 36C
CHD1	0.23	1.17	0.01	0.62	chromodomain helicase DNA binding protein 1
CD2	-0.48	-1.40	0.01	0.62	CD2 molecule
EPAS1	0.24	1.18	0.01	0.62	endothelial PAS domain protein 1
TMEM233	-0.35	-1.27	0.01	0.62	transmembrane protein 233
MIR3650	0.50	1.41	0.01	0.63	microRNA 3650
CPNE8	0.30	1.23	0.01	0.63	copine 8
LOC105373559	-0.37	-1.30	0.01	0.63	uncharacterized LOC105373559
ZNF195	0.70	1.62	0.01	0.63	zinc finger protein 195
CYP4F12	-0.74	-1.68	0.01	0.63	cytochrome P450 family 4 subfamily F member 12
OR4D6	-0.70	-1.63	0.01	0.63	olfactory receptor family 4 subfamily D member 6
GMCL2	-0.50	-1.41	0.01	0.63	germ cell-less 2, spermatogenesis associated
LINC01548	-0.42	-1.34	0.01	0.63	long intergenic non-protein coding RNA 1548
SHISA12B	0.49	1.41	0.01	0.63	shisa like 2B

Supplementary Table 3. Summary results of differentially expressed genes after analysis on the microarray data of nanoparticles exposure to Caco-2 cells for 6 hr. |FC| = log₂ fold change, p.val = p-value.

	TiO ₂		ZnO	
	Transwell	Gut-on-chip	Transwell	Gut-on-chip
log ₂ FC ≥ 1.2	10	53	5	25
p.val < 0.01	275		469	654
FDR < 0.25	4	287	14	268
log ₂ FC and p.val	8	41	5	21
Upregulated	3	11	2	16
Downregulated	5	30	3	5
log ₂ FC and FDR	0	26	0	13

Supplementary Table 4. Differentially expressed genes upon TiO₂ exposure in Caco-2 cells cultured under dynamic and static condition

EntrezID	Gene Symbol	Gene full name	Core function in cells *	Differentially expression	Log2 FC	P-value	FDR
TiO₂ in Transwell							
102724919	LOC102724919	uncharacterized LOC105373215	NA	up	1.72	5.6E-03	9.7E-01
105376839	LOC105376839	uncharacterized LOC105376839	NA	up	1.51	3.6E-04	6.3E-01
283507	SUGT1P3	SUGT1 pseudogene 3	NA	up	1.32	3.9E-03	8.9E-01
102724919	LOC102724919	uncharacterized LOC102724919	NA	down	-1.41	2.0E-03	8.4E-01
101928608	LOC101928608	uncharacterized LOC101928608	NA	down	-1.48	4.7E-04	7.0E-01
283120	H19	H19 imprinted maternally expressed transcript	Non-coding RNA	down	-1.52	1.0E-03	8.0E-01
51351	ZNF117	zinc finger protein 117	DNA binding, Zinc finger	down	-1.64	1.9E-04	4.9E-01
642361	LOC642361	uncharacterized LOC642361	NA	down	-1.68	8.4E-04	8.0E-01
TiO₂ in gut-on-chip							
105369724	LOC105369724	uncharacterized LOC105369724	NA	up	2.18	9.4E-05	1.2E-01
347051	SLC10A5	solute carrier family 10 member 5	Sodium/bile acid cotransporter	up	1.65	1.6E-06	3.3E-02
100033432	SNORD116-21	small nucleolar RNA, C/D box 116-21	NA	up	1.53	2.2E-03	2.4E-01
100528061	LOC100528061	gamma-glutamylcyclotransferase pseudogene	NA	up	1.43	3.4E-05	8.4E-02
100033821	SNORD116-29	small nucleolar RNA, C/D box 116-29	NA	up	1.39	1.2E-03	2.2E-01
3885	KRT34	keratin 34	Cell structure	up	1.38	2.7E-03	2.5E-01
102724810	LINC02062	long intergenic non-protein coding RNA 2062	NA	up	1.37	3.2E-03	2.6E-01
100873856	SNORD116-30	small nucleolar RNA, C/D box 116-30	NA	up	1.30	3.1E-03	2.6E-01
105375913	LOC105375913	uncharacterized LOC105375913	NA	up	1.25	1.9E-03	2.4E-01
55089	SLC38A4	solute carrier family 38 member 4	Sodium-dependent amino acid transporter.	up	1.23	4.2E-03	2.9E-01
101928523	LOC101928523	uncharacterized LOC101928523	NA	up	1.23	1.6E-03	2.3E-01
105374735	LOC105374735	uncharacterized LOC105374735	NA	up	-1.20	6.4E-03	3.2E-01
693166	MIR581	microRNA 581	NA	down	-1.22	8.7E-04	2.1E-01
692211	SNORD98	small nucleolar RNA, C/D box 98	NA	down	-1.23	2.3E-03	2.5E-01
55096	EBLN2	endogenous Bornavirus like nucleoprotein 2	RNA-binding	down	-1.24	1.8E-04	1.4E-01
574508	MIR505	microRNA 505	NA	down	-1.25	3.6E-03	2.8E-01

693229	MIR644A	microRNA 644a	NA	down	-1.27	2.6E-03	2.5E-01
109617024	SNORD38C	small nucleolar RNA, C/D box 38C	NA	down	-1.29	1.9E-03	2.4E-01
100616471	MIR4798	microRNA 4798	NA	down	-1.29	1.8E-03	2.3E-01
4495	MT1G	metallothionein 1G	Mineral absorption, Metal binding	down	-1.34	2.8E-03	2.6E-01
3	FLJ42393	uncharacterized LOC401105	NA	down	-1.36	3.4E-05	8.4E-02
100422865	MIR4320	microRNA 4320	NA	down	-1.36	9.1E-03	3.6E-01
100124537	SNORA70B	small nucleolar RNA, H/ACA box 70B	NA	down	-1.37	2.2E-03	2.4E-01
109616974	SNORA74C-1	small nucleolar RNA, H/ACA box 74C-1	NA	down	-1.37	5.7E-03	3.1E-01
100616668	TPTE2P5	transmembrane phosphoinositide 3-phosphatase and tensin homolog 2 pseudogene 5	NA	down	-1.39	7.1E-03	3.3E-01
151877	MAGI1-JT1	MAGI1 intronic transcript 1	Non-coding RNA	down	-1.41	1.1E-04	1.2E-01
259294	TAS2R19	taste 2 receptor member 19	Taste receptor	down	-1.41	1.1E-03	2.2E-01
259295	TAS2R20	taste 2 receptor member 20	Taste receptor	down	-1.44	1.3E-03	2.3E-01
100422850	MIR548V	microRNA 548v	NA	down	-1.45	1.3E-03	2.3E-01
100499484	SUGT1P4-STR46LP	SUGT1P4-STR46LP readthrough	NA	down	-1.47	3.0E-03	2.6E-01
27099	SND1-JT1	SND1 intronic transcript 1	NA	down	-1.48	1.2E-04	1.2E-01
677818	SNORA36B	small nucleolar RNA, H/ACA box 36B	NA	down	-1.50	4.6E-04	1.9E-01
145474	LOC145474	uncharacterized LOC145474	NA	down	-1.51	4.1E-04	1.8E-01
493861	EID3	EP300 interacting inhibitor of differentiation 3	DNA repair/Transcription regulation	down	-1.52	3.5E-04	1.6E-01
50840	TAS2R14	taste 2 receptor member 14	Taste receptor	down	-1.53	8.3E-04	2.1E-01
693164	MIR579	microRNA 579	NA	down	-1.56	6.8E-04	2.1E-01
106480618	RNU6-890P	RNA, U6 small nuclear 890, pseudogene	NA	down	-1.60	3.3E-03	2.7E-01
101927967	LOC101927967	uncharacterized LOC101927967	NA	down	-1.72	1.5E-04	1.3E-01
100313770	MIR548K	microRNA 548k	NA	down	-1.75	5.6E-03	3.1E-01
100616114	MIR4668	microRNA 4668	NA	down	-1.95	2.2E-03	2.4E-01
693129	MIR548C	microRNA 548c	NA	down	-2.13	6.34E-03	3.20E-01

*References on the gene functions are provided in the table below

Gene Symbol	Core function in cells *	NCBI Database ¹	KEGG Pathway Database ²	Publications
TiO₂ in Transwell				
LOC102724919	NA	-	-	-
LOC105376839	NA	-	-	-
SUGTIP3	NA	-	-	-
LOC102724919	NA	-	-	-
LOC101928608	NA	-	-	-
HI9	Non-coding RNA	-	-	-
ZNF117	DNA binding, Zinc finger	X	X	(Li et al., 1999)
LOC642361	NA	-	-	-
TiO₂ in gut-on-chip				
LOC105369724	NA	-	-	-
SLC10A5	Sodium/bile acid cotransporter	X	X	(Fernandes et al., 2007)
SNORD116-21	NA	-	-	-
LOC100528061	NA	-	-	-
SNORD116-29	NA	-	-	-
KRT34	Cell structure	X	X	(Giesen et al., 2011)
LINC02062	NA	-	-	-
SNORD116-30	NA	-	-	-
LOC105375913	NA	-	-	-
SLC38A4	Sodium-dependent amino acid transporter.	X	X	(Lin et al., 2014)
LOC101928523	NA	-	-	-
LOC105374735	NA	-	-	-
MIR581	NA	-	-	-
SNORD98	NA	-	-	-
EBLN2	RNA-binding	X	X	-
MIR505	NA	-	-	-
MIR644A	NA	-	-	-
SNORD38C	NA	-	-	-
MIR4798	NA	-	-	-

MTIG	Mineral absorption, Metal binding	X	X	(Cheng et al., 2012, Dzięgiel et al., 2016, Subramanian Vignesh and Deepe, 2017)
FLJ42393	NA	-	-	-
MIR4320	NA	-	-	-
SNORA70B	NA	-	-	-
SNORA74C-1	NA	-	-	-
TPTE2P5	NA	-	-	-
MAG11-IT1	NA	-	-	-
TAS2R19	Taste receptor	X	X	(Kaji et al., 2009, Yanagihara et al., 2012)
TAS2R20	Taste receptor	X	X	(Kaji et al., 2009, Yanagihara et al., 2012)
MIR548V	NA	-	-	-
SUGTIP4-STRA6LP	NA	-	-	-
SNDI-IT1	NA	-	-	-
SNORA36B	NA	-	-	-
LOC145474	NA	-	-	-
EID3	DNA repair/ Transcription regulation	X	X	(Sasajima et al., 2005, Wang et al., 2018)
TAS2R14	Taste receptor	X	X	(Yanagihara et al., 2012, Kaji et al., 2009)
MIR579	NA	-	-	-
RNU6-890P	NA	-	-	-
LOC101927967	NA	-	-	-
MIR548K	NA	-	-	-
MIR4668	NA	-	-	-
MIR548C	NA	-	-	-

¹ <https://www.ncbi.nlm.nih.gov/gene>

² <https://www.genome.jp/kegg/genes.html>

• CHENG, Z., TAKO, E., YEUNG, A., WELCH, R. M. & GLAHN, R. P. 2012. Evaluation of metallothionein formation as a proxy for zinc absorption in an in vitro digestion/Caco-2 cell culture model. *Food Funct.* 3, 732-6.

• DZIEGIEL, P., PULA, B., KOBIERZYCKI, C., STASIOLEK, M. & PODHORSKA-OKOLOW, M. 2016. Metallothioneins in Normal and Cancer Cells. *Adv. Anat. Embryol. Cell Biol.* 218, 1-117.

• FERNANDES, C. F., GODOY, J. R., DORING, B., CAVALCANTI, M. C., BERGMANN, M., PETZINGER, E. & GEYER, J. 2007. The novel putative bile acid transporter SLC10A5 is highly expressed in liver and kidney. *Biochem Biophys Res Commun.* 361, 26-32.

• GIESEN, M., GRUEDL, S., HOLTKOETTER, O., FUHRMANN, G., KOERNER, A. & PETERSOHN, D. 2011. Ageing processes influence keratin and KAP expression in human hair follicles. *Exp Dermatol.* 20, 759-61.

• KAJI, I., KARAKI, S., FUKAMI, Y., TERASAKI, M. & KUWAHARA, A. 2009. Secretory effects of a luminal bitter tastant and expressions of bitter taste receptors, T2Rs, in the human and rat large intestine. *Am. J. Physiol. Gastrointest Liver Physiol.* 296, G971-81.

• LI, X. A., KOKAME, K., OKUBO, K., SHIMOKADO, K., TSUKAMOTO, Y., MIYATA, T., KATO, H. & YUTANI, C. 1999. Cloning and characterization of a novel human gene encoding a zinc finger protein with 25 fingers. *Biochim Biophys Acta.* 1489, 405-12.

• LIN, Y., FANG, Z. F., CHE, L. Q., XU, S. Y., WU, D., WU, C. M. & WU, X. Q. 2014. Use of sodium butyrate as an alternative to dietary fiber: effects on the embryonic development and anti-oxidative capacity of rats. *PLoS One.* 9, e97838.

• SASAJIMA, Y., TANAKA, H., MIYAKE, S. & YUASA, Y. 2005. A novel EID family member, EID-3, inhibits differentiation and forms a homodimer or heterodimer with EID-2. *Biochem Biophys Res Commun.* 333, 969-75.

• SUBRAMANIAN VIGNESH, K. & DEEPE, G. S., JR. 2017. Metallothioneins: Emerging Modulators in Immunity and Infection. *Int. J. Mol. Sci.* 18.

• WANG, Y., WANG, Y., LIU, S., LIU, Y., XU, H., LIANG, J., ZHU, J., ZHANG, G., SU, W., DONG, W. & GUO, Q. 2018. Upregulation of EID3 sensitizes breast cancer cells to ionizing radiation-induced cellular senescence. *Biomed Pharmacother.* 107, 606-614.

• YANAGIHARA, S., FUKUDA, S., OHNO, H. & YAMAMOTO, N. 2012. Exposure to probiotic *Lactobacillus acidophilus* L-92 modulates gene expression profiles of epithelial Caco-2 cells. *J. Med. Food.* 15, 511-9.

Supplementary Table 5. Differentially expressed genes upon ZnO exposure in Caco-2 cells cultured under dynamic and static condition

EntrezID	Gene Symbol	Gene full name	Core function in cells *	Differentially expression	Log2 FC	P-value	FDR
ZnO in Transwell							
693129	MIR548C	microRNA 548c	NA	up	1.39	2.4E-02	6.9E-01
105374836	LOC105374836	uncharacterized LOC105374836	NA	up	1.38	7.5E-03	6.1E-01
106480140	RNU6-1316P	RNA, U6 small nuclear 1316, pseudogene	NA	up	1.21	6.4E-04	4.1E-01
105379090	LOC105379090	uncharacterized LOC105379090	NA	down	-1.24	1.2E-03	4.7E-01
105369864	LOC105369864	uncharacterized LOC105369864	NA	down	-1.33	4.0E-03	5.9E-01

ZnO in gut-on-chip

4490	MT1B	metallothionein 1B	Mineral absorption, Metal binding	up	4.88	2.8E-09	4.2E-05
4489	MT1A	metallothionein 1A	Mineral absorption, Metal binding	up	4.31	2.0E-10	5.9E-06
4499	MT1M	metallothionein 1M	Mineral absorption, Metal binding	up	4.03	2.4E-06	6.6E-03
4493	MT1E	metallothionein 1E	Mineral absorption, Metal binding	up	2.27	1.3E-04	5.7E-02
3310	HSPA6	heat shock protein family A (Hsp70) member 6	Stress response	up	2.11	6.3E-03	3.7E-01
326343	MT1DP	metallothionein 1D, pseudogene	NA	up	1.98	4.6E-05	3.2E-02
4495	MT1G	metallothionein 1G	Mineral absorption, Metal binding	up	1.94	8.4E-05	4.3E-02
4496	MT1H	metallothionein 1H	Mineral absorption, Metal binding	up	1.88	1.3E-03	2.0E-01
7780	SLC30A2	solute carrier family 30 member 2	Ion/zinc transporter	up	1.51	2.7E-05	2.7E-02
105369942	LINC02456	long intergenic non-protein coding RNA 2456	NA	up	1.41	8.5E-03	4.2E-01
122748	OR11H6	olfactory receptor family 11 subfamily H member 6	Olfaction receptor, Sensory transduction	up	1.34	1.3E-03	2.0E-01
1959	EGR2	early growth response 2	Transcription regulation	up	1.32	1.5E-05	1.8E-02
4500	MT1L	metallothionein 1L, pseudogene	NA	up	1.26	5.3E-05	3.6E-02
4616	GADD45B	growth arrest and DNA damage inducible beta	Cell growth inhibition, DNA-damage response	up	1.22	2.9E-06	7.1E-03
6004	RGS16	regulator of G protein signaling 16	Signal transduction inhibitor	up	1.21	1.3E-04	5.6E-02
728386	USP17L5	ubiquitin specific peptidase 17 like family member 5	Protein metabolism, Ubiquitination	up	1.21	3.7E-03	3.1E-01
112268112	LOC112268112	uncharacterized LOC112268112	NA	down	-1.14	6.8E-04	1.4E-01
729894	ELMO2P1	engulfment and cell motility 2 pseudogene 1	NA	down	-1.15	6.6E-03	3.8E-01
100422850	MIR548V	microRNA 548v	NA	down	-1.16	9.0E-03	4.3E-01

* References on the gene functions are provided in the table below

Gene Symbol	Core function in cells	NCBI Database ¹	KEGG Pathway Database ²	Publications
ZnO in Transwell				
MIR548C	NA	-	-	-
LOC105374836	NA	-	-	-
RNU6-1316P	NA	-	-	-
LOC105379090	NA	-	-	-
LOC105369864	NA	-	-	-
ZnO in gut-on-chip				
MT1B	Mineral absorption, Metal binding	X	X	(Cheng et al., 2012, Dziegiel et al., 2016, Subramanian Vignesh and Deepe, 2017)
MT1A	Mineral absorption, Metal binding	X	X	(Cheng et al., 2012, Dziegiel et al., 2016, Subramanian Vignesh and Deepe, 2017)
MT1M	Mineral absorption, Metal binding	X	X	(Cheng et al., 2012, Dziegiel et al., 2016, Subramanian Vignesh and Deepe, 2017)
MT1E	Mineral absorption, Metal binding	X	X	(Cheng et al., 2012, Dziegiel et al., 2016, Subramanian Vignesh and Deepe, 2017)
HSPA6	Stress response	X	X	(Daugaard et al., 2007, Malago et al., 2003, Leung et al., 1990)
MT1DP	NA	-	-	-
MT1G	Mineral absorption, Metal binding	X	X	(Cheng et al., 2012, Dziegiel et al., 2016, Subramanian Vignesh and Deepe, 2017)
MT1H	Mineral absorption, Metal binding	X	X	(Cheng et al., 2012, Dziegiel et al., 2016, Subramanian Vignesh and Deepe, 2017)
SLC30A2	Ion/zinc transporter	X	X	(van den Bosch et al., 2007, Palmiter and Huang, 2004)
LINC02456	NA	-	-	-
OR11H6	Olfaction receptor, Sensory transduction	X	X	(Malnic et al., 2004)
EGR2	Transcription regulation	X	X	(Taelehsokhr et al., 2017, Kinga Szigei, 2007)
MT1L	NA	-	-	-
GADD45B	Cell growth inhibition, DNA-damage response	X	X	(Wang et al., 2012, Hoffman and Liebermann, 2009, Youns and Abdel Halim Hegazy, 2017)
RGS16	Signal transduction inhibitor	X	X	(Salaga et al., 2016, Samina Salim, 2004)

USP17L5	Protein metabolism, Ubiquitination	X	X	(de la Vega et al., 2011, McFarlane et al., 2010, Shin et al., 2006)
---------	------------------------------------	---	---	----------------------------------------------------------------------

LOC112268112	NA	-	-	-
ELMO2P1	NA	-	-	-
MIR548V	NA	-	-	-
LOC105375207	NA	-	-	-
LNCRNA-ATB	NA	-	-	-

¹ <https://www.ncbi.nlm.nih.gov/gene>

² <https://www.genome.jp/kegg/genes.html>

- HENG, Z., TAKO, E., YEUNG, A., WELCH, R. M. & GLAHN, R. P. 2012. Evaluation of metallothionein formation as a proxy for zinc absorption in an in vitro digestion/Caco-2 cell culture model. *Food Funct.* 3, 732-6.
- DAUGAARD, M., ROHDE, M. & JAATTELA, M. 2007. The heat shock protein 70 family: Highly homologous proteins with overlapping and distinct functions. *FEBS Lett.* 581, 3702-10.
- DE LA VEGA, M., KELVIN, A. A., DUNICAN, D. J., MCFARLANE, C., BURROWS, J. F., JAWORSKI, J., STEVENSON, N. J., DIB, K., RAPPOPORT, J. Z., SCOTT, C. J., LONG, A. & JOHNSTON, J. A. 2011. The deubiquitinating enzyme USP17 is essential for GTPase subcellular localization and cell motility. *Nat Commun.* 2, 259.
- DZIEGIEL, P., PULA, B., KOBIERZYCKI, C., STASIOLEK, M. & PODHORSKA-OKOLOW, M. 2016. Metallothioneins in Normal and Cancer Cells. *Adv Anat Embryol Cell Biol.* 218, 1-117.
- HOFFMAN, B. & LIEBERMANN, D. A. 2009. Gadd45 modulation of intrinsic and extrinsic stress responses in myeloid cells. *J Cell Physiol.* 218, 26-31.
- KINGA SZIGETI, J. R. L. 2007. INHERITED NEUROPATHIES. In: ANTHONY H.V. SCHAPIRA, E. B., SALVATORE DIMAURO, RICHARD S.J. FRACKOWIAK, RICHARD T. JOHNSON, YOSHIKUNI MIZUNO, MARTIN A. SAMUELS, STEPHEN D. SILBERSTEIN, ZBIGNIEW K. WSZOLEK, (ed.) *Neurology and Clinical Neuroscience*. Mosby.
- LEUNG, T. K., RAJENDRAN, M. Y., MONFRIES, C., HALL, C. & LIM, L. 1990. The human heat-shock protein family. Expression of a novel heat-inducible HSP70 (HSP70B) and isolation of its cDNA and genomic DNA. *Biochem J.* 267, 125-32.
- MALAGO, J. J., KONINKX, J. F., OVELGONNE, H. H., VAN ASTEN, F. J., SWENNENHUIS, J. F. & VAN DIJK, J. E. 2003. Expression levels of heat shock proteins in enterocyte-like Caco-2 cells after exposure to Salmonella enteritidis. *Cell Stress Chaperones*, 8, 194-203.
- MALNIC, B., GODFREY, P. A. & BUCK, L. B. 2004. The human olfactory receptor gene family. *Proc Natl Acad Sci U S A.* 101, 2584-9.
- MCFARLANE, C., KELVIN, A. A., DE LA VEGA, M., GOVENDER, U., SCOTT, C. J., BURROWS, J. F. & JOHNSTON, J. A. 2010. The deubiquitinating enzyme USP17 is highly expressed in tumor biopsies, is cell cycle regulated, and is required for G1-S progression. *Cancer Res.* 70, 3329-39.
- PALMITER, R. D. & HUANG, L. 2004. Efflux and compartmentalization of zinc by members of the SLC30 family of solute carriers. *Physiol Rev.* 447, 744-51.
- SALAGA, M., STORR, M., MARTEM'YANOV, K. A. & FICHNA, J. 2016. RGS proteins as targets in the treatment of intestinal inflammation and visceral pain: New insights and future perspectives. *Bioessays*, 38, 344-54.
- SAMINA SALIM, C. W. D. 2004. Analysis of the Interaction between RGS2 and Adenyllyl Cyclase. In: SIDEROVSKI, D. P. (ed.) *Methods in Enzymology*. Academic Press.
- SHIN, J. M., YOO, K. J., KIM, M. S., KIM, D. & BAEK, K. H. 2006. Hyaluronan- and RNA-binding deubiquitinating enzymes of USP17 family members associated with cell viability. *BMC Genomics*, 7, 292.
- SUBRAMANIAN VIGNESH, K. & DEEPE, G. S., JR. 2017. Metallothioneins: Emerging Modulators in Immunity and Infection. *Int J Mol Sci.* 18.
- TAEFESHOKR, S., KEY, Y. A., KHAKPOUR, M., DADEBIGHLU, P. & OVEISI, A. 2017. Early growth response 2 and Egr3 are unique regulators in immune system. *Cent Eur J Immunol.* 42, 205-209.
- VAN DEN BOSCH, H. M., BUNGER, M., DE GROOT, P. J., VAN DER MEIJDE, J., HOOIVELD, G. J. & MULLER, M. 2007. Gene expression of transporters and phase I/II metabolic enzymes in murine small intestine during fasting. *BMC Genomics*, 8, 267.
- WANG, L., XIAO, X., LI, D., CHI, Y., WEI, P., WANG, Y., NI, S., TAN, C., ZHOU, X. & DU, X. 2012. Abnormal expression of GADD45B in human colorectal carcinoma. *J Transl Med.* 10, 215.

Supplementary Table 6. Downregulated pathways upon TiO₂ exposure of Caco-2 cells cultured in Transwell

KEGG pathway name	KEGG Category	KEGG category subgroup	SIZE	ES	NES	NOM p-val	FDR q-val
Allograft rejection	Human diseases	Immune disease	35	-0.506	-1.800	0.001	0.142
Graft versus host disease	Human diseases	Immune disease	37	-0.493	-1.772	0.002	0.098
Type I diabetes mellitus	Human diseases	Endocrine and metabolic disease	41	-0.474	-1.738	0.003	0.095
Intestinal immune network for IgA production	Organismal systems	Immune system	44	-0.451	-1.691	0.006	0.112
Autoimmune thyroid disease	Human diseases	Immune disease	48	-0.418	-1.593	0.011	0.219

Supplementary Table 7. Downregulated pathways upon TiO₂ exposure of Caco-2 cells cultured in gut-on-chip

KEGG pathway name	KEGG Category	KEGG category subgroup	SIZE	ES	NES	NOM p-val	FDR q-val
Homologous recombination	Genetic information processing	Replication and repair	41	-0.557	-2.050	0.000	0.008
Carbon metabolism	Metabolism	Global and overview maps	114	-0.449	-2.040	0.000	0.004
Pyruvate metabolism	Metabolism	Carbohydrate metabolism	39	-0.536	-1.965	0.000	0.009
Propanoate metabolism	Metabolism	Carbohydrate metabolism	33	-0.542	-1.894	0.000	0.017
DNA replication	Genetic information processing	Replication and repair	36	-0.522	-1.880	0.001	0.017
Fanconi anemia pathway	Genetic information processing	Replication and repair	50	-0.478	-1.857	0.000	0.019
Fatty acid biosynthesis	Metabolism	Lipid metabolism	17	-0.615	-1.820	0.006	0.024
Glyoxylate and dicarboxylate metabolism	Metabolism	Carbohydrate metabolism	29	-0.522	-1.775	0.004	0.034
Valine, leucine and isoleucine degradation	Metabolism	Amino acid metabolism	47	-0.457	-1.747	0.003	0.041
Amino sugar and nucleotide sugar metabolism	Metabolism	Carbohydrate metabolism	47	-0.444	-1.710	0.003	0.053
ECM-receptor interaction	Environmental information processing	Signaling molecules and interaction	85	-0.387	-1.670	0.001	0.070
One carbon pool by folate	Metabolism	Metabolism of cofactors and vitamins	19	-0.545	-1.668	0.015	0.065
Cysteine and methionine metabolism	Metabolism	Amino acid metabolism	47	-0.434	-1.654	0.006	0.068
Fatty acid degradation	Metabolism	Lipid metabolism	43	-0.436	-1.648	0.007	0.067
Taste transduction	Organismal systems	Sensory system	81	-0.383	-1.638	0.002	0.068
Butanoate metabolism	Metabolism	Carbohydrate metabolism	28	-0.478	-1.612	0.016	0.081
Fatty acid metabolism	Metabolism	Global and overview maps	55	-0.403	-1.598	0.011	0.086
HIF-1 signaling pathway	Environmental information processing	Signal transduction	99	-0.359	-1.596	0.003	0.083
Glycolysis/gluconeogenesis	Metabolism	Carbohydrate metabolism	68	-0.386	-1.592	0.007	0.081
Small cell lung cancer	Human diseases	Cancer: specific types	93	-0.359	-1.576	0.004	0.089

Lysine degradation	Metabolism	Amino acid metabolism	59	-0.383	-1.539	0.013	0.115
Ubiquitin mediated proteolysis	Genetic information processing	Folding, sorting and degradation	136	-0.330	-1.536	0.002	0.112
Pyrimidine metabolism	Metabolism	Nucleotide metabolism	54	-0.388	-1.534	0.017	0.110
Biosynthesis of amino acids	Metabolism	Global and overview maps	71	-0.359	-1.499	0.012	0.140
Peroxisome	Cellular processes	Transport and catabolism	82	-0.347	-1.484	0.009	0.151
Fructose and mannose metabolism	Metabolism	Carbohydrate metabolism	32	-0.422	-1.483	0.038	0.146
Glutathione metabolism	Metabolism	Metabolism of other amino acids	51	-0.378	-1.479	0.024	0.145
Purine metabolism	Metabolism	Nucleotide metabolism	125	-0.319	-1.470	0.008	0.151
Central carbon metabolism in cancer	Human diseases	Cancer: overview	65	-0.358	-1.467	0.021	0.148
Phosphatidylinositol signaling system	Environmental information processing	Signal transduction	99	-0.330	-1.464	0.013	0.146
Inositol phosphate metabolism	Metabolism	Carbohydrate metabolism	74	-0.350	-1.461	0.018	0.145
Insulin secretion	Organismal systems	Endocrine system	86	-0.338	-1.458	0.018	0.144
ABC transporters	Environmental information processing	Membrane transport	45	-0.378	-1.439	0.042	0.157
Focal adhesion	Cellular processes	Cellular community - eukaryotes	195	-0.286	-1.401	0.010	0.204
Progesterone-mediated oocyte maturation	Organismal systems	Endocrine system	93	-0.319	-1.399	0.030	0.201
AMPK signaling pathway	Environmental information processing	Signal transduction	119	-0.304	-1.387	0.022	0.214
Cell cycle	Cellular processes	Cell growth and death	124	-0.297	-1.366	0.025	0.243
Thermogenesis	Organismal systems	Environmental adaptation	212	-0.275	-1.357	0.014	0.246

Supplementary Table 8. Upregulated pathways upon ZnO exposure of Caco-2 cells cultured in Transwell

KEGG pathway name	KEGG Category	KEGG category subgroup	SIZE	ES	NES	NOM p-val	FDR q-val
mRNA surveillance pathway	Genetic information processing	Translation	87	0.472	2.062	0.000	0.009
Ribosome biogenesis in eukaryotes	Genetic information processing	Translation	76	0.482	2.059	0.000	0.005
RNA transport	Genetic information processing	Translation	146	0.407	1.943	0.000	0.013
Mineral absorption	Organismal systems	Digestive system	49	0.477	1.862	0.000	0.028
Spliceosome	Genetic information processing	Transcription	128	0.387	1.807	0.000	0.040
TGF Beta signaling pathway	Environmental information processing	Signal transduction	92	0.394	1.747	0.000	0.063

Basal transcription factors	Genetic information processing	Transcription	42	0.450	1.698	0.007	0.087
Hippo signaling pathway	Environmental information processing	Signal transduction	150	0.346	1.656	0.000	0.113
Autophagy-other	Cellular processes	Transport and catabolism	31	0.466	1.639	0.014	0.117
Viral carcinogenesis	Human diseases	Cancer: overview	162	0.338	1.634	0.000	0.111
Cell cycle	Cellular processes	Cell growth and death	124	0.352	1.632	0.001	0.102
Herpes simplex virus 1 infection	Human diseases	Infectious disease: viral	476	0.291	1.595	0.000	0.129
Cellular senescence	Cellular processes	Cell growth and death	158	0.327	1.579	0.001	0.137
Protein processing in endoplasmic reticulum	Genetic information processing	Folding, sorting and degradation	160	0.325	1.563	0.000	0.146
Colorectal cancer	Human diseases	Cancer: specific types	86	0.357	1.562	0.006	0.136
Pancreatic cancer	Human diseases	Cancer: specific types	75	0.363	1.547	0.008	0.146
Chronic myeloid leukemia	Human diseases	Cancer: specific types	76	0.362	1.544	0.009	0.141
Ubiquitin mediated proteolysis	Genetic information processing	Folding, sorting and degradation	136	0.325	1.530	0.002	0.150
Thyroid hormone signaling pathway	Organismal systems	Endocrine system	118	0.333	1.526	0.007	0.147
Human T-cell leukemia virus 1 infection	Human diseases	Infectious disease: viral	217	0.302	1.521	0.003	0.145
Hippo signaling pathway-multiple species	Environmental information processing	Signal transduction	28	0.445	1.519	0.035	0.141
Small cell lung cancer	Human diseases	Cancer: specific types	93	0.341	1.508	0.009	0.146
Adherens junction	Cellular processes	Cellular community - eukaryotes	71	0.360	1.508	0.014	0.141
Ferroptosis	Cellular processes	Cell growth and death	39	0.403	1.496	0.029	0.148
Pathogenic Escherichia coli infection	Human diseases	Infectious disease: bacterial	53	0.373	1.486	0.027	0.154
Mitophagy-animal	Cellular processes	Transport and catabolism	64	0.354	1.462	0.029	0.178
Autophagy-animal	Cellular processes	Transport and catabolism	127	0.313	1.457	0.008	0.177
Epithelial cell signaling in helicobacter pylori infection	Human diseases	Infectious disease: bacterial	70	0.346	1.456	0.023	0.173
RNA degradation	Genetic information processing	Folding, sorting and degradation	78	0.340	1.448	0.027	0.177
Renal cell carcinoma	Human diseases	Cancer: specific types	66	0.347	1.445	0.026	0.176
Lysine degradation	Metabolism	Amino acid metabolism	59	0.354	1.443	0.032	0.172
Prostate cancer	Human diseases	Cancer: specific types	97	0.321	1.434	0.022	0.179
Endometrial cancer	Human diseases	Cancer: specific types	58	0.348	1.409	0.043	0.209
TNF signaling pathway	Environmental information processing	Signal transduction	110	0.309	1.405	0.024	0.209
FoxO signaling pathway	Environmental information processing	Signal transduction	129	0.300	1.402	0.018	0.200
Signaling pathways regulating pluripotency of stem cells	Cellular processes	Cellular community - eukaryotes	135	0.298	1.398	0.022	0.202

Supplementary Table 9. Downregulated pathways upon ZnO exposure of Caco-2 cells cultured in Transwell

KEGG pathway name	KEGG Category	KEGG category subgroup	SIZE	ES	NES	NOM p-val	FDR q-val
Fructose and mannose metabolism	Metabolism	Carbohydrate metabolism	32	-0.560	-1.965	0.000	0.021
Propanoate metabolism	Metabolism	Carbohydrate metabolism	33	-0.490	-1.736	0.004	0.152
Glycolysis/gluconeogenesis	Metabolism	Carbohydrate metabolism	68	-0.411	-1.708	0.002	0.132
Hematopoietic cell lineage	Organismal systems	Immune system	91	-0.391	-1.707	0.001	0.099
Folate biosynthesis	Metabolism	Metabolism of cofactors and vitamins	26	-0.505	-1.700	0.008	0.085
Galactose metabolism	Metabolism	Carbohydrate metabolism	31	-0.466	-1.628	0.014	0.137
Phototransduction	Organismal systems	Sensory system	28	-0.473	-1.615	0.018	0.131
Staphylococcus aureus infection	Human diseases	Infectious disease: bacterial	57	-0.400	-1.604	0.009	0.127
Valine, leucine and isoleucine degradation	Metabolism	Amino acid metabolism	47	-0.407	-1.568	0.013	0.155
Oxidative phosphorylation	Metabolism	Energy metabolism	116	-0.338	-1.543	0.004	0.172
Carbon metabolism	Metabolism	Global and overview maps	114	-0.336	-1.531	0.004	0.173
Primary immunodeficiency	Human diseases	Immune disease	36	-0.424	-1.529	0.023	0.160
Citrate cycle (TCA cycle)	Metabolism	Carbohydrate metabolism	29	-0.440	-1.522	0.032	0.157
Maturity onset diabetes of the young	Human diseases	Endocrine and metabolic disease	26	-0.442	-1.480	0.050	0.206
Fat digestion and absorption	Organismal systems	Digestive system	41	-0.391	-1.461	0.037	0.223

Supplementary Table 10. Upregulated pathways upon ZnO exposure of Caco-2 cells cultured in gut-on-chip

KEGG pathway name	KEGG Category	KEGG category subgroup	SIZE	ES	NES	NOM p-val	FDR q-val
Mineral absorption	Organismal systems	Digestive system	49	0.650	2.439	0.000	0.000
Protein processing in endoplasmic reticulum	Genetic information processing	Folding, sorting and degradation	160	0.518	2.375	0.000	0.000
Legionellosis	Human diseases	Infectious disease: bacterial	53	0.598	2.272	0.000	0.000
Mitophagy-animal	Cellular processes	Transport and catabolism	64	0.542	2.138	0.000	0.001
Apoptosis	Cellular processes	Cell growth and death	133	0.464	2.077	0.000	0.001
SNARE interactions in vesicular transport	Genetic information processing	Folding, sorting and degradation	33	0.598	2.059	0.000	0.001
Apoptosis-multiple species	Cellular processes	Cell growth and death	31	0.602	2.035	0.000	0.001
Toxoplasmosis	Human diseases	Infectious disease: parasitic	111	0.445	1.934	0.000	0.006
Fluid shear stress and atherosclerosis	Human diseases	Cardiovascular disease	131	0.429	1.910	0.000	0.007
Measles	Human diseases	Infectious disease: viral	136	0.420	1.895	0.000	0.007
MAPK signaling pathway	Environmental information processing	Signal transduction	292	0.383	1.891	0.000	0.007
Jak-STAT signaling pathway	Environmental information processing	Signal transduction	158	0.404	1.862	0.000	0.009
Tight junction	Cellular processes	Cellular community - eukaryotes	168	0.390	1.812	0.000	0.015

Autophagy-animal	Cellular processes	Transport and catabolism	127	0.408	1.811	0.000	0.014
Herpes simplex virus 1 infection	Human diseases	Infectious disease: viral	476	0.341	1.772	0.000	0.020
Estrogen signaling pathway	Organismal systems	Endocrine system	136	0.390	1.752	0.000	0.023
Hepatitis B	Human diseases	Infectious disease: viral	160	0.378	1.735	0.000	0.026
Osteoclast differentiation	Organismal systems	Development and regeneration	122	0.386	1.710	0.001	0.032
P53 signaling pathway	Cellular processes	Cell growth and death	72	0.423	1.710	0.002	0.030
TNF signaling pathway	Environmental information processing	Signal transduction	110	0.394	1.703	0.001	0.031
Pertussis	Human diseases	Infectious disease: bacterial	73	0.419	1.701	0.001	0.030
Epithelial cell signaling in Helicobacter pylori infection	Human diseases	Infectious disease: bacterial	70	0.423	1.696	0.002	0.030
Prion diseases	Human diseases	Neurodegenerative disease	35	0.484	1.691	0.008	0.030
Tuberculosis	Human diseases	Infectious disease: bacterial	172	0.363	1.684	0.000	0.031
Hippo signaling pathway-multiple species	Environmental information processing	Signal transduction	28	0.510	1.681	0.009	0.031
Ferroptosis	Cellular processes	Cell growth and death	39	0.467	1.663	0.008	0.035
ErbB signaling pathway	Environmental information processing	Signal transduction	83	0.396	1.645	0.003	0.040
Antigen processing and presentation	Organismal systems	Immune system	67	0.412	1.644	0.003	0.039
Longevity regulating pathway multiple species	Organismal systems	Aging	62	0.419	1.643	0.006	0.038
Cocaine addiction	Human diseases	Substance dependence	49	0.440	1.638	0.007	0.039
Phagosome	Cellular processes	Transport and catabolism	144	0.355	1.603	0.001	0.052
Viral carcinogenesis	Human diseases	Cancer: overview	162	0.346	1.596	0.001	0.053
NOD-like receptor signaling pathway	Organismal systems	Immune system	168	0.340	1.577	0.001	0.061
NF-kappa B signaling pathway	Environmental information processing	Signal transduction	97	0.371	1.574	0.004	0.061
Collecting duct acid secretion	Organismal systems	Excretory system	27	0.481	1.567	0.024	0.063
Chronic myeloid leukemia	Human diseases	Cancer: specific types	76	0.383	1.567	0.007	0.061
Focal adhesion	Cellular processes	Cellular community - eukaryotes	195	0.331	1.559	0.001	0.064
Biosynthesis of unsaturated fatty acids	Metabolism	Lipid metabolism	27	0.480	1.559	0.031	0.063
Glycosphingolipid biosynthesis-ganglio series	Metabolism	Glycan biosynthesis and metabolism	15	0.555	1.554	0.034	0.064
Prostate cancer	Human diseases	Cancer: specific types	97	0.366	1.553	0.006	0.062
Melanoma	Human diseases	Cancer: specific types	72	0.385	1.551	0.009	0.062
Neurotrophin signaling pathway	Organismal systems	Nervous system	119	0.352	1.545	0.004	0.063
Hepatitis C	Human diseases	Infectious disease: viral	153	0.337	1.539	0.004	0.066

Autophagy-other	Cellular processes	Transport and catabolism	31	0.453	1.532	0.028	0.068
Longevity regulating pathway	Organismal systems	Aging	89	0.365	1.531	0.007	0.067
C-type lectin receptor signaling pathway	Organismal systems	Immune system	104	0.355	1.530	0.006	0.066
Toll-like receptor signaling pathway	Organismal systems	Immune system	99	0.358	1.523	0.007	0.068
Inflammatory bowel disease (IBD)	Human diseases	Immune disease	63	0.385	1.518	0.015	0.070
Human papillomavirus infection	Human diseases	Infectious disease: viral	327	0.303	1.516	0.000	0.070
RIG-I-like receptor signaling pathway	Organismal systems	Immune system	67	0.382	1.513	0.016	0.070
FoxO signaling pathway	Environmental information processing	Signal transduction	129	0.338	1.507	0.005	0.072
Colorectal cancer	Human diseases	Cancer: specific types	86	0.359	1.495	0.013	0.078
Vasopressin-regulated water reabsorption	Organismal systems	Excretory system	44	0.409	1.493	0.032	0.078
Yersinia infection	Human diseases	Infectious disease: bacterial	120	0.338	1.486	0.010	0.081
Transcriptional misregulation in cancer	Human diseases	Cancer: overview	162	0.322	1.481	0.004	0.082
Pancreatic cancer	Human diseases	Cancer: specific types	75	0.362	1.473	0.023	0.087
Kaposi sarcoma-associated herpesvirus infection	Human diseases	Infectious disease: viral	182	0.315	1.470	0.004	0.087
Epstein-Barr virus infection	Human diseases	Infectious disease: viral	193	0.312	1.470	0.004	0.086
N-glycan biosynthesis	Metabolism	Glycan biosynthesis and metabolism	50	0.391	1.465	0.034	0.088
Sphingolipid metabolism	Metabolism	Lipid metabolism	46	0.397	1.464	0.034	0.087
Influenza A	Human diseases	Infectious disease: viral	156	0.318	1.459	0.009	0.089
Bacterial invasion of epithelial cells	Human diseases	Infectious disease: bacterial	65	0.367	1.450	0.029	0.094
Leukocyte transendothelial migration	Organismal systems	Immune system	110	0.334	1.447	0.017	0.094
Renal cell carcinoma	Human diseases	Cancer: specific types	66	0.365	1.446	0.029	0.094
Leishmaniasis	Human diseases	Infectious disease: parasitic	68	0.362	1.442	0.031	0.095
Platinum drug resistance	Human diseases	Drug resistance: antineoplastic	69	0.358	1.434	0.029	0.100
Necroptosis	Cellular processes	Cell growth and death	128	0.321	1.428	0.017	0.102
Salmonella infection	Human diseases	Infectious disease: bacterial	83	0.344	1.427	0.026	0.102
Glioma	Human diseases	Cancer: specific types	75	0.348	1.421	0.035	0.105
Lysosome	Cellular processes	Transport and catabolism	122	0.322	1.421	0.020	0.104
Prolactin signaling pathway	Organismal systems	Endocrine system	70	0.352	1.416	0.034	0.106
Chagas disease (American trypanosomiasis)	Human diseases	Infectious disease: parasitic	102	0.330	1.415	0.026	0.106
AGE-RAGE signaling pathway in diabetic complications	Human diseases	Endocrine and metabolic disease	99	0.331	1.415	0.025	0.104
Pathogenic Escherichia coli infection	Human diseases	Infectious disease: bacterial	53	0.367	1.405	0.048	0.111
Endocytosis	Cellular processes	Transport and catabolism	242	0.287	1.398	0.007	0.115

Cortisol synthesis and secretion	Organismal systems	Endocrine system	65	0.351	1.392	0.045	0.118
Parathyroid hormone synthesis secretion and action	Organismal systems	Endocrine system	105	0.322	1.383	0.032	0.124
Non small cell lung cancer	Human diseases	Cancer: specific types	66	0.348	1.382	0.050	0.123
Small cell lung cancer	Human diseases	Cancer: specific types	93	0.326	1.379	0.037	0.124
Natural killer cell mediated cytotoxicity	Organismal systems	Immune system	121	0.313	1.375	0.033	0.126
Human immunodeficiency virus 1 infection	Human diseases	Infectious disease: viral	203	0.289	1.368	0.015	0.131
Oxytocin signaling pathway	Organismal systems	Endocrine system	150	0.299	1.357	0.025	0.139
Relaxin signaling pathway	Organismal systems	Endocrine system	128	0.306	1.357	0.033	0.138
PI3K-Akt signaling pathway	Environmental information processing	Signal transduction	346	0.269	1.353	0.009	0.139
Sphingolipid signaling pathway	Environmental information processing	Signal transduction	119	0.307	1.352	0.037	0.139
Insulin signaling pathway	Organismal systems	Endocrine system	137	0.301	1.349	0.036	0.140
Apelin signaling pathway	Environmental information processing	Signal transduction	133	0.299	1.332	0.040	0.152
Cytokine-cytokine receptor interaction	Environmental information processing	Signaling molecules and interaction	284	0.263	1.302	0.022	0.178
Regulation of actin cytoskeleton	Cellular processes	Cell motility	211	0.269	1.285	0.039	0.192

Supplementary Table 11. Downregulated pathways upon ZnO exposure of Caco-2 cells cultured in gut-on-chip

KEGG pathway name	KEGG Category	KEGG category subgroup	SIZE	ES	NES	NOM p-val	FDR q-val
Pyruvate metabolism	Metabolism	Carbohydrate metabolism	39	-0.633	-2.327	0.000	0.000
DNA replication	Genetic information processing	Replication and repair	36	-0.593	-2.149	0.000	0.001
Mismatch repair	Genetic information processing	Replication and repair	23	-0.643	-2.084	0.000	0.001
Ribosome	Genetic information processing	Translation	113	-0.446	-2.016	0.000	0.002
Homologous recombination	Genetic information processing	Replication and repair	41	-0.536	-2.001	0.001	0.002
Propanoate metabolism	Metabolism	Carbohydrate metabolism	33	-0.553	-1.952	0.000	0.004
Valine, leucine and isoleucine degradation	Metabolism	Amino acid metabolism	47	-0.500	-1.915	0.000	0.005
Lysine degradation	Metabolism	Amino acid metabolism	59	-0.473	-1.893	0.000	0.006
Aminoacyl-tRNA biosynthesis	Genetic information processing	Translation	25	-0.567	-1.862	0.002	0.007
Thermogenesis	Organismal systems	Environmental adaptation	212	-0.363	-1.801	0.000	0.013
Fatty acid biosynthesis	Metabolism	Lipid metabolism	17	-0.581	-1.725	0.010	0.025
Histidine metabolism	Metabolism	Amino acid metabolism	23	-0.528	-1.706	0.011	0.028
Pyrimidine metabolism	Metabolism	Nucleotide metabolism	54	-0.433	-1.704	0.003	0.026
Glycolysis/gluconeogenesis	Metabolism	Global and overview maps	68	-0.409	-1.691	0.002	0.027

Oxidative phosphorylation	Metabolism	Energy metabolism	116	-0.370	-1.684	0.000	0.027
Retrograde endocannabinoid signaling	Organismal systems	Nervous system	138	-0.358	-1.673	0.000	0.028
Butanoate metabolism	Metabolism	Carbohydrate metabolism	28	-0.485	-1.642	0.014	0.035
Parkinson disease	Human diseases	Immune disease	124	-0.348	-1.601	0.003	0.048
Nucleotide excision repair	Genetic information processing	Replication and repair	43	-0.427	-1.598	0.014	0.047
ABC transporters	Environmental information processing	Membrane transport	45	-0.417	-1.578	0.012	0.053
Carbon metabolism	Metabolism	Global and overview maps	114	-0.347	-1.570	0.003	0.054
Tryptophan metabolism	Metabolism	Amino acid metabolism	42	-0.414	-1.555	0.018	0.059
Drug metabolism-other enzymes	Metabolism	Xenobiotics biodegradation and metabolism	70	-0.369	-1.543	0.009	0.062
Huntington disease	Human diseases	Neurodegenerative disease	181	-0.311	-1.510	0.002	0.078
Pancreatic secretion	Human diseases	Digestive system	94	-0.343	-1.507	0.007	0.076
Proximal tubule bicarbonate reclamation	Organismal systems	Excretory system	23	-0.465	-1.495	0.043	0.081
Fat digestion and absorption	Organismal systems	Digestive system	41	-0.390	-1.445	0.040	0.114
Alzheimer disease	Human diseases	Neurodegenerative disease	161	-0.300	-1.430	0.007	0.123
Purine metabolism	Metabolism	Nucleotide metabolism	125	-0.307	-1.416	0.016	0.132
RNA degradation	Genetic information processing	Folding, sorting and degradation	78	-0.330	-1.402	0.032	0.142
Oocyte meiosis	Cellular processes	Cell growth and death	119	-0.298	-1.360	0.029	0.175
Peroxisome	Cellular processes	Transport and catabolism	82	-0.315	-1.352	0.044	0.174
Morphine addiction	Human diseases	Substance dependence	90	-0.308	-1.343	0.042	0.180
Cell cycle	Cellular processes	Cell growth and death	124	-0.284	-1.301	0.049	0.218

Supplementary Table 12. The overlap of gene sets in different culture conditions upon ZnO exposure

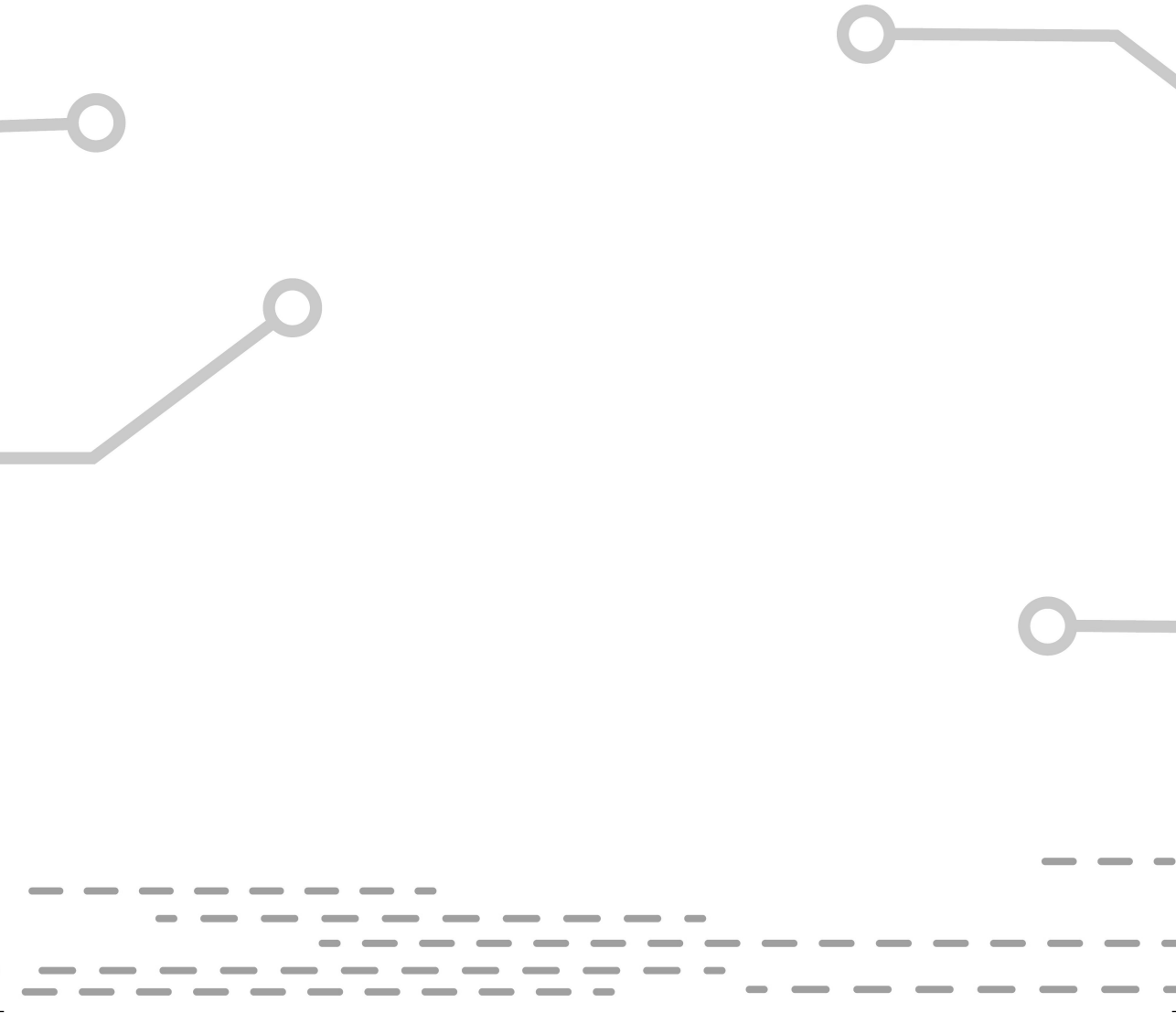
KEGG pathway name	KEGG Category	KEGG category subgroup	SIZE	Transwell				Gut-on-chip			
				ES	NES	NOM p-val	FDR q-val	ES	NES	NOM p-val	FDR q-val
Mineral absorption	Organismal systems	Digestive system	49	0.477	1.862	0.000	0.028	0.650	2.439	0.000	0.000
Autophagy-other	Cellular processes	Transport and catabolism	31	0.466	1.639	0.014	0.117	0.453	1.532	0.028	0.068
Viral carcinogenesis	Human diseases	Cancer: overview	162	0.338	1.634	0.000	0.111	0.346	1.596	0.001	0.053
Herpes simplex virus 1 infection	Human diseases	Infectious disease: viral	476	0.291	1.595	0.000	0.129	0.341	1.772	0.000	0.020
Protein processing in endoplasmic reticulum	Genetic information processing	Folding, sorting and degradation	160	0.325	1.563	0.000	0.146	0.518	2.375	0.000	0.000
Colorectal cancer	Human diseases	Cancer: specific types	86	0.357	1.562	0.006	0.136	0.359	1.495	0.013	0.078
Pancreatic cancer	Human diseases	Cancer: specific types	75	0.363	1.547	0.008	0.146	0.362	1.473	0.023	0.087
Chronic myeloid leukemia	Human diseases	Cancer: specific types	76	0.362	1.544	0.009	0.141	0.383	1.567	0.007	0.061
Hippo signaling pathway-multiple species	Environmental information processing	Signal transduction	28	0.445	1.519	0.035	0.141	0.510	1.681	0.009	0.031
Small cell lung cancer	Human diseases	Cancer: specific types	93	0.341	1.508	0.009	0.146	0.326	1.379	0.037	0.124
Ferroptosis	Cellular processes	Cell growth and death	39	0.403	1.496	0.029	0.148	0.467	1.663	0.008	0.035
Pathogenic Escherichia coli infection	Human diseases	Infectious disease: bacterial	53	0.373	1.486	0.027	0.154	0.367	1.405	0.048	0.111
Mitophagy-animal	Cellular processes	Transport and catabolism	64	0.354	1.462	0.029	0.178	0.542	2.138	0.000	0.001
Autophagy-animal	Cellular processes	Transport and catabolism	127	0.313	1.457	0.008	0.177	0.408	1.811	0.000	0.014
Epithelial cell signaling in helicobacter pylori infection	Human diseases	Infectious disease: bacterial	70	0.346	1.456	0.023	0.173	0.423	1.696	0.002	0.030
Renal cell carcinoma	Human diseases	Cancer: specific types	66	0.347	1.445	0.026	0.176	0.365	1.446	0.029	0.094
Prostate cancer	Human diseases	Cancer: specific types	97	0.321	1.434	0.022	0.179	0.366	1.553	0.006	0.062
TNF signaling pathway	Environmental information processing	Signal transduction	110	0.309	1.405	0.024	0.209	0.394	1.703	0.001	0.031
FoxO signaling pathway	Environmental information processing	Signal transduction	129	0.300	1.402	0.018	0.200	0.338	1.507	0.005	0.072
Propanoate metabolism	Metabolism	Carbohydrate metabolism	33	-0.490	-1.736	0.004	0.152	-0.553	-1.952	0.000	0.004
Glycolysis/gluconeogenesis	Metabolism	Carbohydrate metabolism	68	-0.411	-1.708	0.002	0.132	-0.409	-1.691	0.002	0.027
Valine, leucine and isoleucine degradation	Metabolism	Amino acid metabolism	47	-0.407	-1.568	0.013	0.155	-0.500	-1.915	0.000	0.005
Oxidative phosphorylation	Metabolism	Energy metabolism	116	-0.338	-1.543	0.004	0.172	-0.370	-1.684	0.000	0.027
Carbon metabolism	Metabolism	Global and overview maps	114	-0.336	-1.531	0.004	0.173	-0.347	-1.570	0.003	0.054
Fat digestion and absorption	Organismal systems	Digestive system	41	-0.391	-1.461	0.037	0.223	-0.390	-1.445	0.040	0.114
Cell cycle	Cellular processes	Cell growth and death	124	0.352	1.632	0.001	0.102	-0.284	-1.301	0.049	0.218
RNA degradation	Genetic information processing	Folding, sorting and degradation	78	0.340	1.448	0.027	0.102	-0.330	-1.402	0.032	0.142
Lysine degradation	Metabolism	Amino acid metabolism	59	0.354	1.443	0.032	0.172	-0.473	-1.893	0.000	0.006





CHAPTER 6

General discussion and future perspectives



General discussion

Recent advances in cell biology, microfabrication and microfluidics have led to the development of micro-engineered *in vitro* cellular models that emulate specific functional units of selected human organs. A unique characteristic of these so-called organ-on-chip models is that they allow for flow of cell culture medium over the cells cultured in such a device. This opens new avenues to recapitulate human organ functionality. In recent years the promises of organ-on-chip models have been many, however, at the same time several challenges remain before these new models can become widely accepted as standard *in vitro* models to be used in, for instance, toxicological safety testing. To benefit the development of this technology on the short/medium term, the focus should lie on the qualification of the devices and on the identification of well-defined contexts of use. The typical qualification process applied to organ-on-chip models is a comparison between data obtained in the organ-on-chip model and data derived from conventional *in vitro* approaches and human clinical data if available [1]. The work described in this thesis aimed to characterize a novel gut-on-chip model focused on transport functionality and cellular responses of Caco-2 cells cultured in a gut-on-chip model and compare its performance to that of a conventional static *in vitro* model and to human *in vivo* data. The main results and conclusions of this work are summarized next.

An overview of the state-of-the-art *in vitro* models for the human intestine was provided in **Chapter 1** (including details on various gut-on-chip models in Table 2 and 3). This overview illustrated the current diversity in gut-on chip models and the broad range of applications, i.e. their use for transport studies, local effect studies as well as fundamental studies like studying the influence of shear stress on cellular functions and cell morphology. The data obtained so far suggest that recently developed microfluidic human gut-on-chip models may more closely emulate the structure, function, physiology, and pathology of the human intestine. In **Chapter 2-5**, a novel glass-based commercially available gut-on-chip model was used to culture human intestinal epithelial Caco-2 cells on a porous membrane under dynamic conditions (i.e. flow) and compare its characteristics to those of the same cells grown in a conventional static *in vitro* model. Glass-based chips possess several advantages such as thermal resistance, chemical inertness and low non-specific adsorption, compared to polymeric-based chips. The resealable-chip design, with a separate disposable membrane layer allows for offline visual analysis of the cells such as fluorescence imaging and cell collection. In contrast to static culture conditions, cells cultured under dynamic conditions, in a gut-on-chip, are exposed to shear stress generated by fluid flow and known to be influenced by the applied flow rate and the dimensions of the device. **Chapter 2-5** demonstrated Caco-2 cells can be maintained and form monolayers of cells under the applied flow rate of 25-100 $\mu\text{L/h}$, corresponding to a shear stress of $\sim 0.0001\text{-}0.002$ dyne/cm². To study the applicability domain of the gut-on-chip using Caco-2 human intestinal epithelial cells, several biokinetic (**Chapter 2 and 3**) and biodynamic studies (**Chapter 4 and 5**) have

been performed and the observed effects were compared to those obtained using a conventional static *in vitro* model and, if available, to *in vivo* data obtained from the literature.

In **Chapter 2**, the gut-on-chip model was used to study the potential cellular association and transport of an important group of food contaminants, i.e. dioxins (highly lipophilic compounds). This urged the selection of tubing and syringe materials with minimal non-specific binding on the material surface because of the large (relative) surface areas of the capillary tubing. The results revealed that glass syringes, polytetrafluoroethylene tubing and glass microfluidic chips were able to minimize surface adsorption of the dioxins during the transport studies, indicated by a dioxin mass balance of ~84-100% in the gut-on-chip model.

Caco-2 cells cultured under flow for 7 days formed confluent and polarized monolayers that were visually comparable to cells cultured for 21 days under static conditions in Transwells. In this study, transport of 17 dioxin congeners across the Caco-2 cell layer was investigated. These 17 congeners are all present in a congener mix that is used as a reference set for food monitoring [2]. Gas chromatography-high resolution mass spectrometry analysis demonstrated that the cellular association and transport of individual dioxin congeners across the Caco-2 cell monolayers was similar between the dynamic gut-on-chip model and the static Transwell model. The relationship between the transport of individual congeners and their physicochemical characteristics was studied using computational modelling. Quantitative structure-property relationship modelling revealed that the transport of individual congeners across the cell barrier was dependent on their number of chlorine atoms and substitution patterns. The study showed that the gut-on-chip can be used to study the cellular association and transport of lipophilic compounds like dioxins.

Further optimization and characterization of the gut-on-chip was performed in **Chapter 3**. In this chapter the transport of well-known pharmaceuticals (antipyrene, ketoprofen, digoxin and amoxicillin), for which information was available on *in vivo* bioavailability and transport mechanisms (high and low oral permeability class compounds with different absorption mechanisms), was assessed. In addition, cell layer integrity and cell differentiation were evaluated by determination of lucifer yellow transport and alkaline phosphatase activity in the cells.

It was concluded that the gut-on-chip provides an adequate model for transport studies. The obtained transport values of the compounds were in line with expectations based on the compound properties from the Biopharmaceuticals Classification System. The transport of the low permeability compound, amoxicillin, was similar in both the dynamic and static *in vitro* model, while under the dynamic conditions the transport of the high permeability compounds antipyrene, ketoprofen and digoxin was lower (i.e. 4.2-, 2.7- and 1.9-fold, respectively) in the gut-on-chip model compared to the transport in the static Transwell model. Most likely this can be explained by the laminar flow defined by the low Reynolds number in the gut-on-chip model resulting in less contact of the compounds with the cell surface, which is discussed below. The obtained *in vitro* transport values of the

compounds correlated with data reported *in vivo* (i.e. the fraction absorbed in humans (%Fa)) with the exception of digoxin permeability (higher transport in this study), which likely can be explained by the low expression of P-gp, the efflux transporter, by Caco-2 cells.

After completion of the biokinetic studies, work moved to study responses of cells cultured under both conditions with and without subsequent chemical exposure. As a first step the basal gene expression of Caco-2 cells, cultured statically in a Transwell system or dynamically in a gut-on-chip device, was analyzed and compared to that of intestinal tissues *in vivo* in **Chapter 4**. A whole genome transcriptomics analysis was applied to compare the gene expression profiles on a single gene level and subsequently a principal component analysis was performed. In addition, a comparison of the gene expression profiles of the cells grown in the static and dynamic *in vitro* models was performed on the level of biological pathways. For the *in vivo* data, the data from a publicly accessible database that contained transcriptome profiles (from duodenum, jejunum, ileum, and colon) from healthy human volunteers was used.

Dynamic culture conditions led to a total of 5927 differentially expressed genes (3280 upregulated and 2647 downregulated genes) compared to static culture conditions. Gene set enrichment analysis revealed that upregulated pathways were mainly related to cellular homeostasis, immunological responses, cell growth and death, as well as signal transduction, while general cellular metabolism and absorption pathways were repressed. These differences in expression of genes coding for metabolism and absorption did not result in observable differences in transport of chemicals as studies in **Chapter 2** and **3** showed. It needs to be noted, however, that in these two chapters a lower shear stress was applied to the cells than in **Chapter 4**. The comparison of the *in vitro* gene expression data with transcriptomic profiles of human *in vivo* duodenum, jejunum, ileum and colon tissue samples did not reveal a striking similarity with any of these segments. In the principle component analysis both *in vitro* culturing conditions clustered separate from the *in vivo* human samples. Since some specific gene functions are differently modulated in each model, it is concluded that both the static and the dynamic gut-on-chip model could be used to study human intestinal epithelial responses depending on the endpoint of interest.

Lastly, the responses of cells cultured under both conditions were evaluated following exposure to different classes of nanomaterials, i.e. titanium oxide (TiO₂) and zinc oxide (ZnO) nanomaterials in **Chapter 5**. The potential for use of organ-on-chip applications for toxicological hazard and risk assessment within the industrial development of chemical and agro-food consumer products including nanomaterials, has been advised to be explored by experts in the EU roadmap for organ-on-chip development [1, 3]. Whole genome transcriptomics analysis was performed to compare the cellular responses of Caco-2 cells cultured under dynamic and static conditions following exposure to E171 (TiO₂) and NM110 (ZnO) nanomaterials. The nanomaterials induced a higher number of differentially expressed genes in cells cultured in the gut-on-chip when compared to the static model. The shear stress

in the organ-on-chip might be a major factor in increasing cellular sensitivity to chemicals as observed previously in endothelial cells [4].

The results of transport studies in this thesis indicated that our gut-on-chip can be used as an alternative model to the conventionally static model to evaluate transport (biokinetics). The model performed equally well, while better taking the potential shear stress occurring *in vivo* into account. Shear stress especially influenced the transport of high permeability compounds. This aspect will be discussed in the next section. Generally, use of a simpler and cheaper *in vitro* model is preferred, if the outcome can be used to predict the *in vivo* situation (e.g. a static Transwell model for permeability evaluation). It is quite clear that manipulation of microfluidic devices is more complex and challenging than use of a conventional static model, which is why (for now) the use of the conventional static model is likely preferable for most research questions on transport of compounds. However, a microfluidic system offers several advantages over a conventional model for transport studies in terms of experimental conditions for example, the ability for (real time) semi-automated detection and chemical gradient generation and low reagent consumption [5]. In addition, gut-on-chip models are still in the developmental stage and various models have been described with various outcomes, some studies describe a gut-on-chip model that more closely mimicked the transport of compounds (i.e. FITC-dextran, atenolol) to the human *in vivo* data than the static Transwell model [6, 7]. Therefore, development of dynamic gut-on-chip systems is necessary to get better insights into the potential of these type of models and could possibly result in a better predictive model for transport studies in the future. For biodynamic studies, our gut-on-chip offers an alternative model to the conventional static model with a higher sensitivity to compound exposure. This indicates that the gut-on-chip model might be preferable over the static conventional model for toxicity studies, depending on the research question.

Important points to take into consideration for using gut-on-chip models

In the scientific literature a great diversity of different microfluidic devices are used in organ-on-chip studies. Based on the performed experiments in this thesis a few critical (design) properties can be identified. Firstly, the choice of the materials used to manufacture the microfluidic chips. As shown in **Chapter 2**, glass-based chips and syringes were successfully used with minimal surface adsorption, but only in combination with teflon (polytetrafluoroethylene) tubing, which has unique properties such as nonreactivity, hydrophobicity, and a low friction coefficient [8]. This was the optimal setup for the dioxin transport study, resulting in a mass balance of 84-100%. The use of other materials for the tubing and syringes resulted in a much greater loss of materials (i.e. only 26 % recovery). Therefore, the selection of tubing material for the compounds of interest in a microfluidic system should always be considered during microfluidic model development, since the (relative) surface areas of the capillary tubing is large and can have a large impact on recovery of especially (very) lipophilic compounds. Furthermore, device materials like PDMS are

known to absorb (lipophilic) small molecules [9]. The glass based-chip was therefore selected in this study to avoid loss of compound during transport experiments.

Secondly, the fluid flow that is applied to the system not only affects the cellular responses itself, but might also affect the concentration of a chemical that reaches the cells. In general, the fluid flow within microfluidic channels is laminar and influence of laminar flow on transport of high permeability compounds was reported in **Chapter 3**. In the dynamic gut-on-chip model the transport of the high permeability compounds antipyrine, ketoprofen and digoxin was lower (i.e. 4.2-, 2.7- and 1.9-fold, respectively) compared with the transport in the static Transwell. The transport of the low permeability compound, amoxicillin, was comparable in both the dynamic and static *in vitro* model. From the experiments without cells and without flow it could be concluded that the differences in transport of the high permeability compounds were caused by (laminar) flow related effects (i.e. dosimetry) and by the design of the chip and/or the material of the membrane. Laminar flow consists of long thin parallel layers of liquid with no disruption between them and results in a domination of viscous forces, which implies a low migration (or diffusion) of dissolved chemicals across the layers in cell culture medium resulting in less contact of the compounds with the cell surface [10]. Therefore, the compound concentration, delivered to the cells in the gut-on-chip, was lower than in the static Transwell, leading to the lower permeability. The laminar fluid flow in the gut-on-chip affected the transport of high permeability compounds more than that of low permeability compounds, as demonstrated by transport of dioxins (**Chapter 2**) and amoxicillin (**Chapter 3**), which was similar to the static system. It is likely that for low permeability compounds the cell monolayer mainly dominates their transport. This indicates that to compare the outcome of dynamic and static systems, the exposure concentrations (or doses) to the cells should be taken into account to avoid misinterpretation of the potential of the model.

The critical importance of diffusion, and nanomaterial sedimentation on cells (thus cellular dosimetry) for *in vitro* toxicity studies is well established [11-13] and should be considered when performing comparative studies across multiple systems. In **chapter 5**, three different culturing devices (i.e. 96 well plates for the cell viability experiments and Transwells and gut-on-chips for the gene expression experiments) were used. The three different culturing devices have different dimensions (i.e. the height and width of the cell culture compartment). In order to compare the gene expression profiles between the two different models, the deposited mass of nanomaterials on the cells was predicted. For this the In vitro Sedimentation, Diffusion and Dosimetry (ISDD) model [14] was used to achieve similarity between exposure doses.

Ultimately, dosimetry considerations like discussed above need to be included in future organ-on-chip studies, especially if different designs are combined to study the relevance of dosing compared with *in vivo* conditions. Currently this is lacking in most published studies. For this, developing a strategy such as a computer modeling that can predict the chemical behavior (i.e. localization, sedimentation, binding affinity to the wall)

under fluid flow [15-17] might be a suitable approach to provide the accurate cellular dosage of chemicals and nanoparticles delivered to cells.

Influence of shear stress on cell functionality

The flow of cell culture medium over the cells in a microfluidic device has proven to affect the cells as shown in this thesis (**Chapter 4 and 5**) and in the literature [6, 18, 19]. The liquid flow is thought to emulate the physiological conditions as observed *in vivo*. Yet, there is lacking knowledge on the desired magnitude of the shear stress. Understanding the interplay between cellular behavior and the microenvironmental conditions created by microfluidic devices, such as shear stress would accelerate the development of microfluidic cell culture technology. Recently, the effect of the fluid shear stress on Caco-2 cells, has been investigated in the literature (as shown in **Chapter 1**, Table 2 and 3) and also in the present thesis. Largely different shear stresses magnitudes, ranging from ~ 0.00004 - 0.7 dyne/cm², have been used for Caco-2 cells and differences in cellular behavior were reported under different shear stress conditions. For example, the ALP activity of Caco-2 cells exposed to a shear stress of ~ 0.0002 - 0.0017 dyne/cm² in this thesis (**Chapter 3**) was similar to that of cells cultured under static conditions. A shear stress of 0.02 dyne/cm² resulted in a full Caco-2 differentiation after only 5 days of culturing [6]. Furthermore, the application of ~ 0 - 0.03 dyne/cm² shear stress significantly altered the production of mucus, expression of tight junctions, vacuolization, organization of cytoskeleton, formation of microvilli, mitochondrial activity and expression of cytochrome of Caco-2 cells [20]. Data in literature on *in vivo* shear stress values in the gut are highly variable and range between ~ 0.002 - 12.0 dyne/cm² [6, 21, 22], depending on the intestinal location and viscosity of digesta. Therefore, to mimic the real shear stress experienced by epithelial cells within the intestinal lumen is still challenging *in vitro*. Admittedly, organ-on-chip technology is still in its infancy and efforts in this field are ongoing to improve performance and standardization. Currently, gut-on-chip development is mostly carried out in various academic laboratories using different chip devices and cell culturing protocols, and thus, the results can vary from laboratory to laboratory. However, the knowledge generated by academia will enable the future application of *in vitro* organs-on-chip models with well-defined and designed characteristics and protocols for a specific purpose, and drive the commercialization of organ-on-chip technology to improve manufacturing processes, robustness, cost, and ease of use.

Future perspectives

Improving physiological relevance (biological aspects)

The gut-on-chip reported in this thesis, as well as some of the recently published gut-on-chips (as shown in **Chapter 1**, Table 2 and 3), makes use of the (immortalized) epithelial cell line Caco-2, to replicate the intestinal barrier. But there are many other cell types in the human intestinal epithelium that influence and maintain intestinal function, as was shown in Table 1 of **Chapter 1**. The choice of the cell model to be used should reflect the research questions.

For transport studies well characterized and relatively simple cell model systems (like Caco-2 cells) could be preferred, especially in combination with PBPK modelling. For other research questions, for instance related to local intestinal inflammatory responses, model variants with M cells can be considered. Intestinal M (microfold) cells are reported to take up intestinal microbial antigens and deliver them to gut-associated lymphoid tissue for efficient mucosal as well as systemic immune responses [23], incorporation of immune cells to induce M cell-like morphology *in vitro* can also be considered. The methods for combining the cultivation of immune cells (i.e. Raji, THP-1, RAW264.7 cells) with Caco-2 cells cultured under static conditions are well established in the literature [24-26]. Transferring these models to microfluidic chips would allow to study antigen-cell uptake and subsequent responses under fluid flow as more *in vivo* physical relevance, for example, which is not possible in current static models.

The alternative direction is to move away from cell-line based models, and incorporate stem cell-based models in the gut-on-chip which are expected to better resemble human enterocytes than the cell lines. Both human induced pluripotent stem cells (hiPSCs) and models exploiting adult intestinal stem-cells could be considered. Nowadays, methods to differentiate hiPSCs and adult intestinal stem-cells into intestinal-like cells in static culture as a monolayer have been reported and utilized with success in compound absorption and metabolism studies [27-29]. Moving towards a microfluidic model has shown to be interesting as culturing of primary cell-based intestine (duodenum) in a chip better matched the *in vivo* tissue (transcriptomic profile) than the same organoids cultured without flow [30]. Moreover, the use of patient-derived stem cells in organ-on-chip systems can also contribute to the development of personalized medicine and drug screening technologies [31].

The intestinal microbiome has a crucial effect on intestinal function, development and homeostasis [32]. Co-culturing intestinal bacteria with epithelial cells, however, has several challenges, for which gut-on-chip microfluidic devices might provide some solutions. The constant liquid flow in gut-on-chip systems may facilitate the cocultivation of the cells with the bacteria by washing off the overgrowth of the bacteria in the system with the fluid flow. Some initial work on anaerobic culturing under fluid flow has been reported recently [33, 34]. Future gut-on-chip models that include the intestinal microbiota might further innovate studies on host-microbe interactions. In addition, these might be interesting for toxicological studies as well as the intestinal microbiota are known to mediate biochemical transformations of compounds which can have consequences for the efficacy and toxicity of dietary components and environmental toxins [35, 36].

Generally, to improve physiological relevance of *in vitro* model systems, the balance between model predictive value and complexity should be weighed. If the research question can be addressed by a simple model, the more complex model with additional components is not necessary. If, however, the model is too simple to answer the research question, then extension of the model to incorporate more physiological parameters may be required [37].

Besides the development of *in vitro* single organ-on-a-chip systems including the gut-on-chip, a multi-organ-on-a-chip referred to as “body-on-a-chip” has been proposed with the ultimate aim to obtain a better correlation between *in vitro* and *in vivo* models. It offers the opportunity of combining more tissues, where a completely independent system might adequately provide the physiological function of a tissue, the combination of tissues allows communication between tissues and might better mimic the *in vivo* capacity. Current research has already reported several multi-organ-on-a-chip platforms for ADME studies [38-40].

Improving device design and fabrication

Well-functioning organs-on-chip platforms rely on solid microfluidic engineering and a robust biology. From the studies performed in this thesis, it becomes clear that the engineering choices for basic aspects of the device can influence cellular functioning. Also, the choice of the material has been mentioned (and its consequences for absorption and availability of chemicals). Most of the devices use a rigid substrate to support the cells, however a more natural support or scaffold for the cells could be considered to be incorporated. Cells cultured on an extracellular matrix represent more accurately the actual microenvironment where cells reside in tissues. Thus, the behavior of cells is more reflective of *in vivo* cellular responses. The most simple and already frequently used approach would be to use a collagen coating on the membranes [41, 42]. Care needs to be taken as a collagen scaffold proved to be a barrier to the diffusion of some drugs [43]. Another approach is the use of a biomimetic scaffold. Incorporating scaffolding into microfluidic organ-on-a-chip devices enables the creation of a biomimetic microenvironment with a heterogeneous 3D structure as observed *in vivo*, for instance to generate the crypt-villus architecture of the intestine which supports the growth and differentiation of the intestinal epithelium [44, 45].

As discussed in this thesis the flow, and especially laminar flow can affect the dose of a chemical that reaches the cells. One solution to minimize the influence of laminar flow on compound transport can be to incorporate herringbone-shaped grooves into the model to create a more turbid flow and thus enhance overall compound migration [46]. Another proposed technique is narrowing of the microfluidic channel [47] and integrating artificial cilia, a hair-like structure material, into the system to promote mixing of the liquid in the microchannels [48].

Although, many studies in literature as well the studies in this thesis have revealed that the application of shear stress alone affects the properties of Caco-2 cells grown in microfluidic environments, the study of Kim et al, indicated that the addition of periodic peristalsis of the membrane in the gut-on-chip increased the expression of brush border enzyme (aminopeptidase) levels and induced paracellular permeability, compared with applying fluid flow alone. These authors considered this combination to more closely mimic human intestinal functioning *in vivo*, [6]. Also, Cremer et al., showed that for a co-culture with bacteria the repeated contraction is needed to maintain a stably distributed bacterial density in the gut-like channel microdevice [49]. This might indicate that, depending on the

purpose of use, including peristaltic movements in the intestinal gut on-chip platforms needs to be considered.

Improving readout systems

A microfluidic gut-on-chip system can be explored to enable automated online (real-time) measurement of parameters by readout systems including sensors, reporter cells or online coupling to analytical equipment [50]. Currently existing examples of integrated sensors can be used to evaluate cellular function (secretion) and composition of the cellular microenvironment such as a sensor for detecting glucose and lactate concentrations (mitochondrial function) [51], growth factor release [52], the cell culture medium pH [53], and the oxygen level [54]. Incorporating sensors in microfluidic chips avoids time-consuming, manual sample collection and large working volumes as used in traditional techniques. Also, the detection of cellular secretion of signaling molecules, indicating a certain toxic endpoint upon compound exposure, might be performed (semi) automatically by coupling a microfluid culture device with a reporter cell-based assay (living cells) such as, for example, transfected cells for G protein-coupled receptor activation [55]. A sensor for evaluation of cell monolayer integrity (TEER) can also be integrated into a microfluid system [56, 57]. Attachment of the electrodes to the device itself would eliminate the noise generated by a manual insertion of the detecting electrodes. Online coupling to high-end instrumentation such as a mass spectrometer to detect targeted substances is another crucial future development for these types of systems. In a gut-on-chip model this enabled semi-continuous identification and quantification of multiple target analytes, expected metabolites as well as secreted cell products in a small sample volume with high sensitivity [58].

Combination with computational modelling

In this thesis computational modelling (i.e. QSAR approaches) has been used to correlate observed transport of chemicals in a gut-on-a-chip with physicochemical properties of the chemicals. Further integration of results of microfluidic culture systems with computer modeling such as the physiologically based pharmacokinetic model (PBK) is another possible approach to further utilize the system for comprehensive *in vitro* screening. The PBK model attempts to recapitulate the entire body as a closed circulatory system with interconnected compartments for a pharmacokinetics which specify tissue compartments [59].

The recent literature shows that the *in vitro* to *in vivo* extrapolation of ADME using an *in silico* model built using experimental data obtained from multiple organ-on-chip can be used to predict human PK parameters *in vitro* with high similarity to those obtained in human clinical studies [60].

The use of the gut-on-chip model for risk assessment

Current research, as illustrated in the present work, shows that the convergence of microfabrication and tissue engineering resulting in organ-on-a-chip platforms could offer an alternative to conventional *in vivo* models for drug discovery and chemical or (food) toxicology. As for other *in vitro* models, also for a gut-on-chip it is important that the results obtained correlate with human clinical readouts (i.e. have human physiological relevance). Extrapolation (with computational approaches) to the human *in vivo* situation is important to incorporate in gut-on-chip approaches in an animal free next generation risk assessment framework.

Over the past decades, various alternatives to animal testing have been proposed to overcome the drawbacks associated with animal experiments and avoid unneeded and unethical testing procedures. A strategy of 3 Rs (i.e. reduction, refinement and replacement) is being applied to manage the laboratory use of animals. Often a tiered approach of model complexity is proposed. Such an approach starts with using simple cell free models to study chemical and (nano) material reactivity or single cell type models for hazard screening followed by use of co-culture and other more complex 3D cell culture *in vitro* approaches. Among these methods, there are several *in vitro* models that have been validated and accepted by regulatory agencies to replace the animal studies [61]. The need and desire for replacements of animals used for scientific purposes are still moving forward. Organs-on-chip are the new kid on the block.

Organ-on-chip technology offers interesting opportunities as evidence is growing that these models are able to emulate key aspects of human physiology (and disease) crucial for the understanding of compound effects, improving preclinical safety and efficacy testing. At present, although authorities have already accepted *in vitro* methods for some toxicity endpoints for regulatory safety assessment (e.g. genotoxicity and skin/eye irritation), there is a lack of accepted *in vitro* methods for the more complex and systemic endpoints (e.g. acute toxicity, repeated dose toxicity, carcinogenicity, and neurotoxicity). To address these more complex toxicity endpoints, organ-on-chip systems could potentially be of great value by offering a multi-organ platform to study interactions between cells or tissues as well as systemic toxicity endpoints [62]. In combination with appropriate computational models for biokinetics, *in vitro* results, generated in organ-on-chip systems, can be converted into dose response curves or relative potency information relating to the entire target [63], and the data could then be used to derive safe limit values for humans. It is promising to note that the FDA is currently evaluating the effectiveness of these devices for safety testing [64]. But what is really needed to advance the use of these models in toxicological risk assessment:

- Standard system; a standard model (i.e. design, operational processes) required for specific application endpoints (tests) and target tissues
- Robustness; a reproducible production of stable outcomes over time and in different laboratories (users) when using the same protocol or slightly varied protocol
- Costs; manufacturing costs at an affordable level for users both in academia and industry

- Ease of use; simple devices and operation displaying a user-friendly system
- Reference materials; establishment of relevant sets of benchmarking compounds with well-known study *in vivo* for model quantification
- Proofs of principle; the proofs to support the performance of the models for hazard identification and quantification and ultimately risk and safety assessment

Overall conclusion

The present thesis presents the development, qualification and application of a gut-on-chip model with Caco-2 intestinal epithelial cells. This gut-on-chip has been successfully used to culture intestinal epithelial cells under fluid flow. The gut-on-chip model can be used to study transport of chemicals as shown for dioxins and pharmaceuticals (i.e. antipyrine, ketoprofen, digoxin, amoxicillin). This thesis addressed the interplay between experimental outcome and the microfluidic chip in terms of non-selective binding of compound to the chip and tubing material, laminar flow and shear stress. The influence of (laminar) flow on transport studies has been shown. In addition, the dynamic flow conditions affect the gene expression and biological functioning of Caco-2 cells under control and chemical exposure conditions. Exposure to food-related TiO₂ and ZnO nanomaterials resulted in more prominent effects on the differential gene expression of Caco-2 cells cultured in the microfluidic chip compared to cells grown in the static Transwell model. Taking all together it is concluded that gut-on-chip models provide a promising *in vitro* tool to study absorption and toxicity.

References

1. Mastrangeli, M., et al., *Organ-on-chip in development: Towards a roadmap for organs-on-chip*. ALTEX, 2019. 36(4): p. 650-668.
2. EFSA, *Update of the monitoring of levels of dioxins and PCBs in food and feed EFSA EFSA Journal*, 2012. 10(7): p. 2832.
3. Zhang, B. and M. Radisic, *Organ-on-a-chip devices advance to market*. Lab Chip, 2017. 17(14): p. 2395-2420.
4. Feng, S., et al., *Online Analysis of Drug Toxicity to Cells with Shear Stress on an Integrated Microfluidic Chip*. ACS Sens, 2019. 4(2): p. 521-527.
5. Halldorsson, S., et al., *Advantages and challenges of microfluidic cell culture in polydimethylsiloxane devices*. Biosensors and Bioelectronics, 2015. 63: p. 218-231.
6. Kim, H.J., et al., *Human gut-on-a-chip inhabited by microbial flora that experiences intestinal peristalsis-like motions and flow*. Lab Chip, 2012. 12(12): p. 2165-74.
7. Pocock, K., et al., *Intestine-on-a-Chip Microfluidic Model for Efficient in Vitro Screening of Oral Chemotherapeutic Uptake*. ACS Biomaterials Science & Engineering, 2017. 3(6): p. 951-959.
8. Radulovic, L.L. and Z.W. Wojcinski, *PTFE (Polytetrafluoroethylene; Teflon®)*, in *Encyclopedia of Toxicology (Third Edition)*, P. Wexler, Editor. 2014, Academic Press: Oxford. p. 1133-1136.
9. Nguyen, T., et al., *Robust chemical bonding of PMMA microfluidic devices to porous PETE membranes for reliable cytotoxicity testing of drugs*. Lab on a Chip, 2019. 19(21): p. 3706-3713.
10. Sosa-Hernandez, J.E., et al., *Organs-on-a-Chip Module: A Review from the Development and Applications Perspective*. Micromachines (Basel), 2018. 9(10).
11. Cho, E.C., Q. Zhang, and Y. Xia, *The effect of sedimentation and diffusion on cellular uptake of gold nanoparticles*. Nat Nanotechnol, 2011. 6(6): p. 385-91.
12. Cohen, J.M., J.G. Teeguarden, and P. Demokritou, *An integrated approach for the in vitro dosimetry of engineered nanomaterials*. Particle and Fibre Toxicology, 2014. 11(1): p. 20.
13. DeLoid, G., et al., *Estimating the effective density of engineered nanomaterials for in vitro dosimetry*. Nature Communications, 2014. 5(1): p. 3514.
14. Hinderliter, P.M., et al., *ISDD: A computational model of particle sedimentation, diffusion and target cell dosimetry for in vitro toxicity studies*. Part Fibre Toxicol, 2010. 7(1): p. 36.
15. Gomez-Garcia, M.J., et al., *Nanoparticle localization in blood vessels: dependence on fluid shear stress, flow disturbances, and flow-induced changes in endothelial physiology*. Nanoscale, 2018. 10(32): p. 15249-15261.
16. Fullstone, G., et al., *Modelling the Transport of Nanoparticles under Blood Flow using an Agent-based Approach*. Scientific Reports, 2015. 5(1): p. 10649.
17. Lee, T.R., et al., *A statistical study on nanoparticle movements in a microfluidic channel*. J Nanosci Nanotechnol, 2011. 11(1): p. 281-5.
18. Maggiorani, D., et al., *Shear Stress-Induced Alteration of Epithelial Organization in Human Renal Tubular Cells*. PloS one, 2015. 10(7): p. e0131416-e0131416.
19. Jun, Y., et al., *In vivo-mimicking microfluidic perfusion culture of pancreatic islet spheroids*. Sci Adv, 2019. 5(11): p. eaax4520.
20. Delon, L.C., et al., *A systematic investigation of the effect of the fluid shear stress on Caco-2 cells towards the optimization of epithelial organ-on-chip models*. Biomaterials, 2019. 225: p. 119521.
21. Guo, P., A.M. Weinstein, and S. Weinbaum, *A hydrodynamic mechanosensory hypothesis for brush border microvilli*. American Journal of Physiology-Renal Physiology, 2000. 279(4): p. F698-F712.
22. Hardacre, A.K., et al., *Does viscosity or structure govern the rate at which starch granules are digested?* Carbohydrate Polymers, 2016. 136: p. 667-675.
23. Ohno, H., *Intestinal M cells*. Journal of biochemistry, 2016. 159(2): p. 151-160.
24. Kämpfer, A.A.M., et al., *Development of an in vitro co-culture model to mimic the human intestine in healthy and diseased state*. Toxicology in Vitro, 2017. 45: p. 31-43.

25. Gullberg, E., et al., *Expression of Specific Markers and Particle Transport in a New Human Intestinal M-Cell Model*. Biochemical and Biophysical Research Communications, 2000. 279(3): p. 808-813.
26. Tanoue, T., et al., *In vitro model to estimate gut inflammation using co-cultured Caco-2 and RAW264.7 cells*. Biochemical and Biophysical Research Communications, 2008. 374(3): p. 565-569.
27. Takayama, K., et al., *Generation of Human iPSC-Derived Intestinal Epithelial Cell Monolayers by CDX2 Transduction*. Cellular and molecular gastroenterology and hepatology, 2019. 8(3): p. 513-526.
28. Negoro, R., et al., *Efficient Generation of Small Intestinal Epithelial-like Cells from Human iPSCs for Drug Absorption and Metabolism Studies*. Stem cell reports, 2018. 11(6): p. 1539-1550.
29. Takenaka, T., et al., *Human small intestinal epithelial cells differentiated from adult intestinal stem cells as a novel system for predicting oral drug absorption in humans*. Drug Metab Dispos, 2014. 42(11): p. 1947-54.
30. Kasendra, M., et al., *Development of a primary human Small Intestine-on-a-Chip using biopsy-derived organoids*. Sci Rep, 2018. 8(1): p. 2871.
31. Lee, J., J.H. Choi, and H.J. Kim, *Human gut-on-a-chip technology: will this revolutionize our understanding of IBD and future treatments?* Expert Rev Gastroenterol Hepatol, 2016. 10(8): p. 883-5.
32. Clemente, J.C., et al., *The impact of the gut microbiota on human health: an integrative view*. Cell, 2012. 148(6): p. 1258-1270.
33. Jalili-Firoozinezhad, S., et al., *A complex human gut microbiome cultured in an anaerobic intestine-on-a-chip*. Nat Biomed Eng, 2019. 3(7): p. 520-531.
34. Shah, P., et al., *A microfluidics-based in vitro model of the gastrointestinal human-microbe interface*. Nat Commun, 2016. 7: p. 11535.
35. Claus, S.P., H. Guillou, and S. Ellero-Simatos, *The gut microbiota: a major player in the toxicity of environmental pollutants?* npj Biofilms and Microbiomes, 2016. 2(1): p. 16003.
36. Wang, X.-q., et al., *Gut microbiota as important modulator of metabolism in health and disease*. RSC Advances, 2018. 8(74): p. 42380-42389.
37. van der Meer, A.D. and A. van den Berg, *Organs-on-chips: breaking the in vitro impasse*. Integr Biol (Camb), 2012. 4(5): p. 461-70.
38. Kimura, H., et al., *An on-chip small intestine-liver model for pharmacokinetic studies*. J Lab Autom, 2015. 20(3): p. 265-73.
39. Choe, A., et al., *Microfluidic Gut-liver chip for reproducing the first pass metabolism*. Biomedical Microdevices, 2017. 19(1): p. 4.
40. Maschmeyer, I., et al., *A four-organ-chip for interconnected long-term co-culture of human intestine, liver, skin and kidney equivalents*. Lab Chip, 2015. 15(12): p. 2688-99.
41. Kim, J.H., et al., *A Microfluidic Chip Embracing a Nanofiber Scaffold for 3D Cell Culture and Real-Time Monitoring*. Nanomaterials (Basel), 2019. 9(4).
42. Montanez-Sauri, S.I., et al., *Automation of three-dimensional cell culture in arrayed microfluidic devices*. J Lab Autom, 2011. 16(3): p. 171-85.
43. Yu, F. and D. Choudhury, *Microfluidic bioprinting for organ-on-a-chip models*. Drug Discovery Today, 2019. 24(6): p. 1248-1257.
44. Wang, Y., et al., *A microengineered collagen scaffold for generating a polarized crypt-villus architecture of human small intestinal epithelium*. Biomaterials, 2017. 128: p. 44-55.
45. Creff, J., et al., *Fabrication of 3D scaffolds reproducing intestinal epithelium topography by high-resolution 3D stereolithography*. Biomaterials, 2019. 221: p. 119404.
46. de Haan, P., et al., *Digestion-on-a-chip: a continuous-flow modular microsystem recreating enzymatic digestion in the gastrointestinal tract*. Lab Chip, 2019. 19(9): p. 1599-1609.
47. Zhang, Z., et al., *Focusing-enhanced mixing in microfluidic channels*. Biomicrofluidics, 2008. 2(1): p. 14101-14101.
48. Toonder, J.M.J.d. and P.R. Onck, *Microfluidic manipulation with artificial/bioinspired cilia*. Trends in Biotechnology, 2013. 31(2): p. 85-91.

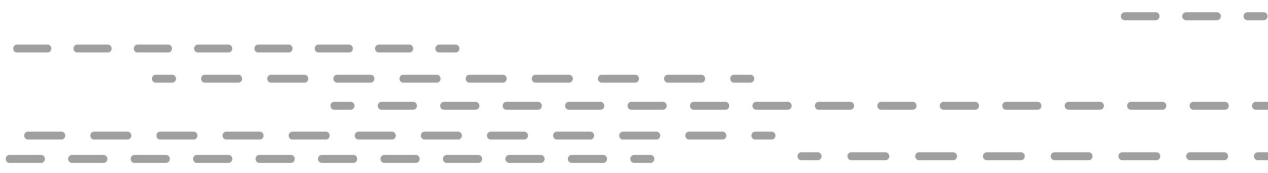
49. Cremer, J., et al., *Effect of flow and peristaltic mixing on bacterial growth in a gut-like channel*. Proc Natl Acad Sci U S A, 2016. 113(41): p. 11414-11419.
50. Santbergen, M.J.C., et al., *Online and in situ analysis of organs-on-a-chip*. TrAC Trends in Analytical Chemistry, 2019. 115: p. 138-146.
51. Bavli, D., et al., *Real-time monitoring of metabolic function in liver-on-chip microdevices tracks the dynamics of mitochondrial dysfunction*. Proceedings of the National Academy of Sciences, 2016. 113(16): p. E2231.
52. Son, K.J., et al., *Detecting cell-secreted growth factors in microfluidic devices using bead-based biosensors*. Microsystems & Nanoengineering, 2017. 3(1): p. 17025.
53. Magnusson, E.B., et al., *Real-time optical pH measurement in a standard microfluidic cell culture system*. Biomed Opt Express, 2013. 4(9): p. 1749-58.
54. Moya, A., et al., *Online oxygen monitoring using integrated inkjet-printed sensors in a liver-on-a-chip system*. Lab on a Chip, 2018. 18(14): p. 2023-2035.
55. Roelse, M., et al., *Calcium Imaging of GPCR Activation Using Arrays of Reverse Transfected HEK293 Cells in a Microfluidic System*. Sensors (Basel, Switzerland), 2018. 18(2): p. 602.
56. Henry, O.Y.F., et al., *Organs-on-chips with integrated electrodes for trans-epithelial electrical resistance (TEER) measurements of human epithelial barrier function*. Lab on a Chip, 2017. 17(13): p. 2264-2271.
57. Au - van der Helm, M.W., et al., *Fabrication and Validation of an Organ-on-chip System with Integrated Electrodes to Directly Quantify Transendothelial Electrical Resistance*. JoVE, 2017(127): p. e56334.
58. Santbergen, M.J.C., et al., *Dynamic in vitro intestinal barrier model coupled to chip-based liquid chromatography mass spectrometry for oral bioavailability studies*. Analytical and Bioanalytical Chemistry, 2020. 412(5): p. 1111-1122.
59. Louisse, J., K. Beekmann, and I.M.C.M. Rietjens, *Use of Physiologically Based Kinetic Modeling-Based Reverse Dosimetry to Predict in Vivo Toxicity from in Vitro Data*. Chemical Research in Toxicology, 2017. 30(1): p. 114-125.
60. Herland, A., et al., *Quantitative prediction of human pharmacokinetic responses to drugs via fluidically coupled vascularized organ chips*. Nat Biomed Eng, 2020. 4(4): p. 421-436.
61. EURL ECVAM, I.f.H.a.C.P., *Alternative methods for regulatory toxicology – a state-of-the-art review*. 2014, European Commission Publications Office of the European Union.
62. Heringa, M.B., et al., *The value of organs-on-chip for regulatory safety assessment*. ALTEX, 2020. 37(2): p. 208-222.
63. Coecke, S., et al., *Toxicokinetics as a key to the integrated toxicity risk assessment based primarily on non-animal approaches*. Toxicology in Vitro, 2013. 27(5): p. 1570-1577.
64. FDA. *FDA Researchers to Evaluate 'Organs-on-Chips' Technology*. 2017; Available from: <https://www.fda.gov/food/cfsan-constituent-updates/fda-researchers-evaluate-organs-chips-technology>.





CHAPTER 7

Summary



Summary

Chapter 1 introduced the principal objectives of this thesis and background information regarding to the small intestinal complex anatomy, functions and the laboratory models that have been employed or developed both *in vivo* animal models and *in vitro* models to investigate specific aspects of its functions focusing on absorption and local responses. The current state of the art and the limitations of each model was reported with the highlighting on the *in vitro* (dynamic) gut-on-chip models. Finally, the general outline of the present thesis was provided.

Chapter 2 reported the development of a gut-on-chip model with aiming to study the potential cellular association and transport of (17 congeners) dioxin which is an important class of food contaminants entered the human body via the oral exposure route. For this, Caco-2 cells were cultured on a porous polyester membrane which assembled between two glass slides to form two separate flow chamber and were then introduced to the fluid flow. Glass syringes, polytetrafluoroethylene tubing and glass microfluidic chips were selected to minimize surface adsorption of the highly lipophilic dioxins during the transport studies. Confocal microscopy studies was used to visualize cell barrier formation and polarization and gas chromatography-high resolution mass spectrometry, a very sensitive method, was used to assess the cellular association and transport of individual dioxin congeners across the Caco-2 cell monolayers. The relationship between dioxin structures and their transport across a cell monolayer was revealed by quantitative structure–property relationship modelling. The results obtained showed that cells upon culturing under constant flow in the gut-on-chip model formed complete and polarized monolayers as observed under static conditions in Transwells. The amount of transported dioxin mixture was similar in both the dynamic gut-on-a-chip model and the static Transwell model. The transport of individual congeners corresponded with their number of chlorine atoms and substitution patterns. The general conclusion was the gut-on-a-chip model can be used, as well as the traditional static Transwell system, to study the cellular association and transport of lipophilic compounds like dioxins.

In **Chapter 3**, the development and characterization of the gut-on-chip model was further explored. In this chapter the transport of well-known pharmaceuticals (antipyrene, ketoprofen, digoxin and amoxicillin) with available information on *in vivo* bioavailability and transport mechanisms (high and low oral permeability class compounds with different absorption mechanisms) was assessed. In addition to visualizing the (Caco-2) cells by confocal microscopy as in **Chapter 2**, cell layer integrity and cell differentiation was additionally evaluated by determination of lucifer yellow transport and alkaline phosphatase activity in the cells. The interplay between experimental outcome and engineering in microfluids (geometry, laminar flow) was also reported. The results obtained showed that in the dynamic gut-on-chip model the transport of the high permeability compounds antipyrene,

ketoprofen and digoxin was lower (*i.e.* 4.2-, 2.7- and 1.9-fold respectively) compared to the transport in the static Transwell model which most likely can be explained by the laminar flow defined by the low Reynolds number in the gut-on-chip model resulting in less contact of the compounds with the cell surface. The transport of the low permeability compound, amoxicillin, was similar in both the dynamic and static *in vitro* model. The obtained transport values of the compounds were in line with the compound Biopharmaceuticals Classification System and were also line with data reported in human *in vivo*, fraction absorbed in human (%Fa) with the exception of Digoxin permeability (higher transport in this study) which likely can be explained by the low expression of P-gp, the efflux transporter, in Caco-2 cells. The general conclusion was the gut-on-chip provides an adequate model for transport studies based on the tested pharmaceutical compounds.

Chapter 4 assessed the basal gene expression of Caco-2 cells, cultured statically or dynamically in the gut-on-chip device and compared to that of intestinal tissues *in vivo*. For this, a whole genome transcriptomics analysis was applied to compare the gene expression profiles on a single gene level and the level of biological pathways. For the *in vivo* data, the data from a publicly accessible database that contained transcriptome profiles from duodenum, jejunum, ileum, and colon) from healthy human volunteers was used and a principal component analysis was performed. The results obtained showed dynamic culture conditions led to a total of 5927 differentially expressed genes (3280 upregulated and 2647 downregulated genes) compared to static culture conditions. Gene set enrichment analysis revealed that upregulated pathways were mainly related to cellular homeostasis, immunological responses, cell growth and death, as well as signal transduction, while general cellular metabolism and absorption pathways were repressed. The comparison of the *in vitro* gene expression data with transcriptomic profiles of human *in vivo* duodenum, jejunum, ileum and colon tissue samples did not reveal a striking similarity with any of these segments, even though both models slightly vary from each other. Since some specific gene functions are differently modulated in each model, it is concluded that both the static and the dynamic gut-on-chip model could be used to study human intestinal epithelial responses depending on the endpoint of interest.

Chapter 5 presented the responses of Caco-2 cells cultured under statically or dynamically in the gut-on-chip device following exposure to different classes of nanomaterials, *i.e.* titanium (TiO₂) and zinc oxide nanomaterials (ZnO) at both a single gene level and the level of biological pathways by applying whole genome transcriptomics analysis and the comparison of the results to their respective control groups and between the two culture conditions. TiO₂ and ZnO nanomaterials are among the most popular food-related nanomaterials used in the food industry and these two nanomaterials cover extreme physicochemical properties. TiO₂ remains as a particle in suspension whereas ZnO nanomaterials readily dissolve. *In vitro* Sedimentation, Diffusion and Dosimetry (ISDD)

model was used to calculate deposited mass of nanomaterials on the cells according to their predicted sedimentation, diffusion to achieve the similarly exposed doses between the different models. The results obtained showed that both nanomaterials induced stronger response at a single gene level and affected pathways revealed by gene set enrichment analysis in cells cultured in the gut-on-chip when compared to the static model. It might be concluded that the fluid flow resulting in shear stress in the gut-on-chip is a major factor in the difference in cell responses (sensitivity) as observed in **Chapter 4**. The dynamically cultured cells influence on sensitivity in response to nanomaterial exposure, and thus might be an attractive tool to create a custom use model in the toxicological hazard identification.

Chapter 6 of the present thesis included an overview on principal results and the discussion with remarks of the results obtained in the thesis and future perspectives. Also, in this chapter the concluding on the value obtained from an organ-on-chip model to support of the use of the model in toxicological risk assessment was incorporated.



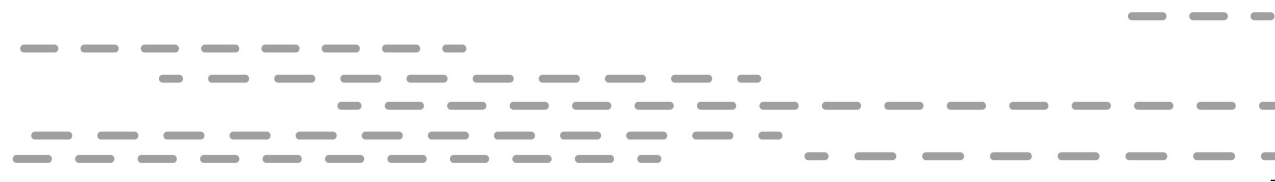


Acknowledgements

About the author

List of publications

Overview of completed training activities



Acknowledgements

This journey would not have been possible without the support of countless people. I would like to take this opportunity to express my thanks to them for giving me enormous assistance.

First, I would like to give my sincere gratitude to my promotion team. I am deeply grateful to my co-promotors (supervisors) Hans and Meike. Let's start with Hans. We have known each other by the introducing of Dr Stefan Weigel after he visited my lab in Thailand, thank you also Stefan. After the discussion with my boss, Hans finally accepted me as his student and continuously supported me through these years. Hans, thank you for your big doses of patience, knowledge and full support. Your hard questions allowed me to improve myself and your insightful answers make me think wider. My other co-promotor is Meike who gave me also assistance especially with her meticulous opinion. Thank you Meike for your enthusiasm to help and being a buffer person during tough discussion we sometimes had. Also, your talent in art is very helpful to clearly represent scientific data as a schematic in this thesis. It inspires me to learn arts for making my presentation more attractive and understandable.

My sincere thanks next go to Ivonne, my promotor. Thank you for giving me an opportunity to be a member at TOX. I still remember how excited I was when I received the acceptance letter from you. During these 5 years, I really appreciate your useful guidance on my project as well as extremely fast and helpful suggestions on my thesis chapters. Your critical feedback always makes my work better and more completed.

Next comes to my office mates, I would like to start with Ashraf and Milou who had the same fate with me in the same room as a PhD candidate. We shared moments of deep anxiety but also excitement, and of course knowledge. I have learnt a lot from them. They could help me to finish a task within few minutes while I would spend a day to get it done myself. Thanks for being supportive and understanding, it was very meaningful for me. The others are Loes and Nicole who worked among the three stressful PhD candidates. It was not easy for them (I guess) but they managed!! Loes, thank you very much for your help with my experiments. You are also the important person of this success. Nicole, thanks for being kind and friendly, especially your positive words whenever I was demotivated.

I want to thank all colleagues at WFSR (RIKILT) who I got their kind support. All members in the toxicology group; Ad, Aafke, Deborah, Jochem, Geert, Ron and Ans Punt, thanks for your suggestions and ideas on my work during a regular meeting. Specially, Ans, many thanks for your guideline on the calculation related to compound permeability and so on. Ron, Gerlof and Yoran, I really appreciate your supporting knowledge about dioxin and CALUX assay. Geert, Astrid, Henry and Liza, thank you for your support and guidance in lab procedures and machine manipulation. Victor, many thanks for all simulation data and kindly teaching me computer modelling, you have made a great impact on my work. I have learnt a lot from you. Special thanks also go to Greet, for teaching me the HPLP operation and troubleshooting. We worked with the special (old) model HPLC which was needed a

very special care as well. Although you were super busy with your own projects, you were still available for me and never complained when I asked for help even a small thing I should have known myself. My thanks extend to Guillaume for his help in GC-MS analysis. Rudd Peters, thank you for providing me the material used in my last chapter.

There are people at WFSR that I would like to extend my thanks to them for being supportive; Lonneke, Corina, Toine, Hannie, Marcia and all administrative staffs. This includes my students who did their internship/thesis at WFSR; Samuel, Huiyi and Jiaqing. It was a great experience working with you and you all did a good job.

My sincere thanks must also go to the members of the assessment committee; Assoc. Prof. Dr. Chuda Chittasupho, Dr. Evita van de Steeg, Prof. Dr. E.M.J. Sabeth Verpoorte and Prof. Dr. J.M. Jerry Wells for reading and allowing me to defend my thesis.

I would like to thank all the staffs and PhD at TOX for their prompt support and friendship (also people who already left the department); Lu, Jia, Ixchel, Qianrui, Mengying, Shou, Danlei, Annelies, Diana, Katja, Chen, Bohan, Mebrathom, Jing, Rozani, Isaac, Artem, Akanksha, Bert, Laura, Hans vdB, Lidy, Sebas, Nico, Carla and Gerda. Special mention goes to my office mates at TOX where I sit from time to time. Aziza, Biyao, Shen Sheng, thanks for a good atmosphere and a good wish whenever I had a meeting. Felicia, thanks for checking on me always. Miaoying, Marta and Lenny thank you for encouraging, your warm words and playing squash with me. Diego and Suparmi, many thanks for your useful advice during my stressful moment of finalizing the thesis. I felt very lucky to have you, although I was in the difficult time.

Nacho, there is no proper word to express how supportive you are for me. Thanks for believing in me and keeping me motivated. Sharing experiences with you made me stronger and more optimistic. Georgia, I don't see how I could have passed all those difficulties without you. Thanks a million for supporting and being there for me. You have always been a major source of backing when my life gets me down.

I am very grateful to Guido for his amazing expertise in bioinformatic when helping me with transcriptomic data analysis and the editing of the thesis. Guido, you are very helpful and thoughtful. I would like to thank also Remco Fokkink who supported me with the DLS analysis.

A very special word of thanks goes for my paranympths Milou and Menno, who have been helping me for all over these years. Thank you for introducing me a traditional Dutch culture. It is a pity that our regular dinner has been ruined by Coronavirus but I promise I will be in the Netherlands again and learn (eat) more!!

I gratefully acknowledge the funding I received from the Royal Thai Government Scholarship through National Nanotechnology center (Nanotec) and Ministry of Higher Education, Science, Research and Innovation to undertake my PhD project and the people in my institute, Nanotec who always support me since the first day I decided to apply for the scholarship. Special thanks go to Pi Ung (my ex-boss), Pa Da, Pa May, Dr Bum, Dr Air, Dr

Ying and Dr Yui. My appreciation extends also to Ple, Lux, Dr Kate, Nong Koy and Annie (Apiwan) for an encouragement and Aj Chalong who inspired me to pursue a PhD program.

I am always grateful to the Thai community in Wageningen for their friendship, help and tasty food. They made my time in the Netherlands more joyful and memorable. Special mention goes to my tour guide: Kun Nong, Jae and Nong Ohm and MilkTea council: Nong Aim and Nong Wee. Besides, I deeply acknowledge people, Porgaew, NiNew, Nong Mam, Pi Waew and Kees who were by my side when I was under a lot of stress during thesis writing.

ขอบคุณเพื่อนเลิฟ พินนี่ ที่เป็นเพื่อนซ้อป เพื่อนเที่ยว เพื่อนที่เข้าใจ ดูแล ระหว่างที่ ต้องห่างบ้านไกลมือง และยังช่วยทำปกเล่ม ธีชชด้วย ขอขอบคุณ เพื่อนๆ ที่เมืองไทย โอ้ จี หนึ่ง (กอล์ฟ น้ำหนุน น้ำเหนือ) ต้น อ้อย อัง ที่คอยให้กำลังใจ พาไปเที่ยว ไปกินทุกครั้งทีกลับ ไทยและยังช่วยเหลือดูแลคนที่บ้านให้ด้วย ขอขอบคุณ หนู พี่นุ (น้องมุก น้องเมย์) ที่ส่งสมุนไพรมารักษาและมาเจอกันตอนกลับไทย ขอขอบคุณ เบญ กาญจน์ บิ ที่มาเจอ คอยทักทายถามไถ่ ให้กำลังใจเสมอๆ

(I would like to thank my lovely friend, Pinnie. Thank you for being a travel (shopping) buddy, understanding and caring when I was far away from home and creating the wonderful thesis cover. My thanks also go to friends in Thailand; Oha, G, Nueng (Nam Noon, Nam Nuca, Golf), Ton, Oil and Aung, who always encourage me and arranged trips (also eating) whenever I returned to Thailand. My appreciation goes to them for taking care of my family as well. My thanks next come to Noo and Pi Nu (Nong Mook, Nong May) for sending me herbs and joining a party during my home visit and to Ben, Kan and Bee for encouraging and a joyful meeting in Thailand.)

สุดท้าย บุคคลที่สำคัญที่สุด ขอขอบคุณพ่อ แม่ ไข่มุน กฤษ ที่คอยให้กำลังใจตลอดอดทนทำให้ผ่านเวลาที่ยากลำบากมาได้ รวมถึงดูแลตอนที่ป่วยและกลับไปรักษาตัวที่ประเทศไทย และขอขอบคุณ ไข่มุนกับกฤษ ที่ช่วยดูแลเป็นธุระเรื่องทางประเทศไทยให้ทุกอย่าง ในระหว่างที่อยู่เนเธอร์แลนด์ โดยเฉพาะช่วยดูแล พ่อกับแม่

(Lastly, the most important people, I would like to give a big thanks to my parents, Khai Toon and Kit for their supporting and encouraging. This made me get through all difficult times and they also took a good care of me when I was sick and returned to Thailand. Thank you!! Khai Toon and Kit for taking care of everything in Thailand during my study in the Netherlands, especially for taking care of parents.)

Kornphimol Kulthong
2020

About the author

Kornphimol Kulthong was born on 22nd June 1978 in Chai Nat, Thailand. In 2000, she completed her BSc studies in Chemistry at Srinakharinwirot University. Afterwards, she worked as R&D for 5 years in the cosmetic industry and realized that doing research is her most favourite job. Therefore, she decided to follow her MSc program in Pharmacology at Chulalongkorn University with the thesis related to drug metabolism enzymes (2005-2008). She has been working as an assistant researcher for National Nanotechnology Centre in Thailand (Ministry of Higher Education, Science, Research and Innovation) since 2008 and has professional experience in conducting research on toxicity of nanoparticles and nano-products. In addition, Kornphimol was an exchange researcher at Kanazawa University, Japan (in 2010) where she investigated effects of silver nanoparticles on hepatic cytochrome P450 enzymes. Kornphimol got a scholarship from the Royal Thai Government and moved to the Netherlands in 2015 to be a PhD candidate at WFSR and the division of Toxicology of Wageningen University & Research under the supervision of Prof. Dr Ivonne M.C.M Rietjens, Dr Hans Bouwmeester and Dr Meike van der Zande. During the PhD project, Kornphimol participated in the post graduate education in toxicology (PET) which will allow her to register as European Registered Toxicologist (ERT). Recently, Kornphimol has returned to Thailand to continue her job with the aim of implementing an *in vitro* model for nanotoxicity evaluation.



List of publications

This thesis

- Kornphimol Kulthong, Loes Duivenvoorde, Barbara Z. Mizera, Deborah Rijkers, Guillaume ten Dam, Gerlof Oegema, Tomasz Puzyn, Hans Bouwmeester and Meike van der Zande. **Implementation of a dynamic intestinal gut-on-a-chip barrier model for transport studies of lipophilic dioxin congeners.** *RSC Adv.* 2018, 8: 32440-32453.
- Kornphimol Kulthong, Loes Duivenvoorde, Huiyi Sun, Samuel Confederat, Jiaqing Wu, Bert Spenkelink, Laura de Haan, Victor Marin, Meike van der Zande, Hans Bouwmeester. **Microfluidic chip for culturing intestinal epithelial cell layers: Characterization and comparison of drug transport between dynamic and static models.** *Toxicol In Vitro.* 2020; 65: 104815.

Other publications

- Nootcharin Wasukan, Sujittra Srisung, Kornphimol Kulthong, Suwimon Boonrungsiman and Rawiwan Maniratanachote. **Determination of silver in personal care nanoproducts and effects on dermal exposure.** *J. Nanopart. Res.* 2015, 17: 1-11.
- Nootcharin Wasukan, Sujittra Srisung, Mayuso Kuno, Kornphimol Kulthong, Rawiwan Maniratanachote. **Interaction evaluation of silver and dithizone complexes using DFT calculations and NMR analysis.** *Spectrochimica Acta Part A: Molecular and Biomolecular Spectroscopy.* 2015, 149: 830–838.
- Porn-tipa Chairuangkitti, Somsong Lawanprasert, Sittiruk Roytrakul, Sasitorn Aueviriyavit, Duangkamol Phummiratch, Kornphimol Kulthong, Pithi Chanvorachote, and Rawiwan Maniratanachote. **Silver nanoparticles induce toxicity in A549 cells via ROS-dependent and ROS-independent pathways.** *Toxicology In Vitro.* 2013, 27: 330-338.
- Sasitorn Aueviriyavit, Duangkamol Phummiratch, Kornphimol Kulthong, and Rawiwan Maniratanachote. **Titanium dioxide nanoparticles-mediated in vitro cytotoxicity does not induce Hsp70 and Grp78 expression in human bronchial epithelial A549 cells.** *Biological Trace Element Research.* 2012, 149: 123-132.
- Kornphimol Kulthong, Rawiwan Maniratanachote, Yuki Kobayashi, Tatsuki Fukami, and Tsuyoshi Yokoi. **Effect of silver nanoparticles on rat hepatic cytochrome P450.** *Xenobiotica.* 2012, 42: 854-862.
- Kornphimol Kulthong, Sujittra Srisung, Kanittha Boonpavanitchakul, Wiyong Kangwansupamonkon, and Rawiwan Maniratanachote. **Determination of silver nanoparticles released from antibacterial fabrics into artificial sweat.** *Particle and Fibre Toxicology.* 2010, 7: 8.

Overview of completed training activities

Discipline specific courses

Molecular toxicology, PET (Amsterdam, 2016)

Cell Toxicology, PET (Leiden, 2016)

Organ Toxicology, PET (Nijmegen, 2017)

Pathobiology, PET (Utrecht, 2016)

Epidemiology, PET (Utrecht, 2016)

Immunotoxicology, PET (Utrecht, 2016)

Toxicogenomic, PET (Maastricht, 2017)

8th International congress of Asian society of toxicology, Asian Society of Toxicology (Thailand, 2018)

General courses

VLAG PhD week, VLAG (Baarlo, 2016)

Laboratory animal science, PET (Utrecht, 2017)

Risk assessment, PET (Wageningen, 2017)

Writing successful grant proposals, Elevate (online, 2019)

Searching and organizing literature, WUR (Wageningen, 2019)

Adobe InDesign, WUR (Wageningen, 2019)

Optional courses and other activities

Preparation of research proposal

Group meetings and attending scientific presentations, TOX/WFSR

Food toxicology, WUR (Wageningen, 2016)

Environmental toxicology, WUR (Wageningen, 2017)

General toxicology, WUR (Wageningen, 2018)

**Approved by graduate school VLAG*

The research described in this thesis was financially supported by the Royal Thai Government through a doctoral scholarship of National Nanotechnology Center (Ministry of Higher Education, Science, Research and Innovation) for Kornphimol and the Dutch Ministry of Agriculture, Nature and Food Quality (project KB-23-002-022).

Financial support from Wageningen University & Research for printing this thesis is gratefully acknowledged.

Cover design: Pintip Vajaroithai and Kornphimol Kulthong

Printing: ProefschriftMaken

